Development of a Wide Band MeV Gamma-Ray Telescope Based on a Gaseous Time Projection Chamber and a Scintillation Camera

Kazuki Ueno

Department of Physics, Faculty of Science, Kyoto University
Kitashirakawa Oiwake-cho, Sakyo-ku, Kyoto, 606-8502, Japan

This thesis was submitted to the Department of Physics,
Graduate School of Science, Kyoto University
on Jan 5, 2011
in partial fulfillment of the requirements
for the degree of Doctor of Philosophy in physics.

Abstract

In the MeV gamma-ray astronomy, some observations with telescopes using a Compton scattering or pair-creation have been successful. However, the detection sensitivity and angular resolution of those in the energy range from sub to several tens of MeV are worse than those of detectors in the X-ray, GeV, and TeV gamma-ray regions due to the difficulty of the detection of Compton scattering or pair-creation events. Thus, a new observation technique for MeV gamma-ray telescope is required. Therefore, we have developed a tracking Compton and pair-creation gamma-ray telescope using a gaseous time projection chamber (μ-TPC) and a GSO(Ce) scintillation camera for the aim to conduct all sky survey with a sensitivity 10 times better than that of COMPTEL and an angular resolution of 1 degree. In the Compton mode, μ-TPC detects the 3-dimensional tracks and energy of recoil electron and scintillation camera detects the absorption point and the energy of Compton scattered gamma ray event by event. In the pair-creation mode, the μ-TPC detects the 3-dimensional tracks of electron-positron pair and the scintillation camera detects the energy of those event by event. Several prototypes were developed and their performances with Compton mode in the sub MeV region were already studied. As the preliminary step toward the all sky survey, we proceed the balloon experiments, and first experiment for the purpose of the observation of the cosmic diffuse and atmospheric background gamma rays with Compton mode was done in 2006.

For the next balloon experiment, we have developed a large size gamma-ray telescope with Compton mode in order to improve the effective area. The telescope consisted of a $30\times30\times30$ cm^3 μ-TPC filled with Ar and C_2H_6 gas mixture at 1 atm and a 30×30 cm^2 scintillation camera. Using the radioactive sources, the fundamental performances of the telescope was investigated. We succeeded in the 2-dimensional imaging and obtained the energy and angular resolutions of 12.3% and 9.8° (FWHM) at 662 keV, respectively. The detection efficiency and FOV were 9.0×10^{-6} and 1 str, respectively. Furthermore, we developed the readout system with low power consumption of the scintillation camera for the experiment in the sky. We succeeded in the power saving of the readout system without degradation of performances of the scintillation camera.

In parallel, we started to develop the telescope with pair-creation mode and performed the principle-proof experiment using a laser inverse Compton gamma-ray beam at National Institute of Advanced Industrial Science and Technology (AIST). Using the gamma-ray beam with the mean energies of 8.7 and 18.0 MeV, the 3-dimensional tracks of electron-positron pair were obtained. From the data, we succeeded in the 2-dimensional imaging, and then the fundamental performances were investigated. For the 18.0 MeV gamma rays, the angular resolution and the detection efficiency were 7.0° at 68% containment and 1.77×10^{-5}, respectively. These values were consistent with those simulated for the same setup. From these results and simulation, the potential which the angular resolution and the detection efficiency will be better than those of the silicon strip detector aboard the Fermi satellite was shown.

Contents

I Introduction **13**

1 MeV gamma-ray astronomy **14**

1.1 Production mechanism of gamma ray 14

1.1.1 Synchrotron radiation 16

1.1.2 Bremsstrahlung 17

1.1.3 Inverse Compton scattering 17

1.1.4 Nuclear transitions and decay 17

1.1.5 Annihilation 18

1.2 Sky in gamma ray 19

1.2.1 All sky map 19

1.2.2 Galactic diffuse gamma ray 19

1.2.3 Extragalactic diffuse gamma ray 19

1.3 Source of gamma rays 23

1.3.1 Supernova remnant 23

1.3.2 Spin down pulsars 24

1.3.3 Black hole 27

1.3.4 Galactic center 28

1.3.5 Active galactic nuclei (AGN) 29

1.3.6 Solar flare 30

1.3.7 Gamma ray burst 30

2 Instruments for MeV gamma-ray astronomy **33**

2.1 Interaction of gamma rays with matter 33

2.1.1 Photoelectric absorption 33

2.1.2 Compton scattering 34

2.1.3 Pair creation 35

2.2 MeV gamma-ray imaging 35

2.2.1 Active and passive collimators 36

2.2.2 Coded aperture imaging 37

2.2.3 Gamma-ray lenses 38

2.2.4 Compton imaging 39

2.2.5 Pair tracking 41

2.2.6 Summary of MeV gamma-ray imaging 42

2.3 Low and medium energy gamma-ray observatories 44

2.3.1 CGRO 44

2.3.2 INTEGRAL 46

3 Future of a Compton and pair tracking telescope **47**
3.1 Goal for the future of gamma-ray telescope . . . 47
3.2 Compton mode in the low energy band . . . 49
3.2.1 Principle of electron tracking Compton imaging . . . 49
3.2.2 Angular resolution determination . . . 50
3.2.3 Doppler broadening . . . 51
3.2.4 Multiple scattering . . . 52
3.3 Pair creation mode for high energy band . . . 54
3.3.1 Principle of pair tracking imaging . . . 54
3.3.2 Angular resolution determination . . . 56
3.4 Simulation study for pair creation mode . . . 57
3.4.1 Setup . . . 59
3.4.2 Angular resolution . . . 59
3.4.3 Detection efficiency . . . 60
3.5 SMILE . . . 64

II Improvement of the gamma-ray telescope with Compton mode **67**

4 Telescope with Compton mode for a next balloon experiment **68**
4.1 Overview of SMILE-2 . . . 68
4.2 Enlargement of a gaseous time projection chamber . . . 68
4.2.1 Micro pixel chamber (μ-PIC) . . . 68
4.2.2 Readout system . . . 70
4.2.3 Performances of large size μ-PIC . . . 74
4.2.4 Time projection chamber with μ-PIC and GEM . . . 74
4.2.5 Performances of large size μ-TPC . . . 77
4.3 Scintillation camera . . . 84
4.3.1 Scintillator and PMT . . . 84
4.3.2 Readout system and compactification . . . 85
4.3.3 Performance of scintillation camera . . . 88
4.4 Large size gamma-ray telescope with Compton mode . . . 91
4.4.1 Setup . . . 91
4.4.2 Performance of a large size gamma-ray telescope . . . 96

5 Low power consumption readout system for scintillation camera **103**
5.1 Low power consumption readout system for scintillation camera . . . 103
5.1.1 ASIC readout system . . . 103
5.1.2 Attenuator board . . . 103
5.1.3 Measurements and results . . . 105

III First light of the gamma-ray telescope with pair creation mode **111**

6 Prototype telescope with pair creation mode **112**
6.1 Detector concept . . . 112
6.1.1 Detector design . . . 112
6.1.2 μ-TPC for the prototype telescope with pair creation mode . . . 112
6.1.3 Scintillation camera for the prototype telescope with pair creation mode . . . 114
6.2 New DAQ system for tracking . . . 114
6.2.1 TPC mode-II . . . 115

6.2.2 Performance of TPC mode-II . . . 116
6.3 Performance of the μ-TPC . . . 119
6.3.1 Gain uniformity . . . 119
6.3.2 Energy resolution . . . 119
6.3.3 Drift velocity and position resolution . . . 119
6.4 Prototype telescope with pair creation mode . . . 123

7 Beam experiment **125**
7.1 Experimental setup . . . 125
7.1.1 Laser-Compton scattering gamma ray . . . 125
7.1.2 AIST LCS gamma-ray facility . . . 125
7.1.3 Setup of the prototype telescope . . . 126
7.2 Status of beam experiment . . . 126
7.2.1 Experiment 1 . . . 128
7.2.2 Experiment 2 . . . 128
7.2.3 Run summary . . . 131

8 Event reconstruction **132**
8.1 Clustering method . . . 132
8.1.1 Outline of the clustering method . . . 132
8.1.2 Rough event selection . . . 134
8.1.3 Clustering . . . 134
8.1.4 Calculation of vector and vertex point of electron-positron pair for two or more clusters event . . . 136
8.1.5 Calculation of vector and vertex point of electron-positron pair for one cluster event . . . 137
8.1.6 Event selection . . . 137
8.2 Hough transform method . . . 138
8.2.1 Hough transform . . . 138
8.2.2 Outline of the Hough transform method . . . 141
8.2.3 Hough transform for obtained data . . . 143
8.2.4 Calculation of vector and vertex point for large opening angle event . . . 144
8.2.5 Calculation of vector and vertex point for small opening angle event . . . 145
8.2.6 Event selection and reconstruction . . . 145
8.3 Validity confirmation . . . 146

9 Results **148**
9.1 Results using clustering method . . . 148
9.2 Results using Hough transform method . . . 153

IV Summary **161**

10 Discussion **162**
10.1 Current status . . . 162
10.2 Future work . . . 164

11 Conclusion **166**

List of Figures

1.1 The history of Gamma-Ray Observatories [1] . . . 15
1.2 The attenuation by atmosphere in multi-wavelength [2] . . . 16
1.3 The distribution of the gamma-ray objects by EGRET [6] . . . 19
1.4 The all sky map by COMPTEL (1 - 30 MeV) [1] . . . 20
1.5 The all sky map in 1.8 MeV by COMPTEL [1] . . . 20
1.6 The all sky map by EGRET ($\geq$100 MeV) [1] . . . 20
1.7 The spectrum of galactic diffuse gamma ray [7]. Also shown is the bremsstrahlung (dot-dashed line), inverse Compton scattering (short-dashed line), and π^0 (triple-dot dashed line) model, positronium continuum (long-dashed line) and the thermal Raymond-Smith plasma component (dotted line). The total of the model components is also presented (solid line). . . . 21
1.8 The spectrum of extragalactic diffuse gamma ray [8]. The dot-dashed line and dashed line are estimated contributions from Seyfert I and Seyfert II, respectively. The tiple dot-dashed line is steep-spectrum quasar contribution, and the dotted line is Type Ia supernovae. Also the long dashed line is a possible blazar contribution assuming an average power law index of -1.7 below 4 MeV and -2.15 at higher energies. The solid line indicates the sum of all components. . . . 22
1.9 The light curve of SN1987A (infrared - ultraviolet) [9] . . . 23
1.10 The schematic view of pulsar [10] . . . 24
1.11 The spectra of gamma-ray pulsars [11] . . . 25
1.12 The pulse profile of crab pulsar [12] . . . 26
1.13 The spectrum of crab nebula (solid line: synchrotron radiation, dashed line: inverse Compton scattering) [13] . . . 26
1.14 The light curve of Cyg X-1 [14] . . . 27
1.15 The spectra in Soft state and Hard state (Cyg X-1) [14] . . . 27
1.16 The emission model of Soft(High) State [14] . . . 28
1.17 The emission model of Hard (Low) State [14] . . . 28
1.18 The spectrum of Galactic Center by OSSE [15] . . . 28
1.19 The map of Galactic Center at 511 keV by SPI/INTEGRAL [16] . . . 28
1.20 The schematic view of AGN [18] . . . 29
1.21 The multiwave spectrum of Centaurus A [19] . . . 29
1.22 The Spectrum of Blazar Mkn501 [20] . . . 29
1.23 The spectrum of Solar Flare (June 4, 1991) [21] . . . 30
1.24 light curve of GRB by BATSE and COMPTEL [22] . . . 31
1.25 The spectrum of GRB [22] . . . 32
1.26 The all sky map of GRB by BATSE [23] . . . 32

2.1 The cross section of the interaction of gamma rays and matter (Ar) [24] . . . 33
2.2 The significant interaction of gamma rays and matter [25] . . . 33
2.3 The angular distribution of Compton scattering [25] . . . 35

2.4 The schematic view of an X-ray focusing [26] . . . 36
2.5 The effective area of X-ray telescopes [26] . . . 36
2.6 The schematic view of passive collimator . . . 36
2.7 Coded mask [27] . . . 37
2.8 The schematic view of Laue Lens [29] . . . 38
2.9 The schematic view of Classical Compton Imaging . . . 39
2.10 The Imaging of Classical Compton and the detection of GRB with COMPTEL (GRB910505 [31]) . . . 40
2.11 The schematic view of a Multiple Compton camera . . . 41
2.12 The schematic view of an Electron Tracking Compton camera . . . 42
2.13 The schematic view of MEGA [34] . . . 42
2.14 The schematic view of pair tracking camera . . . 42
2.15 The schematic view of OSSE [1] . . . 44
2.16 The schematic view of COMPTEL [30] . . . 44
2.17 The schematic view of EGRET [1] . . . 46

3.1 The continuum sensitivities of X/Gamma-ray observatories . . . 47
3.2 The angular resolutions of X/Gamma-ray observatories . . . 48
3.3 The schematic view of the gamma-ray telescope . . . 49
3.4 The parameters in Electron Tracking Compton Imaging . . . 49
3.5 The E_γ dependence of ϕ, ψ, α ($E_0 = 662$ keV) . . . 51
3.6 The E_0 dependence of $\alpha_{\rm lim}$ . . . 51
3.7 The definition of ARM & SPD . . . 51
3.8 The ARM distribution of each electron orbit ($E_0 = 200$keV, Si) [35] . . . 52
3.9 The Z dependence of the ARM [35] . . . 53
3.10 The energy dependence of Doppler broadening [35] . . . 53
3.11 The cross section of the Compton scattering and the pair creation in Ar and ethane gas mixture(left) and Xe (right) . . . 54
3.12 The parameters in Pair Tracking Compton Imaging . . . 54
3.13 The distribution of the scattered angle of electron (positron) depending on the energy of incident gamma ray (5 - 40 MeV). Lines show the mean value of the distribution. . . . 56
3.14 The simplification to two dimension . . . 57
3.15 The probability of the energy dependency of the pair creation [37]. . . . 58
3.16 The calculated angular resolution limit in Ar (blue line) and Si (black line). The thickness is 500μm. The resolutions from the multiple scattering are given by blue and black dashed line corresponding to Ar and Si, respectively. The red dashed line is the resolution from the uncertainty of the opening angle. . . . 58
3.17 The schematic view (left) and the example of the 3-dimensional view (right) of the gamma-ray telescope in the simulation. . . . 59
3.18 The reconstructed images in Ar based gas mixture (left) and Xe based gas mixture (right) at 20 MeV by Equation (3.17) . . . 60
3.19 The ideal θ squared distribution of Ar based gas mixture (left) and Xe based gas mixture (right) at 20 MeV by Equation (3.17). . . . 60
3.20 The angular resolution as a function of the incident gamma-ray energy in Ar based gas mixture (blue) and Xe based gas mixture (red) from Equation (3.17). . 61
3.21 The reconstructed images in Ar based gas (left) and Xe based gas (right) by Equation (3.18) . . . 61
3.22 The θ squared distribution of Ar based gas mixture (left) and Xe based gas mixture (right) at 20 MeV by Equation (3.18). . . . 62

3.23 The angular resolution as a function of the incident gamma-ray energy in Ar based gas mixture (blue) and Xe based gas mixture (red) from Equation (3.18). . 62
3.24 The detection efficiencies of Ar based gas mixture (red line) and Xe based gas mixture (blue line). For the comparison, the probabilities of the pair creation of Ar based gas mixture (red dashed line) and Xe based gas mixture (blue dashed line) are also plotted. 63
3.25 The load map of SMILE. 65
3.26 The obtained fluxes of cosmic (left) and atmospheric (right) gamma rays in SMILE-1 [54]. 65

4.1 The schematic view of the gamma-ray telescope in the ideal condition. 69
4.2 The detection efficiency of large size telescope with the size of 30×30×30 cm^3 filled with CF_4 at 2 atm (red circle) and of SMILE-1 telescope (blue circle) as a function of the energy of the incident gamma rays. For comparison, the probability of Compton scattering in the CF_4 gas is also plotted (red line). 69
4.3 The schematic view of the prototype of the large size gamma-ray telescope. . . . 70
4.4 A schematic view of μ-PIC 70
4.5 A schematic cross-section of the pixel structure of the μ-PIC 71
4.6 The photograph of 30×30 cm^2 μ-PIC (left) and the photomicrograph of the μ-PIC (right) 71
4.7 Data acquisition system for 30×30 cm^2 μ-PIC 71
4.8 The photograph of the hight voltage supply and signal-extension board (left) and the circuit diagram of that (right) 72
4.9 A schematic view of the connection of a μ-PIC and a high voltage supply and signal-extension board 73
4.10 ASD board 73
4.11 ASD rack 73
4.12 Position encoding module 74
4.13 A block diagram of position encoding module 75
4.14 The effective gas gain of 30×30 cm^2 μ-PIC in comparison to the 10×10 cm^2 μ-PIC. 76
4.15 The effective gain map of 30×30 cm^2 μ-PIC (SN041129-1). 76
4.16 A energy spectrum of the X-rays from ^{109}Cd. The gas gain is about 4000, and the energy resolution (FWHM) is about 50% at 8.05 keV. 76
4.17 The photograph of 23×28 cm^2 GEM (left) and the photomicrograph of the GEM (right-top) The GEM is segmented in eight region. The width of region between two segments is 0.8 mm (right-bottom). 77
4.18 A schematic view of the μ-TPC with the μ-PIC and the GEM. 78
4.19 A photograph of 30 cm drift cage. 78
4.20 Gas gains as a function of the voltage supplied to the anode of the μ-PIC. The gas gains measured with GEM voltages of 275, 325, 350, and 375 are shown . . . 79
4.21 The effective gain map of 30×30×30 cm^3 μ-TPC composed of 30×30 cm^2 μ-PIC (SN071210-4) and 23×28 cm^2 GEM. 79
4.22 A typical energy spectrum of the X-rays from ^{133}Ba. 80
4.23 Energy resolution as a function of the energy. 80
4.24 Energy resolution uniformity. 81
4.25 The setup for cosmic muon detection. 81
4.26 The distribution of the drift time in clock counter. 82
4.27 The examples of the cosmic muon tracks. 82
4.28 The histogram of residual between the obtained points and the fitted straight line. The solid line is obtained by fitting with two-dimensional Gaussian. 83

4.29 The position resolution as a function of drift length. 84
4.30 .The GSO(Ce) PSA with the H8500. 85
4.31 The resistor chain board. 85
4.32 DC to HV converter (EMCO Q12N-5) 86
4.33 A schematic view of the compact PSA unit. 86
4.34 High voltage supply board 87
4.35 4ch preamplifier board 87
4.36 A photograph of the compact PSA unit. 87
4.37 The center of gravity image from ^{137}Cs source. 88
4.38 (X_{COG}, Y_{COG}) (top) and (X_{real}, Y_{real}) (bottom). 89
4.39 The image before correction (left) and the one after correction (right). 90
4.40 The x-projection of the forth row from top. 90
4.41 The spectrum of ^{137}Cs measured with the scintillation camera. 91
4.42 The energy resolution as a function of energy of the scintillation camera. 91
4.43 The photograph of the bottom absorber 92
4.44 The side view of alignment 93
4.45 The photograph of the prototype large size gamma-ray telescope 93
4.46 The diagram of data acquisition system 94
4.47 The timing charts of a cycle of the data acquisition. 95
4.48 The timing charts of a clear cycle. 95
4.49 The typical event of the reconstructed gamma ray 97
4.50 The obtained images of the different source positions at (x, y) = (0, 0) (left), (x, y) = (10,0) (center), and (x, y) = (20, 0) (right). The gamma ray sources of all images are ^{137}Cs, and the energy range is 580 - 744 keV. 97
4.51 The obtained images of several different sources, ^{133}Ba (289 - 423 keV) (left), ^{137}Cs (580 - 744 keV.) (center), and ^{54}Mn (747 - 923 keV) (right). The source position of all image are (x, y) = (0, 0). 98
4.52 The obtained spectrum (upper left) and image (upper right). If the energy cut was applied to the obtained image, images which have unique peaks were obtained. These images are in the energy range of 580 - 740 keV (lower left) and 760 - 910 keV (lower right), respectively. 99
4.53 The energy resolution as a function of the energy of the gamma rays. Red points are the results. For comparison, the simulated ones (black) and those of the $10\times10\times15$ cm^3 telescope (blue) are plotted. 100
4.54 The histograms of the uncertainty of ARM (left) and SPD (right) for ^{137}Cs. The solid lines are obtained by fitting with Lorentzian (left) and Gaussian. 100
4.55 The angular resolutions of ARM and SPD as a function of the energy of the gamma rays (red). For comparison, the simulated ones (black) and those of the $10\times10\times15$ cm^3 telescope (blue) are plotted. 101
4.56 The detection efficiency as a function of the energy of the gamma rays (red). For comparison, the simulated ones (black) and those of the $10\times10\times15$ cm^3 telescope (blue) are plotted. 101
4.57 The effective area as a function of the zenith angle for the 662 (red square and solid line) and 356 (red circle and dashed line) keV gamma rays. For comparison, the simulated ones for the 662 (black square) and 356 (black circle) keV gamma rays are also plotted. 102

5.1 Picture of CP80168. CP80168 consists of the board containing two VA32_HDR11 chips and two TA32CG2 chips, and the connector board which connects ASIC chips to the H8500. The connector board is replaceable. 104

5.2 Schematic view of data acquisition system. Red block box shows the CP80168. . 104
5.3 Schematic view of the attenuator board(left, dashed line) and picture of the attenuator board(right). The connector board (Figure 5.1) can be replaced with the attenuator board. 105
5.4 Anode gain uniformity map of the H8500 that we used (top), resistance value (in units of Ω) map of the attenuator board that we developed corresponding to the top one (middle), and the measured 662 keV peak map (bottom), where the maximum peak is normalized to 100. 106
5.5 Flood field image of ^{137}Cs irradiation (upper left), x-projection of the image at the 2nd row (lower left), y-projection of the image at the 4th row (upper right), and typical energy spectrum (lower right). 108
5.6 Measured energy resolution using the attenuator board. The best-fit line is described in the text. 109

6.1 The energy dependencies of the scattering angles of electron in Al (Black) and CFRP (Red). 113
6.2 The energy loss in CFRP window for the incident gamma-ray energy of 10 MeV. 113
6.3 A photograph of μ-TPC for the gamma-ray telescope with pair creation mode (top) and a schematic view of that (bottom). 114
6.4 10×10 cm^2 μ-PIC. 115
6.5 10×10 cm^2 GEM. 115
6.6 Scintillation camera for the prototype telescope with pair creation mode. 115
6.7 The coincidence signal of anode and cathode hits by existing position encoding system. The lines are cathode hits (blue), anode hits (red), coincidence of anode and cathode hits (green), and analog signal of cathode (purple). 116
6.8 The old encoding mode (top) and the new one (bottom). X, Y, and T mean the hit point of anode, that of cathode, and the elapsed time, respectively. 117
6.9 The tracks of cosmic muons. These are obtained by the old encoding mode (top) and the new TPC mode-II (bottom). X, Y, and Z are the strip numbers of the anode, that of the cathode, and the clock, respectively. In the bottom-right one, hit points from the anodes and cathodes when they coincide in two clocks interval are paired and plotted. 118
6.10 The numbers of hit points per cosmic muon with the old encoding mode (left) and the new TPC mode-II (right) 118
6.11 The gain uniformity of the μ-PIC of the pair mode telescope. 119
6.12 The typical energy spectrum of the X-rays from ^{133}Ba measured by the μ-TPC of the pair mode telescope. 120
6.13 The energy resolution of the μ-TPC of the pair mode telescope. 120
6.14 The histograms of the clock counter to the anode (left) and the cathode (right). . 121
6.15 The drift velocity as a function of the electric field for the gas mixture of Ar and C_2H_6 (90:10) at 1 atm. 121
6.16 The histograms of residual between the obtained points and the fitted straight line at the drift length of 8 - 9 cm. 122
6.17 The one-dimensional position resolutions as a function of drift length. 122
6.18 A photograph of the prototype of gamma-ray telescope with pair creation mode. 124

7.1 The photograph of the experimental setup. 126
7.2 The schematic view of the experimental setup. 127
7.3 Top view of the experimental setup. 127
7.4 The decay curve of stored current. (Experiment 1) 128

7.5 NaI hit rate. (Experiment 1) . . . 129
7.6 The DAQ trigger rate (left) and the ratio of the DAQ live time to the real measured time (right). (Experiment 1) . . . 129
7.7 The energy spectrum of the 10 MeV LCS gamma rays measured by NaI. The mean energy of LCS gamma rays is 8.7 MeV. . . . 129
7.8 The decay curve of stored current. (Experiment 2) . . . 130
7.9 NaI hit rate. (Experiment 2) . . . 130
7.10 The DAQ trigger rate (left) and the ratio of the DAQ live time to the real measured time (right). (Experiment 2) . . . 130
7.11 The energy spectrum of the 20 MeV LCS gamma rays measured by NaI. The mean energy of the incident gamma rays is 18.0 MeV. . . . 131

8.1 The concept of track finding in the clustering method. Hit points of an electron and positron pair (a) are divided by two regions (b), and then two clusters are found (c). . . . 133
8.2 The flow chart of clustering method. . . . 133
8.3 Rough event selection. (a) All hit points of true pair creation event are in fiducial volume. (b) If there are hit points out of the fiducial volume, the event is rejected. 135
8.4 The definition of the clustering region corresponding to the region of beam-downstream side. . . . 135
8.5 The example of clustering. (a) The hit points in the clustering region are obtained. (b) X-Z (Y-Z) plane is divided by S × T regions and each area is tagged as (Z_q, X_p) $(p = 1, 2, \cdots, S, q = 1, 2, \cdots, T)$. (c) If there exist hit points in (Z_q, X_p), $f(Z_q, X_p) = 1$ is applied. (d) Neighboring regions are clustered. C_1 and C_2 are the maximum and secondary maximum clusters, respectively. . . . 136
8.6 The example of the parameterized line with r and θ in X-Y plane. . . . 139
8.7 Two examples of the $r(\theta)$ in the r-θ plane (right) corresponding to all lines passing through the one point in X-Y plane (left). Each line in the X-Y plane (left) corresponds to each point on the sine curve as the same color in r-θ plane (right). 139
8.8 The example of the Hough transform. . . . 140
8.9 The example of the Hough transform. . . . 141
8.10 The flow chart of Hough transform method. . . . 142
8.11 The examples of the events with large (top) and small (bottom) opening angle from simulation. Left figures are the events in data space. Right figures are the events in Hough space. . . . 143
8.12 The simulated examples of the clustering using the residual distributions. Simulated hit points and the approximate lines, L1 and L2, given by Hough transform are plotted (upper left). Residual distributions of L1 (lower left) and L2 (lower right) are calculated by upper right one. For each distribution, the hit points with the condition of $|residual| < \sigma_{res}$ are clustered (upper right). . . . 144
8.13 The examples of the hit points from simulation and the approximate line from the Hough transform. . . . 145
8.14 The gamma-ray telescope in the simulation, which is the same geometry as that in the experiment. . . . 146
8.15 The reconstructed image (left) and the distribution of the squared angular deviation between the obtained and real origin (right) of 10 (top) and 20 (bottom) MeV gamma rays using the clustering method. . . . 147
8.16 The reconstructed image (left) and the distribution of the squared angular deviation between the obtained and real origin (right) of 10 (top) and 20 (bottom) MeV gamma rays using the Hough transform method. . . . 147

9.1 The event view of the pair creation event with large opening angle using the clustering method in the beam experiment. 149
9.2 The event view of the pair creation event with large opening angle using the clustering method in the beam experiment. 149
9.3 The obtained images at 8.7 (left) and 18.0 (right) MeV using the clustering method in the beam experiment. 150
9.4 The θ squared distributions at 8.7 (left) and 18.0 (right) MeV using the clustering method in the beam experiment. 150
9.5 The angular resolutions of the gamma-ray telescope with pair creation mode (68% containment) The filled circles are the measured resolutions. For comparison, the resolutions of EGRET (green) and MEGA (blue) and the calculated ideal ones (pink and red)are also shown. 151
9.6 The estimated detection efficiency of the gamma-ray telescope with pair-creation mode using the clustering method. The solid line and dashed line are the probability of pair creation in the μ-TPC with Ar and C_2H_6 gas mixture (90:10) and Xe, respectively. 152
9.7 The event view of the pair creation event with large opening angle using the Hough transform method in the beam experiment. 154
9.8 The event view of the pair creation event with large opening angle using the Hough transform method in the beam experiment. 155
9.9 The event view of the pair creation event with large opening angle using the Hough transform method in the beam experiment. 155
9.10 The obtained images at 8.7 (left) and 18.0 (right) MeV using the Hough transform method in the beam experiment. 156
9.11 The θ^2 distributions at 8.7 (left) and 18.0 (right) MeV using the Hough transform method in the beam experiment. 156
9.12 The angular resolutions of the gamma-ray telescope with pair creation mode (68% containment) using the Hough transform method. The resolutions using the clustering method are also plotted (filled brown circles). Black line show the ones from simulation. For comparison, the resolutions of EGRET (green) and MEGA (blue) and the calculated ideal ones (pink and red)are also shown. 157
9.13 The estimated detection efficiency of the gamma-ray telescope with pair-creation mode using the Hough transform method. The efficiencies using the clustering method are also plotted. Blue solid and dashed lines show the ones from simulation and ones with the systematic error of 10 %, respectively. The black solid line and dashed line are the probability of pair creation in the μ-TPC with Ar and C_2H_6 gas mixture (90:10) and Xe, respectively. 158
9.14 The expected effective area. For comparison, the effective area in other mission are also plotted [30, 79–81]. 159

10.1 The angular resolution of our prototype gamma-ray telescope with both Compton and pair creation modes. For comparison, the angular resolutions of other missions are also plotted [30, 79, 80, 84, 85]. 163
10.2 The sensitivity of our prototype gamma-ray telescope with both Compton and pair creation modes for continuum component. For comparison, the sensitivity of other missions are also plotted [30, 79, 80, 84, 85]. 163
10.3 The expected angular resolution of our gamma-ray telescope with both Compton and pair creation modes. 165
10.4 The expected sensitivity of our gamma-ray telescope with both Compton and pair creation modes. 165

List of Tables

1.1 The gamma rays by nuclear transitions [1, 3, 4] 18
1.2 Gamma-ray Pulsars [5] 24

2.1 The summary of MeV gamma-ray imaging 43
2.2 The properties of some gamma-ray telescopes [1] 43
2.3 The detected sources with COMPTEL and EGRET [1, 5] 45

4.1 The properties of EMCO Q12N-5 86
4.2 The specification of prototype absorber 92
4.3 The specification of prototype tracker 94

6.1 The specification of the scintillation camera in prototype pair telescope. 123
6.2 The specification of the μ-TPC in prototype gamma-ray pair telescope 123

7.1 Run summary of the beam experiment using the prototype pair telescope. 131

Part I

Introduction

Chapter 1

MeV gamma-ray astronomy

Once, the mean of astronomy was the studies of the stars' and planets' movements with the visible light observation, and hence the image of the universe was static and silent. However, astronomers now observe not only the electromagnetic waves from radio to gamma ray but also cosmic rays, neutrinos and so on. From these new windows, we have got the new various information that the universe is active and violent.

Gamma ray is one of these new windows. Figure 1.1 shows the history of the gamma-ray observatories in space. The gamma-ray observations started in 1961, which was almost the same time as the discovery of Sco X-1. After the prediction by Hayakawa et al. in early 1950s about the existence of the gamma-ray radiation due to the decay of π^0 created by the interaction of cosmic rays and interstellar matter, several gamma-ray sources were discovered by the satellites, OSO-7 ($\geq$ 500 MeV) in 1967, SAS-2 ($>$ 30 MeV) in 1972 and COS-B (2 keV - 5 GeV) in 1975. Besides, low-energy gamma-rays were observed by Granat which was launched in 1989 by Russia and France, and CGRO which was launched in 1991 by United States. Recently, INTEGRAL was launched in 2004 by ESA, and GLAST will be launched soon in 2007. On the ground, very high-energy gamma-rays of energy about 10^{12} eV were observed by Cherenkov telescopes, Whipple, HEGRA and CANGAROO, in 1990s.

Although gamma rays mean all electromagnetic waves with the energy above a few hundred keV, the gamma rays of each MeV - TeV energy region provide us the different information even if they were emitted from same object. A gamma-ray observation in the MeV region provides the information of the nucleosynthesis, the particle acceleration and the interaction of cosmic rays and interstellar matter. MeV gamma rays are hardly attenuated from source objects to the earth, but can't pass through the atmosphere (Figure 1.2). Thus celestial MeV gamma rays must be obtained outside the atmosphere. In this energy band, the number of photons is less than X-ray, and the complete absorption of photon is difficult because of the dominated process of Compton scattering. Besides this energy band has the backgrounds of photons produced by the hadron process of cosmic ray and satellite body, although the band above 100 MeV has no background. Consequently the observation is very difficult, and the MeV gamma-rays astronomy has not be advanced than other energy bands.

1.1 Production mechanism of gamma ray

Thermal radiation is an emission from a large population of electromagnetically interacting particles in equilibrium, with their mean energy characterized by temperature T. The spectrum of radiation intensity follows the 'black body' distribution, and the energy density of radiation

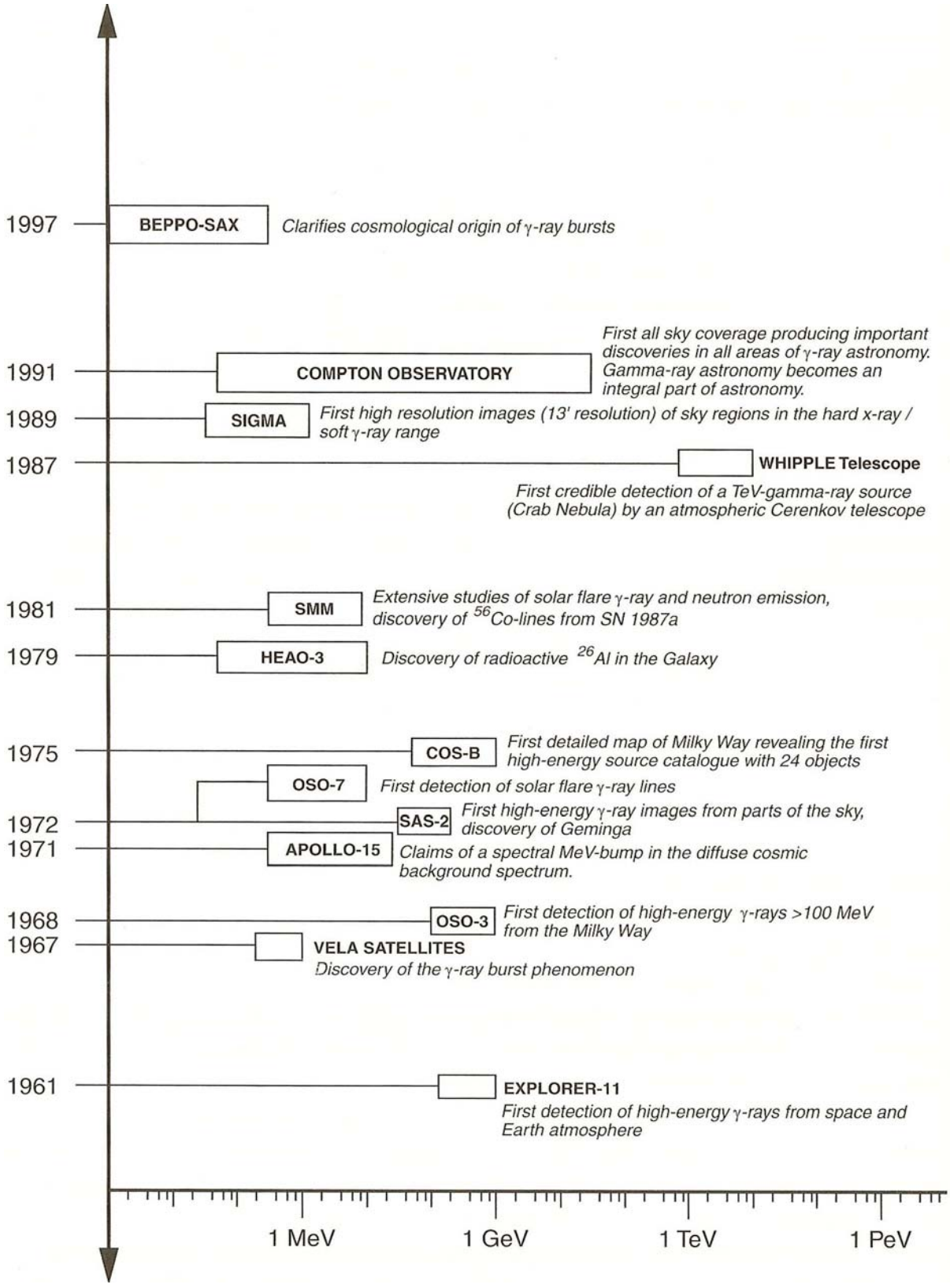

Figure 1.1: The history of Gamma-Ray Observatories [1]

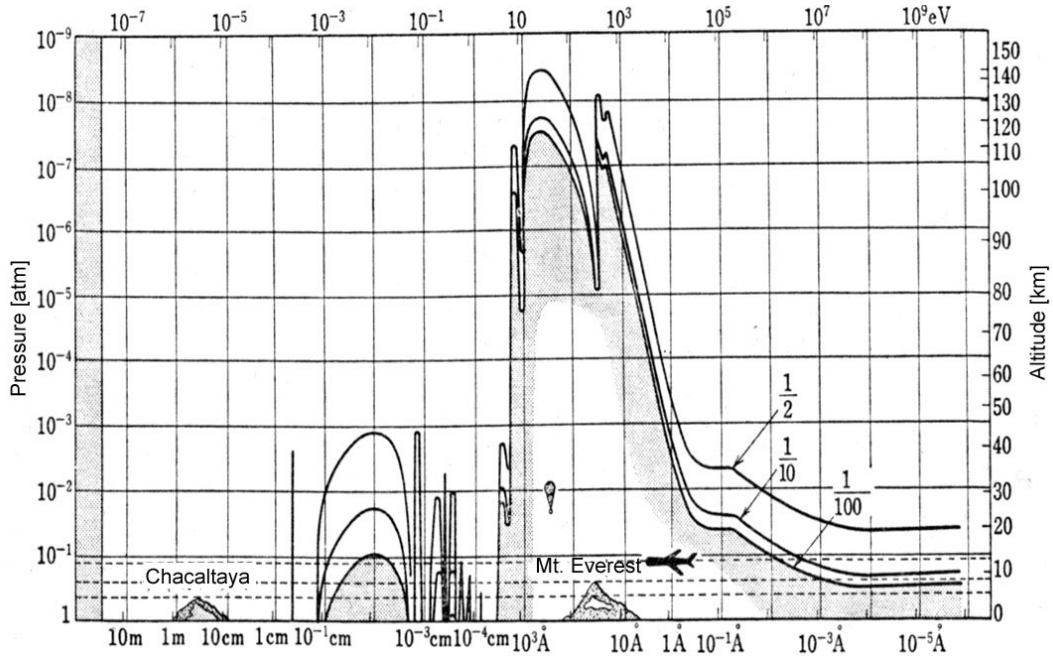

Figure 1.2: The attenuation by atmosphere in multi-wavelength [2]

at frequency ν is

$$I_\nu = \frac{8\pi h\nu^3}{c^3}\frac{1}{e^{h\nu/k_BT}-1}, \tag{1.1}$$

where h is Planck's constant, and k_B is Boltzmann's constant. For the thermal gamma rays of 1 MeV, the corresponding temperature would be above 10^9 K. Thus, thermal process is not reasonable, and nonthermal processes are the more reasonable source of gamma rays. In the MeV region, several nonthermal processes exist as follows.

1.1.1 Synchrotron radiation

When a relativistic electron moves via the magnetic field B, an electron trajectory will be changed by the Lorentz force. Because any acceleration of the charged particle can be viewed as the modification of the field, the kinetic energy of the electron is transformed into the energy of the electromagnetic field. For the relativistic electron, such an energy lose as an emission of photon, which is called Synchrotron Radiation.

Synchrotron radiation spectrum has a peak at the characteristic as

$$h\nu_c = \frac{3h}{4\pi}\frac{eB_\perp}{m_ec}\left(\frac{E_e}{m_ec^2}\right)^2, \tag{1.2}$$

where, e, m_e, E_e are charge, mass, energy of the electron, respectively, and $B_\perp = B\sin\theta$ with the pitch angle θ which is the angle between the particle trajectory and the direction of the magnetic field. The total energy loss rate by synchrotron radiation of an electron moving in the magnetic field B is

$$-\left(\frac{dE_e}{dt}\right)_{\rm syn} = \frac{4}{3}\sigma_T c\frac{B^2}{8\pi}\gamma^2\beta^2, \tag{1.3}$$

where $\sigma_T = \frac{8\pi e^4}{3m_e^2c^4}$ is Thomson cross section.

1.1.2 Bremsstrahlung

Another important process of gamma-ray production is 'Bremsstrahlung'. When an electron passes very near the nucleus, the electron's trajectory is substantially changed by the strong electric field of the nucleus, and photons are emitted.

The spectrum of bremsstrahlung radiation remains flat up to roughly the electron kinetic energy, and it drops sharply toward zero above. For relativistic electrons in a fully ionized plasma (no screening), the bremsstrahlung loss is

$$-\left(\frac{dE_e}{dt}\right)_{\rm B} = 4n_a Z^2 r_0^2 \alpha c \left(\ln\frac{E_e}{m_e c^2} + 0.36\right) E_e. \tag{1.4}$$

In the case of total screening, above formula is modified to

$$-\left(\frac{dE_e}{dt}\right)_{\rm B} = 4n_a Z^2 r_0^2 \alpha c \left(\ln\frac{183}{Z^{-1/3}} - \frac{1}{18}\right) E_e, \tag{1.5}$$

where n_a is the target atom density, $r_0 = \frac{e^2}{m_e c^2}$ is the classical radius of the electron, and α is the fine structure constant.

1.1.3 Inverse Compton scattering

When an energetic photon collides with a low energy electron, the photon is scattered and some of the photon energy transfers to the electron. This process is called Compton scattering. The inverse process also surely exists, and generates a gamma ray: when the low energy photons collide with energetic electrons, these photons gain the some amount of the energy of the electron via the collision. This 'Inverse Compton Scattering' is important in the regions of the high photon density.

The energy loss for an electron in the photon field energy density $w_{\rm ph}$ is written as

$$-\left(\frac{dE_e}{dt}\right)_{IC} = \frac{4}{3}\sigma_T c w_{\rm ph} \gamma^2 \beta^2. \tag{1.6}$$

1.1.4 Nuclear transitions and decay

A nucleus has several specific, quantized states of the energy to bind the nucleons. These nuclear states have typical energy bands of the MeV scale, and hence the transition between those states of a nuclear absorbs or emits the MeV gamma-ray photons. Thus, the gamma rays are emitted from 'de-excitation' of a nucleus:

$$X^* \longrightarrow X + \gamma, \tag{1.7}$$

and 'radioactive decay':

$$X \longrightarrow Y^* + e^+ \longrightarrow Y + \gamma. \tag{1.8}$$

De-excitation occurs by the energetic collisions of cosmic rays with the interstellar gas nuclei, in the space. On the other hand, a radioactive decay occurs by nuclearsynthesis in a supernova and a core of heavy stars. The examples of line gamma-ray emissions by nuclear transitions expected in the universe are listed up in Table 1.1.

Pion is a boson involved in the strong nuclear interaction, and is created during the strong-interaction events such as collisions of cosmic-ray protons with ambient-gas nuclei. The dominant π-producing channels in hadronic interactions are as follows

$$p + p \longrightarrow p + p + a\pi^0 + b(\pi^+ + \pi^-), \tag{1.9}$$

$$p + p \longrightarrow p + n + \pi^+ + a\pi^0 + b(\pi^+ + \pi^-), \tag{1.10}$$

Table 1.1: The gamma rays by nuclear transitions [1, 3, 4]

process		Energy [MeV]
De-Excitation	$^{12}C^*$	4.438
	$^{14}N^*$	2.313, 5.105
	$^{16}O^*$	2.741, 6.129, 6.917, 7.117
	$^{26}Mg^*$	1.809
	$^{56}Fe^*$	0.847, 1.238, 1.811
radioactive decay	^{56}Ni (6.10 d)	0.158, 0.270, 0.480, 0.759, 0.812
	^{56}Co (77.2 d)	0.847, 1.238, 2.598
	^{57}Co (271.7 d)	0.122, 0.136
	^{44}Ti (63 y)	1.157
	^{26}Al (7.4×10^5 y)	1.809
	^{60}Fe (1.5×10^6 y)	1.173, 1.333
capture	$n + {}^1\mathrm{H} \rightarrow {}^2\mathrm{D} + \gamma$	2.223

where a and b are positive integers. A π^0 decays rapidly into two gamma rays with a proper time of 9×10^{-17} sec, and the distribution of the photon energy has a peak at about 70 MeV at the center of gravity system, which is the half of the rest mass of pion. Because pions created by energetic protons has a momentum distribution, the observed gamma-ray spectrum of the pion decay is broadened by Doppler shift.

1.1.5 Annihilation

An electron-positron annihilation is an important source of gamma rays. In the annihilation, two or more photons are created, and the total energy of electron and positron is distributed to these photons. Positron and electron may form a bound system, which is called positronium, and two different states exist. One is the ground state, and a positronium decays to two gamma rays. In this case, each photon has an energy of 511 keV, which is equal to the rest energy of an electron. The other state is the parallel-spin state, and it decays to three gamma rays having the continuum spectrum.

Actually, the 511 keV line was observed at near the Galactic Center by SMM and OSSE, and implied the annihilation rate of $\sim 2 \times 10^{43}$ sec^{-1}. Annihilation photons suggests the existence of the electron-positron plasma. Positrons are produced by β^+-decay, decay of π^+ and the collision of hadronic antiparticles and normal matter. The examples of the radioactive isotopes causing β^+-decay are ^{26}Al, ^{44}Ti, ^{56}Co, and the distinct nova products ^{13}N and ^{18}F. On the other hand, π^+s would be produced at the vicinity of the compact stars.

However, positrons would be also produced by the decay of the intrinsic radioactive isotopes or the interactions of the cosmic rays with the satellite platform. Therefore, spectral decomposition of annihilation photons from the inner Galaxy is considered to be quite difficult.

1.2 Sky in gamma ray

1.2.1 All sky map

For the gamma-ray all-sky survey, Compton Gamma-Ray Observatory (CGRO) satellite had 4 detectors: COMPTEL, EGRET, OSSE and BATSE. COMPTEL found about 30 gamma-ray sources in the MeV region [5], and EGRET found about 270 sources in the sub GeV region [6]. Figures 1.3 and 1.4 show the all sky maps of the gamma ray obtained by EGRET and COMPTEL, respectively. These images show that the gamma rays are radiated from not only the compact objects but also the solar flare. Besides, in EGRET observations, Figure 1.3 says there are about 170 undefined objects of which counter part are not identified by other energy bands.

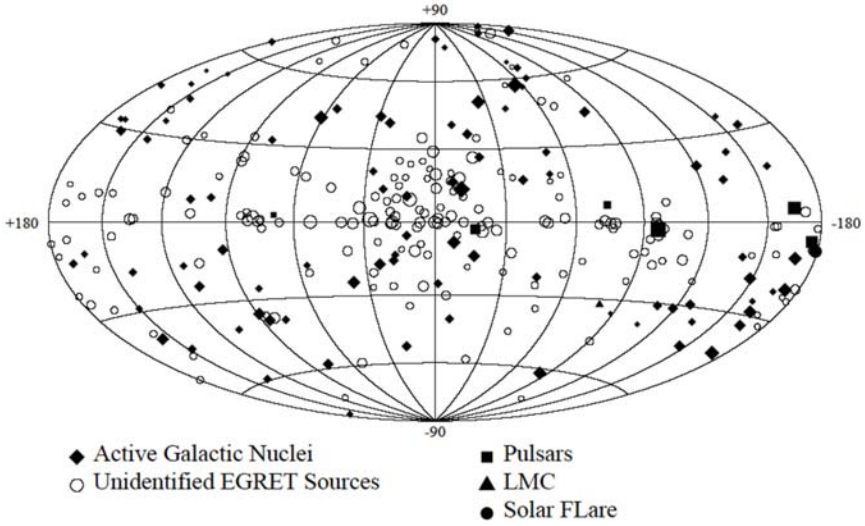

Figure 1.3: The distribution of the gamma-ray objects by EGRET [6]

1.2.2 Galactic diffuse gamma ray

The gamma rays from the Galactic Plane were also observed by those detectors. Figures 1.4, 1.5 and 1.6 show the galactic diffuse gamma-ray radiation in both energy regions.. Figure 1.7 shows the multi-wave energy spectrum of the galactic diffuse gamma rays and X-rays. In the energy region from sub MeV to MeV, photons are mainly produced by the bremsstrahlung and the inverse Compton scattering of an electron [7].

On the other hand, the galactic diffuse gamma rays in the MeV region consist of not only the continuum component but also the line emissions. Figure 1.5 the all sky map of 1.8 MeV from the decay of ^{26}Al. The source of the gamma ray of 1.8 MeV is the decay of ^{26}Al ($T_{1/2} =\sim 10^6 year$), which is considered to be synthesized in the cores of massive stars.

However, in the observation of the point-sources near the galactic plane, the galactic diffuse gamma rays make difficult to observe them as the background.

1.2.3 Extragalactic diffuse gamma ray

Extragalactic diffuse gamma rays come from the outside of the Galaxy, of which the distribution is uniform in the all sky. Figure 1.8 is the spectum of the extragalactic diffuse gamma ray. The spectrum is explained by the combination of the emissions from Active Galactic Nuclei (AGNs)

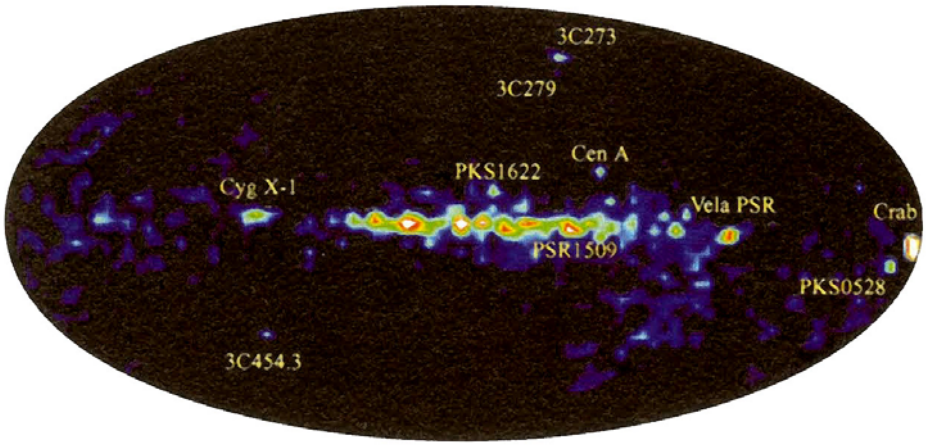

Figure 1.4: The all sky map by COMPTEL (1 - 30 MeV) [1]

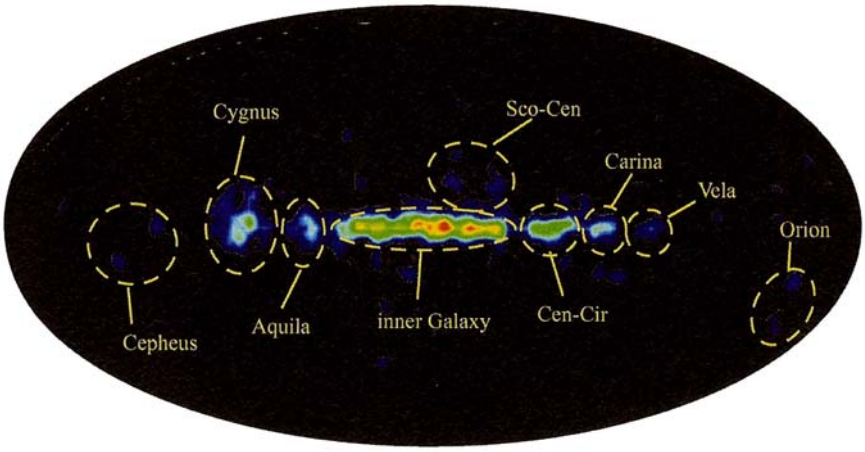

Figure 1.5: The all sky map in 1.8 MeV by COMPTEL [1]

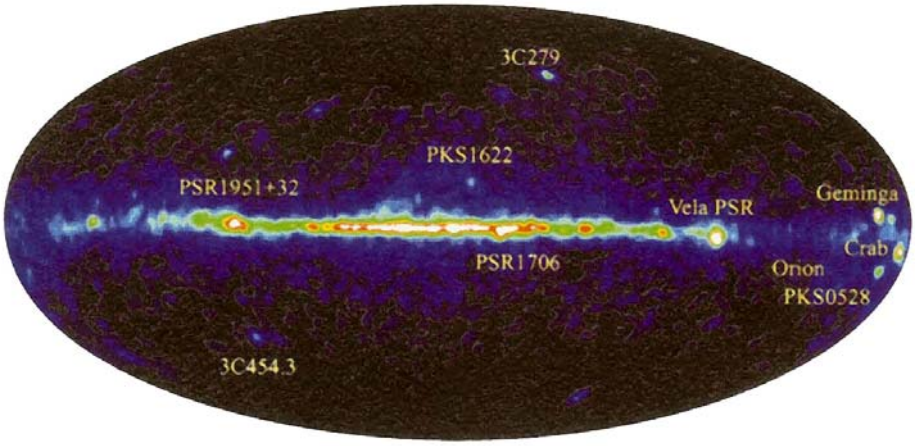

Figure 1.6: The all sky map by EGRET ($\geq$100 MeV) [1]

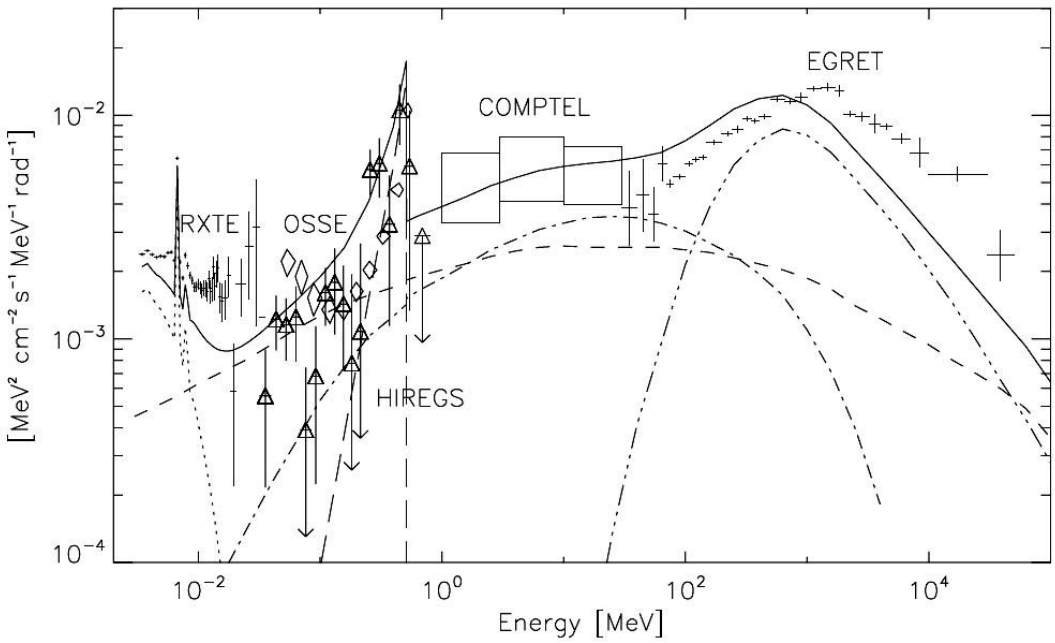

Figure 1.7: The spectrum of galactic diffuse gamma ray [7]. Also shown is the bremsstrahlung (dot-dashed line), inverse Compton scattering (short-dashed line), and π^0 (triple-dot dashed line) model, positronium continuum (long-dashed line) and the thermal Raymond-Smith plasma component (dotted line). The total of the model components is also presented (solid line).

and the type Ia supernovae. Particularly, in the energy region of MeV gamma rays, the mojority is considered to be gamma rays by type Ia supernovae in galaxies.

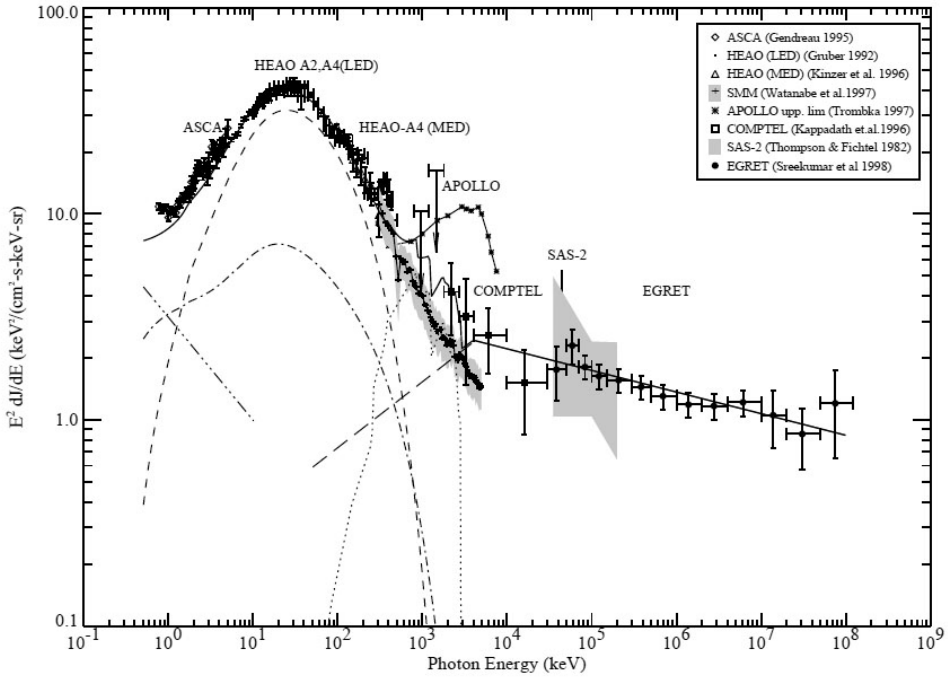

Figure 1.8: The spectrum of extragalactic diffuse gamma ray [8]. The dot-dashed line and dashed line are estimated contributions from Seyfert I and Seyfert II, respectively. The tiple dot-dashed line is steep-spectrum quasar contribution, and the dotted line is Type Ia supernovae. Also the long dashed line is a possible blazar contribution assuming an average power law index of -1.7 below 4 MeV and -2.15 at higher energies. The solid line indicates the sum of all components.

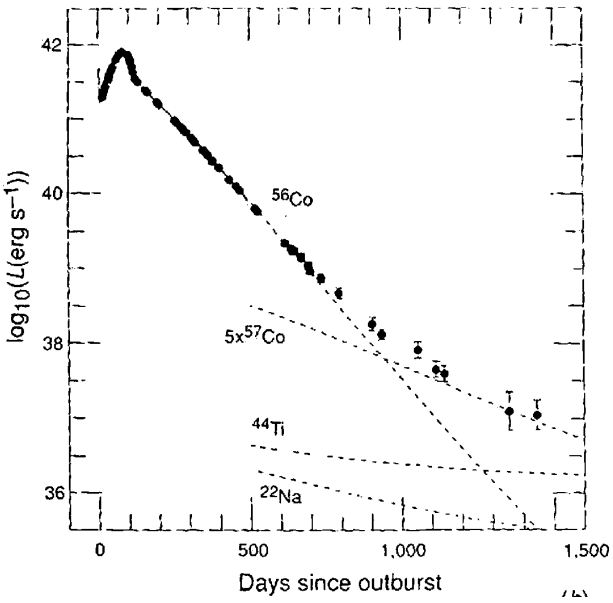

Figure 1.9: The light curve of SN1987A (infrared - ultraviolet) [9]

1.3 Source of gamma rays

1.3.1 Supernova remnant

The supernova is an important site of the nucleosynthesis, and is considered to create the heavier nuclei than Fe. In the nucleosynthesis process in the supernova explosion, the radio isotopes are also produced, and hence the gamma-ray emission by the decay of those isotopes is a good probe to investigate the nucleosynthesis.

If a binary includes a white dwarf, the material from a companion star gradually accretes onto the white dwarf. Then it makes the pressure in the core of the white dwarf higher. Eventually the white dwarf explodes with the thermonuclear supernova explosion (type Ia supernova). In the type Ia supernova, ^{56}Ni is expected to be produced of which amount is predicted about 0.6 $M_{\odot}$, and after the explosion ^{56}Ni decays such as:

$$^{56}\mathrm{Ni} \longrightarrow ^{56}\mathrm{Co} \longrightarrow ^{56}\mathrm{Fe}. \tag{1.11}$$

The light curve of the type Ia supernova is well explained by the combination of the decay time of those nuclear transitions. In the type II supernova, which is the gravitational collapse of the iron core as the final stage of the stellar evolution of the stars more massive than about 8 - 10 $M_{\odot}$, ^{56}Ni is also produced, although the amount is less than that of a type Ia supernova. Figure 1.9 shows the light curve of SN1987A, which is explained by the decay time of ^{56}Co practically. Also the gamma-ray emission due to the ^{56}Co decay was observed from SN1987A.

In the supernova explosion, a lot of neutrons are ejected from the core, the nuclei of the outer shell rapidly capture the neutrons before the transition to a stable states, and changes to neutron-rich isotopes. Since such nuclei are so unstable, they transmit to the stable nuclei through β-decays. This process rapidly proceeds, which are called r-process. The existence of the isotopes in Table 1.1 has been observed in the supernova remnants so far.

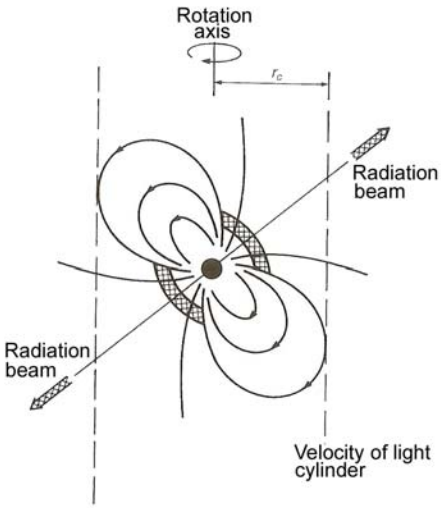

Figure 1.10: The schematic view of pulsar [10]

1.3.2 Spin down pulsars

Gamma ray pulsars

Pulsars radiate a short periodic pulse, and hence are considered to be neutron stars spinning with a high speed. A neutron star also has a strong magnetic field of about 10^{12} G. Because the magnetic axis inlines to the rotation axis generally, as shown in Figure 1.10, the emission near the magnetic poles sweeps around the rotation axis. Since the emission region of the pulsar rotating around the axis is observed from the earth, we see it like a light house. Within thousand pulsars observed so far, the emission of gamma rays are only observed from several of them (Table 1.2). The multiwave spectra of the gamma-ray pulsars are presented in Figure 1.11.

Table 1.2: Gamma-ray Pulsars [5]

Pulser	Period P [msec]	$\dot{P}$ $[10^{-15}]$	distance d [kpc]
Crab	33.34	421.2	2.0
PSR B1509-58	150.65	1537	4.4
Vela	89.29	124.3	0.5
PSR B1706-44	102.4	93.0	1.8
PSR B1951+32	39.53	5.849	2.5
Geminga	237.1	10.98	0.16
PSR B1055-32	197.1	5.8	1.5

Especially, the Crab pulsar was observed from the radio to the GeV gamma ray, and it is one of the most famous pulsars. Figure 1.12 are light curves in each energy region. These figures say that the sub MeV to the MeV energy bands have 2 features:

- Although the first peak is dominant in other energy bands, the dominant in this band varies to the second peak.
- The pulse profile has the 'Bridge' structure between the first and the second peak.

The study of the emission from the pulsar is still underway, and these features in the MeV band have not been explained.

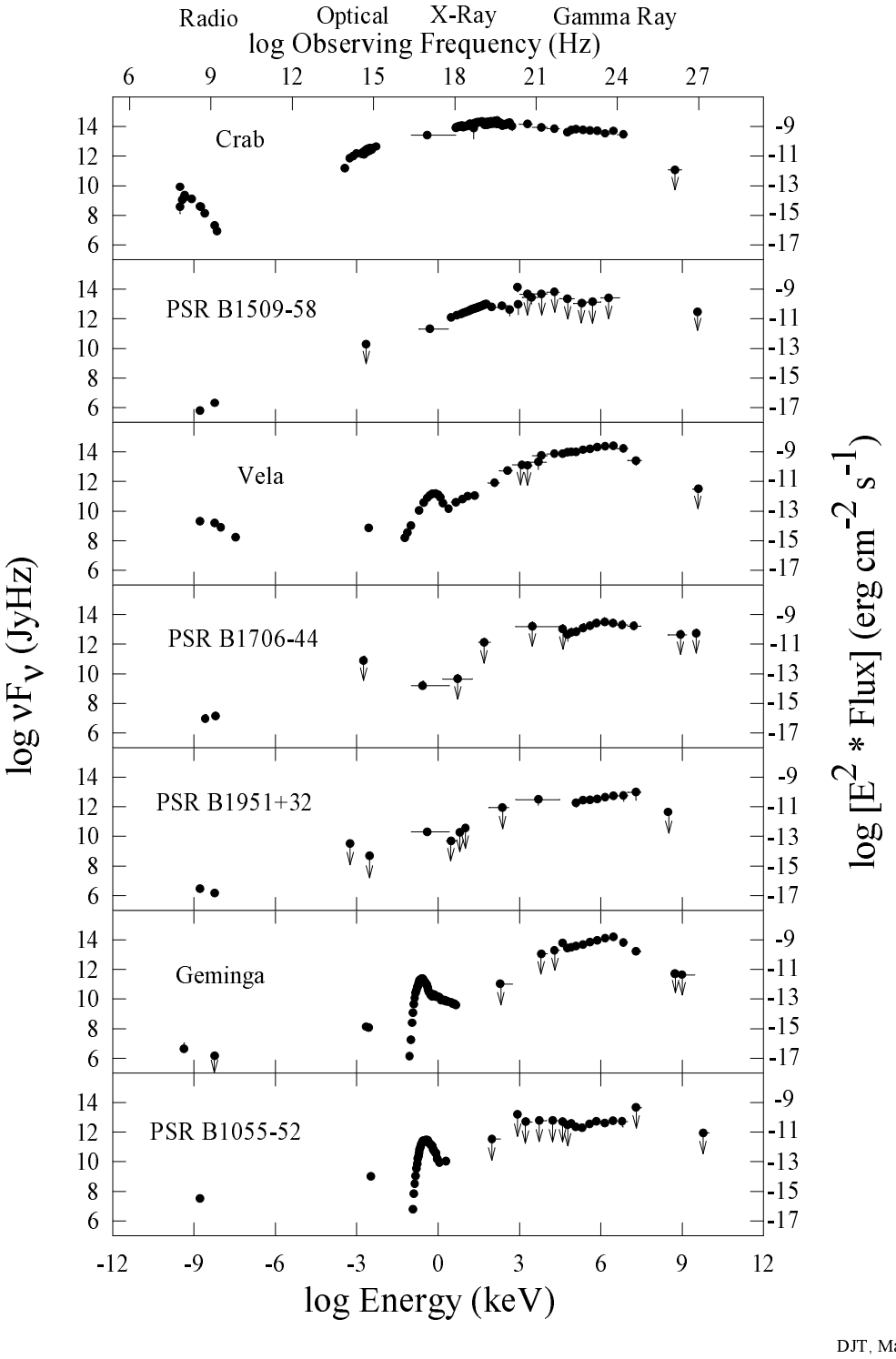

Figure 1.11: The spectra of gamma-ray pulsars [11]

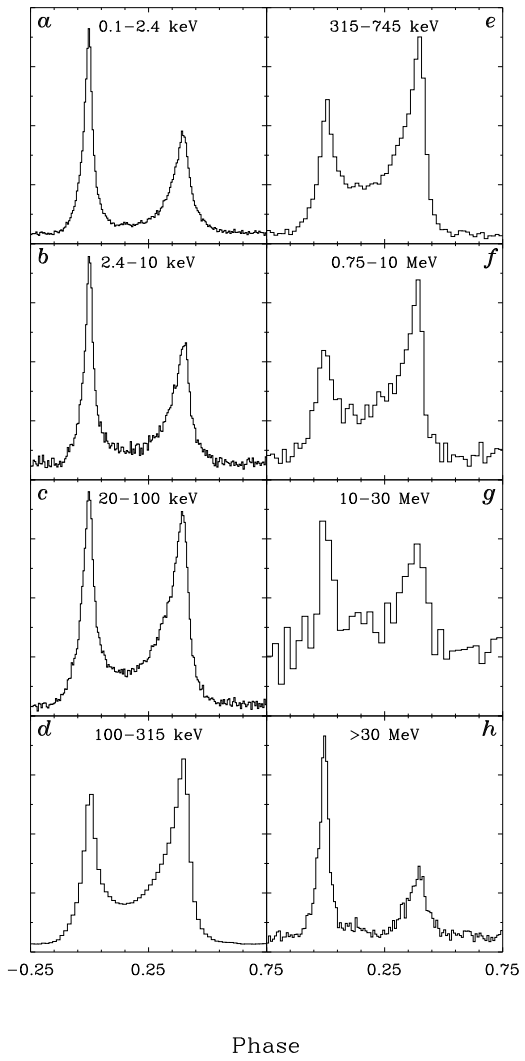

Figure 1.12: The pulse profile of crab pulsar [12]

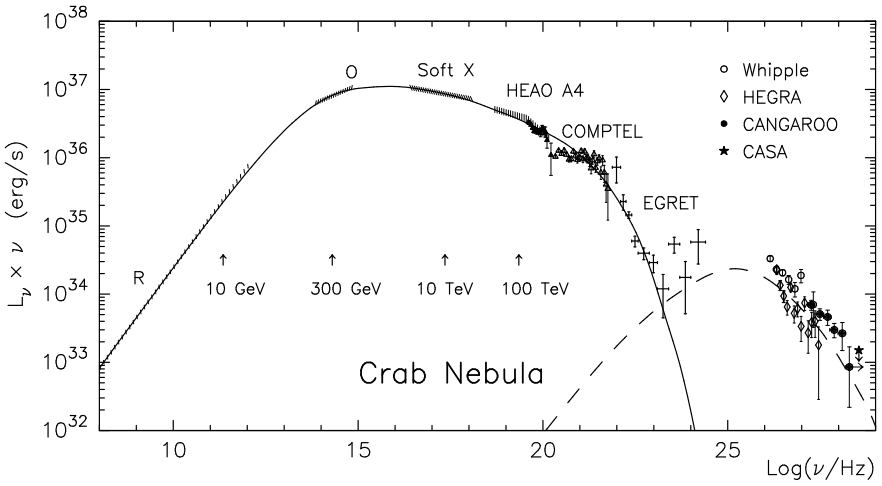

Figure 1.13: The spectrum of crab nebula (solid line: synchrotron radiation, dashed line: inverse Compton scattering) [13]

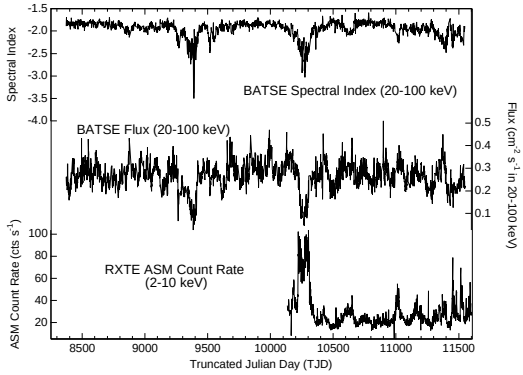

Figure 1.14: The light curve of Cyg X-1 [14]

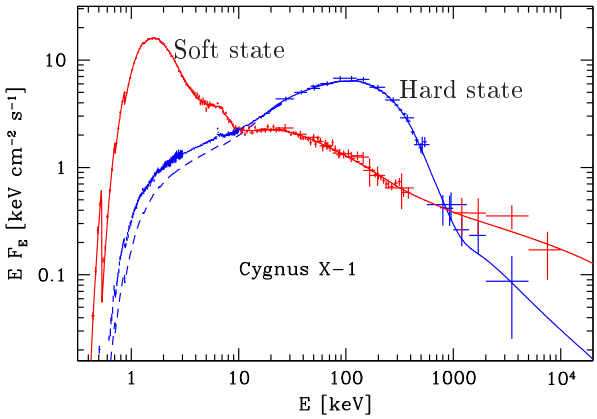

Figure 1.15: The spectra in Soft state and Hard state (Cyg X-1) [14]

Pulsar nebula

Crab pulsar has a nebula around it. The nebula is observed from the radio to the TeV gamma ray as a non-pulsed emission. Figure 1.13 shows the multi-wave spectrum of the Crab nebula. The spectrum is explained by the combination of synchrotron radiation and inverse Compton scattering. Also in the MeV band, the emission from the Crab nebula was observed by COMPTEL and OSSE, and it is suggested that the emission is due to synchrotron radiation.

1.3.3 Black hole

In the final evolution of a heavy star with a mass above $30M_{\odot}$, the core is considered to collapse to a black hole after a type II supernova. A black hole has a boundary line, which is called 'event horizon', from where the electromagnetic wave can't escape. However if a black hole makes a binary system with a star, an accretion disk is created similar to the white dwarf because the matter from the companion star flows onto the black hole. This accretion disk radiates photons in wide band including X-rays and gamma rays. Until now, there is no solid evidence for the existence of a black hole.

Although the existence of the black hole is not established, there are several 'black hole candidates', which are infered with its mass and the size. Cygnus X-1 is the most prominent black hole candidate. Those black hole candidates commonly indicate a violent time profile, as shown in Figure 1.14. Another feature of the time variability is that the energy spectrum changes suddenly between Soft state and Hard State at time. Figure 1.15 shows the spectra of the Soft/Hard state of Cyg X-1.

The emission model of the Soft state is depicted in Figure 1.16, and the model of the Hard state in Figure 1.17. In the soft state, the disk is bright in the X-ray region, in which the blackbody radiation from the accretion disk and the Compton scattering by the non-thermal electron are dominant in this state. On the other hand, the hard state has a peak at a few hundred keV, and the dominant component is the Compton scattering by the thermal electron. In addition, both states look to have the component of Compton reflection with the cold disk [14].

Near the event horizon, ions accelerate up to 100 MeV by the strong gravitational potential, and hence surely π^0 must be created. Therefore, a thermal radiation of π^0, which makes a peak at 70 MeV, is expected to be observed. Such radiation may be an evidence for the existence of black hole.

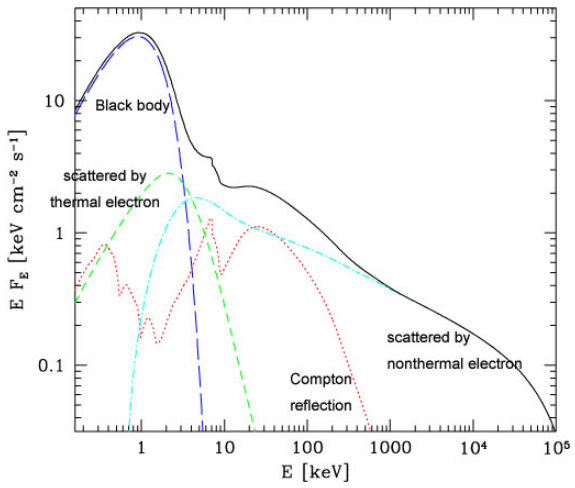

Figure 1.16: The emission model of Soft(High) State [14]

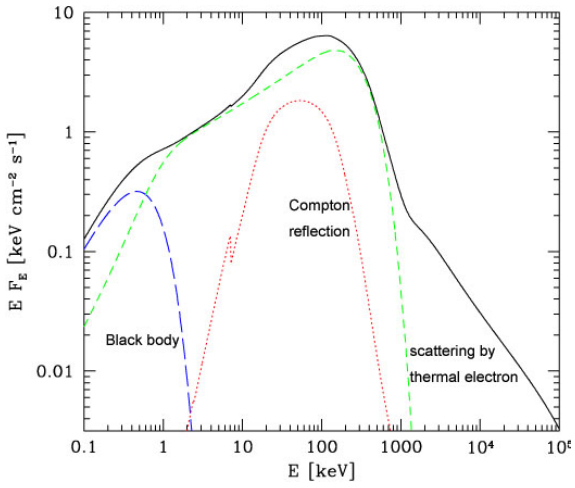

Figure 1.17: The emission model of Hard (Low) State [14]

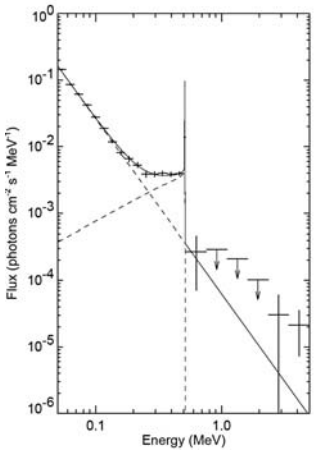

Figure 1.18: The spectrum of Galactic Center by OSSE [15]

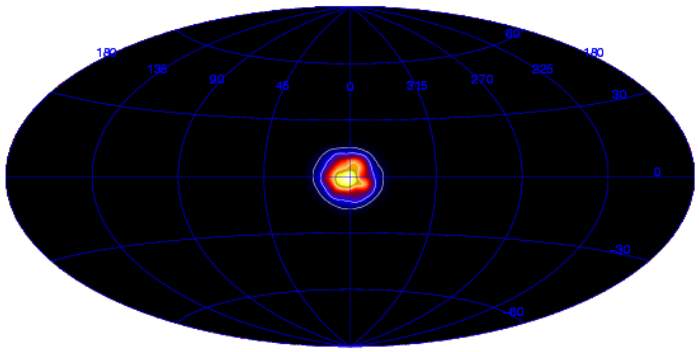

Figure 1.19: The map of Galactic Center at 511 keV by SPI/INTEGRAL [16]

1.3.4 Galactic center

When an electron meets a positron, two or three gamma rays are produced by the annihilation. When the annihilation occurs at rest, the photon energy is 511 keV equal to the rest energy of an electron (section 1.1.5). Actually, OSSE observed the 511 keV from the Galactic Center in Figure 1.18, which says that the annihilation in the Galactic Center exists certainly.

The distribution of 511 keV was broad in the Galactic Plane. The 511 keV emission means the existence of the positron, and the positrons are produced by the β^+ decay of radioactive isotopes, which are provided by the nucleosynthesis in the supernovae and heavy stars.

At the Galactic Center, the existence of a black hole with the mass of $\sim 3 \times 10^6 M_\odot$ is strongly considered [17]. Therefore, if there is a mass accretion, the MeV gamma-ray radiation due to π^0 decay is also expected.

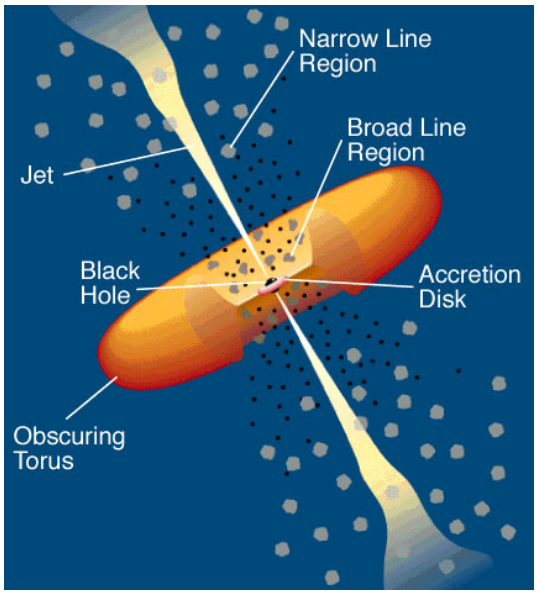

Figure 1.20: The schematic view of AGN [18]

1.3.5 Active galactic nuclei (AGN)

The Active Galaxy is a galaxy with the strong emission from its nuclei, and the nuclei of such a galaxy is called Active Galactic Nuclei. At the Active Galactic Nuclei, the existence of a black hole with the mass of $10^6 - 10^9 M_\odot$ is considered. Figure 1.20 shows the schematic view of AGN. Radio wave observation indicates that many AGN have jets, which is emitted with a narrow beam from the center. If the radiation from the jets is stronger than the radiation from the accretion disk or the thermal radiation of the near disk, the obtained multiwave spectrum is explained by the combination of synchrotron radiation and inverse Compton scattering (Figure 1.21, 1.22).

There are 10 AGNs detected by COMPTEL and 94 AGNs by EGRET, respectively. Thus, AGNs are also the important observable sources in the sub-MeV/MeV gamma-ray bands.

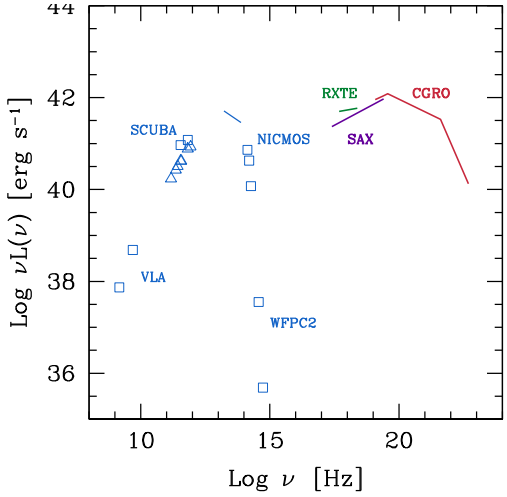

Figure 1.21: The multiwave spectrum of Centaurus A [19]

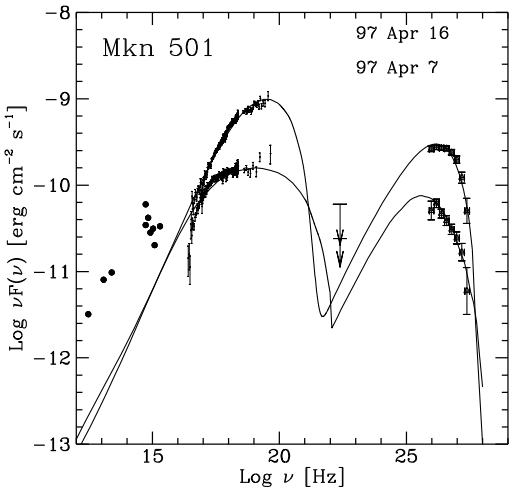

Figure 1.22: The Spectrum of Blazar Mkn501 [20]

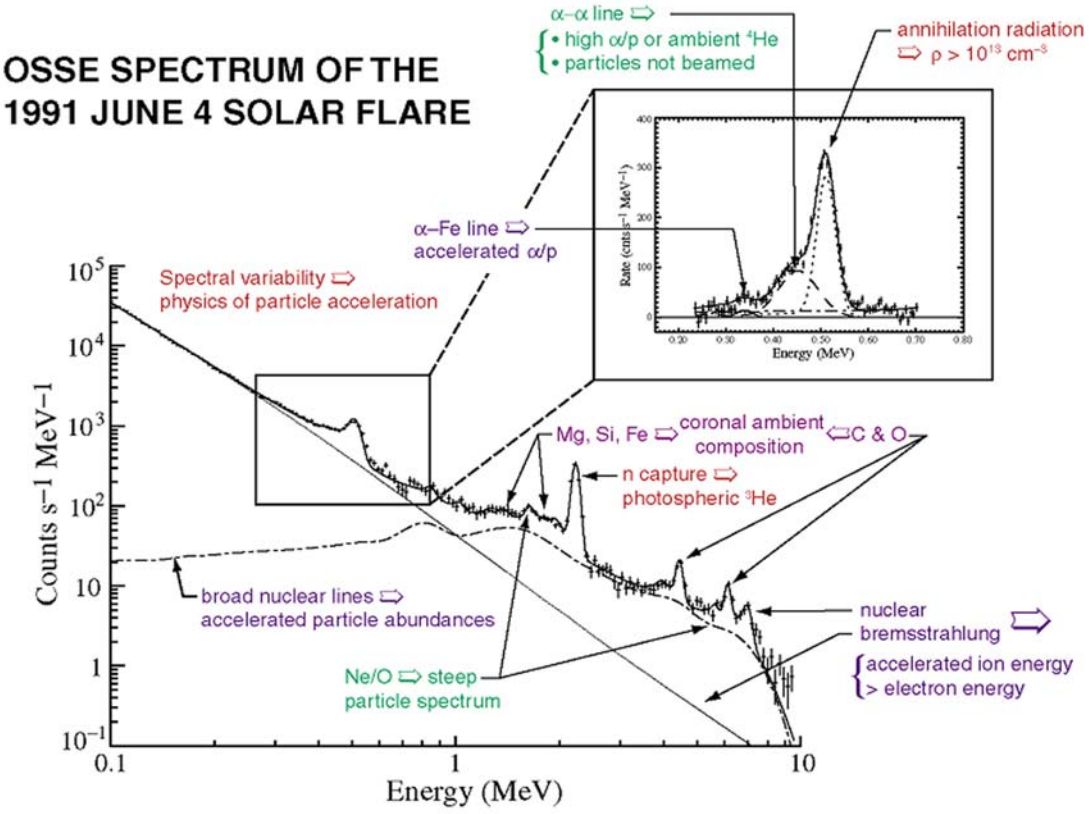

Figure 1.23: The spectrum of Solar Flare (June 4, 1991) [21]

1.3.6 Solar flare

The Sun, the most familiar celestial object, also radiates gamma rays. From 1970's, a few line gamma rays have been known to be emitted in the solar flare sometimes.

Figure 1.23 shows the spectrum of the solar flare. By these measurements, many of the neutron and positron are expected to be produced in the region of flare. Moreover, by the acceleration and the heating of the particles in the corona at the time of solar flare, the accelerated electrons emit X/gamma-ray with bremsstrahlung. Because the Sun is the nearest star, it is the most detailed observable star and is a very important gamma-ray source.

1.3.7 Gamma ray burst

The Gamma-Ray Burst (GRB) was discovered by the Vela satellite in early 1970's. It is a transient phenomenon that gamma rays arrival from specified direction suddenly. GRB has a violent time profile, and the bursting time is very short, but spread in several orders (Figure 1.24).

Until now, many observations such as HETE-2 and SWIFT have been carried out, and our understanding for GRB is dramatically recovered: GRB is a very giant burst at the distance of cosmology, and GRB has a mother galaxy. The obtained spectrum can be explained with MeV gamma ray from synchrotron radiation(Figure 1.25). BATSE on CGRO discovered 2700 GRBs, and the distribution is flat in the all sky (Figure 1.26). But GRB is a puzzle, that is not understood of even the central engine until now.

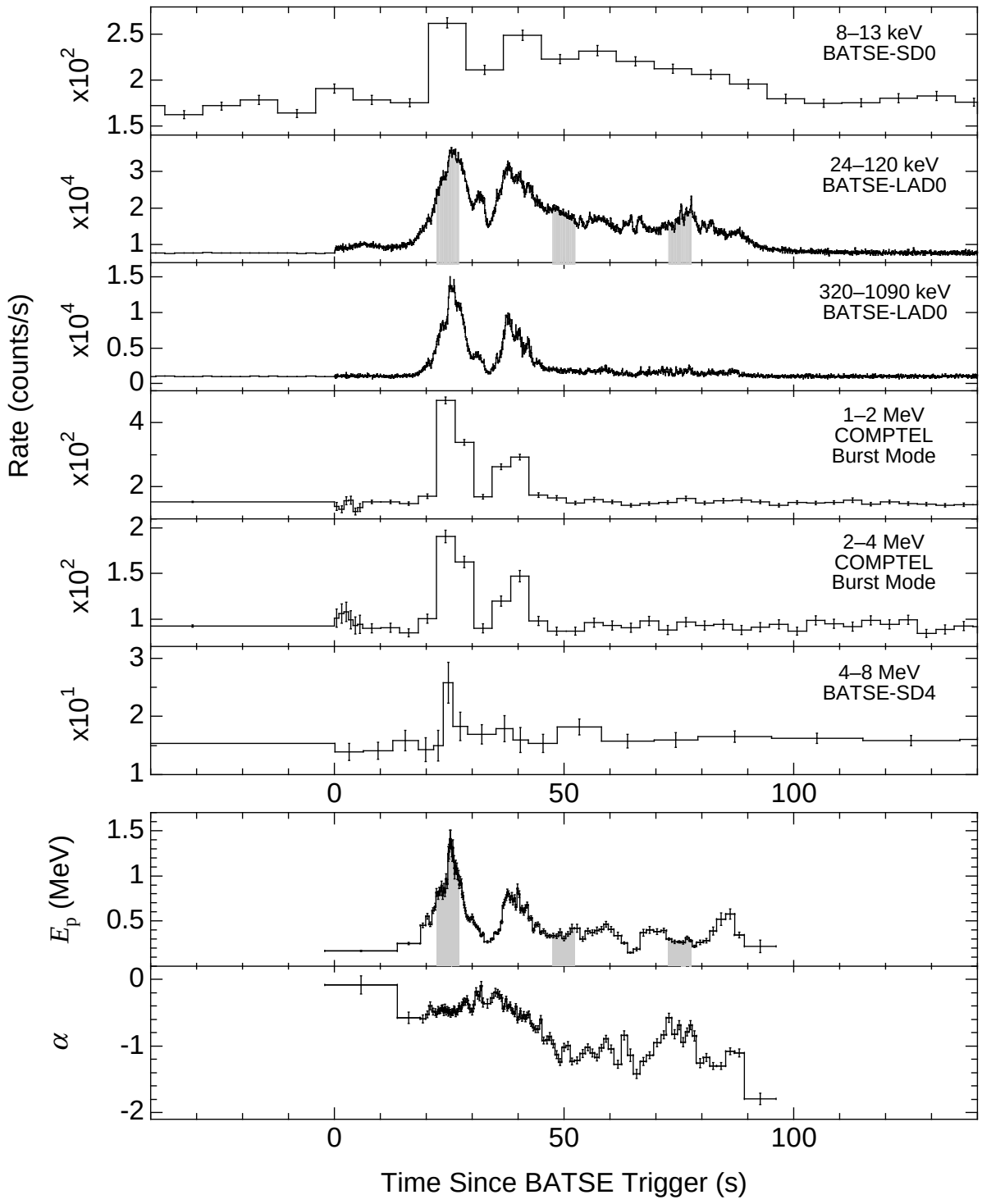

Figure 1.24: light curve of GRB by BATSE and COMPTEL [22]

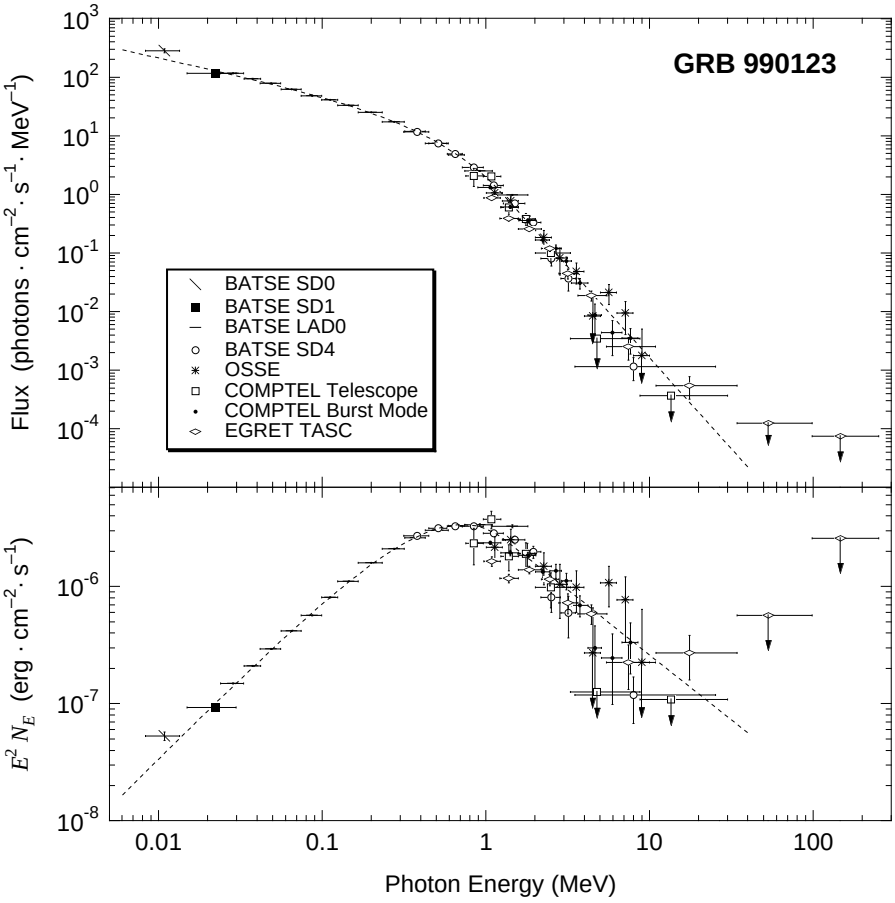

Figure 1.25: The spectrum of GRB [22]

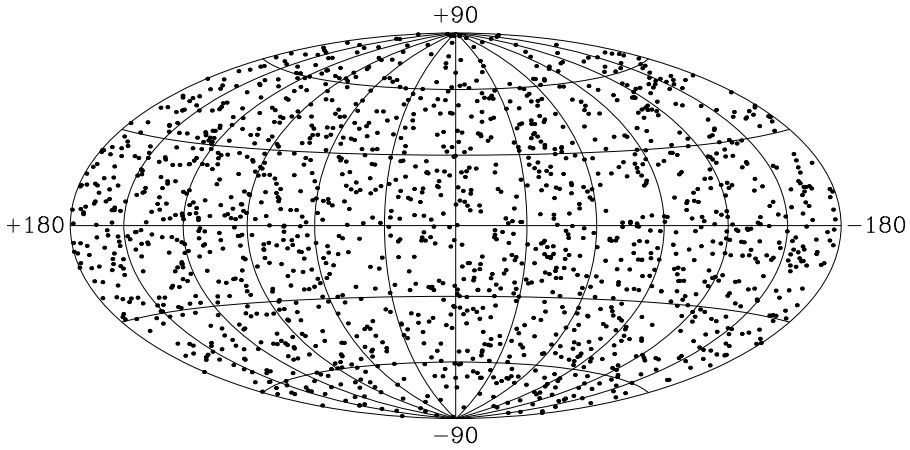

Figure 1.26: The all sky map of GRB by BATSE [23]

Chapter 2

Instruments for MeV gamma-ray astronomy

2.1 Interaction of gamma rays with matter

It is not possible that photons ionize the material because photons are electrically neutral. However, high energy photons interact with material, an electron is emitted via several processes depending on their energy. The ionization of the surrounding material by such an electron enables us to detect X-rays and gamma rays.

There are three processes in the interaction between X/gamma-rays and the matter mainly: photoelectric absorption, Compton scattering and pair creation. The cross sections of these interactions depend on the energy of X/gamma-rays and the atomic number Z of the matter. Figure 2.1 shows each cross section of the interaction with Ar, and Figure 2.2 shows which interaction is dominant.

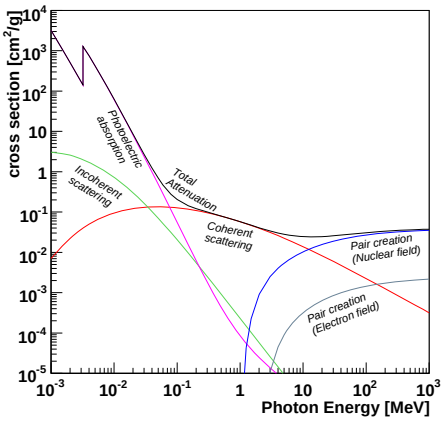

Figure 2.1: The cross section of the interaction of gamma rays and matter (Ar) [24]

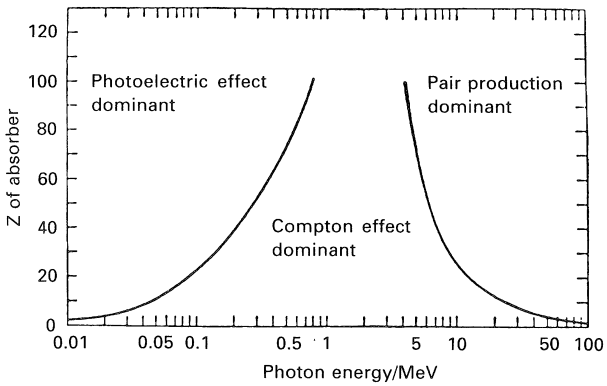

Figure 2.2: The significant interaction of gamma rays and matter [25]

2.1.1 Photoelectric absorption

The photoelectric absorption is a dominant interaction of photons with the energy less than about 100 keV. In this process, a photon provides all energy to a electron in the atom, and then

this electron, called photoelectron, is ejected from the atom. When a photon of the energy E_0 makes a photoelectron, the kinetic energy of the photoelectron is as follows,

$$K_e = E_0 - E_{\rm bind}, \tag{2.1}$$

where $E_{\rm bind}$ is the binding energy of the photoelectron in the atom. If E_0 is higher than the binding energy of the K shell, the probability of the interaction with an electron in K shell is highest. Then the cross section of the photoelectric absorption of a K shell electron is:

$$\sigma_K = 4\sqrt{2}Z^5 \left(\frac{8\pi}{3}r_e^2\right)\left(\frac{e^2}{4\pi\varepsilon_0\hbar c}\right)^4\left(\frac{m_e c^2}{E_0}\right)^{7/2}, \tag{2.2}$$

where σ_K is proportional to Z^5 and $E_0^{-7/2}$, and r_e is the classical electron radius: $r_e = \frac{e^2}{4\pi\epsilon_0 m_e c^2}$. If E_0 is less than the binding energy of K shell, the photon interacts with an L shell electron. Therefore, near the K shell binding energy, the energy dependence of the cross section has a large discontinuity edge (Figure 2.1). Simultaneously a binding electron in the higher energy level trends to transit to the empty level by an emitting X-ray. The energy of the emitted X-ray is equal to the energy difference of those two levels. Also sometimes an electron of the nearly same energy is ejected instead of the X-ray emission, which is called Auger electron.

2.1.2 Compton scattering

In the energy region from a few hundred keV to 10 MeV, the dominant interaction is the Compton scattering, which is an elastic scattering of a gamma ray and an electron. When a gamma ray makes Compton scattering, the gamma ray provides a part of the initial energy to an electron, then the recoil electron runs away, and simultaneously the gamma ray is scattered as its energy becomes lower. When the gamma ray in the energy of E_0 makes Compton scattering with a free electron, the energy of the scattered gamma ray is

$$E' = \frac{E_0}{1 + \frac{E_0}{m_e c^2}(1 - \cos\phi)}, \tag{2.3}$$

and the energy of the recoil electron is

$$K_e = E_0 - E' = \frac{\frac{E_0}{m_e c^2}(1 - \cos\phi)}{1 + \frac{E_0}{m_e c^2}(1 - \cos\phi)}E_0, \tag{2.4}$$

where ϕ is a scattering angle. The angular distribution of the scattered gamma rays is represented by the differential scattering cross section as follows,

$$\frac{d\sigma}{d\Omega} = Zr_e^2\left(\frac{1}{1 + k(1 - \cos\phi)}\right)^2\left(\frac{1 + \cos^2\phi}{2}\right)\left(1 + \frac{k^2(1 - \cos\phi)^2}{(1 + \cos^2\phi)\,[1 + k(1 - \cos\phi)]}\right), \tag{2.5}$$

where σ is the cross section, Ω is the solid angle and $k = \frac{E_0}{m_e c^2}$. Then the cross section is proportional to Z. The angular distribution is shown in Figure 2.3, where you note that the forward scattering is dominant when E_0 is higher.

In a real detector, electrons do not rest and they have the finite momentum of the orbit. Therefore, the gamma ray scattered at the fixed angle from a monoenergetic source have some fluctuation in their energy (the "Doppler broadening", see section 3.2.3).

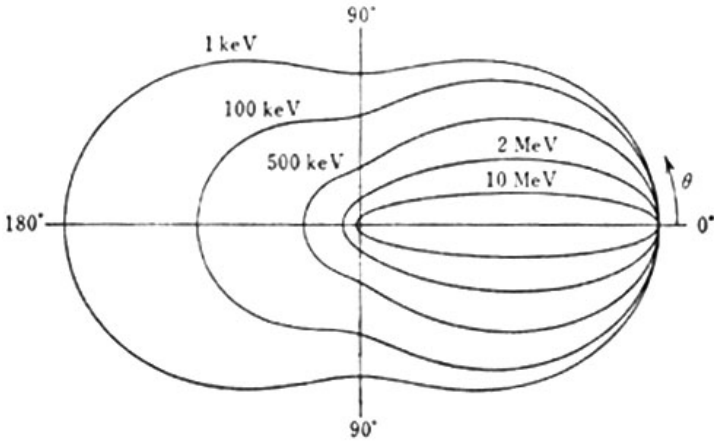

Figure 2.3: The angular distribution of Compton scattering [25]

2.1.3 Pair creation

If the gamma-ray energy exceeds twice of the rest mass of the electron, a pair of an electron and a positron are created with the interaction between the photon and an electric field around the nucleus. This process is called a pair creation, which is a dominant interaction of the photons above 10 MeV. The energies of an electron and a positron emitted from the photon of the energy E_0 must be satisfied with the following equation,

$$E_0 = E_- + E_+ + 2m_e c^2. \tag{2.6}$$

The cross section is proportional to Z^2.

2.2 MeV gamma-ray imaging

For the astronomy, it requires both measurements of the energy and the incident direction of photon for imaging generally. For the X-ray imaging, the photons can be focused by reflection. Figure 2.4 is a schematic view of an X-ray focusing. Only when an X-ray comes to the mirror at a very shallow angle, the X-ray makes reflection. The mirror is Al or glass coated by Au generally. Because the focusing is a mapping from the direction to the position, we can get the energy and the incident direction of each photon at the same time using a 2-dimensional position sensitive detector on the focal plane. However the limit of the energy in focusing by reflection is order of 10 keV, and the reflection ratio falls suddenly in the higher energy (Figure 2.5). For this reason, the focusing of sub-MeV/MeV gamma rays by reflection is impossible, and the other techniques are necessary.

On the other hand, around a satellite, lots of MeV gamma rays are generated by the excitation of the nuclei in the material of the satellite by the cosmic rays, and furthermore such a MeV gamma ray is scattered several times by Compton process. Therefore, the observations of the MeV gamma rays in space severely suffer from huge background gamma rays.

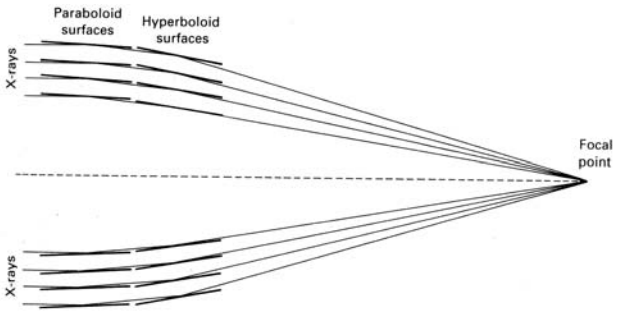

Figure 2.4: The schematic view of an X-ray focusing [26]

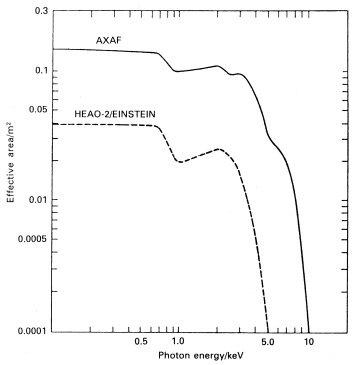

Figure 2.5: The effective area of X-ray telescopes [26]

2.2.1 Active and passive collimators

In order to obtain the incident direction of a photon, the simplest method is the collimation of the Field Of View (FOV). The camera consists of a position sensitive detector and collimators, as shown in Figure 2.6. By collimators, the detected photons are expected to come from the inside of FOV of the collimator. However, for higher energy photons, some photons are scattered in the collimator or come through the collimator. Thus, gamma-ray sources outside of FOV make many background, and obstruct the detection of a faint source in FOV.

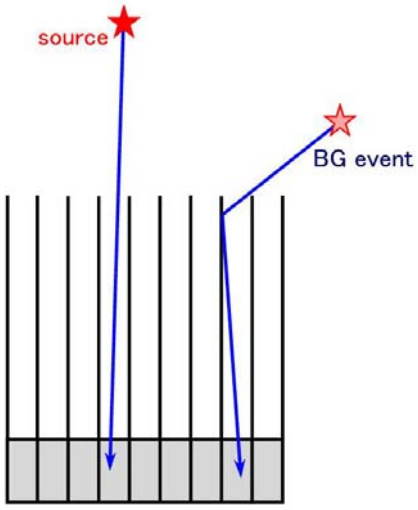

Figure 2.6: The schematic view of passive collimator

For surely rejecting gamma rays from the outside of FOV, there are two possible improvements. One is the simple method: using a thicker collimator. The collimator becomes thicker, the higher stopping power the collimator has. But, in this way, FOV is narrower, effective area is smaller and the collimator is heavier. Because the observations of MeV gamma ray in astronomy require the measurements on the satellite-borne or balloon-borne, these depravations make large demerits for the actual detector-construction. The other way is using an active collimator. For the rejection of the reaction in the collimator, a veto-counter having sensitivity for gamma rays, like a high-Z scintillator, is useful. The background events, scattering in the collimator, can be rejected by the anti-coincidence of the veto-counter. On the other hand, the camera

may become more sensitive for intrinsic background and the dead time of the measurement may increase. Therefore, the observation with collimator is not so sophisticated but quite simple and conventional in astronomy.

Until now, OSO-3, SMM and OSSE were based on this method, and HXD loaded on Suzaku is also a telescope of this kind.

2.2.2 Coded aperture imaging

Now, the practical imaging method is the Coded Aperture Imaging, which was adopted in SIGMA, INTEGRAL and SWIFT. The detector of coded aperture imaging consists of a position sensitive detector and a coded mask which carries out a mapping from the incident direction to the image of the mask's shadow. The coded mask consists of the optical thin material and the optical thick material, and the mask can be described with a matrix:

$$\mathbb{M}_{ij} = \begin{cases} 1 & : \text{the optical thin part,} \\ 0 & : \text{the optical thick part.} \end{cases} \tag{2.7}$$

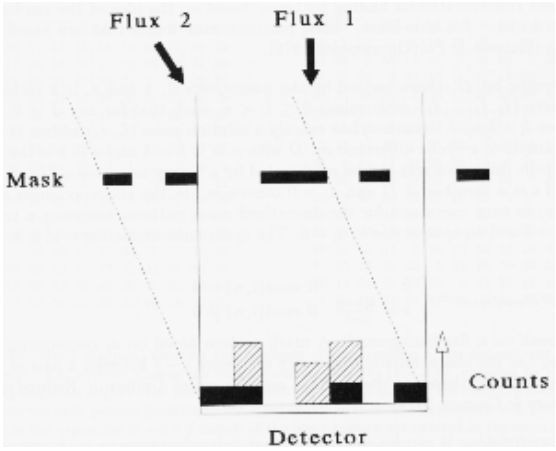

Figure 2.7: Coded mask [27]

When the gamma rays come from the direction of j with the intensity of s_j, the direction is projected to the image of mask's shadow, and the photon number of $\mathbb{M}_{ij}s_j$ arrive to the detector of the position i, as shown in Figure 2.7. Therefore, in the detector of position i, the detected photon number is:

$$d_i = \sum_j \mathbb{M}_{ij}s_j + b_i, \tag{2.8}$$

where b_i is the number of the background photons detected in the position i, because the photons from the outside of FOV is the background. Although the photon intensity from the incident direction s_j is obtained by resolving this formula, there are two unknown parameters of s_j and b_i, so that the estimation of background is very important.

The angular resolution and the FOV depend on the distance between the coded mask and the detector. For the same mask and the same detector, the camera has a larger FOV in the shorter distance of them, while it has a better angular resolution in the longer distance. IBIS loaded on INTEGRAL used the full coded FOV of $9^\circ \times 9^\circ$ and obtained the angular resolution of 0.2° in FWHM [1].

The coded mask is a kind of a collimator, and it is expected that the mask ideally absorbs the gamma ray completely. But, because the cross section of the photoelectric absorption is decreased in proportion to $E^{-7/2}$, the Coded Aperture Imaging is not so good for the imaging of the high energy photons basically. The imaging of high energy photons is required of the thicker mask. Actually, the mask of IBIS (20 keV - 10 MeV; INTEGRAL) is made of a 1.6 cm thick tungsten plate, and SPI (3 keV - 8 MeV; INTEGRAL) has a 3 cm thick tungsten mask. Still, there remains another problem, that gamma rays scattered in the mask are detected as background.

2.2.3 Gamma-ray lenses

Although gamma rays can't be focused by reflection, there are two focusing methods for MeV gamma rays. These focusing methods are called Gamma-Ray Lenses. One makes use of Laue diffraction, and the other makes use of a phase Fresnel lens. Generally, the focusing has the high angular resolution, but the FOV is narrow. Besides, the focusing can reduce the intrinsic background, because the detection volume is quite smaller than other imaging methods.

Laue lenses

The focusing by Laue diffraction is called Laue lens. Although the Laue lenses give us a very good angular resolution, they focus only the gamma ray of specific energy due to the principle of the Blagg scattering as follows,

$$2d \sin\theta = n\lambda. \tag{2.9}$$

Then it is impossible to get the wide band energy spectrum using this lens. Here d is the crystal plane spacing, θ is the diffraction angle, n is the reflection order and λ is the wavelength. The lens of CLAIRE, which was launched in the balloon experiment in 2001, has the FOV of $45''$, the energy band of 169 - 171 keV and the focal length 3 m [28].

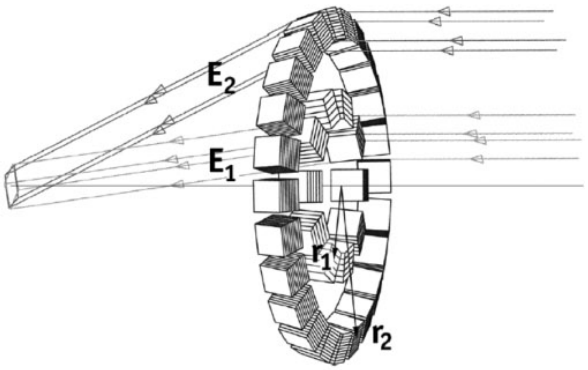

Figure 2.8: The schematic view of Laue Lens [29]

Fresnel lenses

The other method is a phase Fresnel lens. Because the refraction index for gamma ray in matter is slightly lower than 1, it is possible to focus gamma ray. The Fresnel lenses have the angular resolution limit in the μarcsec, but they require a very long focal length of 10^9 m. Therefore it is difficult to realize this method currently.

2.2.4 Compton imaging

When the gamma ray makes Compton scattering in a detector, it is hard to detect the total photon energy because the scattered gamma ray brings out some part of the incident photon energy. Then, the Compton scattering is a hard process in an usual detector, although it is the most dominant interaction in the sub-MeV and MeV energy regions.

If the information of both the scattered gamma ray and the recoil electron are detected, the energy and the direction of the incident gamma ray can be reconstructed. This imaging method is called "Compton Imaging". The detector based on Compton imaging has a large FOV because no collimator is required. In actual, COMPTEL loaded on CGRO had a FOV of 1 steradian [30].

Compton imaging is an unique imaging method to detect both the energy and the direction for photon by photon, in the sub-MeV/MeV band. Therefore this imaging is an attractive method, and many detectors are in development: MEGA, NCT, LXeGRIT, TIGRE and so on.

Classical Compton imaging

The Classical Compton Imaging used in COMPTEL makes use of the first Compton scattering in the material. A classical Compton imaging camera consists of two Z detectors of which materials are light (low-Z) and heavy (high-Z), respectively. A low-Z position sensitive detector is placed forward, and a high-Z position sensitive detector is placed backward. Figure 2.9 is a schematic view of a classical Compton imaging camera. An incident gamma ray makes a Compton scattering in the low-Z detector, and the scattered gamma rays are absorbed in the high-Z detector. From these detectors, the following information are measured,

- the low-Z detector: the recoil electron energy E_1, and the Compton Point (scattering point)
- the high-Z detector: the scattered gamma-ray energy E_2, and the absorption point of the scattered gamma ray

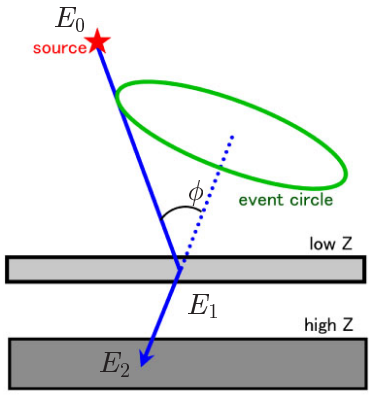

Figure 2.9: The schematic view of Classical Compton Imaging

Then, using E_1 and E_2, the incident gamma-ray energy E_0 and the scattering angle ϕ are calculated

$$E_0 = E_1 + E_2, \tag{2.10}$$

$$\cos\phi = 1 - m_e c^2 \left(\frac{1}{E_2} - \frac{1}{E_1 + E_2} \right). \tag{2.11}$$

The direction of the scattering gamma ray is also obtained by connecting the Compton point and the absorption point, although the two parameters of the direction of the recoil electron is not measured. Therefore the reconstructed direction of the incident gamma ray is limited in a circle (called an event circle as shown in Figure 2.9).

For getting the direction of the gamma-rays source, the detector requires at least 3 photons, as shown in Figure 2.10, where the source position is determined fully by piling up circles (the right figure of Figure 2.10). Although COMPTEL rejected background by using the time of flight between the up and down detectors [30], the signal to noise ratio was not high, and FOV is limited.

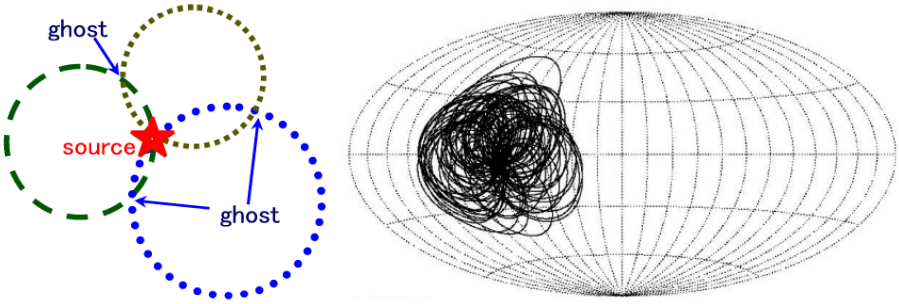

Figure 2.10: The Imaging of Classical Compton and the detection of GRB with COMPTEL (GRB910505 [31])

Multiple Compton imaging [32]

For the classical Compton imaging, a good process to obtain the correct direction of an incident gamma ray is one Compton scattering in the forward detector and a perfect photoelectric absorption in the backward detector. However, sometimes the gamma ray scattered in the forward detector makes also a Compton scattering in the backward detector, and the second scattered gamma ray escapes. Then such as multiple Compton scattering event becomes background for the classical Compton imaging.

The Multiple Compton Imaging is an advanced method to resolve this problem. Figure 2.11 is a schematic view of a detector for the multiple Compton imaging, and the detector consists of layers of several thin position-sensitive detectors. The semiconductor detectors, such as CdTe or Si/Ge strip detector, are used as a thin detector. When a gamma ray makes more times Compton scattering in the detector, the incident gamma-ray energy E_0, the first scattering angle ϕ_1 and the second scattering angle ϕ_2 are absolutely obtained

$$E_0 = E_1 + \frac{E_2 + \sqrt{{E_2}^2 + \frac{4m_e c^2 E_2}{1-\cos^2\phi_2}}}{2}, \tag{2.12}$$

$$\cos\phi_1 = 1 - m_e c^2 \left(\frac{1}{E_2 + E_3} - \frac{1}{E_1 + E_2 + E_3} \right), \tag{2.13}$$

$$\cos\phi_2 = 1 - m_e c^2 \left(\frac{1}{E_3} - \frac{1}{E_2 + E_3} \right). \tag{2.14}$$

where E_1, E_2, E_3 are the deposit energies of the first, the second and the third interaction, respectively. These equations say that it can detect the incident gamma-ray energy even if the final scattered gamma ray escapes from the detector. Also this method may reduce background due to the improvement of the efficiency. On the other hand, the reconstructed direction remains

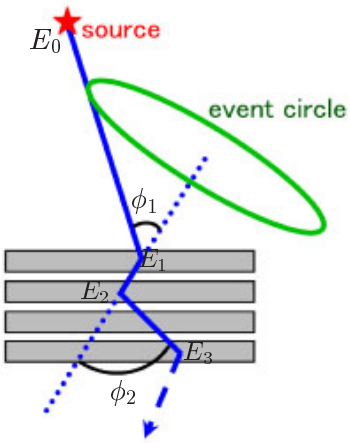

Figure 2.11: The schematic view of a Multiple Compton camera

an event circle same as the classical Compton imaging. Besides, in the reconstruction of an event, there is a problem of sorting the detected points in the interaction order.

Nuclear Compton Telescope (NCT) is an example of the multiple Compton imaging. NCT consists of some 3-dimensional position sensitive germanium detectors, and it measured the background of 200 - 800 keV on balloon experiment in 2005 [33].

Electron tracking Compton imaging

In comparison to the multiple Compton imaging, which is an improvement method on the energy information, the Electron Tracking Compton Imaging aims to improve the measurement of the direction of the incident gamma ray. In the classical/multiple Compton imaging, only the energy and the position of the recoil electron is measured, which makes it hard to specify which part of the event circle the gamma ray comes from.

The camera based on the electron tracking Compton imaging consists of a tracker, which detects the track and energy of the recoil electron, and an absorber, which detects the absorption point and the scattered gamma-ray energy (Figure 2.12). By the detection of the direction of the recoil electron, we obtain the fully ray-traced gamma-ray image.

The angle α between the recoil electron and the scattering gamma ray is measured for each gamma ray geometrically, and also this angle is obtained by the calculation using the energy of recoil electron and scattered gamma ray kinematically. Therefore we can select the good events of which the kinematic calculated angle is consistent with the measured one. Because of the background rejection by the angle α, the electron tracking Compton imaging fits for the MeV gamma-ray astronomy, whose serious problem is the obstruction by background.

Medium Energy Gamma-ray Astronomy (MEGA) is an example of the advanced Compton camera. Figure 2.13 is the schematic view of MEGA. The tracker consists of the stack of the silicon strip detector and the absorber is CsI scintillator. MEGA detects gamma ray with classical Compton imaging below 2 MeV, with electron tracking Compton imaging in 2 - 8 MeV [34]. But the accuracy of α is low because MEGA uses the solid tracker.

2.2.5 Pair tracking

Above 10MeV, a pair creation becomes a dominant interaction, and the pair tracking camera consists of a tracker, a converter and a calorimeter, as shown in Figure 2.14. When the gamma ray comes in the camera, it makes a pair creation in the converter made of the tungsten sheets.

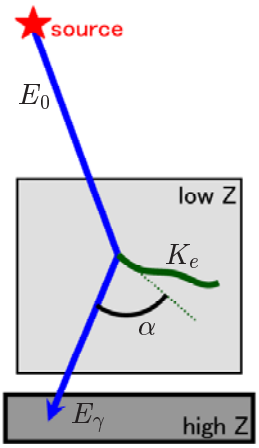

Figure 2.12: The schematic view of an Electron Tracking Compton camera

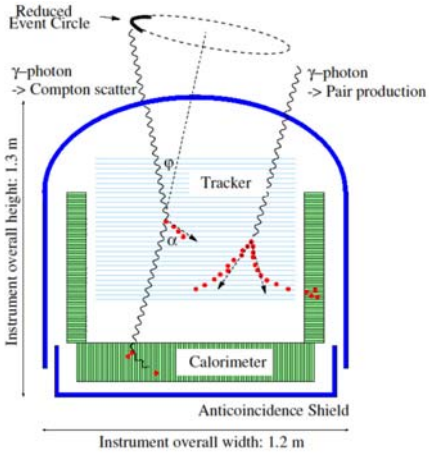

Figure 2.13: The schematic view of MEGA [34]

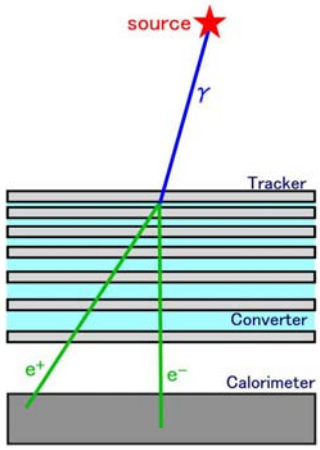

Figure 2.14: The schematic view of pair tracking camera

The created electron and positron run through the tracker, and stop in the calorimeter. By measuring the tracks in the tracker and deposit energies in the calorimeter, respectively, the momenta of the electron and the positron are measured. Then the momentum of the incident gamma ray is obtained by the sum of them. SAS-2, COS-B and EGRET were pair tracking telescopes using a spark chamber, and LAT of Fermi is also one of similar detectors using the silicon tracker.

The pair tracking camera is very similar to the advanced Compton camera. In actual, MEGA makes use of pair tracking for the detection of gamma ray above 8 MeV.

2.2.6 Summary of MeV gamma-ray imaging

The characters of each sub-MeV/MeV gamma-rays imaging method are summarized in Table 2.1. This table says that there is no 'all-rounder'. Therefore, the selection of suited method for the observation target is required, for example, Laue Lenses fits for observation of the radioactive isotopes distribution in the supernova remnant, Advanced Compton Imaging is suited to the all sky survey.

Table 2.1: The summary of MeV gamma-ray imaging

	with Collimator		Focusing		Compton Imaging			Pair Tracking
	Collimator	Coded Mask	Laue	Fresnel	Classical	Multiple	Advanced	
energy band	≤ 100 keV	$\leq$ MeV	fixed energy	fixed energy	100 keV - 10 MeV			≥ 100 MeV
true imaging	○	×	○	○	×	×	○	○
limitation for 1 photon	opening angle	can't limit	point	point	circle	circle	point	point
specify incident direction	○	×	○	○	△	△	○	○
detect for point source	△	○¶(△†)	○	○	△	△	○	○
detect for spread source	×	×	○	○	△	△	○	○
field of view	×	○	×	×	○	○	○	○
Angular resolution	×	○	○	○	△	△	△	○
minimum photon	1	0.5× pixel number	1	1	3	3	1	1
background rejection	×	×	×	×	×	△	○	△
escape event	×	×	×	×	×	detect	reject	×

¶: Full coded, †: Partial coded.

Table 2.2: The properties of some gamma-ray telescopes [1]

Parameter	OSSE	COMPTEL	EGRET	SPI	IBIS
Satellite	Compton Gamma-Ray Observatory			INTEGRAL	
Energy range¶	0.1 - 10	1 - 30	$20 - 3 \times 10^4$	0.02 - 8	0.015 - 10
Imaging method	Passive collimator	Classical Compton	Pair Tracking	Coded Mask	
Energy resolution	6.8 % @ 1 MeV	6.5 % @ 3 MeV	~ 20 %	2 keV @ 1 MeV	10 % @ 1 MeV
Field of View	$3.8° \times 11.4°$	1 str			$9° \times 9°$ ($19° \times 19°$)
Angular resolution		1.25°		2.5°	12 arc min
Narrow-line sensitivity†	$2 - 5 \times 10^{-5}$	$0.3 - 3 \times 10^{-5}$		5×10^{-6} @ 1 MeV	4×10^{-4} @ 1 MeV
Continuum sensitivity‡	2×10^{-4} @ 1 MeV	1.7×10^{-4} @ 1 - 3 MeV	5×10^{-6} @ > 100 MeV	$\sim 10^{-4}$	5×10^{-4}
Location accuracy	10 arc min	8.5 arc min	$5 - 10$ arc min	$\sim 1°$	30 arc sec

¶: in unit of MeV, †: 3σ for 10^6 sec and the unit is $\gamma/\mathrm{cm}^2/\mathrm{sec}$, ‡: 3σ for 10^6 sec and the unit is $\gamma/\mathrm{MeV}/\mathrm{cm}^2/\mathrm{sec}$.

2.3 Low and medium energy gamma-ray observatories

In this section, we briefly summarize several detectors loaded on the satellites for the low energy gamma-ray observation so far.

2.3.1 CGRO

NASA's Compton Gamma-Ray Observatory (CGRO) was operated from April 1991 to June 2000. Its mission was the first all sky survey in the wide energy bands between Sub-MeV and GeV. CGRO had 4 telescopes: OSSE, COMPTEL, EGRET and BATSE. In these instruments, BATSE was a gamma-ray telescope for GRB observations. The main properties of OSSE, COMPTEL and EGRET are listed up in Table 2.2, and the detected sources with COMPTEL and EGRET are listed in Table 2.3.

OSSE

The Oriented Scintillation-Spectrometer Experiment (OSSE) used the active and passive collimators. Figure 2.15 shows the schematic view of the one detector of OSSE, in which there were 4 identical detectors on CGRO. The main detector is a phosphor-sandwich (phoswich) detector consisting of the NaI(Tl) crystal (diameter: 33 cm, thickness: 10.2 cm) and the CsI(Na) crystal (thickness of 7.6 cm). In front of the NaI(Tl) crystal, a passive tungsten collimator was mounted. Around the main detector and the tungsten collimator, there was the annular shield of 8.5 cm thick NaI(Tl) crystal for the anticoincidence. For the rejection of charged particles, a thin plastic scintillator (0.6 cm thick) was placed on the collimator. OSSE had an energy range from 0.1 MeV to 10 MeV and had a FOV of $3.8° \times 11.4°$.

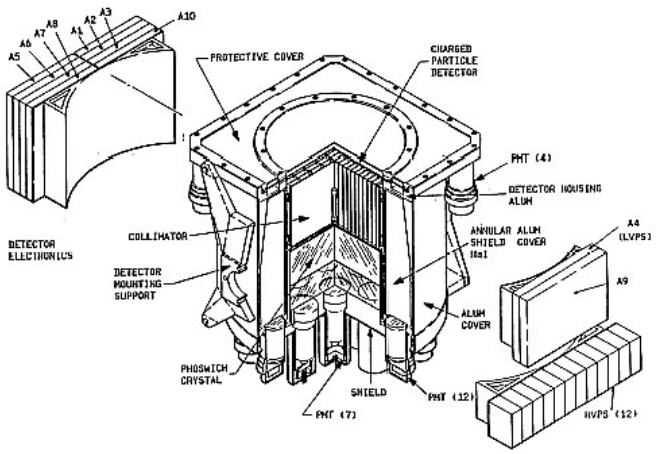

Figure 2.15: The schematic view of OSSE [1]

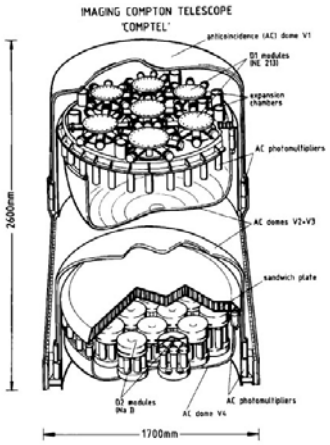

Figure 2.16: The schematic view of COMPTEL [30]

COMPTEL

The COMPTEL was the first Compton telescope launched on a satellite and was based on classical Compton imaging. The schematic view of COMPTEL is shown in Figure 2.16. The low-Z detector of it was a liquid organic scintillator NE213A (geometrical area: 4188 cm^2), and the high-Z detector was a NaI(Tl) crystal (geometrical area: 8744 cm^2). For the rejection of charged particles, each detector was surrounded by an anticoincidence counter dome. For the

background rejection, COMPTEL used the time of flight between the low-Z detector and the high-Z detector. COMPTEL had a angular resolution of $\sim 1.25^\circ$ for 10 MeV gamma ray.

Table 2.3: The detected sources with COMPTEL and EGRET [1, 5]

Type of source	COMPTEL		EGRET	
Spin-Down Pulsars	3	Crab, Vela, PSR 1509-58	6	Crab, Vela Geminga, PSR 1786-44, PSR 1055-52, PSR 1951+32
Other Galactic sources $\|b\| < 10^\circ$	7	Cyg X-1, Nova Persei 1992, GRO J1823-12, GRO J2228+61, GRO J0241+6119, Crab Nebula, Carina/Vela region	2	Cen X-3, Crab Nebula
Normal Galaxies			1	LMC
Active Galactic Nuclei	10	Cen A, etc.	77	Cen A, etc.
Gamma-Ray Line Source	7	SN191T (^{56}Co), SNR RX J0852-4642 (^{44}Ti), Cas A (^{44}Ti), Vela (^{26}Al), Carina (^{26}Al), Cyg region (^{26}Al), RE J0317-853 (2.223 MeV)		
Unidentified Sources	5		186	
Total Number	32		273	
Gamma-Ray Burst	31		4	

As shown in Table 2.3, EGRET detected about 270 gamma-ray sources. On the other hand, COMPTEL detected only about 30 steady sources. It seems the reason is that COMPTEL could not reject backgrounds completely by the TOF of both detectors. Therefore, the actual sensitivity of COMPTEL was lower than the design sensitivity.

EGRET

The Energetic Gamma-Ray-Experiment Telescope (EGRET) was based on pair tracking imaging detector. The schematic view of EGRET is shown in Figure 2.17. The central unit of EGRET was a multilevel wire-grid spark chamber with interleaved tantalum conversion layers. The trigger counter consists of the plastic scintillator sheets inserted into the lower part of the spark chamber, and the calorimeter consists of NaI(Tl) crystal with the thickness of 20 cm. For rejection of charged particles, the anticoincidence hood with the 2 cm thick plastic scintillator surrounded the spark chamber.

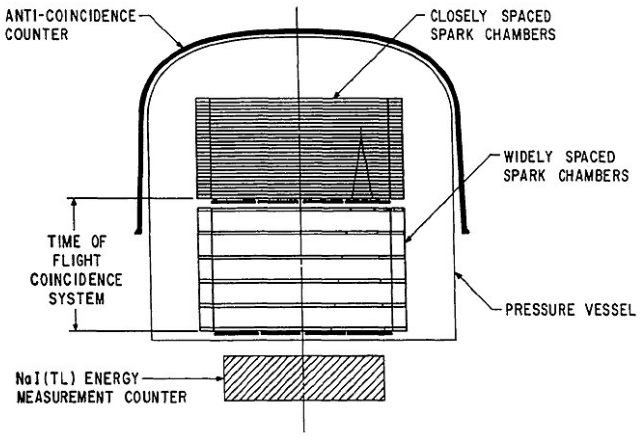

Figure 2.17: The schematic view of EGRET [1]

2.3.2 INTEGRAL

The INTErnational Gamma-Ray Astrophysics Laboratory (INTEGRAL) mission of the ESA was launched in 2002. INTEGRAL has two gamma-ray telescopes: SPI and IBIS, and also has two additional monitor instruments: JEM-X, an X-ray instrument between 3 keV and 35 keV, and OMC, an optical telescope observing at 500-850 nm. The main properties of SPI and IBIS are listed up in Table 2.2.

SPI

The SPectrometer on Integral (SPI) is based on coded aperture imaging. The detector of SPI consists of the array of 19 Ge crystals cooled to 85 K, and thus, SPI has a good energy resolution of 2 keV for 1 MeV. The mask of SPI is made by the 3 cm thick tungsten, and the distance between the mask and the detector is 1.71 m. The whole detector is surrounded by the active BGO shield of mass of 511 kg viewed by 181 PhotoMultiplier Tubes (PMT). Due to the high energy resolution, the SPI's sensitivity for narrow-line gamma rays is improved at least by a factor of 10 better than other gamma-ray telescopes.

IBIS

The Imager on Board of the Integral Satellite (IBIS) also uses a coded aperture imaging. The coded mask of IBIS is the 16 mm thick tungsten mask. The detector consists of 2 layers. The lower layer is the array of 4096 CsI scintillators viewed by the silicon PIN photodiodes (each CsI size: $9 \times 9 \times 30$ cm^3, total area: 3318 cm^2), named PICsIT. The upper layer is the array of 16384 CdTe pixels (pixel size: $4 \times 4 \times 2$ mm^3, total area: 2621 cm^2), named ISGRI. ISGRI detects from 15 keV to 400 keV, and PICsIT covers from 200 keV to 10 MeV. The detector layers are surrounded by the BGO active shield, and a passive tungsten collimator is placed between the mask and BGO shield. The distance between the tungsten mask and the upper layer detector is 3.2 m, so that IBIS has a good angular resolution of 12 arc sec.

Chapter 3

Future of a Compton and pair tracking telescope

3.1 Goal for the future of gamma-ray telescope

In the X-ray astronomy, the observation technique has been almost established, and the sensitivity less than 1mCrab is achieved. In addition, GeV and TeV gamma-ray astronomies have recently accomplished rapid progress. In these regions, the sensitivity less than or equal to 10mCrab has been achieved because of large-area stereoscopic Cherenkov telescopes and Fermi satellite launched in 2008. On the other hand, in the energy range from sub to several tens of MeV, all sky survey was done only by COMPTEL and the sensitivity is worse than that of other region as shown in Figure 3.1. After COMPTEL, INTEGRAL satellite was launched and observes the sub MeV gamma rays. Since SPI and IBIS onboard INTEGRAL use a coded aperture imaging, the sensitivity is worse than that of COMPTEL. Thus, the sub to several tens of MeV region remains as a "sensitivity gap".

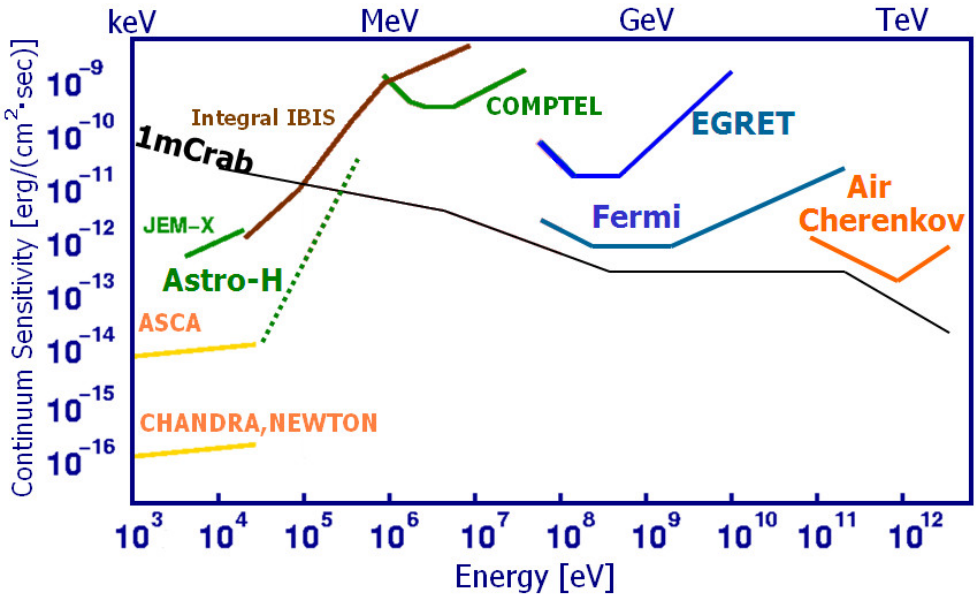

Figure 3.1: The continuum sensitivities of X/Gamma-ray observatories

Although the technology of the X-ray telescope which can take the image with an extremely

high angular resolution of a few second has established, it is difficult in the gamma-ray region to use the focusing mirror because of the short wavelength. On the other hand, the coded aperture imaging for up to sub MeV region is effective. However, the sensitivity for the coded aperture imaging is not good due to the large noises. Since over sub MeV gamma rays behaves as a quantum, the reconstruction of physics process is needed for obtaining the arrival directions of photons. Then, the Compton imaging for MeV region and the pair tracking for GeV region were used as the imaging method. Figure 3.2 shows the achieved angular resolutions in the energy range from X-ray to GeV gamma-ray regions. Although the angular resolutions of about 10 minute in the X-ray, sub MeV and GeV gamma-ray region have been achieved, there still remains only observation with the angular resolution worse than 1 degree in the MeV gamma-ray region.

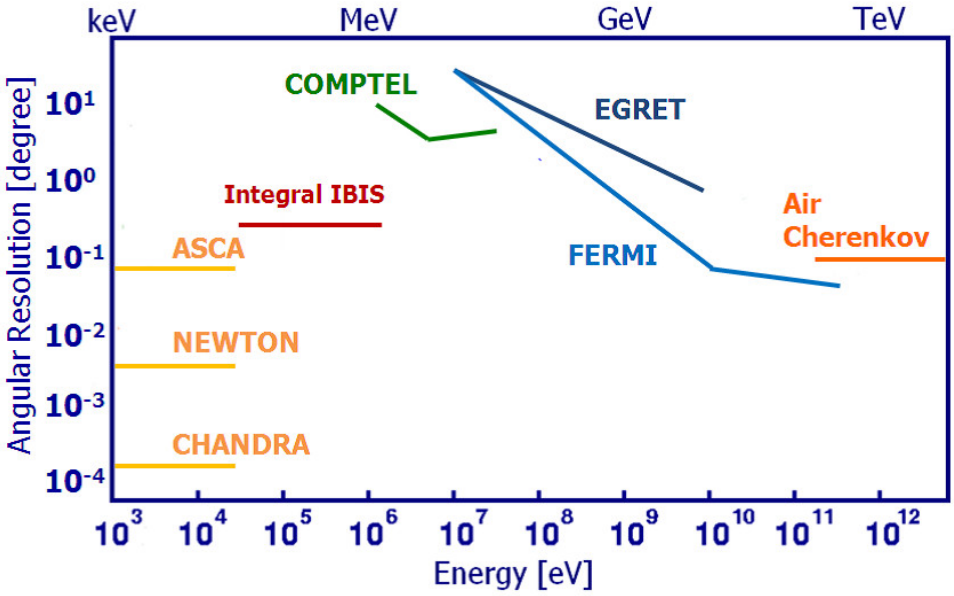

Figure 3.2: The angular resolutions of X/Gamma-ray observatories

Though the MeV gamma-ray astronomy has a lot of unique and interesting topics and plays an important role as a bridge between X-ray and GeV gamma-ray astronomy, the observation technology is still immature as described above. Therefore, the developments of the telescope with better sensitivity and angular resolution in the MeV gamma-ray region are necessary. Then, we are developing a telescope having a good sensitivity and wide field of view with a wide band energy range from sub to 100 MeV. We set the goal to "ten times better sensitivity than COMPTEL with the angular resolution of about 1 degree". The gamma-ray telescope is based on electron-tracking Compton imaging in the low energy band from sub to 10 MeV and pair-tracking imaging in the high energy band from a few to 100 MeV. Figure 3.3 shows a schematic view of the telescope. This telescope consists of a gaseous time projection chamber (μ-TPC) and a scintillation camera surrounding the μ-TPC. For Compton mode, the energy and the track of the recoil electron are measured in the μ-TPC, and the energy and the absorption point of the scattered gamma ray are measured in the scintillation camera. For pair creation mode, the tracks of the electron and the positron are measured in the μ-TPC and the energies of them are measured in the scintillation camera. Several prototypes of the gamma-ray telescopes with a detection volume of $10 \times 10 \times 10$ cm^3 were developed and their performances with Compton mode in the low energy range were studied. In addition, we started to develop the prototype telescope for the pair creation mode using the same μ-TPC. In the following, I explain the

principle and the concept of the gamma-ray imaging method of our telescope, and then show the result of the simulation study for pair creation mode. Finally, I describe the plan for the development of the telescope in this chapter.

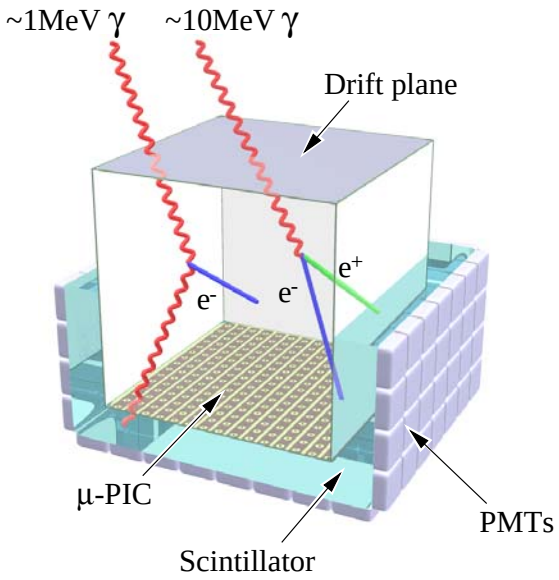

Figure 3.3: The schematic view of the gamma-ray telescope

3.2 Compton mode in the low energy band

3.2.1 Principle of electron tracking Compton imaging

For the electron tracking Compton imaging, four physical parameters; both the energy and the direction of both the scattered gamma ray and the recoil electron, are measured in order to obtain both the energy and the direction of the incident gamma ray. Figure 3.4 shows the definition of the parameters in the electron tracking Compton imaging. The energy and direction of the scattered gamma-ray are E_γ and $\vec{g}$. The energy and direction of the recoil electron are K_e and $\vec{e}$. Also the scattering angle and the recoil angle are ϕ and ψ. The differential angle between $\vec{g}$ and $\vec{e}$ is α, where $\vec{g}$ and $\vec{e}$ are the unit vectors.

The incident energy E_0 and the incident direction $\vec{s}$ of the initial gamma-ray are described by

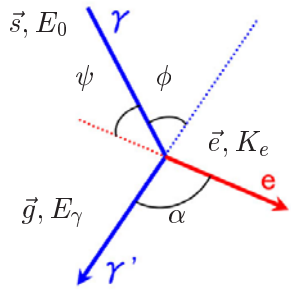

Figure 3.4: The parameters in Electron Tracking Compton Imaging

following equations:

$$E_0 = E_\gamma + K_e, \tag{3.1}$$

$$\vec{s}_{\rm rcs} = \left(\cos\phi - \frac{\sin\phi}{\tan\alpha}\right)\vec{g} + \frac{\sin\phi}{\sin\alpha}\vec{e}, \tag{3.2}$$

$$= \frac{E_\gamma}{E_\gamma + K_e}\vec{g} + \frac{\sqrt{K_e(K_e + 2m_e c^2)}}{E_\gamma + K_e}\vec{e}. \tag{3.3}$$

Here the scattering angle ϕ and the recoil angle ψ are written as follows,

$$\cos\phi = 1 - \frac{m_e c^2}{E_\gamma + K_e}\frac{K_e}{E_\gamma}, \tag{3.4}$$

$$\cos\psi = \left(1 + \frac{m_e c^2}{E_\gamma + K_e}\right)\sqrt{\frac{K_e}{K_e + 2m_e c^2}}. \tag{3.5}$$

The differential angle α between $\vec{g}$ and $\vec{e}$ is described by the definition:

$$\cos\alpha_{\rm geo} = \vec{g}\cdot\vec{e}. \tag{3.6}$$

On the other hand, α is described with E_γ and K_e by the Compton kinematics:

$$\cos\alpha_{\rm kin} = \left(1 - \frac{m_e c^2}{E_\gamma}\right)\sqrt{\frac{K_e}{K_e + 2m_e c^2}}. \tag{3.7}$$

The angle α has a minimum value depending on the energy of the incident gamma-ray, and the minimum is described:

$$\cos\alpha_{\rm lim} = \begin{cases} 0 & (k < 1) \\ \frac{k-1}{k+2}\sqrt{\frac{k^2-1}{k(k+2)}} & (k \geq 1) \end{cases}, \qquad k = \frac{E_0}{m_e c^2}. \tag{3.8}$$

Figure 3.5 shows the dependence of ϕ, ψ and α on E_γ respectively, and Figure 3.6 shows the dependence of α_{lim} on E_0, respectively.

The angle α is a characteristic parameter of the electron tracking Compton imaging. The α makes it possible to select the Compton scattering events from the backgrounds. The α is obtained from the equation (3.6) and (3.7), where (3.6) depends on only the geometrical information, and (3.7) depends on only the kinematic information. Thus, the $\alpha_{\rm geo}$ is independent from the $\alpha_{\rm kin}$. For this reason, we can select good events, in which Compton scattering occurs in the tracker and scattered photon absorbs perfectly in the absorber, by requiring the follows

$$\alpha_{\rm geo} = \alpha_{\rm kin}. \tag{3.9}$$

3.2.2 Angular resolution determination

Uncertainties in the measurement limit the accuracy of the angular resolution. For the electron tracking imaging, the angular resolution is described in terms of the Angular Resolution Measure (ARM) and the Scatter Plane Deviation (SPD). Figure 3.7 shows the definition of the ARM and the SPD. The ARM is the accuracy of the scattering angle:

$$\Delta\phi_{\rm ARM} = \arccos\left(\vec{s}\cdot\vec{g}\right) - \arccos\left(1 - \frac{m_e c^2}{E_\gamma + K_e}\frac{K_e}{E_\gamma}\right). \tag{3.10}$$

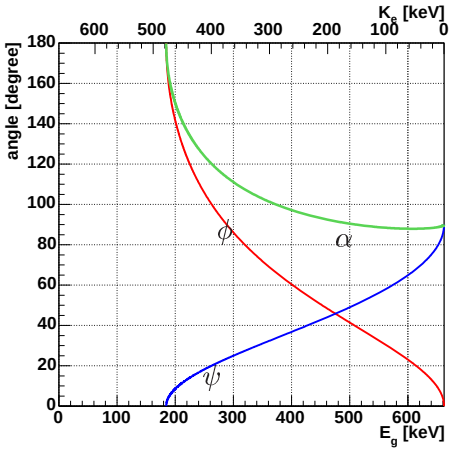

Figure 3.5: The E_γ dependence of ϕ, ψ, α ($E_0 = 662$ keV)

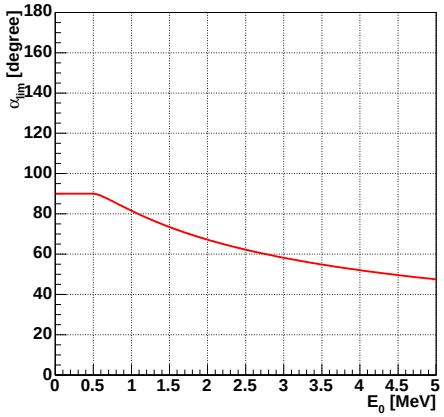

Figure 3.6: The E_0 dependence of $\alpha_{\rm lim}$

The SPD is the accuracy of the determination of the scattering plane:

$$\Delta\nu_{\rm SPD} = \mathrm{sign}\left(\vec{g}\cdot\left(\frac{\vec{s}\times\vec{g}}{|\vec{s}\times\vec{g}|}\times\frac{\vec{s}_{\rm rcs}\times\vec{g}}{|\vec{s}_{\rm rcs}\times\vec{g}|}\right)\right)\arccos\left(\frac{\vec{s}\times\vec{g}}{|\vec{s}\times\vec{g}|}\cdot\frac{\vec{s}_{\rm rcs}\times\vec{g}}{|\vec{s}_{\rm rcs}\times\vec{g}|}\right), \tag{3.11}$$

where $\vec{s}$ is the real direction, and $\vec{s}_{\rm rcs}$ is the reconstructed direction of the incident gamma-ray. The SPD is relevant only when the direction of the recoil electron can be measured. Thus, SPD is a unique parameter in the electron tracking Compton mode. The error region of an event is determined by a sector shape.

3.2.3 Doppler broadening

In actual detectors, the electrons are neither free nor at rest, but bound to a nucleus or a molecular. Thus, the electrons have a kinematic energy before Compton scattering. Compared with the Compton scattering on free electrons at rest, three consequences on the actual scattering arise:

- The total scattering cross section changes. Especially, at low energy under 100 keV, photons have a slightly higher cross section than predicted by (2.5).
- The distribution of scattering angle changes. Compared to (2.5), small and large scatter angles are slightly suppressed.

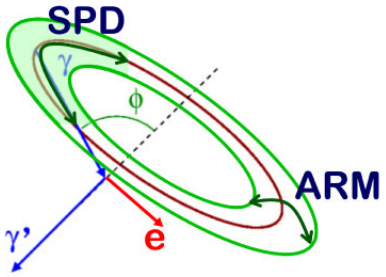

Figure 3.7: The definition of ARM & SPD

- The energy distribution between scattered gamma ray and recoil electron changes, while the sum of the interaction energies is still exactly equal to the total gamma-ray energy. Because the electron before the scattering has a finite energy, the energy of scattered gamma-ray that is scattered at a fixed angle from a mono-energetic source has a narrow distribution around the estimated energy from an unbound Compton scattering. This effect is called Doppler broadening.

For Compton imaging, the scattering angle is obtained using the energy of scattered gamma-ray and the energy of recoil electron. Therefore, the accuracy of the scattering angle (ARM) is essentially affected by Doppler broadening, and hence Doppler broadening makes the intrinsic limit for the angular resolution of the ARM. Figure 3.8 shows the deviation of the ARM due to

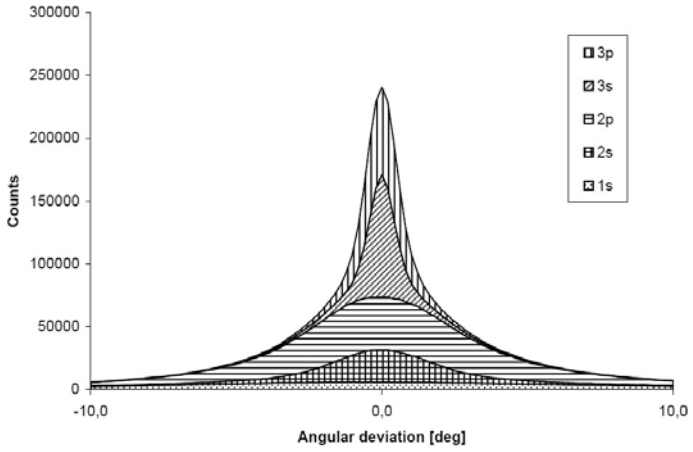

Figure 3.8: The ARM distribution of each electron orbit ($E_0 = 200$keV, Si) [35]

Doppler-broadening. The total profile is composed of each profile of the different orbit. Because the electron at the outer orbit has the lower kinematic energy, the effect of Doppler broadening is smaller. Figure 3.9 shows the dependence of the angular resolution on the atomic number. On average, the angular resolution worsens with increasing Z. Figure 3.10 shows the energy dependence of Doppler broadening. The energy of an incident gamma-ray is higher, the effect of Doppler broadening is smaller because the initial energy of an electron is negligible.

3.2.4 Multiple scattering

In the material, A charged particle is deflected by many small angle scattering processes. Most of this deflection is due to Coulomb scattering from nuclei, and hence the effect is called multiple Coulomb scattering. The uncertainty of the multiple Coulomb scattering is described by Moliere theory. It is represented by a form of Gaussian for small deflection angles [36]. At the range x, the distribution of the scattered angle is given by,

$$\theta_{\mathrm{mul}} = \frac{13.6\mathrm{MeV}}{\beta cp} z \sqrt{\frac{x}{X_0}} \left[1 + 0.038 \ln \left(\frac{x}{X_0} \right) \right], \tag{3.12}$$

where βc, p, z, and X_0 are the velocity of an electron, the momentum, charge number of the incident particle, and the radiation length, respectively.

In the electron tracking Compton imaging, the scatter plane is determined by the direction of the recoil electron. The electron loses the directional information because of the multiple scattering in the material as described above. Thus, multiple scattering process set an intrinsic limit of the SPD. If the direction of the recoil electron in Ar gas at 1 atm is obtained at 1 mm, the scattered angle is about 15° corresponding to the intrinsic limit of the SPD.

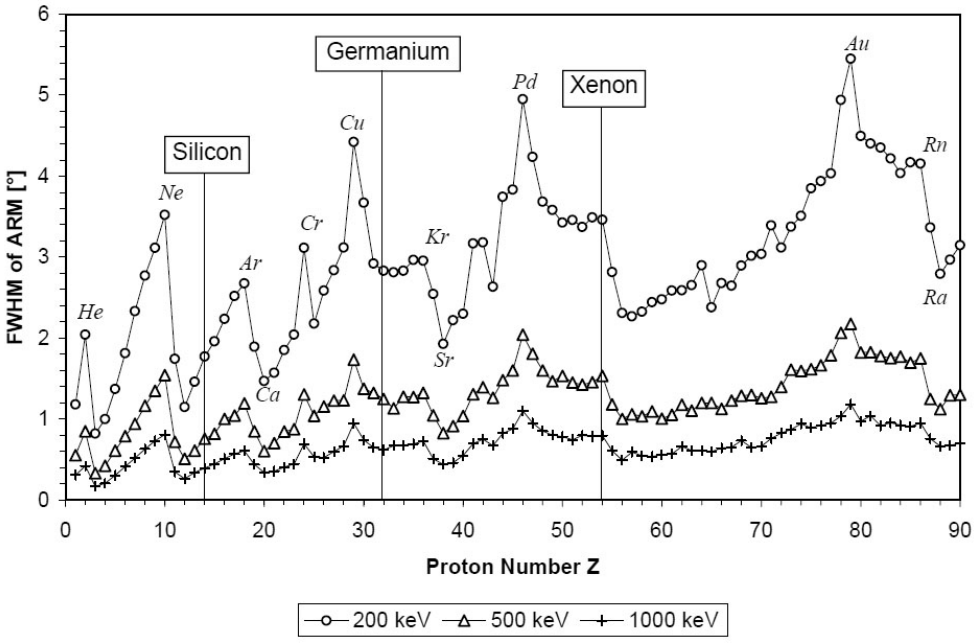

Figure 3.9: The Z dependence of the ARM [35]

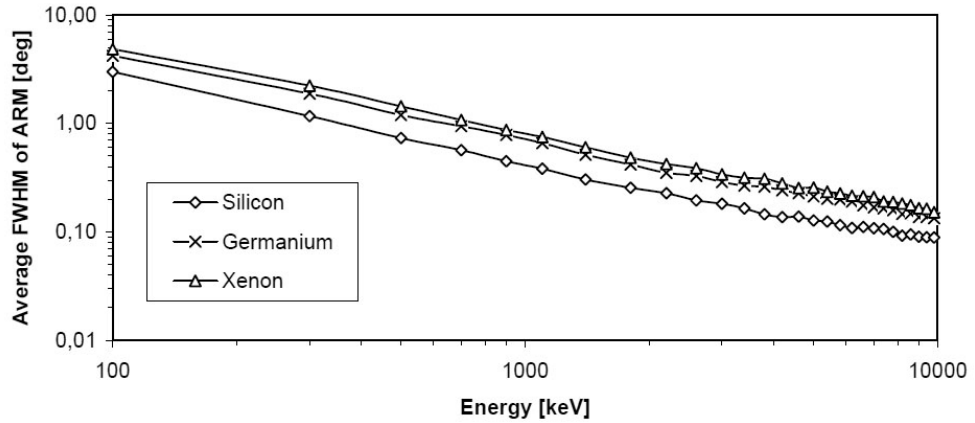

Figure 3.10: The energy dependence of Doppler broadening [35]

3.3 Pair creation mode for high energy band

3.3.1 Principle of pair tracking imaging

When the energy of the incident gamma ray exceeds two times the rest mass of an electron, 1.022 MeV, the conversion of the gamma ray to an electron-positron pair in the electromagnetic field of a nucleus starts and plays a role in the interaction between the photon and the material above several MeV. Especially, above about 10MeV, the pair creation becomes a dominant interaction as shown in Figure 3.11.

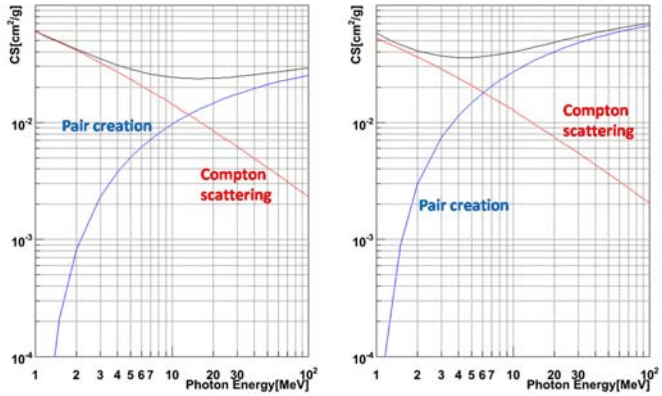

Figure 3.11: The cross section of the Compton scattering and the pair creation in Ar and ethane gas mixture(left) and Xe (right)

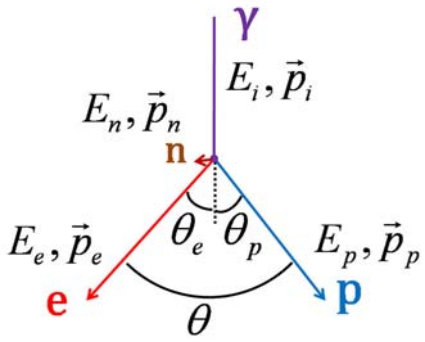

Figure 3.12: The parameters in Pair Tracking Compton Imaging

If the energy of a photon exceeds four times the rest mass of an electron, 2.044 MeV, the pair creation also occur in the field of an atomic electron. In the pair creation in the field of an electron, the momentum is not transferred to the nucleus, but to the electron. In this process, the photon is converted to one positron and two electrons. In an atom of any atomic number, Z, the ration of the probability for the pair creation in the field of an electron to that for the pair creation in the field of a nucleus can be written:

$$\frac{P_{electron}}{P_{nucleus}} = \frac{1}{CZ} \tag{3.13}$$

where C is a factor which depends on the energy of the incident gamma ray, but not on Z. C is about 2.6 at 6.5 MeV, about 1.2 at 100 MeV, and to approach 1 as the energy approaches

infinity [37]. In the prototype gamma-ray telescope, this effect is negligible because the material with $Z > 10$ is used.

Figure 3.12 shows the definition of the parameters in the pair tracking imaging. The energy of the incident gamma ray, electron, and positron are E_i, E_e, and E_p, respectively. The energy transfered to the nucleus is E_n. The momentum of the incident gamma ray, electron, positron, and nucleus are $\vec{p_i}$, $\vec{p_e}$, $\vec{p_p}$, and $\vec{p_n}$, respectively. The scatter angles of the electron and the positron are θ_e, θ_p, respectively. The opening angle is θ.

The incident energy and the incident momentum are described by following equations:

$$E_i = E_e + E_p + E_n + 2m_e c^2, \tag{3.14}$$

$$\vec{p_i} = \vec{p_e} + \vec{p_p} + \vec{p_n}, \tag{3.15}$$

where m_e is the rest mass of the electron.

The most probable momentum transfer to the nucleus is about 0.511 MeV/c [38, 39] which is not very large, and the mass of nucleus is much larger than that of electron (positron). So, E_n is negligible compared to E_e and E_p. For example, the energy transfered to nucleus is about 3.5 eV for Ar. Thus, the influence of the recoil nucleus can be neglected, and the energy and the direction of the incident gamma ray can be approximately written as follows:

$$E_i \simeq E_e + E_p + 2m_e c^2, \tag{3.16}$$

$$\vec{e_i} \simeq \frac{E_e \vec{e_e} + E_p \vec{e_p}}{E_e + E_p}, \tag{3.17}$$

where, $\vec{e_i} = \frac{\vec{p_i}}{|\vec{p_i}|}$, $\vec{e_e} = \frac{\vec{p_e}}{|\vec{p_e}|}$, and $\vec{e_p} = \frac{\vec{p_p}}{|\vec{p_p}|}$.

In the pair tracking imaging, the energy and the track of electron and positron are needed to measure in order to reconstruct the energy and the direction of the incident gamma ray. In the case of our prototype gamma-ray telescope, the energy of electron and positron cannot be determined completely because of the readout system of the scintillation camera as described in Chapter 6. Thus, the more simplification for Equation (3.17) is needed. We used the next expression:

$$\vec{e_i} \simeq \vec{e_e} + \vec{e_p}. \tag{3.18}$$

The validation of this expression is studied by simulation (See next section).

Because the nucleus obtains the momentum after conversion, the electron and the positron are assumed to have an angular distribution. The energy-angle distribution is given by [40, 41] as follows:

$$\begin{aligned}\frac{d\sigma}{dp_e d\Omega} =& \frac{2\alpha^3 E_e^2}{\pi E_i m_e^4}\left\{\left[\frac{2x(1-x)}{(1+l)^2} - \frac{12lx(1-x)}{(1+l)^4}\right](Z^2+Z)\right. \\ &\left. + \left[\frac{2x^2-2x+1)}{(1+l)^2} + \frac{4lx(1-x)}{(1+l)^4}\right]\left[X - 2Z^2 f((\alpha Z)^2)\right]\right\},\end{aligned} \tag{3.19}$$

where $x = E_e/E_i$, $l = E^2\theta_e^2/m^2$, $f(z) = 1.202z - 1.0369z^2 + 1.008z3/(1+z)$, and X is the constant value depending on Z.

Equation (3.19) is for the electron. If p_p, E_p, and θ_p are used instead of p_e, E_e, and θ_e, the distribution for the positron is given. However, this distribution is quite complicated and can be approximated by a density function as follows [42]:

$$f(u) = \frac{9a^2}{9+d}\left[ue^{-au} + due^{-3au}\right], \tag{3.20}$$

where $a = 5/8$, $d = 27$, and $\theta_e = \frac{m_e^2}{E_e}u$ (or $\theta_p = \frac{m_e^2}{E_p}u$). Figure 3.13 shows the distribution of the scatter angles of the electron (positron) depending on the energy of incident gamma ray. For the low energy gamma rays, the scatter angle changes about 12 degree in each gamma ray even if the gamma ray has the same energy.

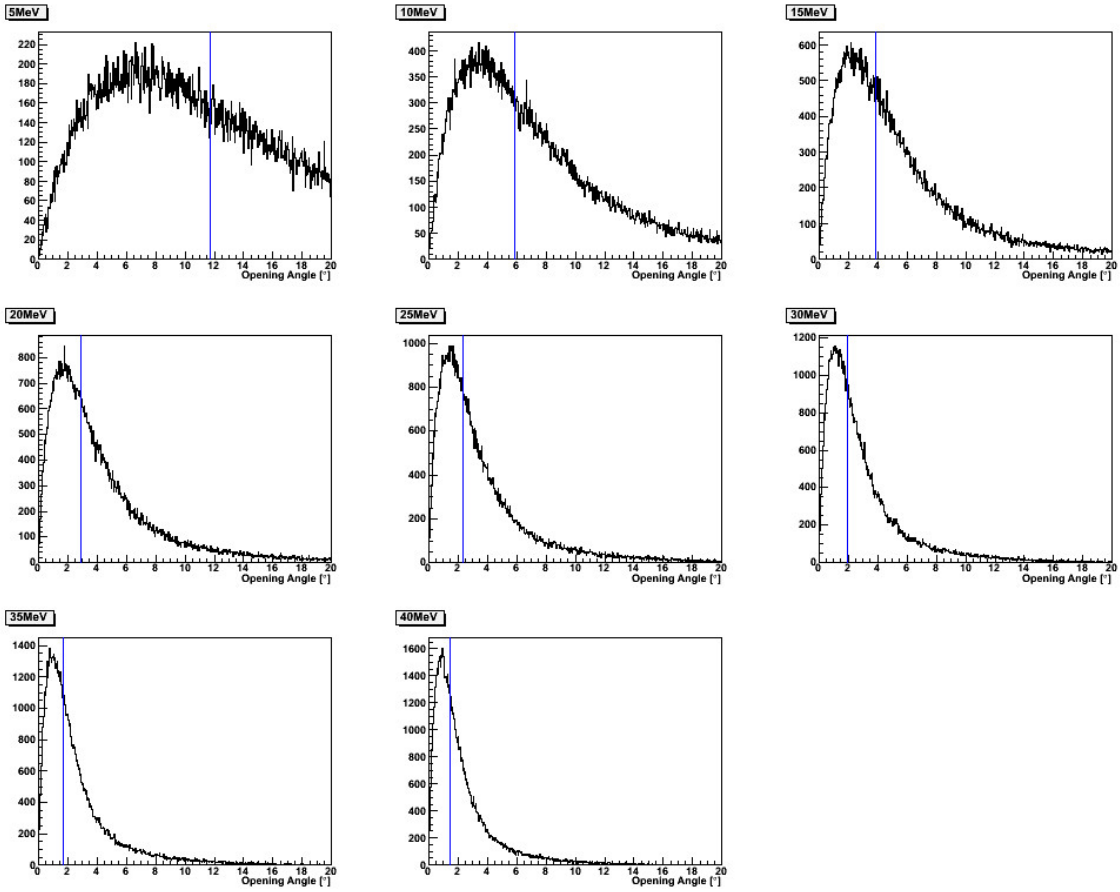

Figure 3.13: The distribution of the scattered angle of electron (positron) depending on the energy of incident gamma ray (5 - 40 MeV). Lines show the mean value of the distribution.

3.3.2 Angular resolution determination

Pair tracking imaging is limited in the angular resolution by three reasons: (1) the uncertainty of the opening angle in the pair creation, (2) the multiple scattering, and (3) the accuracy of the track and the energy measured in the detector. (1) and (2) essentially limit the intrinsic angular resolution of the pair tracking imaging. This intrinsic resolution is estimated as follows. The uncertainty of the opening angle is due to the difficulty of the measurement of the recoil of the atomic nucleus. The most probable momentum transfer to the nucleus (P_n) is about 0.511 MeV/c, and the most probable scattered angle is about $70 - 90^\circ$ corresponding to the incident energy of *over* $20 - 5$ MeV [38,39]. If we think it by two dimensional approximation as shown in Figure 3.14. The limit angle, θ_{lim}, is estimated to be:

$$\theta_{lim} \simeq arctan\frac{m_e c^2 sin\phi}{E_i - m_e c^2 cos\phi} \tag{3.21}$$

where ϕ is the most probable scattered angle of the recoil of the atomic nucleus.

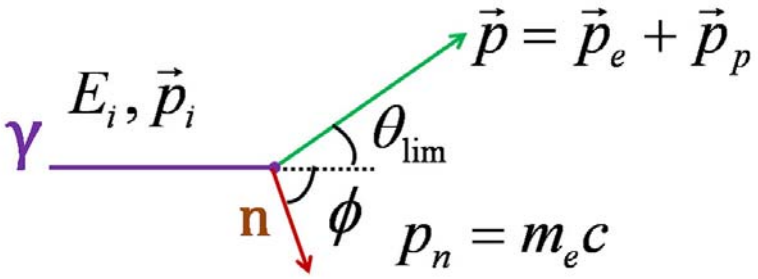

Figure 3.14: The simplification to two dimension

The multiple scattering limit is estimated by Equation (3.12). In the pair creation, the differential cross section, $d\sigma_e$, for the creation of an electron of E_e can be written as:

$$d\sigma_e = \frac{\sigma_0 Z^2 P}{E_i - 2m_e c^2} dE_e \tag{3.22}$$

where $\sigma_0 = \frac{1}{137}(\frac{e^2}{m_e c^2})^2$ (e is elementary charge) and P is a complicated function of E_i and Z [37]. Figure 3.15 is the energy dependence of the pair creation from Equation (3.22). This figure says the probability of the energy transfer to the electron is symmetrical on the boundary of about 0.5 which means the incident photon's energy is shared evenly between electron and positron. Thus, as for the estimation of the multiple scattering limit, rough approximation is used. Specifically, in the calculation of the estimation, the half energy of the incident gamma ray except for the rest mass is used for the energy in Equation (3.12).

Figure 3.16 shows the calculated limit for Ar and Si using Equation (3.21) and (3.12). In this calculation, we assumed that $\phi = 90°$ in Equation (3.21) and only the uncertainty from the multiple scattering of the electron (or positron) contributes to the multiple scattering limit. It is noted that the resolution limit is actually better than that of the calculation because ϕ is less than 90°. If the silicon tracker is used for the pair creation telescope, the resolution is about 12° at 10 MeV and 2° at 60 MeV. On the other hand, if the gas (Ar) is used, the resolution is about 3° at 10 MeV and 0.5° at 60 MeV. So, the resolution using the gas is four times better than that using the silicon. Therefore, we can say that our telescope is useful as the pair creation telescope in the energy range from a few to 100 MeV.

3.4 Simulation study for pair creation mode

Monte Carlo Simulation is an important task for designing the detector. We use a "Geometry and Tracking 4 (GEANT4) " for simulation of our telescope and the calculation of an enhanced performance. The GEANT4 was originally developed by CERN [43] in 1994 - 1998 and is being maintained and improved. The GEANT4 is written in C++ using an object oriented approach, and provides facilities for modeling the complex-instrument geometry, composition and operating parameters within the context of a substantial range of particle interaction physics. Recently, the GEANT4 is used in various fields such as the high energy physics, astrophysics, medical, and so on, and it is a reliable tool. We use a GEANT4.9.3 [44] all for the following simulations. Using GEANT4, the fundamental performances of the gamma-ray telescope with pair creation mode in the ideal condition were studied.

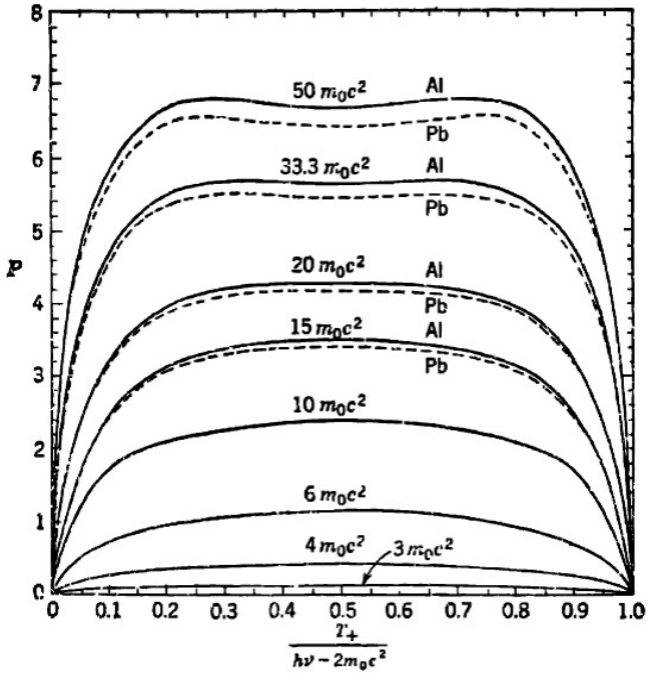

Figure 3.15: The probability of the energy dependency of the pair creation [37].

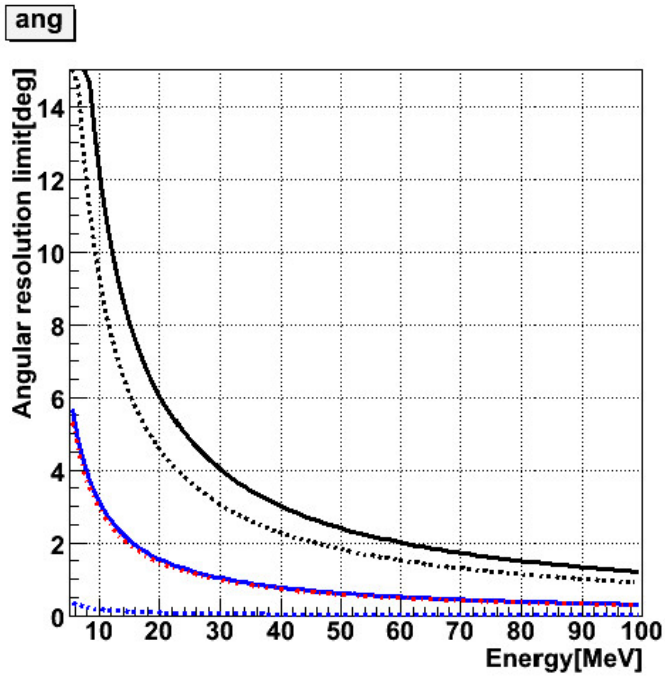

Figure 3.16: The calculated angular resolution limit in Ar (blue line) and Si (black line). The thickness is 500μm. The resolutions from the multiple scattering are given by blue and black dashed line corresponding to Ar and Si, respectively. The red dashed line is the resolution from the uncertainty of the opening angle.

3.4.1 Setup

Simulations were done based on Ar based gas mixture (Ar : C_2H_6=90:10) or Xe based gas mixture (Xe : Ar : C_2H_6 = 80 : 18 :2) at 1 atm as a 10×10×15 cm^3 μ-TPC, and 1.3 cm thick Gd_2SiO_5 (GSO) which surrounds the μ-TPC with the clearance of 1 cm as a scintillation camera as shown in Figure 3.17. This setup is thought about as application of the existing telescope with Compton mode. The position and energy resolutions of both the μ-TPC and the scintillation camera were not considered in this simulation in the ideal condition. We adopted the Livermore low-energy electromagnetic model [45] based on the Livermore data library [46–48] and multiple scattering model complemented by the old process [49, 50].

The position of incident gamma rays was over the center of the μ-TPC as shown in Figure 3.17. Here, we selected the events in which the incident gamma ray converted the electron and positron in the gas of the μ-TPC and converted electron (positron) deposited its energy in the scintillation camera. The vector of the electron (positron) is calculated using the conversion point and first interaction point between electron (positron) and the gas in order to consider the influence of the multiple scattering.

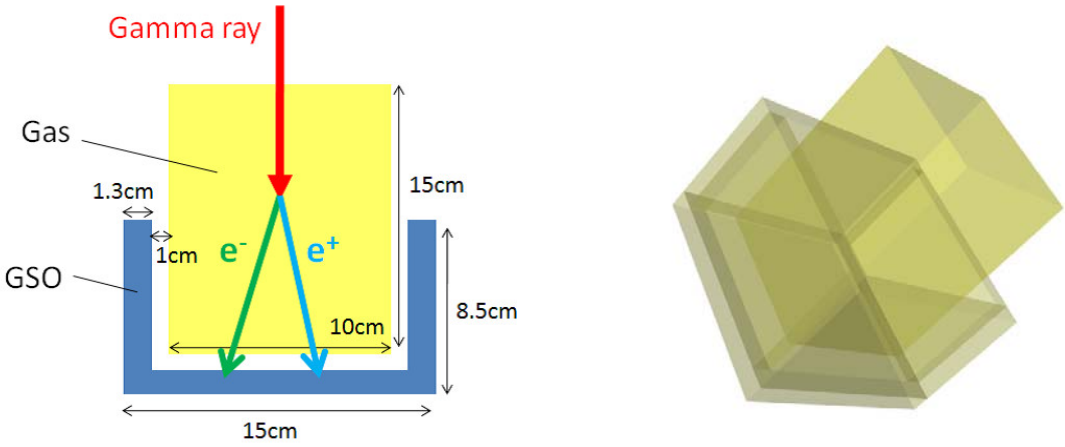

Figure 3.17: The schematic view (left) and the example of the 3-dimensional view (right) of the gamma-ray telescope in the simulation.

3.4.2 Angular resolution

At first, the images are obtained with the energy information of an electron and a positron using Equation (3.17). Figure3.18 shows the reconstructed images for 20 MeV gamma rays in Ar based gas mixture and Xe based gas mixture. Consequently, the angular resolution was determined simply from the deviation (θ) of the calculated from the generated direction. The angular resolution for the pair creation is usually defined by the half-angle of a cone containing 68 % of all reconstructed events, while FWHM is used for the Compton mode. Figure 3.19 shows the distributions of the squared angular deviations in Ar based gas mixture and Xe based gas mixture. Figure 3.20 shows the angular resolution as a function of the incident gamma-ray energy in Ar based gas mixture and Xe based gas mixture. This angular resolutions are 0.59° and 1.22° at 20 MeV in Ar based gas mixture and Xe based gas mixture, respectively. These angular resolutions can be considered to be the actual intrinsic angular resolutions.

Figure 3.21 shows the reconstructed images for 20 MeV gamma rays in Ar based gas mixture and Xe based gas mixture without the energy information of electron and positron using Equation (3.18). Figure 3.22 shows these distributions of the squared angular deviations. The

angular resolutions as a function of the incident gamma-ray energy in Ar based gas mixture and Xe based gas mixture are shown in Figure 3.23. The resolutions are 3.28° and 3.79° at 20 MeV in Ar based gas mixture and Xe based gas mixture, respectively. Thus, we checked that the imaging without energy information of electron and positron using Equation 3.18 is allowable as a first step, though these resolutions are several times worse than those from Equation (3.17).

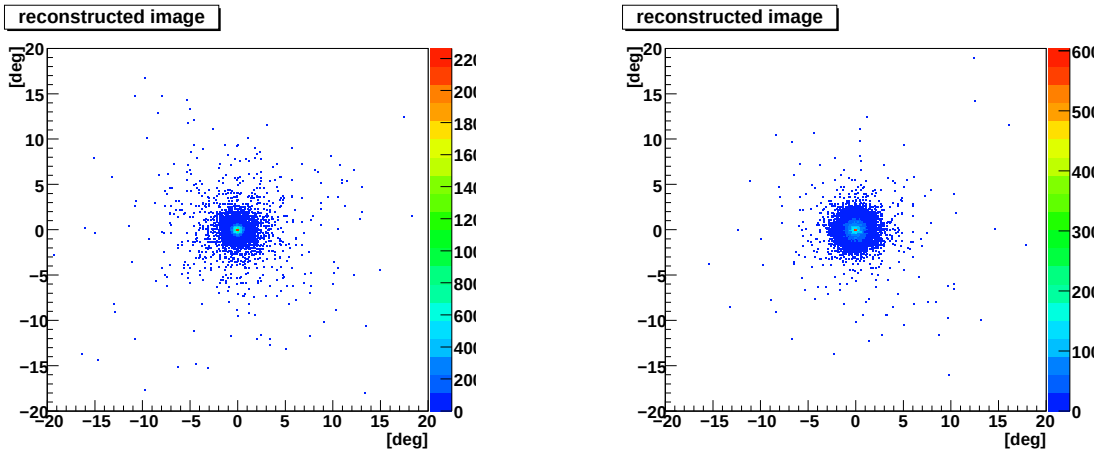

Figure 3.18: The reconstructed images in Ar based gas mixture (left) and Xe based gas mixture (right) at 20 MeV by Equation (3.17)

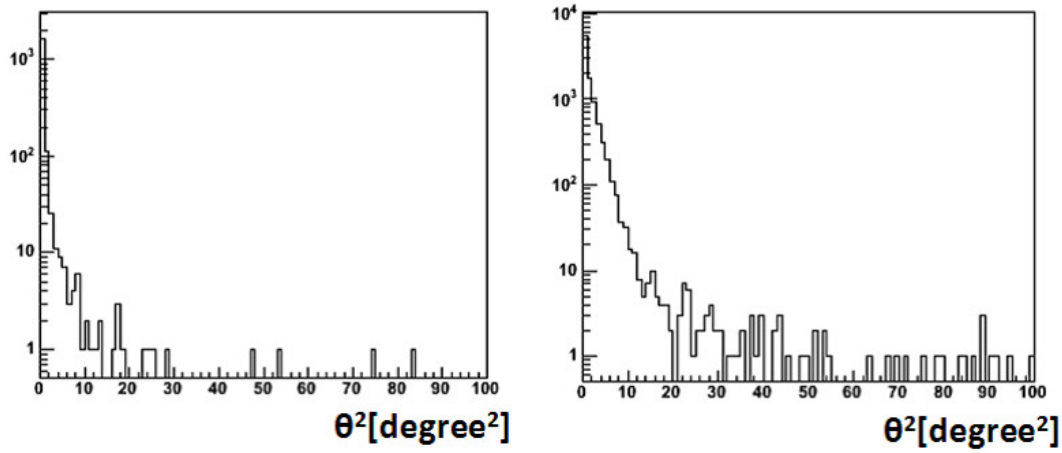

Figure 3.19: The ideal θ squared distribution of Ar based gas mixture (left) and Xe based gas mixture (right) at 20 MeV by Equation (3.17).

3.4.3 Detection efficiency

Next, the detection efficiency was calculated. Figure 3.24 shows the detection efficiencies as a function of the incident energy of gamma rays. In this result, the detection efficiency is very close to that of the probability of the pair creation in the ideal condition since μ-TPC measures lots of points on the track. Thus, it is expected that the detection efficiency of our gamma-ray telescope depends on the geometry of the detector (for example, coverage of the scintillation camera for the μ-TPC) and the analysis method.

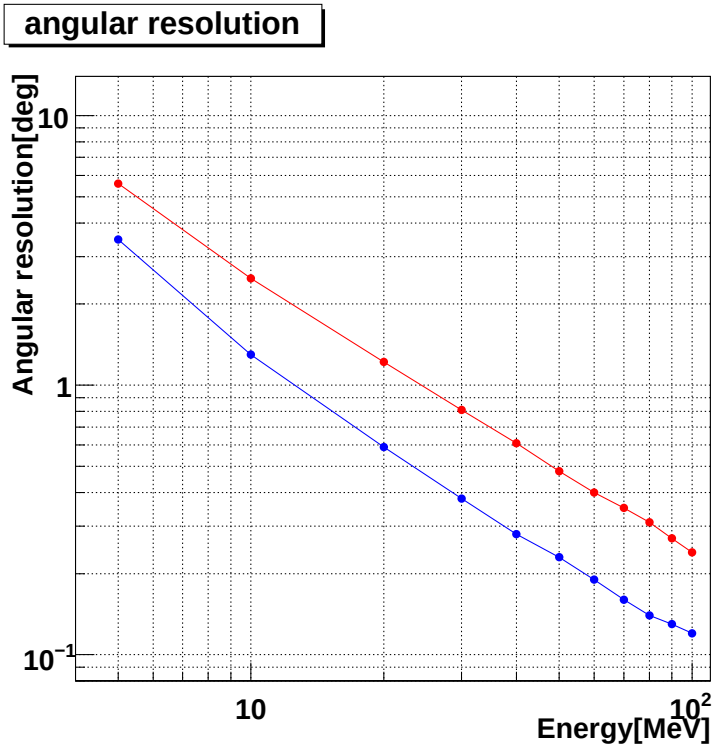

Figure 3.20: The angular resolution as a function of the incident gamma-ray energy in Ar based gas mixture (blue) and Xe based gas mixture (red) from Equation (3.17).

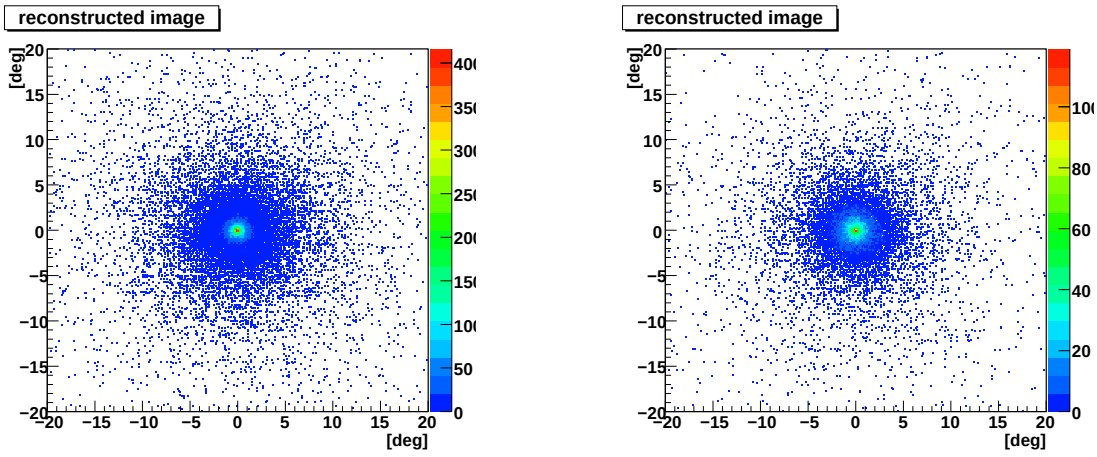

Figure 3.21: The reconstructed images in Ar based gas (left) and Xe based gas (right) by Equation (3.18)

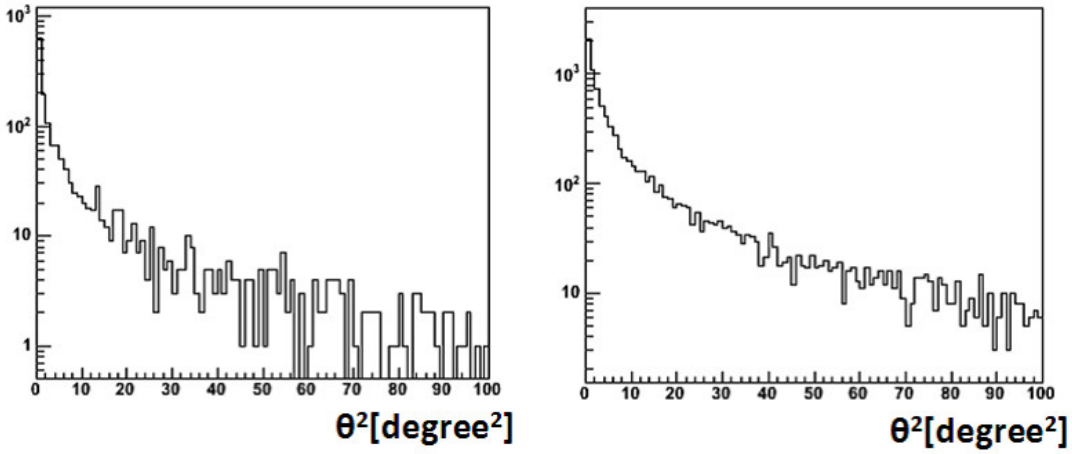

Figure 3.22: The θ squared distribution of Ar based gas mixture (left) and Xe based gas mixture (right) at 20 MeV by Equation (3.18).

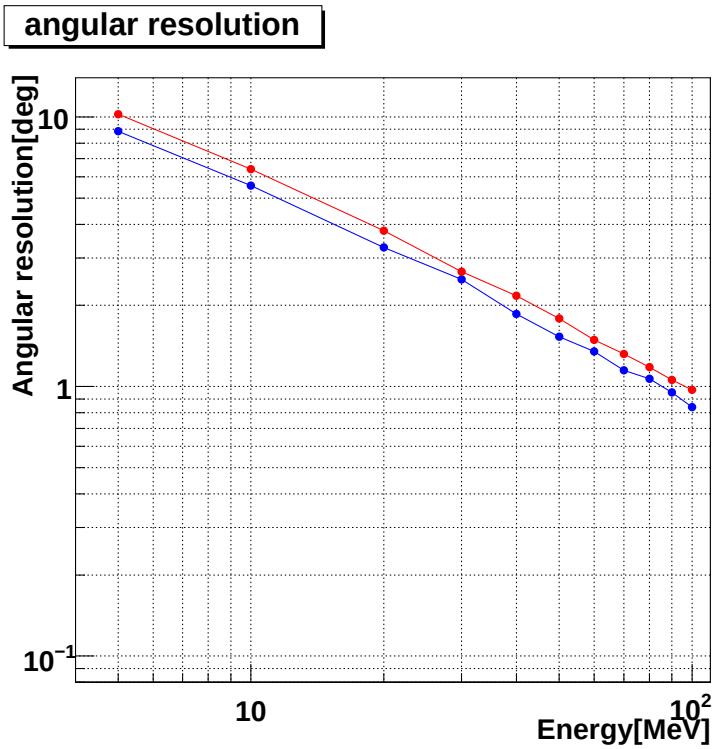

Figure 3.23: The angular resolution as a function of the incident gamma-ray energy in Ar based gas mixture (blue) and Xe based gas mixture (red) from Equation (3.18).

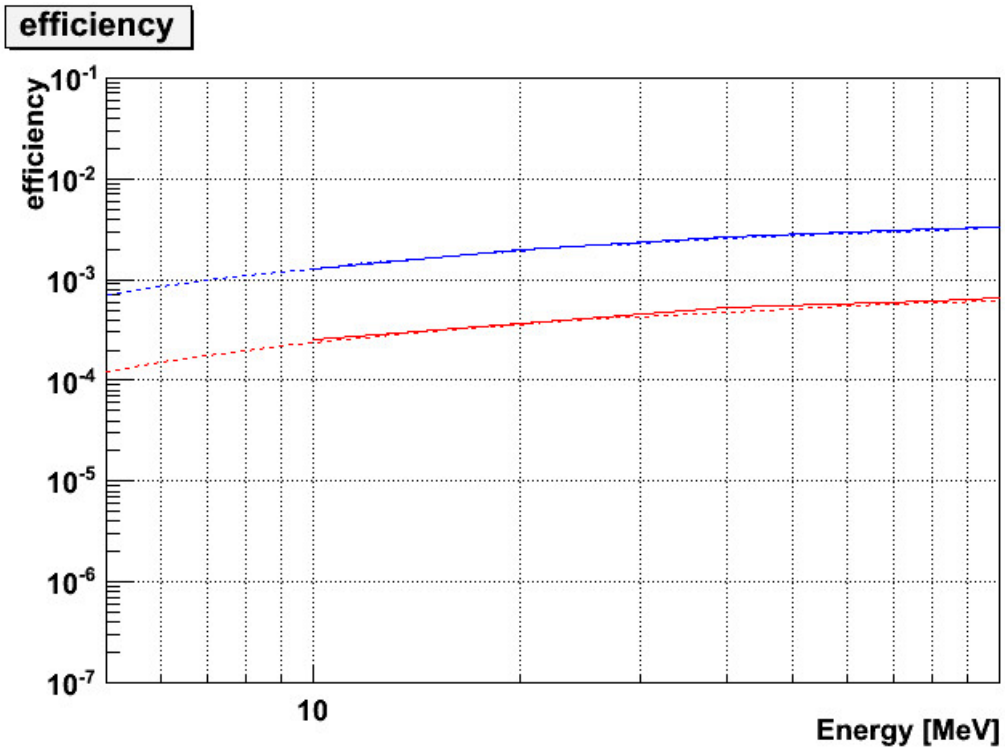

Figure 3.24: The detection efficiencies of Ar based gas mixture (red line) and Xe based gas mixture (blue line). For the comparison, the probabilities of the pair creation of Ar based gas mixture (red dashed line) and Xe based gas mixture (blue dashed line) are also plotted.

3.5 SMILE

For exploring MeV gamma-ray astronomy, we eventually aim to launch the telescope in space as described in Chapter 1. Then, we are now enlarging and improving our gamma-ray telescope for a satellite equipment in the future. As the preliminary step toward that, we proceed the balloon experiments, Sub-MeV to MeV gamma-ray Imaging Loaded-on-balloon Experiment (SMILE). The strategy of SMILE consists of 4 steps as shown in Figure 3.25. At the first step, we confirmed the gamma-ray detection using our prototype gamma-ray telescope with Compton mode for observing diffuse cosmic and atmospheric gamma rays, which was already done. At the second step, we will observe the bright sources like Crab or Cyg X-1 with the 30 cm cube telescope with Compton mode in the short time of about 6 hours. At the third step, we will observe several sources in the long time more than several days with the 40 cm class cube telescope. In this step, we will also confirm the gamma-ray detection with pair creation mode in the air. At the final step, the observation with $\geq$ 50 cm cube telescope on a satellite will be done.

In the first step (SMILE-1), we used the $10\times10\times14$ cm^3 μ-TPC filled with Xe based gas mixture (Xe : Ar : C_2H_6 = 80 : 18 :2) at 1 atm and the 33 PSAs which surrounded the μ-TPC. The experiment was done at Sanriku Balloon Center in 2006. In this experiment, we detected 420 photons in 3 hours, which this value is consistent with the simulated one [54], and obtained fluxes of diffuse cosmic and atmospheric gamma rays, which are consistent with the past experiments as shown in Figure 3.26. From the results of SMILE-1, we confirmed that our gamma-ray telescope could detect gamma rays with the ability of strong background rejection.

In the second step (SMILE-2), the aim is the test of imaging power of our gamma-ray telescope with Compton mode using the bright sources. Because the large number of the photons is needed for the imaging, we have to improve the effective area of the gamma-ray telescope. Thus, we are developing the large size telescope with the size of $30\times30\times30$ cm^3 μ-TPC and the large size scintillation camera composed of 36 PSAs. In addition, we need to develop the readout system with low power consumption for the large size telescope. Thus, we are also developing such readout system.

Furthermore, we starts to develop the telescope with pair creation mode for the third step (SMILE-3). For the first step of SMILE-3, we performed the principle-proof experiment for the detection of pair creation events.

In this thesis, we describe the improvement of the large size telescope with Compton mode and the development of the readout system with the low power consumption in next part, and then describe the principle-proof experiment of the telescope with pair creation mode in part 3.

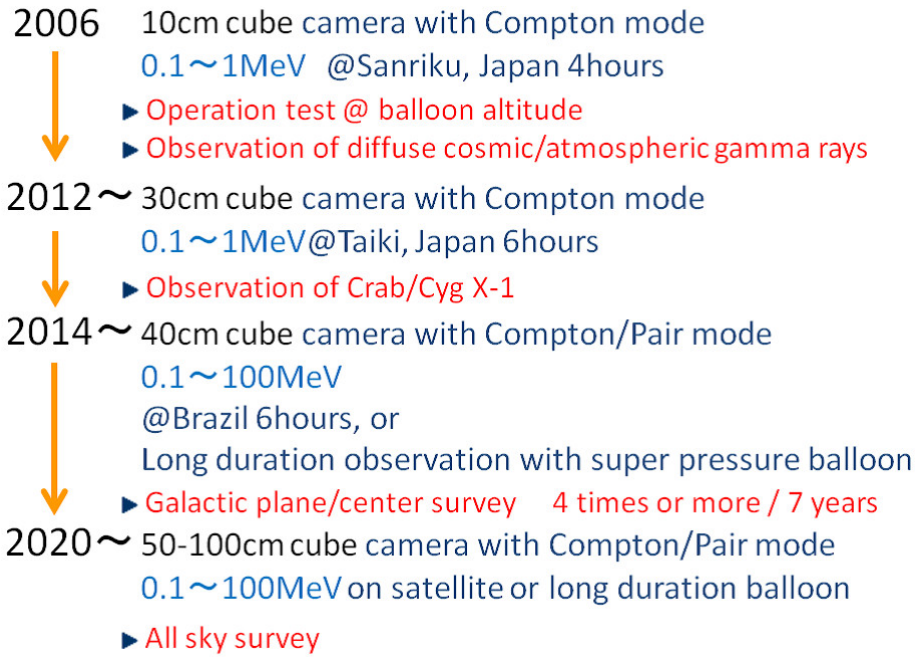

Figure 3.25: The load map of SMILE.

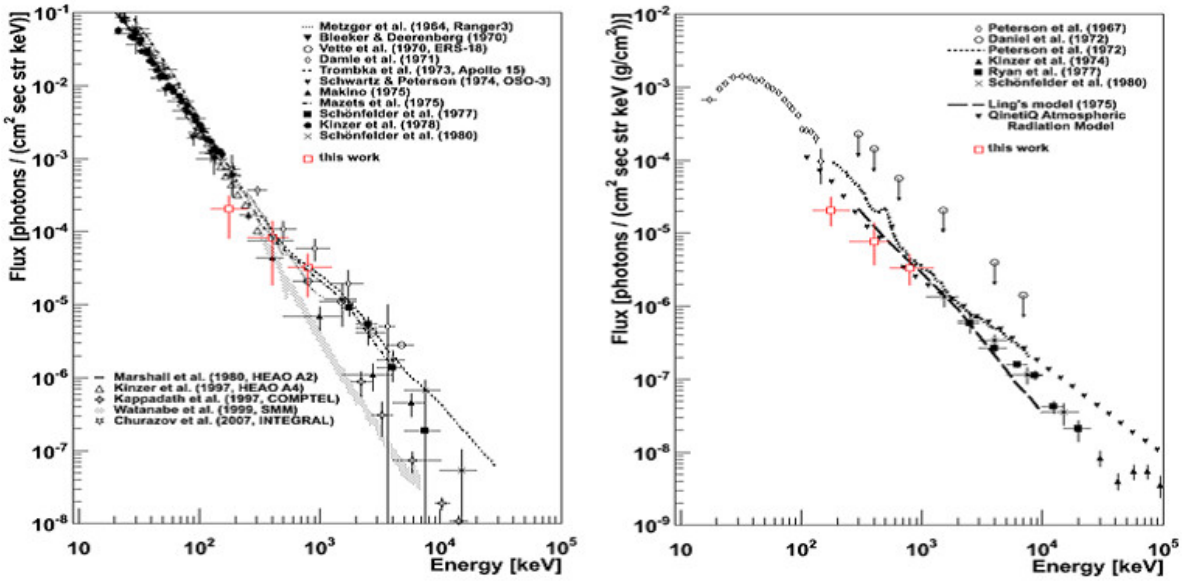

Figure 3.26: The obtained fluxes of cosmic (left) and atmospheric (right) gamma rays in SMILE-1 [54].

Part II

Improvement of the gamma-ray telescope with Compton mode

Chapter 4

Telescope with Compton mode for a next balloon experiment

4.1 Overview of SMILE-2

The purpose of the SMILE-2 is the test of the imaging power of our gamma-ray telescope, by the observation of a bright object like Crab or Cyg X-1. In order to detect photons for the significance of at least 5 σ by 6 hours level fright, the sensitivity which is about 100 times better than that of the telescope used in SMILE-1 is needed. For the aim, we have to improve the detection efficiency 10 times higher than that of SMILE-1 telescope, in case of using the large size μ-PIC which is 10 times larger than that of SMILE-1. We estimated the improvement of the detection efficiency using the Geant4 simulation. In this simulation, only the gas and the scintillator were considered as the gamma-ray telescope, and the physics models were the same as those in Section 3.4. The detection efficiency in this simulation was defined by the ratio of the number of the events, which the incident gamma rays were Compton scattered in the gas and the sum of the deposit energies of both the recoil electrons and the scattered gamma rays were equal to the energy of the incident gamma rays, to the number of incident gamma rays. From the simulation, if we use the μ-TPC with the size of 30×30×30 cm^3 filled with CF_4 at 2 atm and the GSO scintillation camera surrounding the μ-TPC as shown in Figure 4.1, the improvement of the detection efficiency satisfies our requirement as shown in Figure 4.2. Therefore, we are developing large size telescope and having gas study for the μ-TPC, step by step. For the first step, we have developed the prototype of the large size telescope based on a 30×30×30 cm^3 μ-TPC filled with the gas mixture (Ar : C_2H_6 = 90 : 10) at 1 atm and a 30×30 cm^2 scintillation camera as shown in Figure 4.3. The aim of this work is development of the prototype telescope which has about 3 times higher detection efficiency than that of the 10×10×15 cm^3 telescope filled with the same gas [54]. In parallel, the gas study was progressed and detailed in [51].

In this chapter, we describe the details of development of the large size telescope with Compton mode and its fundamental performance.

4.2 Enlargement of a gaseous time projection chamber

4.2.1 Micro pixel chamber (μ-PIC)

Micro Pixel Chamber (μ-PIC) is a two-dimensional micro-pattern gaseous detector fabricated by printed circuit board technology [52,53]. Figure 4.4 is a schematic view of μ-PIC. The μ-PIC has a pixel electrode like a sliced proportional counter. Anode and cathode strips of the μ-PIC are formed orthogonally on a polyimide substrate with a pitch of 400 μm. As shown in Figure 4.5, anode electrodes are located in the center of each pixel and connected by a strip under a

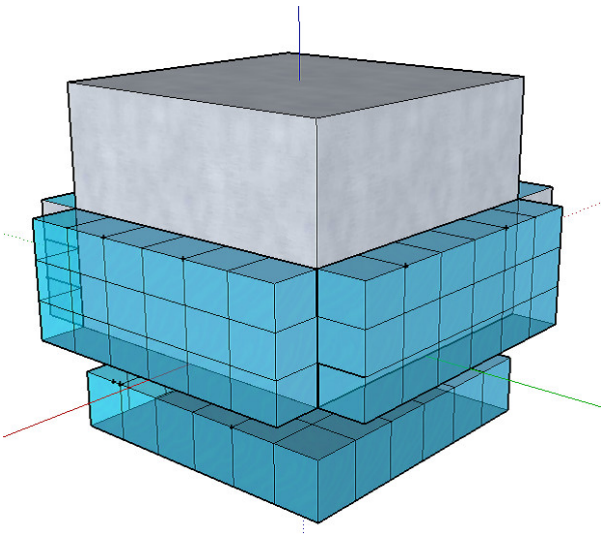

Figure 4.1: The schematic view of the gamma-ray telescope in the ideal condition.

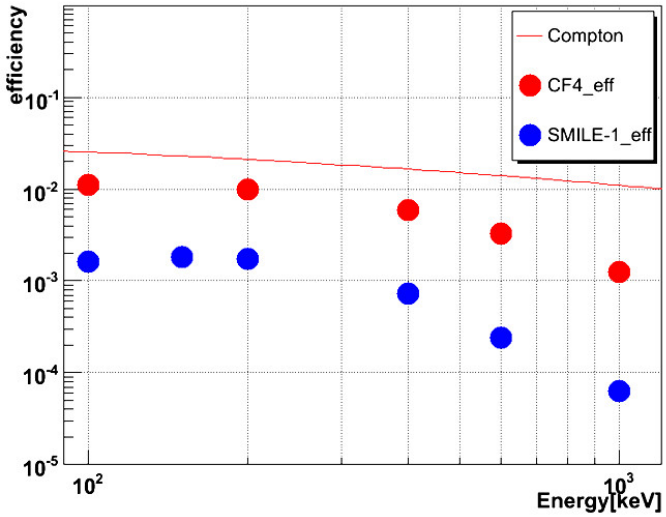

Figure 4.2: The detection efficiency of large size telescope with the size of 30×30×30 cm^3 filled with CF_4 at 2 atm (red circle) and of SMILE-1 telescope (blue circle) as a function of the energy of the incident gamma rays. For comparison, the probability of Compton scattering in the CF_4 gas is also plotted (red line).

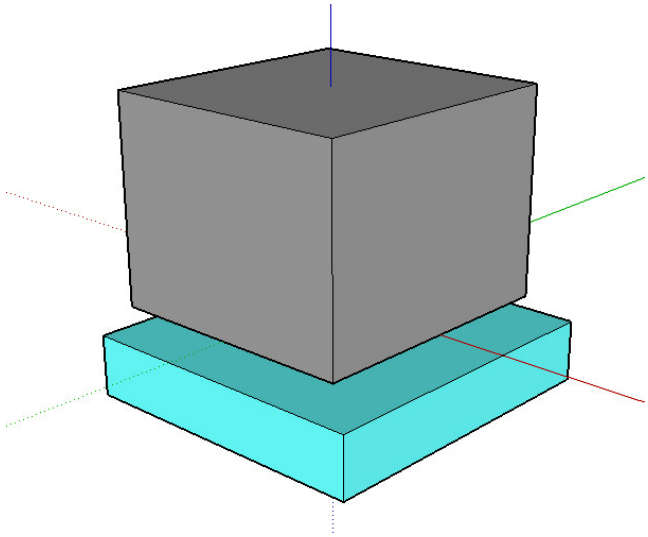

Figure 4.3: The schematic view of the prototype of the large size gamma-ray telescope.

100 μm thick polyimide substrate fabricated by an electric plating process. The electrodes made of Cu are coated with Ni. Lots of μ-PICs with the size of 10×10 cm^2 and the pixel number of 65536 were developed, and their performances are investigated in detail [54]. In order to enlarge the effective area, we have developed a 30×30 cm^2 μ-PIC which has 589824 pixels and also started to develop 20×20 cm^2 μ-PIC which has 262144 pixels. The μ-PIC with the size of 20×20 cm^2 is designed to be combined to a 40×40cm^2 large detector. In the present work, a μ-PIC of 30×30 cm^2 was used. Figure 4.6 shows the picture of a 30×30 cm^2 μ-PIC and the microscopic image of the electrode.

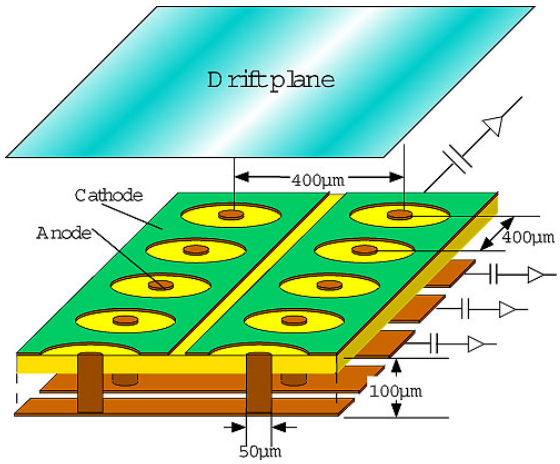

Figure 4.4: A schematic view of μ-PIC

4.2.2 Readout system

Owing to the strip structure, a 30×30 cm^2 μ-PIC has 768 channels readout for both anode and cathode electrodes, which are divided into three 256 channel connectors. The schematic view of the readout system is shown in Figure 4.7. Each strip connects to a preamplifier via the high voltage supply and signal-extension board. The preamplifier feeds both an analog signal

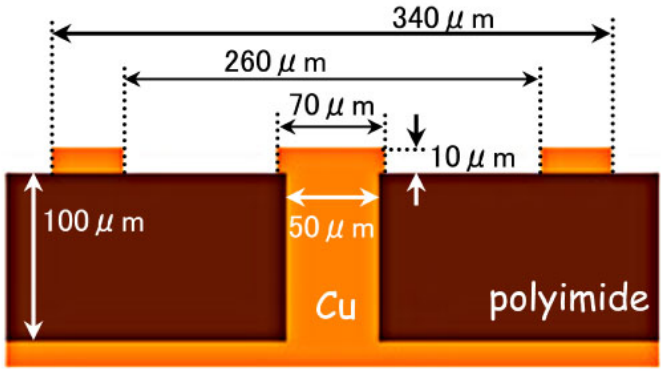

Figure 4.5: A schematic cross-section of the pixel structure of the μ-PIC

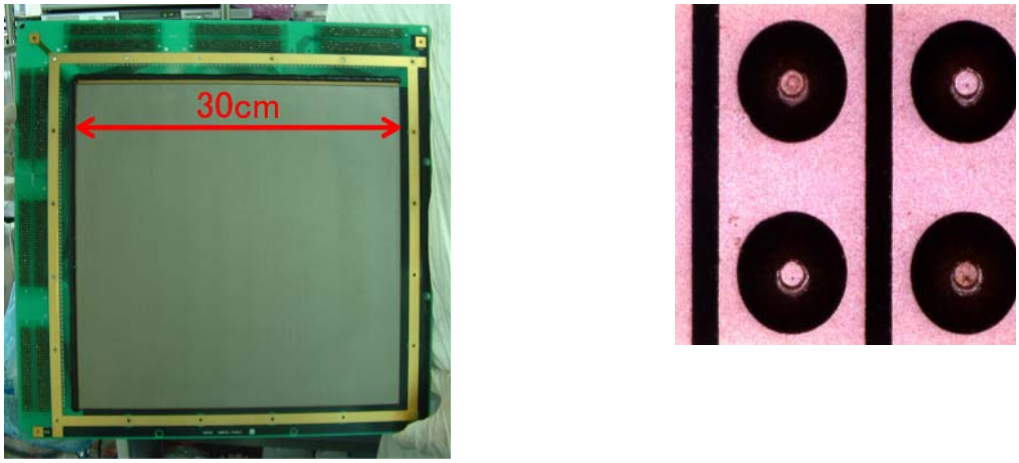

Figure 4.6: The photograph of 30×30 cm^2 μ-PIC (left) and the photomicrograph of the μ-PIC (right)

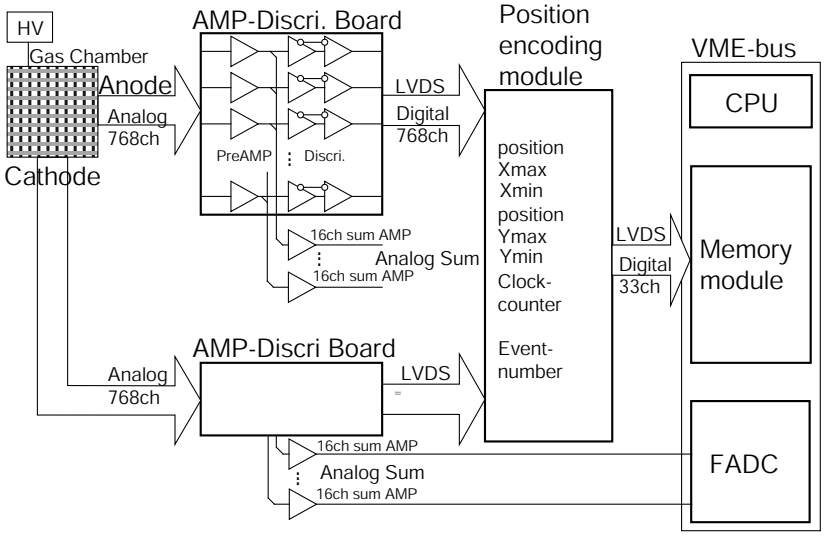

Figure 4.7: Data acquisition system for 30×30 cm^2 μ-PIC

and a discriminated digital signal. The analog signals are summed with every 16 channels and their wave forms are recorded by Flash ADC (FADC) on a Versa Module Eurocard (VME) bus system. The discriminated digital signals are fed to the position encoding module composed of 8 Field Programmable Gate Array (FPGA) chips operated with a 100 MHz clock. Here the hit signals are synchronized with the clock, and both the position and the elapsed time from the trigger are recorded successively when anode and cathode hit signals coincide with one clock. Then these position and elapsed time are sent to a memory module on a VME.

High voltage supply and signal-extension board

The μ-PIC is installed in a gas vessel. To connect all strips of the μ-PIC to the preamplifier outside the gas vessel, we developed the high voltage supply and signal-extension board as shown in Figure 4.8. The readout of such huge numbers of signals using commercial vacuum feed-through connectors is very hard. The signals before a preamplifier is too small to be sent via a long cable. The high voltage and signal-extension board works as a part of the feed-through as shown in Figure 4.9. The high voltage supply and signal-extension board also works as a high voltage supplier to all anodes of μ-PIC. In this board, 256 strips are gathered into 16 groups, and each group is connected to the high voltage supply via a register of 1 GΩ, then each group is almost insulated from other groups. Thus, even if the leak current flows in one group, the pixels of other groups can be operated safely. In one group, a high voltage is supplied to every 4 strips, so that the effective area is not reduced with the current flow of one strip. For the 30×30 cm^2 μ-PIC, three boards are used for anodes and cathodes readout, respectively.

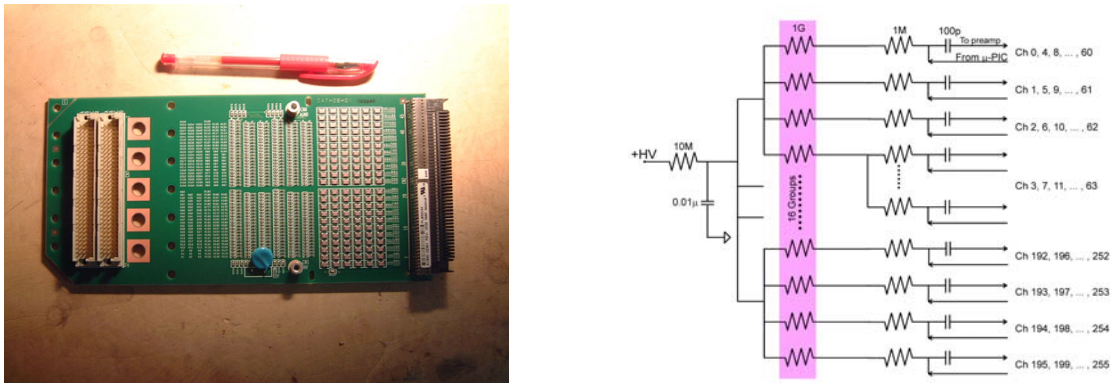

Figure 4.8: The photograph of the hight voltage supply and signal-extension board (left) and the circuit diagram of that (right)

Amplifier-shaper-discriminator (ASD) board

For a preamplifier, we use Amplifier-Shaper-Discriminator (ASD) chips developed by KEK for Thin Gap Chamber of ATLAS experiment in LHC at CERN [55]. The ASD chip has 4 input channels and analog and digital outputs. Each channel has a preamplifier, shaping amplifier, and discriminator. There are two types of the chip which has the time constant of 16 nsec and 80 nsec. For the μ-PIC of 30×30 cm^2, the chip with the time constant of 16 nsec was used. Analog signals from the μ-PIC are preamplified and shaped in this chip, and then sent to output channels. Discriminated signals are fed to output channels in LVDS. We use this ASD chip on the ASD board shown in Figure 4.10. The board has 64 input channels corresponding to 16 ASD chips, and has analog 4 output channels and 64 digital output channels. Analog signals are summed in 16 or 32 channels. Digital outputs are fed one bye one. The ASD board is inserted in

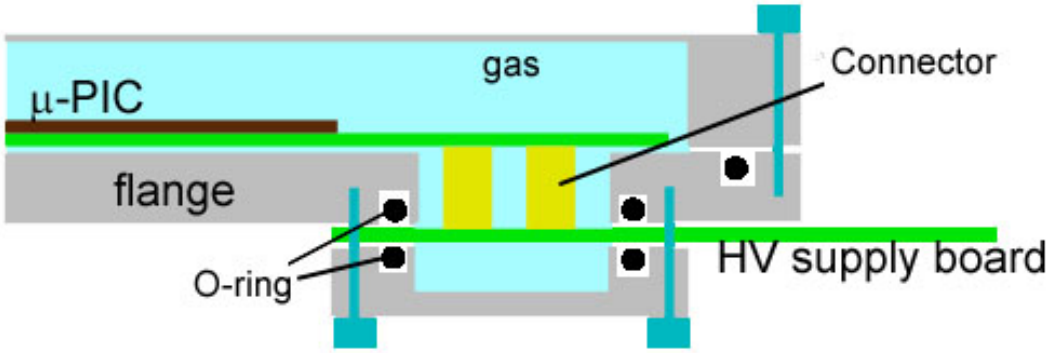

Figure 4.9: A schematic view of the connection of a μ-PIC and a high voltage supply and signal-extension board

the rack as shown in Figure 4.11. The ASD rack has 4 ASD board, in which a common threshold level is supplied for the discriminator of ASD chips. In addition, a high voltage is supplied in the board.

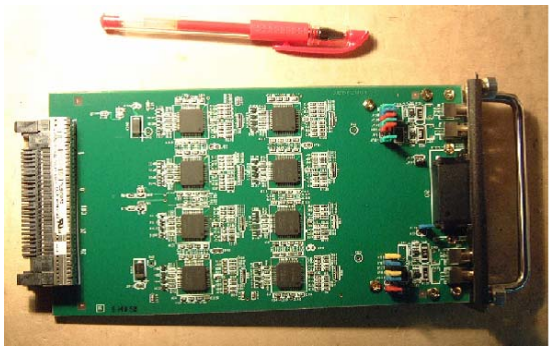

Figure 4.10: ASD board

Figure 4.11: ASD rack

Position encoding module

Digital signals from ASD board are fed to the position encoding module shown in Figure 4.12. The position encoding module consists of 8 FPGAs, 100 MHz clock, 1576 LVDS digital inputs, 5 LVDS I/O ports, and the memory-writing port. In this module, the hit position and the time in which anode and cathode hits coincided in one clock are recorded. These are sent to the memory module on a VME system. Figure 4.13 shows the block diagram of the position encoding module. Digital signals from ASD board are sampled at their rising edge by FPGAs, and the timing of those is synchronized with the clock. The Anode hit signals are fed into FPGA 1-3 and the cathode ones are into FPGA 4-6. When the synchronized cathode and anode signals coincide in one clock interval (10 ns), the two positions of cathode and anode are recorded with a resolution of 10 ns in FPGA 7. If two or more channels generate signals within a 10 ns clock, the average of the hit positions for the maximum and minimum hit positions is calculated in FPGA 7. These positions and clock are recorded. FPGA 8 is used for the communication with other modules such as ADCs and CPU.

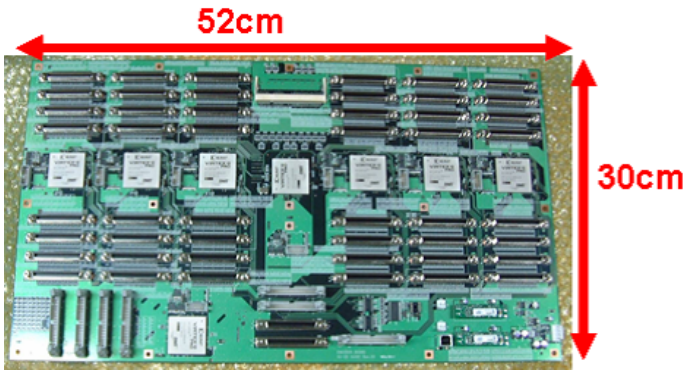

Figure 4.12: Position encoding module

4.2.3 Performances of large size μ-PIC

Basic performance of a 30×30 cm^2 μ-PIC (SN041129-1) was investigated using above system. In this section, all experiments are carried out under the condition with the flow of Ar and C_2H_6 (90:10) gas mixture at 1 atm. The obtained gas gain as a function of the anode voltage is shown in Figure 4.14. Here the large μ-PIC has the maximum gas gain of about 7000. This μ-PIC worked with a stable gas gain of about 3500 during more 1000 hours. Figure 4.15 shows the gain map of a 30×30 cm^2 μ-PIC. The ratio of the maximum gain to minimum one is 2.2, and the gas gain uniformity is 16.7 % at the RMS. The energy resolution was measured using 22.2 keV X-ray from a ^{109}Cd source. Figure 4.16 shows the energy spectrum obtained by 30×30 cm^2 μ-PIC. We can also find the peak of Cu (8 keV) of the μ-PIC electrode clearly. The energy resolution is about 50 % (FWHM) at 8 keV with a gas gain of 4000. The energy resolution is worse than 10×10 cm^2 μ-PIC due to the ununiformity.

4.2.4 Time projection chamber with μ-PIC and GEM

In the gas, the charged particles ionized the gas atoms and causes the ion and electron clouds. Under an adequate electric field in the gas, the electron cloud drifts toward the electric field with the constant velocity. The electron clouds generated at the different height in the gas reach the anode at the different drift time. Thus, their relative position is obtained using the drift time. If we know the start timing of the drift, the distance between the ionization point and the anode is reconstructed. Such a system is called Time Projection Chamber (TPC). Using the two dimensional detector as a readout of TPC, three dimensional position of tracks of a charged particle is measured. Then, the μ-PIC is actually used as a readout detector of TPC, to which we say μ-TPC. In our gamma-ray telescope, the μ-TPC is used as a tracker for a recoil electron.

The energy deposit of Minimum Ionizing Particle (MIP) in Ar gas is 2.54 keV/cm at 1 atm, and a MIP makes about 3.9 electrons per 400μm. In order to detect the MIP tracks, the μ-TPC needs to detect few electrons in one pixel. Thus, the detection of the MIP tracks needs a high gas multiplication of about 2×10^4 at least with the μ-TPC. However, the stable gas gain of 30×30 cm^2 μ-PIC is only about 3.5×10^3. Then, we use a Gas Electron Multiplier (GEM) [56] as a pre-amplification device. The GEM also plays a role in high signal-to-noise ratio for the μ-TPC. For 30×30×30 cm^3 μ-TPC, we adopted the GEM with a detection area of 23×28 cm^2 manufactured by Scienergy Co. Ltd. in Japan. Figure 4.17 shows the photograph and the photomicrograph of the GEM. The size is limited by the working size for the fabrication. The GEM consists of a 50 μm thick polyimide insulator covered by a copper electrode on each side. The holes were 70 μm in diameter with a pitch of 140 μm. In order to reduce both current and

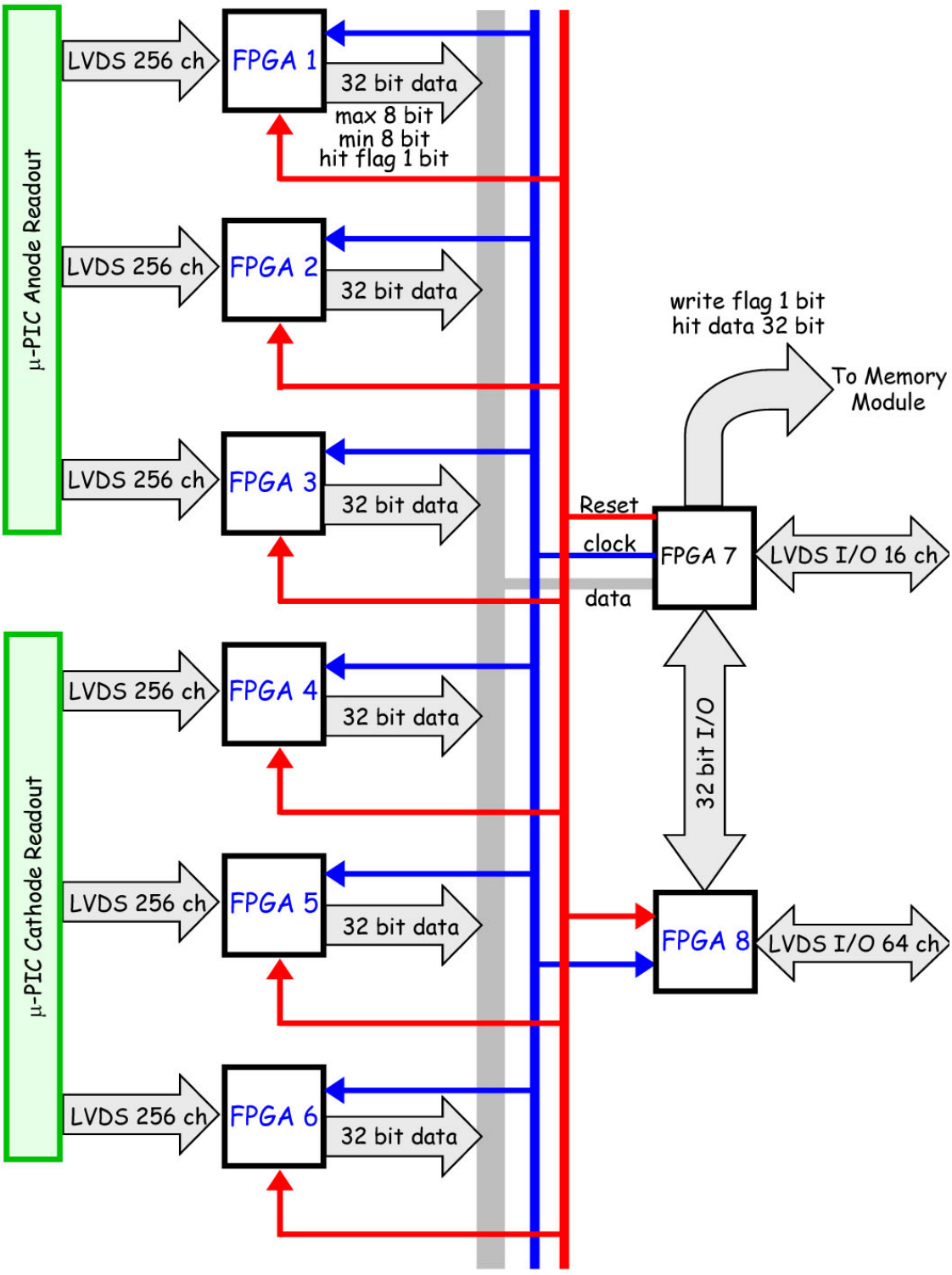

Figure 4.13: A block diagram of position encoding module

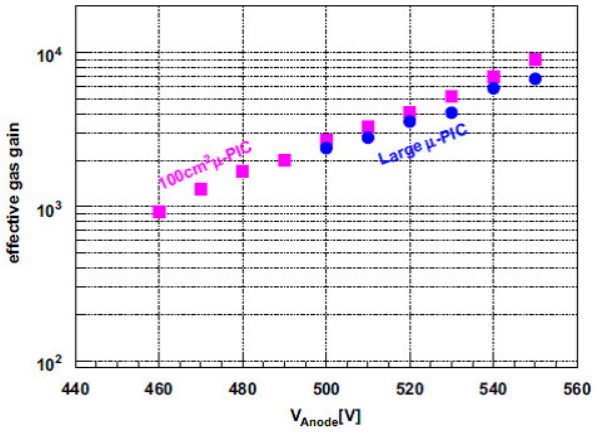

Figure 4.14: The effective gas gain of 30×30 cm^2 μ-PIC in comparison to the 10×10 cm^2 μ-PIC.

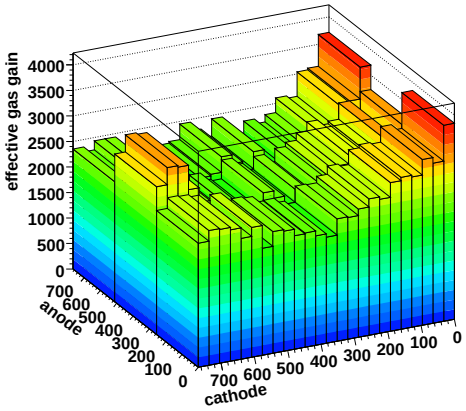

Figure 4.15: The effective gain map of 30×30 cm^2 μ-PIC (SN041129-1).

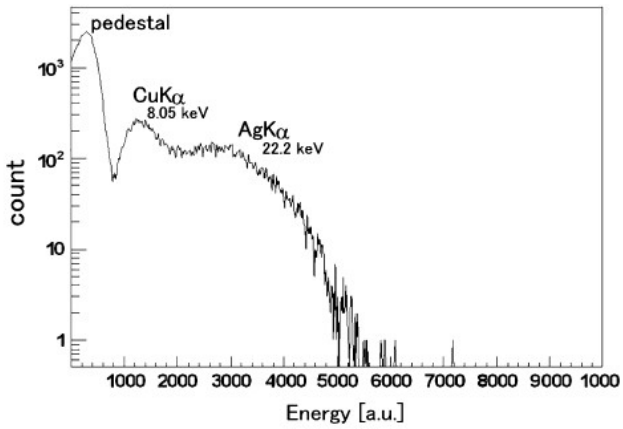

Figure 4.16: A energy spectrum of the X-rays from ^{109}Cd. The gas gain is about 4000, and the energy resolution (FWHM) is about 50% at 8.05 keV.

damage caused by discharges, the GEM is segmented in eight regions, which also reduces its capacitance. The gap between two segments is 0.8 mm (Figure 4.17), and the dead region is of about 2%.

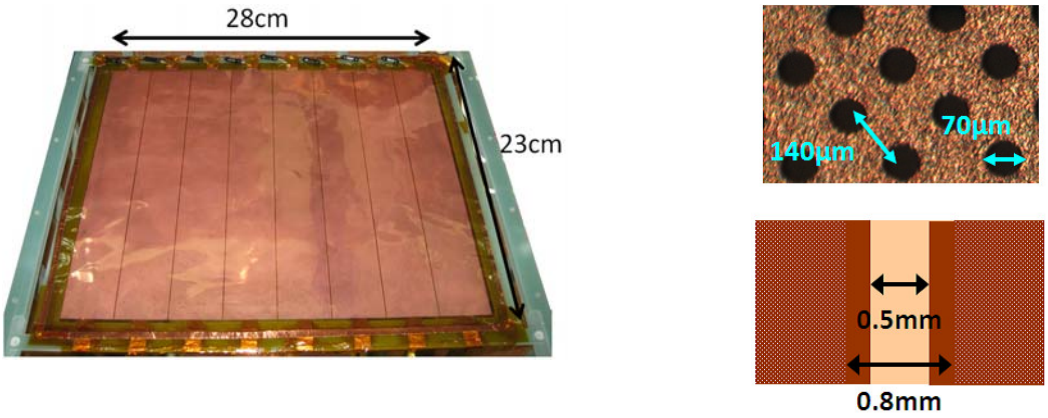

Figure 4.17: The photograph of 23×28 cm^2 GEM (left) and the photomicrograph of the GEM (right-top) The GEM is segmented in eight region. The width of region between two segments is 0.8 mm (right-bottom).

We use a 30×30 cm^2 μ-PIC and a 23×28 cm^2 GEM for the large size μ-TPC. Figure 4.18 shows a schematic view of the μ-TPC with the μ-PIC and the GEM. Electrons generated in the gas drift into the GEM, and the first multiplication is caused by the GEM with the gain of about 10. Then, multiplied electrons drift to μ-PIC and the second multiplication is caused by the μ-PIC with the gain of several thousands. Consequently, we obtained the total gain of about 4×10^4.

4.2.5 Performances of large size μ-TPC

We developed a μ-TPC with the drift length of 30 cm as shown in Figure 4.19. The third generation 30×30 cm^2 μ-PIC (SN071210-4) was used for the readout of the μ-TPC. The production yield was increased to more than 90% as the result of an improvement of the plating technology. Using this 30×30×30 cm^3 μ-TPC, the fundamental performances were investigated. The μ-TPC was set in an aluminum vessel filled with Ar and C_2H_6 gas mixture (90:10) at 1 atm. A drift voltage of -7.5 kV was supplied to the drift plane, which generated a drift electric field of 0.23 kV/cm. Several combinations of voltages were examined to the anode of μ-PIC (V_μ) and the GEM ($\Delta V_{GEM} = V_B - V_T$, where V_B and V_T are the voltages of the bottom and top planes of the GEM). The distance between the GEM and the μ-PIC was set to 6 mm.

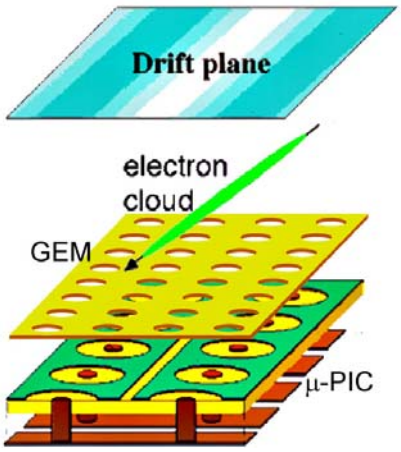

Figure 4.18: A schematic view of the μ-TPC with the μ-PIC and the GEM.

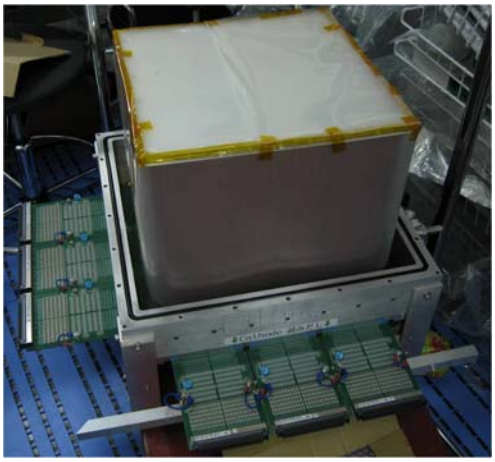

Figure 4.19: A photograph of 30 cm drift cage.

Gas gains

The gas gains were measured using 31 keV X-rays from a ^{133}Ba source. The gas gain measured with several combinations of voltages of V_μ and ΔV_{GEM} are shown in Figure 4.20. The maximum gas gain of about 140000 was achieved with $V_\mu = 460\ V$ and $\Delta V_{GEM} = 375\ V$. Then we determined a stable operation condition of the μ-TPC with a gas gain of about 100000 during more than 1000 hours. This gain is enough for tracking the MIPs adequately. Afterwards, the μ-TPC was operated with these voltages. Figure 4.21 shows the gain map of the 30×30×30 cm^3 μ-TPC. The ratio of the maximum gain to minimum one is 1.4, and the gas gain uniformity is 9.2 % at the RMS.

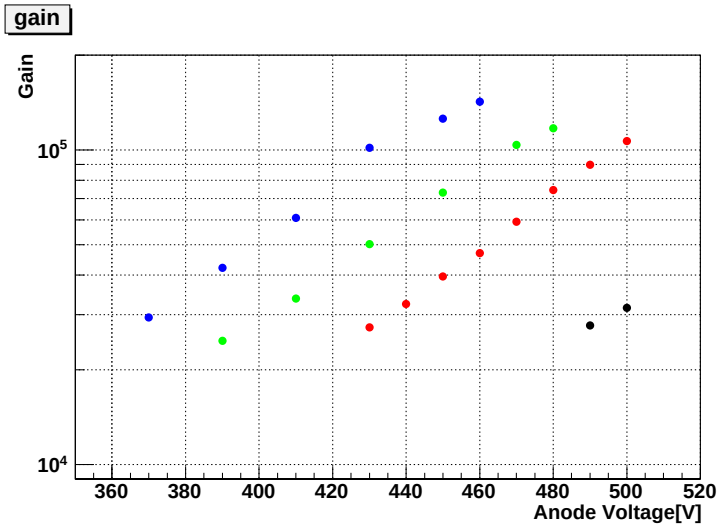

Figure 4.20: Gas gains as a function of the voltage supplied to the anode of the μ-PIC. The gas gains measured with GEM voltages of 275, 325, 350, and 375 are shown

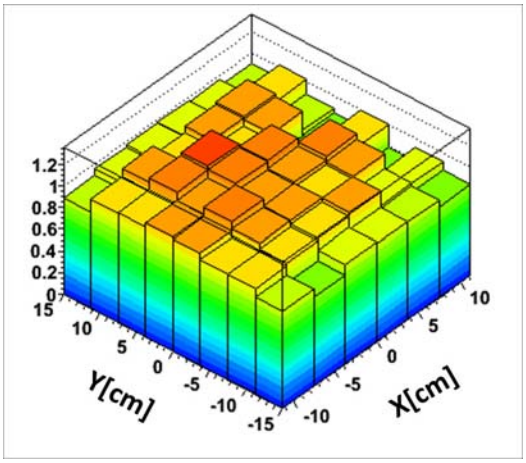

Figure 4.21: The effective gain map of 30×30×30 cm^3 μ-TPC composed of 30×30 cm^2 μ-PIC (SN071210-4) and 23×28 cm^2 GEM.

Energy resolutions

An energy spectrum was obtained by 31 keV X-rays from a ^{133}Ba source as shown in Figure 4.22. The whole volume of the μ-TPC was irradiated. We note the peak of ^{133}Ba (31 keV), the peak of Cu (8 keV) from both the GEM and the μ-PIC, and the peak of Cl (3 keV) from the insulating tape in the gas vessel. The energy resolution was 32.1% (FWHM) at 31 keV. The energy resolutions were measured for the energy range between 8 and 60 keV using three radiative sources, ^{109}Cd, ^{133}Ba, and ^{241}Am. The measured energy resolutions are shown in Figure 4.23. In this figure, the line is fitted as

$$\frac{\Delta E}{E}[\%] = 1.25 \times 10^2 \left(\frac{E}{keV}\right)^{-0.39} . \tag{4.1}$$

Figure 4.24 shows the energy resolution uniformity of the 30×30×30 cm^3 μ-TPC using 31 keV X-rays. The energy resolution uniformity is 7.1 % at the RMS.

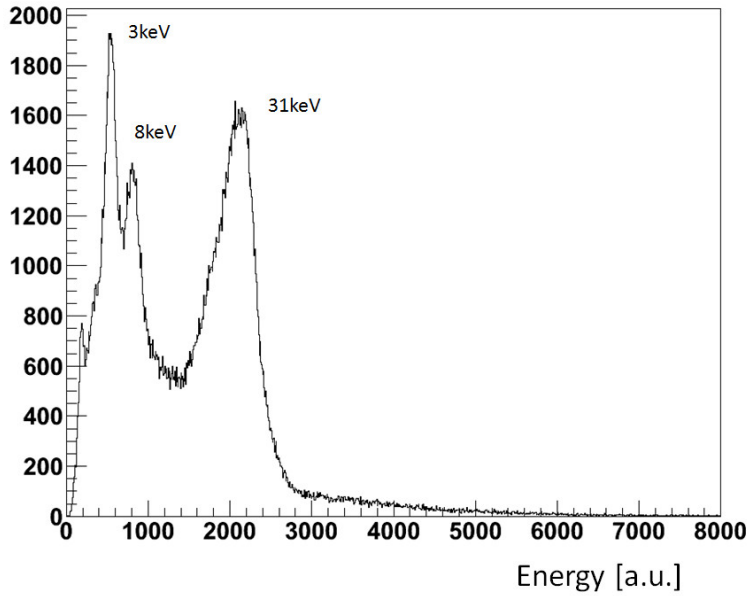

Figure 4.22: A typical energy spectrum of the X-rays from ^{133}Ba.

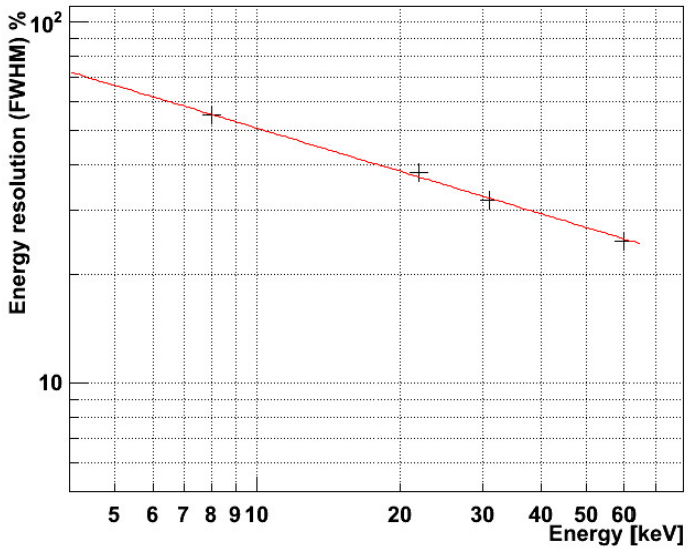

Figure 4.23: Energy resolution as a function of the energy.

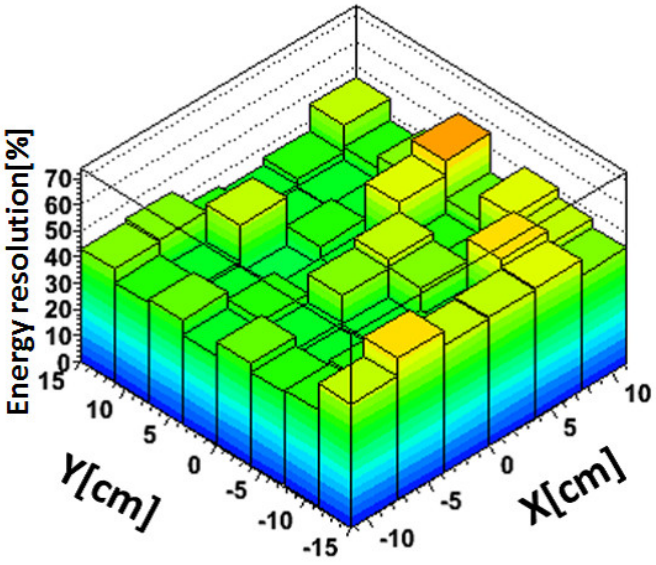

Figure 4.24: Energy resolution uniformity.

Drift velocity and Position resolution

The three dimensional position resolution of the 30×30×30 cm^3 μ-TPC was measured using tracks of cosmic muons. We placed two plastic scintillators with the size of 5×5×1 cm^3 above and below the μ-TPC as shown in Figure 4.25. The coincidence signal of these scintillators was used for the trigger of μ-TPC.

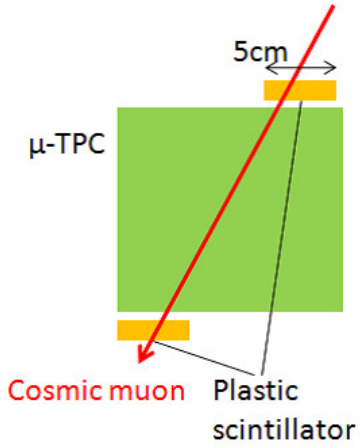

Figure 4.25: The setup for cosmic muon detection.

We measured the drift velocity as following. Figure 4.26 shows the distribution of the drift time of the μ-PIC. Here the drift region corresponds to the clock of 30 - 760, which corresponds to a 30 cm drift region. For this distribution, the electron drift velocity was obtained to be 4.1 cm/μsec.

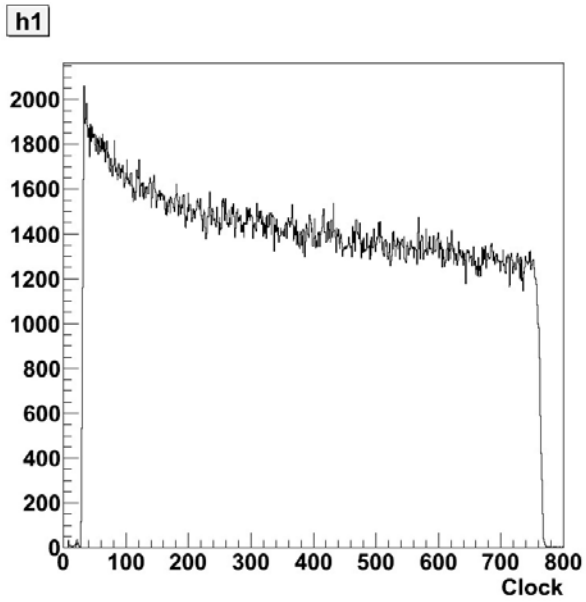

Figure 4.26: The distribution of the drift time in clock counter.

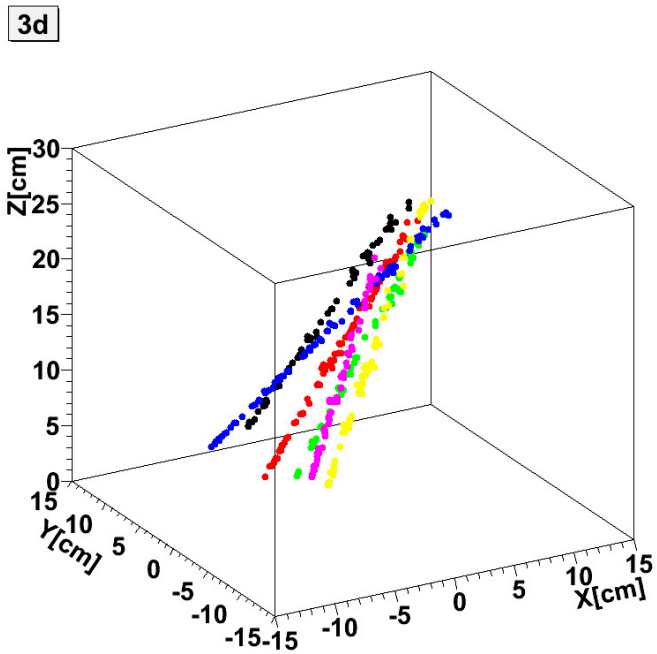

Figure 4.27: The examples of the cosmic muon tracks.

Typical three-dimensional image of muon tracks reconstructed in the μ-TPC are shown in Figure 4.27. We then fit the muon tracks with straight lines, and the residual was calculated for each hit point. Here, the residual was defined as the minimum distance between a hit point and the fitted straight line. Figure 4.28 shows the histogram of the residuals at the drift length

of 15 - 18 cm. In this figure, the data were fitted with a two-dimensional Gaussian,

$$P(r)dr = A\frac{\sqrt{2\pi}}{\sigma^2} r \exp\left(-\frac{r^2}{2\sigma^2}\right) dr, \tag{4.2}$$

where A is the normalization factor, r is the residual (distance from the fit line) and σ^2 is the variance of the two-dimensional Gaussian. The obtained σ^2 was given by the sum of the detector-intrinsic residual term, σ_{det}, and the diffusion term, σ_{dif},

$$\sigma^2(z) = \sigma_{det}^2 + \sigma_{dif}^2 = \sigma_{det}^2 + (D\sqrt{z})^2, \tag{4.3}$$

where z is the drift length and D is the diffusion constant. Thus, σ was plotted as a function of drift length and fitted with Equation (4.3) as shown in Figure 4.29. As a result of the fitting, $\sigma_{det} = 0.58\ mm$ and $D = 0.33\ mm/\sqrt{cm}$ were obtained. The detector-intrinsic resolution projected to the z-direction, σ_z, was estimated by using the drift velocity:

$$\sigma_z = \frac{0.41[mm]}{\sqrt{12}} = 0.29[mm]. \tag{4.4}$$

Using these results, one-dimensional detector-intrinsic resolution projected to x or y-direction, σ_{det1D}, was estimated;

$$\sigma_{det1D} = 0.36[mm], \tag{4.5}$$

where, $\sigma_{det}^2 = \sigma_x^2 + \sigma_y^2 + \sigma_z^2$ and $\sigma_{det1D} = \sigma_x = \sigma_y$ were used.

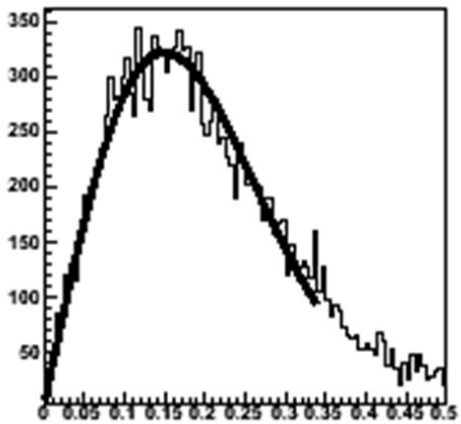

Figure 4.28: The histogram of residual between the obtained points and the fitted straight line. The solid line is obtained by fitting with two-dimensional Gaussian.

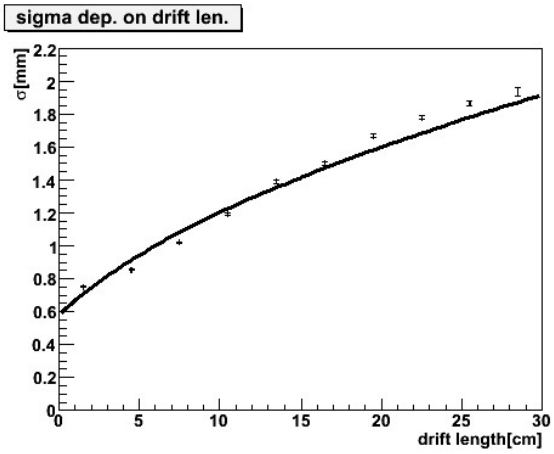

Figure 4.29: The position resolution as a function of drift length.

4.3 Scintillation camera

4.3.1 Scintillator and PMT

For the absorber of the gamma-ray telescope for scattered gamma rays, we use a scintillation camera that consists of a position-sensitive photomultiplier (PSPMT) and a pixelated scintillator array (PSA) [54]. We adopt the combination of the Hamamatsu 64-channel multi-anode PSPMT H8500 [57] and a GSO(Ce) (Gd_2SiO_5:Ce) crystal array fitting to the anode pitch of the H8500 [58]. The H8500 was recently developed for applications in nuclear physics and medical imaging: for example, a Cherenkov detector, PET, and SPECT [59–63]. It has the advantage of a much smaller dead space and a larger effective area (89 % of the package size) than previous multi-anode PMTs. GSO(Ce) has advantages of greater radiation hardness than most of the known scintillators, and easy processability such as nonhygroscopicity.

The H8500 has a compact size of 52×52×28 mm^3 with 12-stage metal channel anodes. The active photo-cathode area is 49×49 mm^2 with a matrix of 8×8 anodes. Each anode pixel size is 5.8×5.8mm^2, and the pitch between the centers of the anodes is 6 mm. The typical anode gain is about 10^6 under a high voltage of -1000 V, and the typical anode gain uniformity (ratio of the maximum to a minimum gain) is about 3.0. The GSO(Ce) PSA consists of 8×8 pixels of 6×6×13 mm^3 with the same pixel pitch as that of the anodes of H8500. Each of the 64 pixels is optically isolated by a Vikuti 3M ESR, which is a multilayer polymer mirror with a thickness of 65 μm and a reflectance of 98 %. The PSA is glued to the H8500 with OKEN-6262A optical grease. Figure 4.30 shows a picture of our scintillation camera.

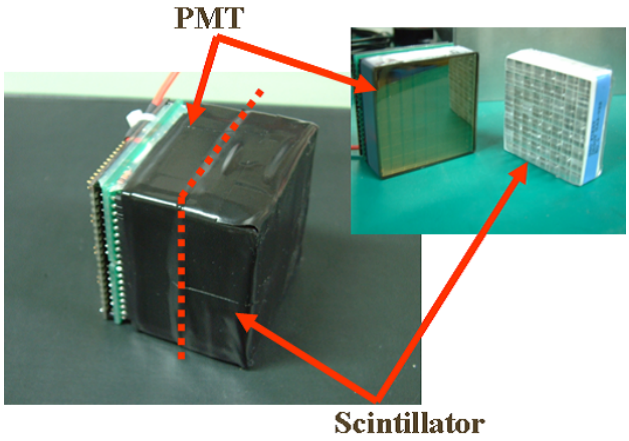

Figure 4.30: .The GSO(Ce) PSA with the H8500.

4.3.2 Readout system and compactification

For the reductions of both the number of the readout channel and the power saving of the readout modules, we use the resistor-chain readout board as shown in Figure 4.31. On this board, the anodes in horizontal row and both edges of those matrix chains are connected with 100 Ω resistor for 3 PSAs. Thus, we can obtain a hit position by reading 4 readouts from the corners. These four readouts are individually connected to the preamplifier board with a time constant of 5.4 μsec. The output signals of the preamplifier are fed into the shaping amplifier with a time constant of 0.5 μsec. Then the shaping signals are fed to the peak hold ADC on VME. The sum of signals from 4 preamplifier is used for the trigger signal.

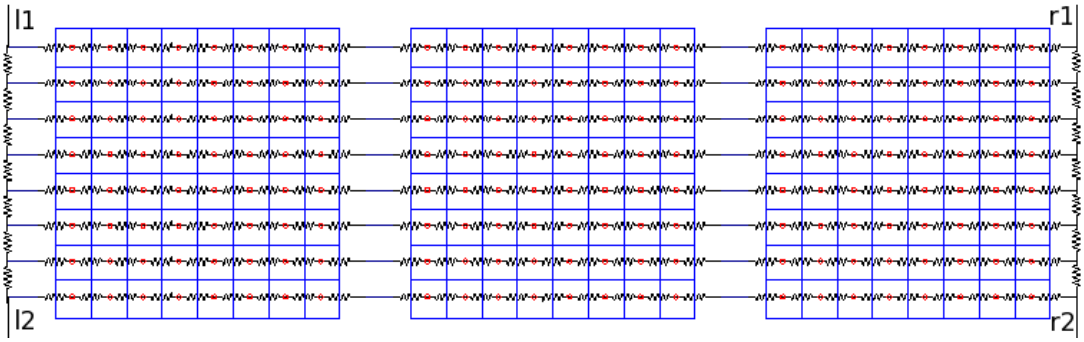

Figure 4.31: The resistor chain board.

For the satellite of balloon loading, a compact high voltage power system for PMTs is needed. We adopted a compact high voltage supplier EMCO Q12N-5 as a DC-HV converter shown in Figure 4.32. Table 4.1 shows the specification of the DC-HV converter. The DC-HV converter is controlled by DC level signal from DAC which is operated by a CPU on VME. This converter is connected to PMT one by one. Therefore the high voltage of each PMT can be controlled individually.

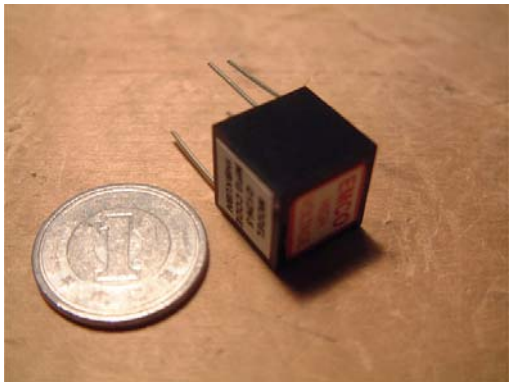

Figure 4.32: DC to HV converter (EMCO Q12N-5)

Table 4.1: The properties of EMCO Q12N-5

parameter	value
Input Voltage	0.7 - 5 V
Input Current	< 50 mA (No load)
	< 175 mA (Full load)
Output Voltage	0 - -1.2 kV
Output Current	< 0.4 mA
Conversion Factor	~ 60 %
Ripple Noise	< 0.25 %
Weight	4 g
Size	$1.27 \times 1.27 \times 1.27$ cm^3
Operating Temp.	-25 - $+70$ °C

Using the DC-HV converter, we constructed the compact PSA unit. As shown in Figure 4.33, 3 PSAs, the preamplifier board, and the DC-HV converter were mounted together on one circuit board. In the region 1 of this figure, DC-HV converter, and a noise filter were arranged on the board. This board has a D-sub 9 pin power line (3 lines of DAC and preamplifier power) (Figure 4.34). The region 2 shows the preamplifier board (Figure 4.35), and the region 3 shows PSAs. Figure 4.36 shows the compact PSA unit. The PSA unit has the small and compact size of $5 \times 15 \times 12$ cm^3. Furthermore, the interface of the PSA is composed of only 4 channel analog signal lines, trigger line, and D-sub power line. Thus, a large area absorber is easily constructed by arranging several PSA units around the μ-TPC.

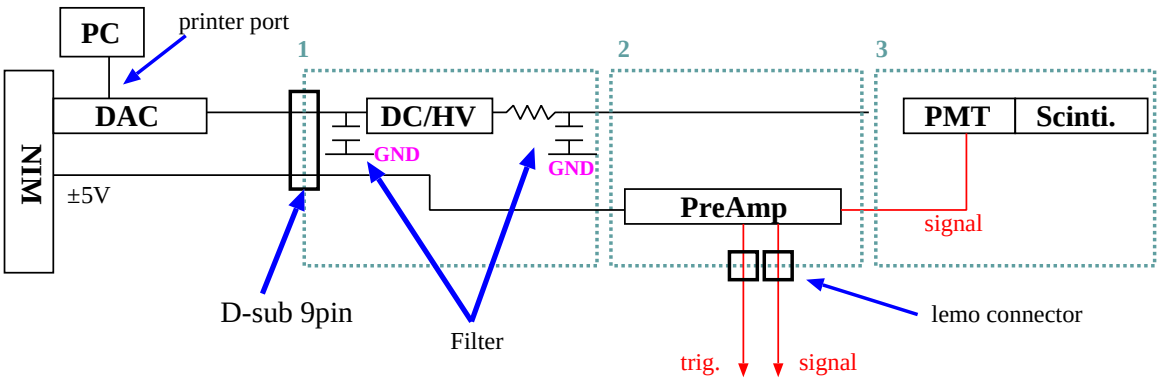

Figure 4.33: A schematic view of the compact PSA unit.

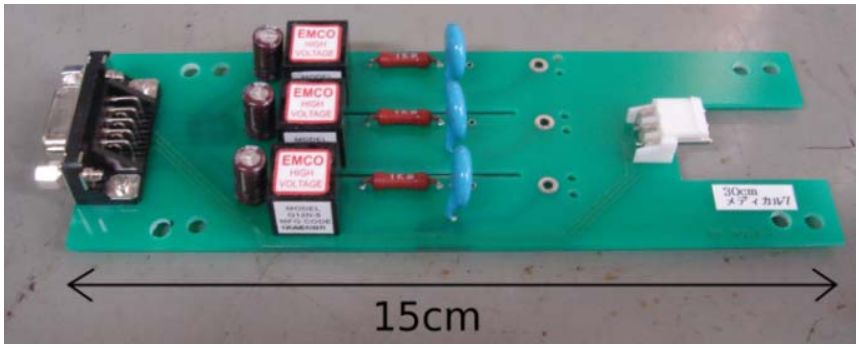

Figure 4.34: High voltage supply board

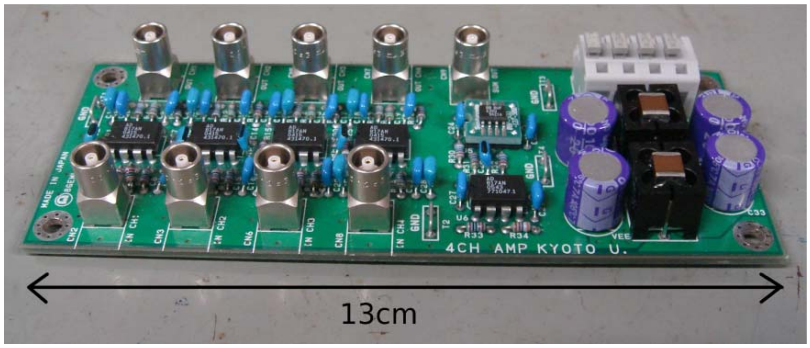

Figure 4.35: 4ch preamplifier board

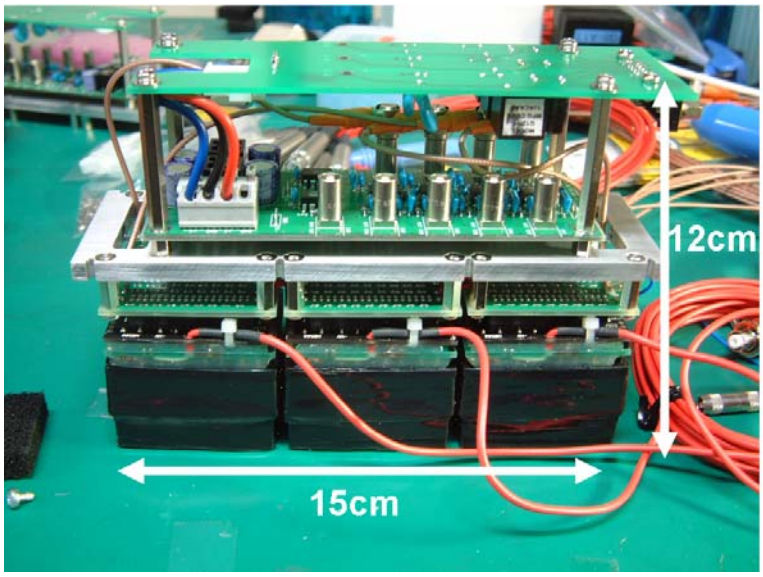

Figure 4.36: A photograph of the compact PSA unit.

4.3.3 Performance of scintillation camera

Position resolution

In the PSA, the position resolution is determined by its pixel size intrinsically. However, since the resistor chain is used for the readout of the PSA, we cannot obtain the position of hit pixel directly. Therefore, we have to develop the analysis method for the position determination of hit pixel.

We used the center of gravity of 4 outputs from the PSA unit. The hit position (X, Y) and the charge information P are given by

$$X = \frac{l_1 + l_2}{l_1 + l_2 + l_3 + l_4} \tag{4.6}$$

$$Y = \frac{l_2 + r_2}{l_1 + l_2 + l_3 + l_4} \tag{4.7}$$

$$P = l_1 + l_2 + l_3 + l_4, \tag{4.8}$$

where l_i and r_i $(i = 1, 2)$ are 4 outputs from the PSA (See Figure 4.31). Using this method, the flood irradiation image with ^{137}Cs source was obtained as shown in Figure 4.37. In this figure, we can see that each pixel is distinguished clearly. Thus, the position resolution of the PSA was 1.73 mm at RMS corresponding to 6 mm pixel size.

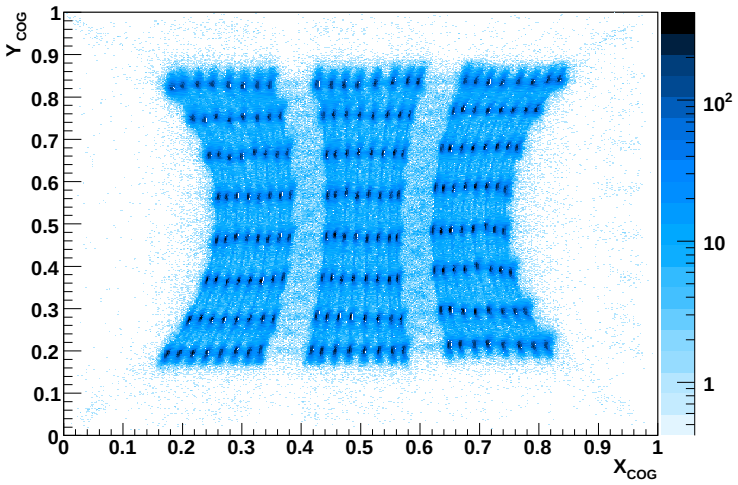

Figure 4.37: The center of gravity image from ^{137}Cs source.

The position resolution of the PSA was good enough to use for the absorber of the gamma-ray telescope. However, the obtained image was distorted by the influence of resistors, and much time for energy calibration of all pixels was necessary. Then, we developed the image correction as follows. We used the two dimensional coordinate transformation from the plane of the center of gravity position coordinates, (X_{COG}, Y_{COG}), to the one of the real position coordinates, (X_{real}, Y_{real}) was adopted. Specifically, we extracted the peak position, (X_{COG}, Y_{COG}), from the obtained image and prepared (X_{real}, Y_{real}) as shown in Figure 4.38. Then, we obtained the transfer function, f and g:

$$X_{real} = f(X_{COG}, Y_{COG}), \tag{4.9}$$

$$Y_{real} = g(X_{COG}, Y_{COG}), \tag{4.10}$$

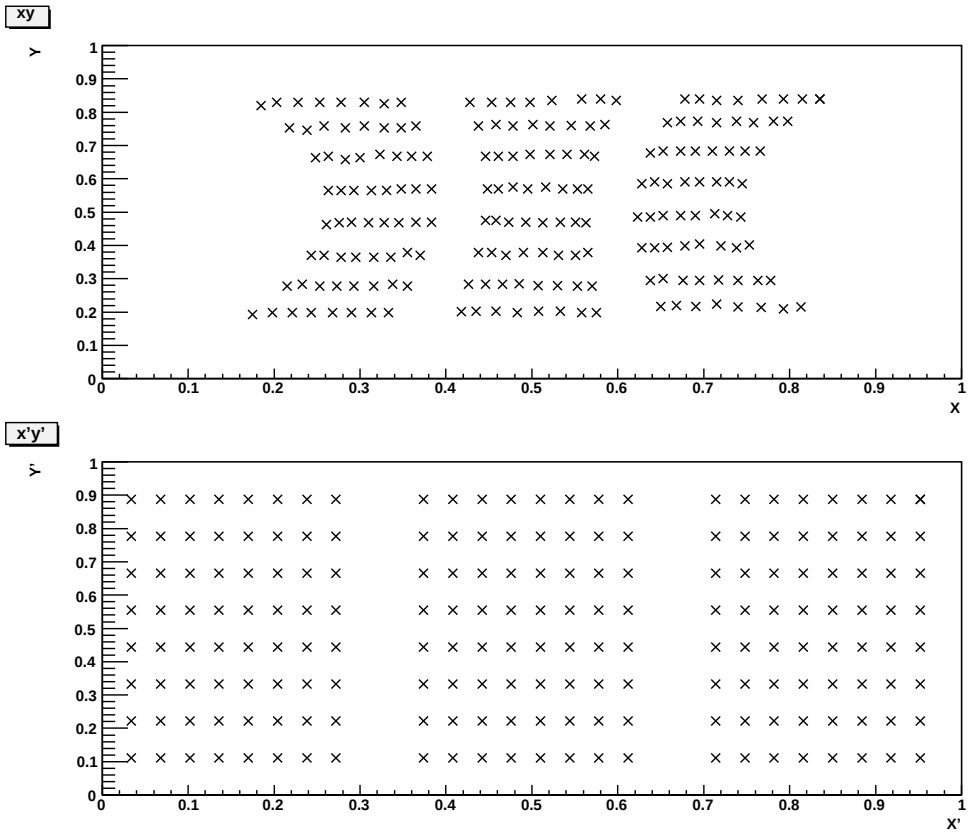

Figure 4.38: (X_{COG}, Y_{COG}) (top) and (X_{real}, Y_{real}) (bottom).

by fitting with the polynominal as follows:

$$f(X_{COG}, Y_{COG}) = \sum_{i=0}^{n} a_i X_{COG}^i + b_i Y_{COG}^i, \tag{4.11}$$

$$g(X_{COG}, Y_{COG}) = \sum_{i=0}^{n} c_i X_{COG}^i + d_i Y_{COG}^i. \tag{4.12}$$

Figure 4.39 shows the images before and after the correction with the functions f and g. Figure 4.40 shows the x-projection of the forth row from the top one. We can resolve each pixel obviously in this figure, and this correction obviously looks effective.

.

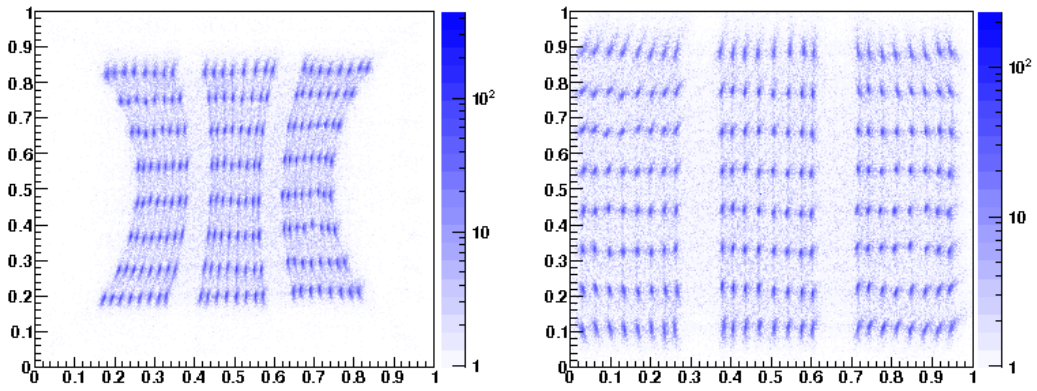

Figure 4.39: The image before correction (left) and the one after correction (right).

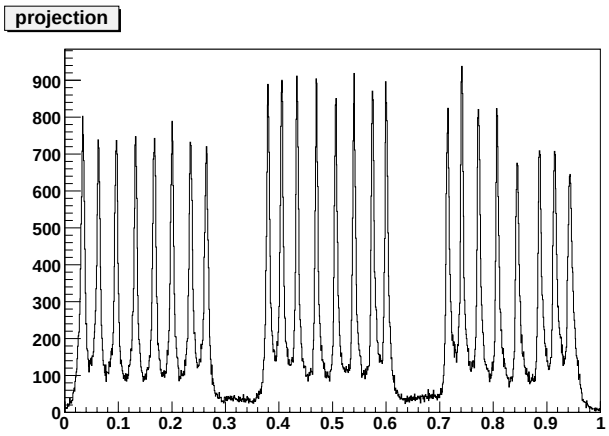

Figure 4.40: The x-projection of the forth row from top.

Energy resolution

Energy resolution was also investigated for the PSAs. We constructed the large area scintillation camera using 36 PSAs. Figure 4.41 shows the ^{137}Cs spectrum obtained from the whole area (36 PSAs) of the scintillation camera. The typical energy resolution was about 11 % (FWHM) at 662 keV. The energy dependence of the energy resolution is shown in Figure 4.42, In this Figure, the dotted line is fitted as

$$\frac{\Delta E}{E}[\%] = 10.6 \times \left(\frac{E}{662[\mathrm{keV}]}\right)^{-0.53}. \tag{4.13}$$

We found that the large scintillation camera has a dynamic range of 80 keV - 1 MeV over the whole area.

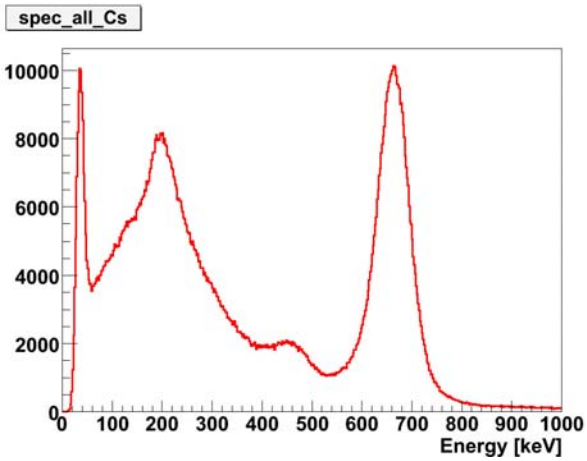

Figure 4.41: The spectrum of ^{137}Cs measured with the scintillation camera.

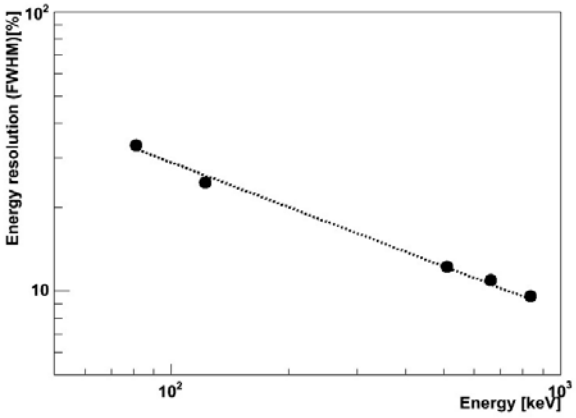

Figure 4.42: The energy resolution as a function of energy of the scintillation camera.

4.4 Large size gamma-ray telescope with Compton mode

We constructed a prototype large size gamma-ray telescope based on a 30×30×30 cm^3 μ-TPC and a large size scintillation camera. In this chapter, I describe the system and the fundamental performances of the prototype large size gamma-ray telescope with Compton mode.

4.4.1 Setup

The specifications of the scintillation camera and the μ-TPC in the large size gamma-ray telescope are summarized in Table 4.2 and Table 4.3, respectively. Figure 4.43 is the photograph of the bottom scintillation camera. Using the scintillation camera and the μ-TPC, we constructed a large size gamma-ray telescope.

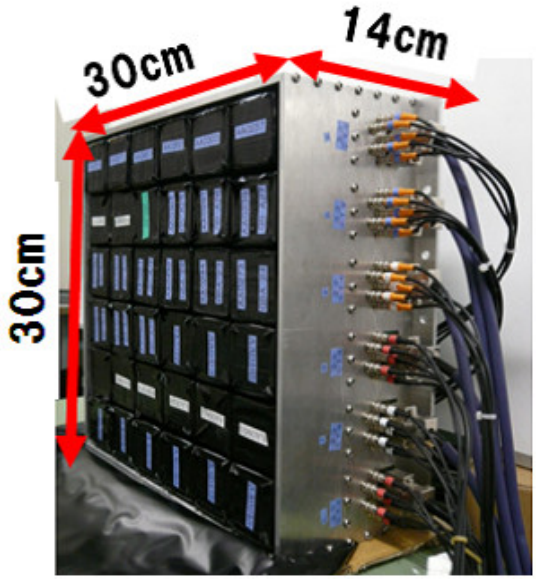

Figure 4.43: The photograph of the bottom absorber

Alignment of the large size gamma-ray telescope

When we observe the gamma rays of a quite far point source such as a celestial object, the gamma rays emitted from the objects come into a telescope in parallel. However, in the laboratory, it is very difficult to obtain the parallel gamma rays using a radioactive source. Simulation says that, in order to obtain the parallel gamma rays ($< 1^\circ$) from radioactive source, we have to put the source at $\sim$ 5 m from the detector. In this condition, the intensity of gamma rays is too weak. Then, we put a radioactive isotope at the appropriate distance from the telescope, and obtain an image by obtaining the cross point of the source plane and the reconstructed line, as shown in Figure 4.44, where we use this distance as a known parameter.

Figure 4.44 and Figure 4.45 also show the alignment of the prototype large size gamma-ray telescope and the photograph of the large size telescope, respectively. The distance between the telescope window and the source plane is about 30 cm. Around this telescope, there is no shield and no veto counter.

Data Acquisition System

Figure 4.46 is the diagram of the data acquisition system for the large size gamma-ray telescope. Sum of the signals from the scintillation camera is used for the trigger decision of the data acquisition. The trigger signal generated by the sum of those signals is fed to the position

Table 4.2: The specification of prototype absorber

Scintillator	GSO:Ce
PMT	Hamamatsu Photonics H8500
Pixel Size	$6 \times 6 \times 13$ mm^3
Bottom Camera	300×300 mm^2 (6×6 PMTs)
Energy Range	80 - 900 keV
Energy Resolution	FWHM[%] $= 10.6 \times (E_\gamma/662 \text{ keV})^{-0.53}$

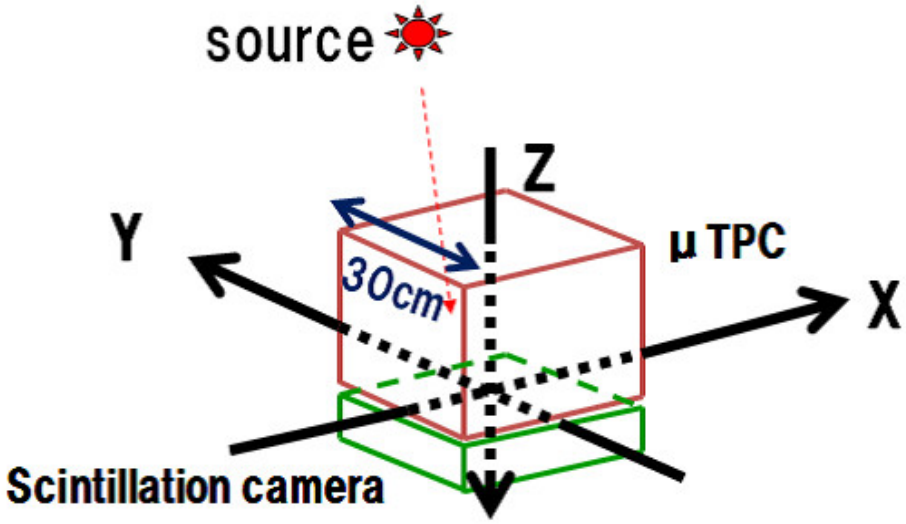

Figure 4.44: The side view of alignment

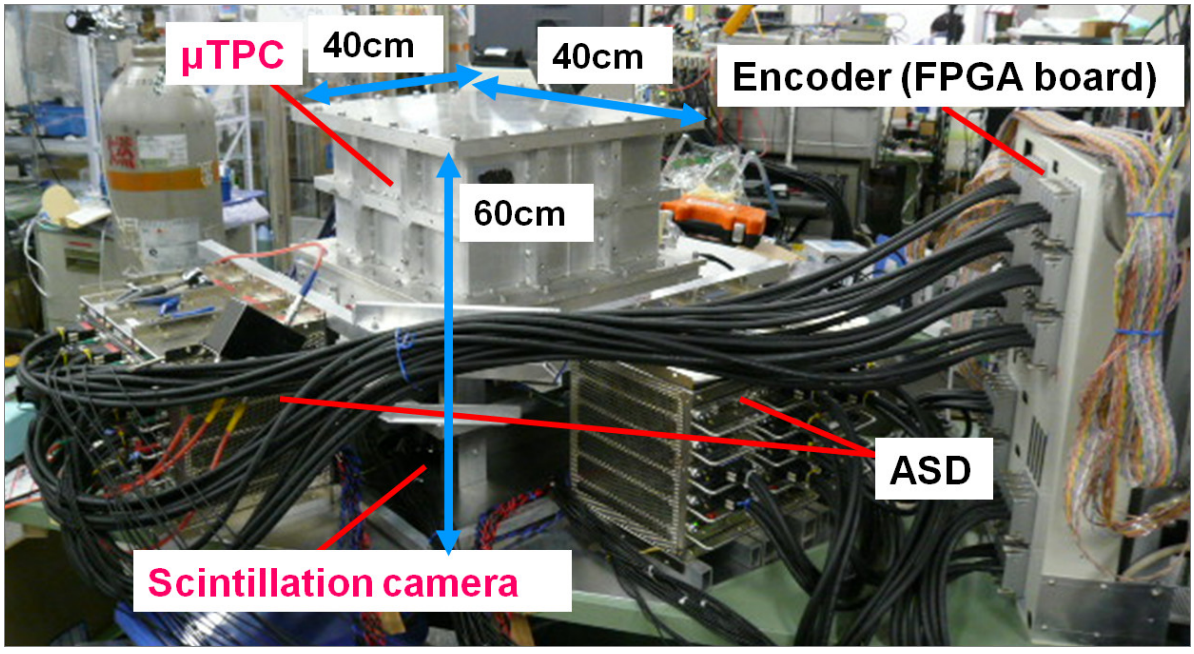

Figure 4.45: The photograph of the prototype large size gamma-ray telescope

Table 4.3: The specification of prototype tracker

Gas	Ar 90 % + C_2H_6 10 %, gas sealed 1 atm
Volume	$30 \times 30 \times 30$ cm^3
Effective Volume	$23 \times 28 \times 30$ cm^3
Gas Gain	~ 100000
Drift Velocity	4.1 cm/μsec
Encoding Clock	100 MHz
Position Resolution	~ 580 μm
Energy Resolution	FWHM[%] $= 1.25 \times 10^2 \left(\frac{K_e}{\mathrm{keV}}\right)^{-0.39}$

encoding module and the position and timing of hit electrodes are held once. Then, the position encoding module generates the veto signal for the trigger and the gate signal for the peak hold ADCs and also starts the 100 MHz clock counter. In counting the clock, the position encoding module waits the signal from the electrodes of the μ-TPC during 8 μsec. In the case of no TPC signal, the position encoding module sends a clear signal to the peak hold ADC for canceling the held data, and clears the veto signal for waiting a next trigger. On the other hand, when the TPC signal comes to the position encoding module, the hit information are accumulated in the position encoding module for 8 μsec from the triggered time, and are sent to the memory module. The stop signal is sent to the flash ADC after 8.5 μsec from the trigger. After finishing the data transfer to the memory module, the position encoding module generates an interrupt signal to the CPU on VME. The CPU takes the data of the memory module, peak hold ADCs, and the flash ADC. Finally, the CPU sends the acquisition end signal to the position encoding module. If the acquisition end signal is received by the position encoding module, the veto signal is cleared by the position encoding module. Figure 4.47 and 4.48 show the timing charts of a cycle of the data acquisition and a clear cycle, respectively.

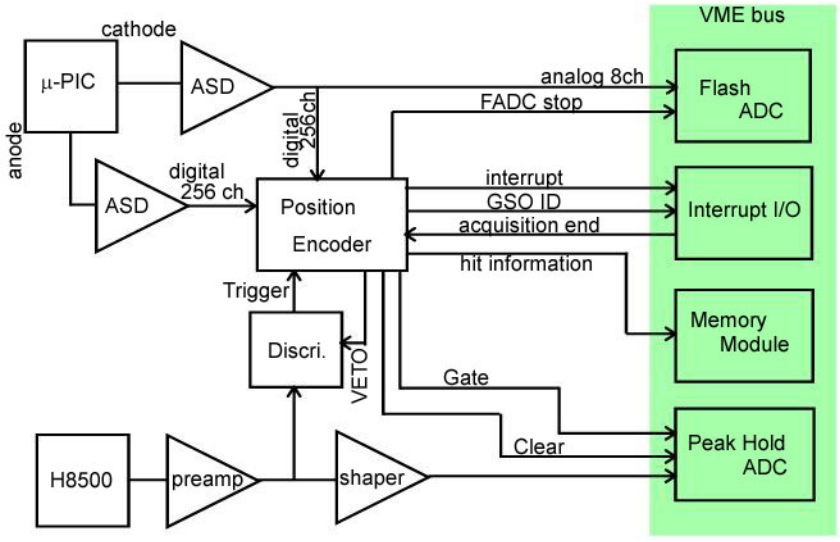

Figure 4.46: The diagram of data acquisition system

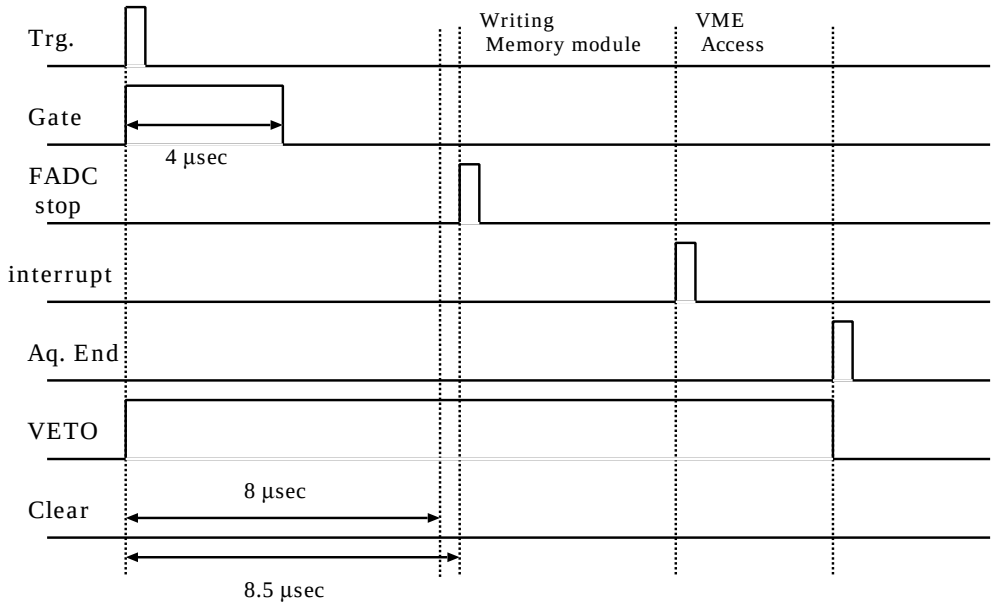

Figure 4.47: The timing charts of a cycle of the data acquisition.

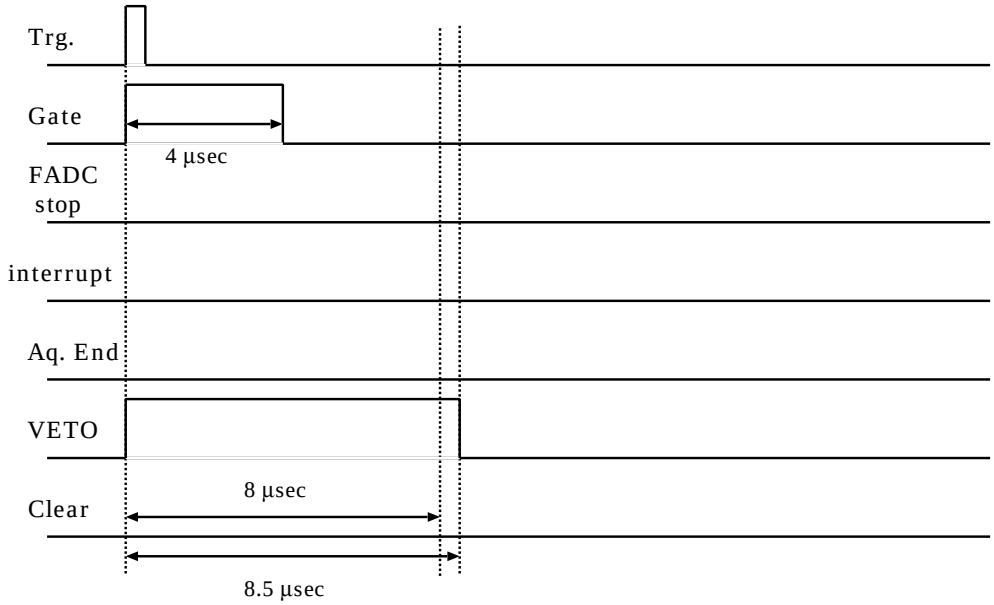

Figure 4.48: The timing charts of a clear cycle.

4.4.2 Performance of a large size gamma-ray telescope

In order to reconstruct the direction of the incident gamma rays using Equation (3.1) and (3.2), we applied following several event selection.

Hit Number Cut: A real Compton scattering event must have one electron track in the μ-TPC and only one hit in the PSA units. Thus, if the number of the triggered PSA units, N_{trg}, is more than 2, the event is due to the background such as a charged particle event, an event which scattered gamma ray scatters several times in PSA, and a random coincidence event. We required $N_{trg} = 1$.

Fiducial Volume Cut: We applied the fiducial cut for the track in the μ-TPC. From the distortion of the electric field around the fringe of the drift volume of the μ-TPC, we used a $22\times26\times24$ cm^3 volume of the center part of the TPC for effective area. The events which have a Compton scattering points out of this region are rejected.

Effective Event Cut: In order to determine the direction of the recoil electron, we used TPC events which have at least 3 hit points ($N_{hit} \geq 3$) in above fiducial volume.

Electron Selection: The correlation between the energy and the track length (L_e) of the recoil electron was studied in detail [54]. We used the events which satisfy $K_e > 0$, and then following condition is required,

$$\left| \frac{L_e}{cm} - 3.6 \times 10^{-3} \left(\frac{K_e}{keV} \right)^{1.82} \right| < 3.0. \tag{4.14}$$

Compton Scattering Kinematics: With the reconstruction of the incident gamma ray, we obtain the scatter angle by Equation (3.4). Because the $\cos\phi$ must be between -1 and 1, following relation is required,

$$0 \leq \frac{m_e c^2}{E_\gamma + K_e} \frac{K_e}{E_\gamma} \leq 2. \tag{4.15}$$

α Cut: For matching to the kinematics of Compton scattering, the event which has a large inconsistency between α_{geo} and α_{kin} are rejected.The incident direction is described as follows:

$$\vec{s_{kin}} = \frac{E_\gamma}{E_\gamma + K_e} \vec{g} + \frac{\sqrt{K_e(K_e + 2m_e c^2)}}{E_\gamma + K_e} \vec{e}. \tag{4.16}$$

For the true event, $\vec{s_{kin}}$ is a unit vector within the measurement errors. Thus, we require the following condition as the α cut:

$$||\vec{s_{kin}}| - 1| \leq 0.07. \tag{4.17}$$

The reconstruction method and the event selection parameters described above were the same as those in [54]. Figure 4.49 shows a typical Compton event measured by the large size gamma-ray telescope, where all information, the energy and track of the recoil electron, the energy and absorbed point of scattered gamma ray are obtained. We can see that the Compton scattering is reconstructed correctly. Moreover, the source position is also reconstructed accurately.

With changing the source position, we measured the movement of the images as shown in Figure 4.50. All images have a peak near the real source position. On the other hand, in order to test the energy range in which this camera can reconstruct, Figure 4.51 shows the obtained

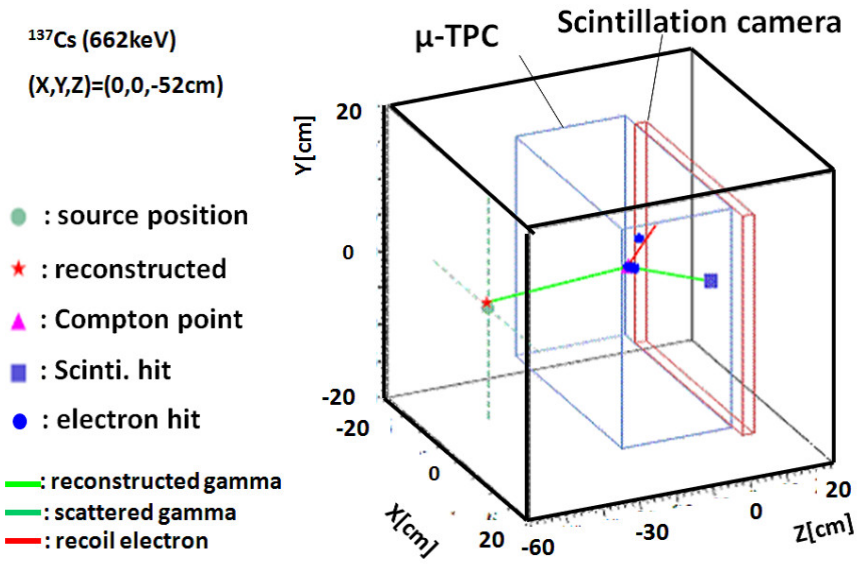

Figure 4.49: The typical event of the reconstructed gamma ray

images of the gamma rays with the energies of 356, 662, and 835 keV. It is clearly seen that the peak of the obtained image spreads for the lower energy of the incident gamma-rays.

Two different energy sources of a ^{137}Cs (662 keV) and a ^{54}Mn (835 keV) were put at (5cm, 5cm) and (−5cm, −5cm), respectively, and we obtained the spectrum of the reconstructed events as shown in the upper left figure of Figure 4.52. The peaks of 662 keV and 835 keV are clearly seen in this spectrum, and the continuum component of the gamma rays scattered at the outside of the camera is also seen under 580 keV. On the other hand, the Compton edge is not seen in this histogram, because this camera measures both the recoil electron and the scattered gamma ray. The upper right figure of Figure 4.52 is the obtained image by this measurement. This image has peaks near the ^{137}Cs and ^{54}Mn. Applying the energy cut of 580 - 740 keV and 760 - 910 keV, we obtained the images as shown in lower left and lower right of Figure 4.52, respectively. Both images have an unique peak near the gamma-ray source corresponding to the energy range. Therefore, the telescope with the Compton mode can separate multi-energy

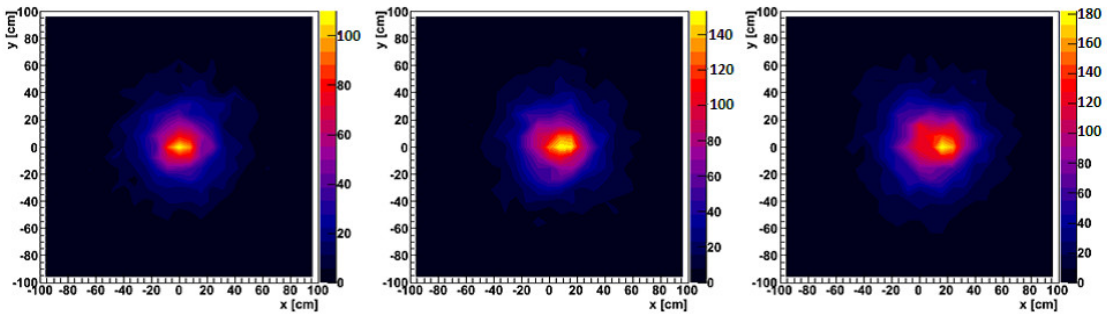

Figure 4.50: The obtained images of the different source positions at (x, y) = (0, 0) (left), (x, y) = (10,0) (center), and (x, y) = (20, 0) (right). The gamma ray sources of all images are ^{137}Cs, and the energy range is 580 - 744 keV.

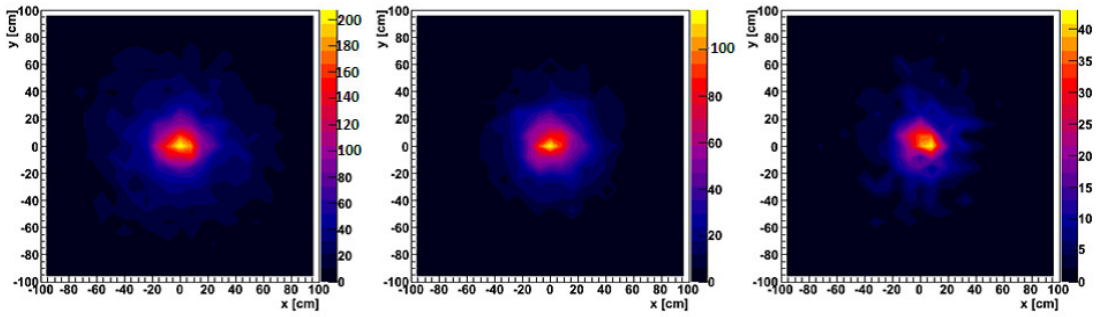

Figure 4.51: The obtained images of several different sources, ^{133}Ba (289 - 423 keV) (left), ^{137}Cs (580 - 744 keV.) (center), and ^{54}Mn (747 - 923 keV) (right). The source position of all image are (x, y) = (0, 0).

sources using the energy information.

Figure 4.53 shows the energy resolutions of the gamma-ray telescope. For the 662 keV gamma rays, the resolution was 12.3±0.3% (FWHM). For comparison, the resolutions from simulation and the ones of the 10×10×15 cm^3 telescope were also plotted in this figure. The resolutions are roughly consistent with the simulated ones. However, it was worse than that of the 10×10×15 cm^3 telescope due to the worse energy resolution of the μ-TPC.

Left and right figures of Figure 4.54 show the resolutions of the ARM and SPD, respectively. We obtained the resolution of the ARM by fitting with a Lorentzian, and obtained the resolution of the SPD by fitting with a Gaussian. For the 662 keV gamma rays, the ARM and SPD were 9.8±0.3 ° and 147±18 ° (FWHM), respectively. Figure 4.55 shows the energy dependence of the resolution of ARM and SPD. The resolution of the ARM becomes better as the energy of the incident gamma-ray increases, because it depends on the energy resolution of the scintillation camera and the μ-TPC. On the other hand, FWHM of the SPD is nearly constant. This reason is that the detectable energy range of the recoil electron has little change with the energy of the incident gamma rays, because that range is limited by the drift volume. In this result, there are the gap between the obtained resolutions of ARM and the simulated ones systematically. This is because the simulation does not include the complete diffusion model for the drift electrons and response of the preamplifier. The obtained resolutions were roughly consistent with the ones of the 10×10×15 cm^3 telescope.

The detection efficiency is shown in Figure 4.56. For comparison, the efficiencies from simulation and the ones of the 10×10×15 cm^3 telescope were also plotted in this figure. At the 662 keV gamma rays, the detection efficiency was 9.0×10^{-6}. This value is better by a factor of 2.4 than that of 10×10×15 cm^3 telescope. The gap between the obtained and simulated ones are due to the uncertainty of the diffusion model and the response of preamplifier in the simulation. Figure 4.57 shows the dependence of the effective area on the zenith angle. This figure says that the FWHM of the effective area is $\sim 60°$, therefore the FOV of the prototype of the large size telescope with Compton mode is about 1 str.

As described above, we succeeded in the imaging of the gamma rays using the large size telescope with Compton mode. In order to detect photons of a bright source like Crab or Cyg X-1, we need more improvement of the detection efficiency of the telescope. For the improvement, we consider the use of CF_4 gas for the μ-TPC at 2 atm. After adding this improvement, our telescope would be able to obtain a few hundred photons from Crab during a level flight for 6 hours, because the efficiency will be 10 times larger than that of the telescope of the first experiment.

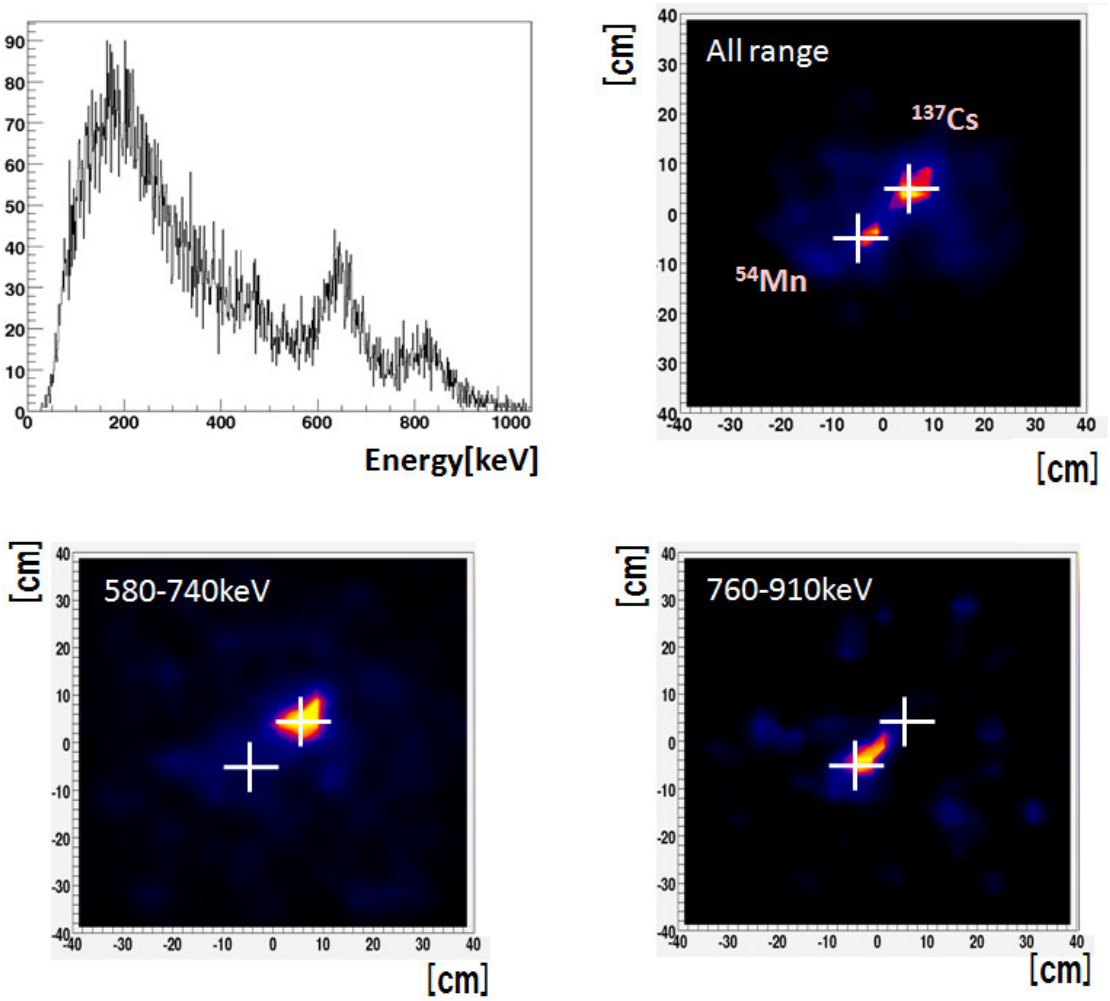

Figure 4.52: The obtained spectrum (upper left) and image (upper right). If the energy cut was applied to the obtained image, images which have unique peaks were obtained. These images are in the energy range of 580 - 740 keV (lower left) and 760 - 910 keV (lower right), respectively.

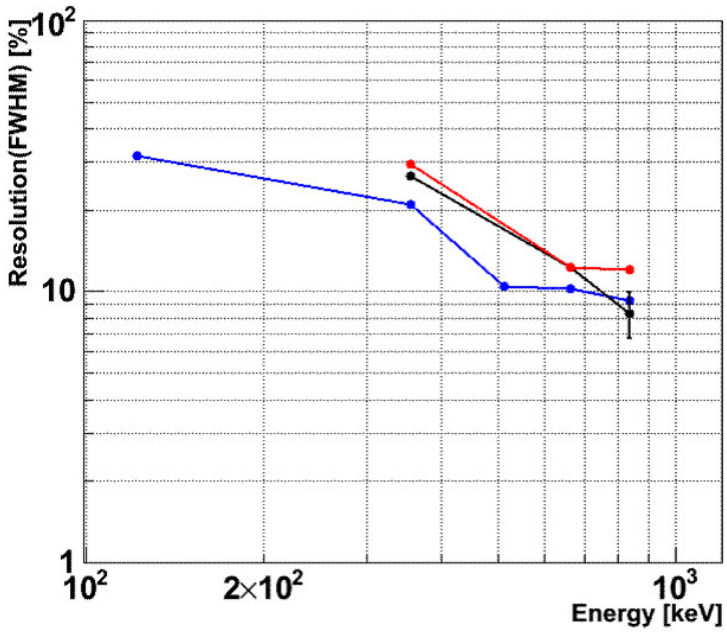

Figure 4.53: The energy resolution as a function of the energy of the gamma rays. Red points are the results. For comparison, the simulated ones (black) and those of the 10×10×15 cm^3 telescope (blue) are plotted.

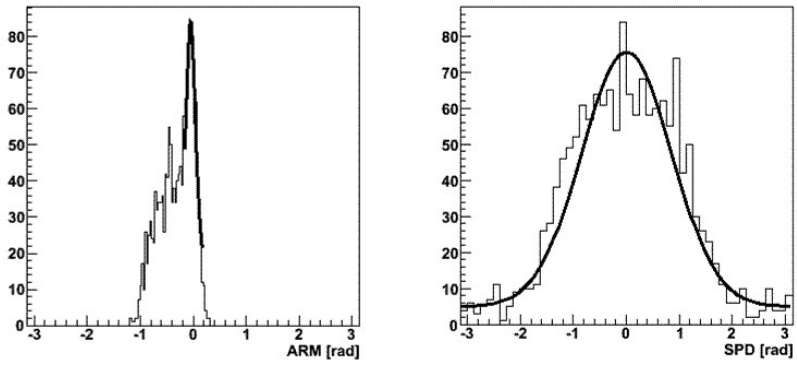

Figure 4.54: The histograms of the uncertainty of ARM (left) and SPD (right) for ^{137}Cs. The solid lines are obtained by fitting with Lorentzian (left) and Gaussian.

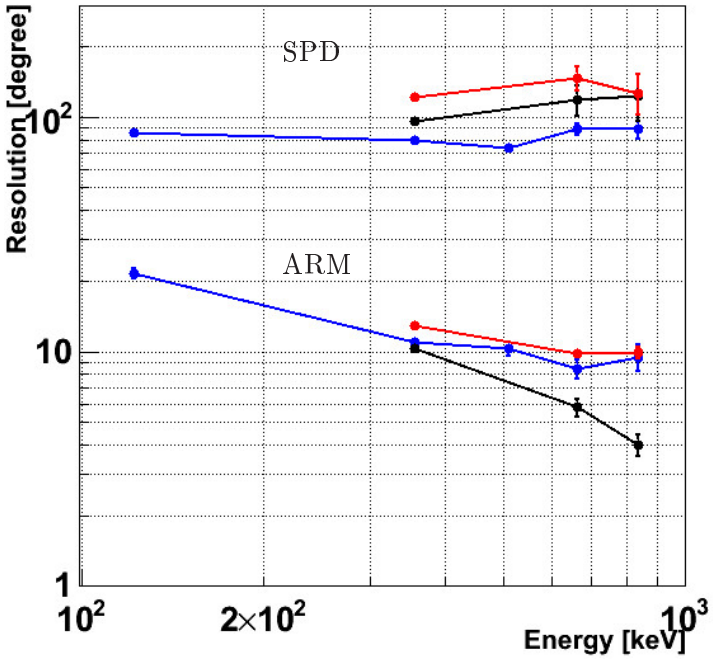

Figure 4.55: The angular resolutions of ARM and SPD as a function of the energy of the gamma rays (red). For comparison, the simulated ones (black) and those of the 10×10×15 cm^3 telescope (blue) are plotted.

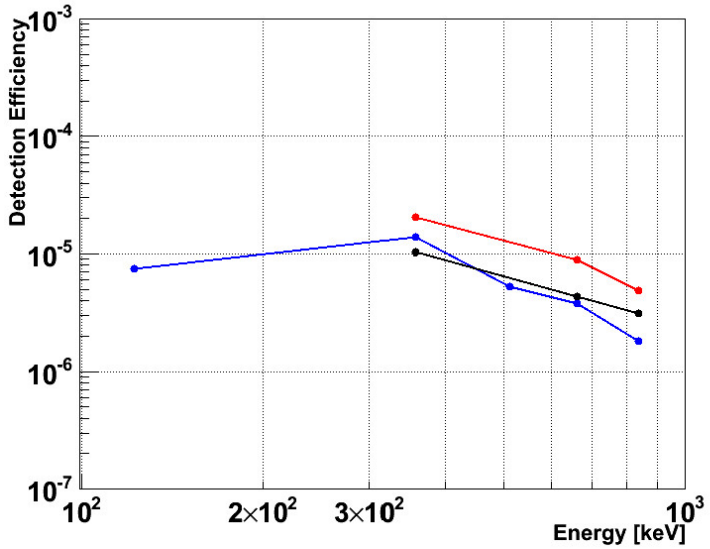

Figure 4.56: The detection efficiency as a function of the energy of the gamma rays (red). For comparison, the simulated ones (black) and those of the 10×10×15 cm^3 telescope (blue) are plotted.

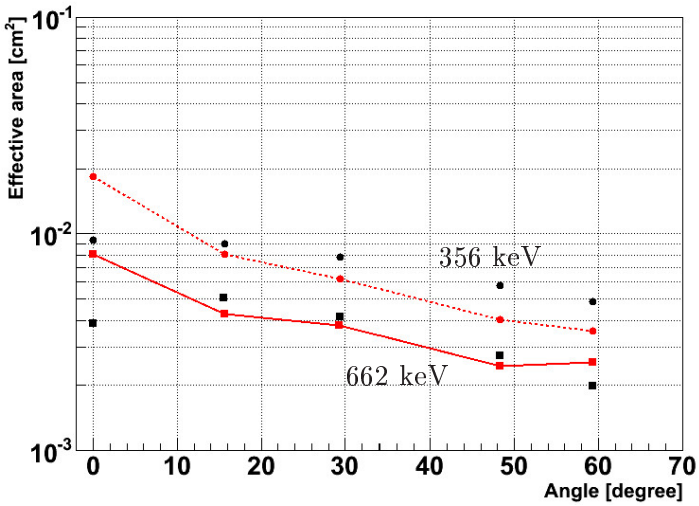

Figure 4.57: The effective area as a function of the zenith angle for the 662 (red square and solid line) and 356 (red circle and dashed line) keV gamma rays. For comparison, the simulated ones for the 662 (black square) and 356 (black circle) keV gamma rays are also plotted.

Chapter 5

Low power consumption readout system for scintillation camera

5.1 Low power consumption readout system for scintillation camera

For the balloon-borne experiment, saving power consumption of all the system of the MeV gamma-ray telescope is quite important. In the first experiment, the readout system of the scintillation camera (33 PMTs) consumed the most power. For the next experiment, we need 108 or more PMTs in order to improve the effective area. Thus, a readout system with low power consumption ($\leq$ 2 W/64 ch) for the scintillation camera is indispensable. We then developed the new readout system and investigated the performance of the scintillation camera with the system.

5.1.1 ASIC readout system

In order to satisfy the requirement, we adopted the compact readout system of scintillation camera (CP80168 by Clear Pulse Co. Ltd.) using the ASIC chips, IDEAS VA32_HDR11. This ASIC has both low power consumption of 1.3 W/64 ch and dynamic range of $\sim$-35pC, which is one of chips with widest range among commercial ones.

Figure.5.1 shows the CP80168, which read the 64 channel signals of H8500 PMT individually. It is designed for two dimensional array of the H8500 and has the size of 52 mm$\times$52 mm$\times$95 mm. CP80168 uses two types of analog ASICs, 32 channel VA32_HDR11 and TA32CG2 manufactured by IDEAS ASA. The VA32_HDR11 contains pre-amplifiers with input dynamic range of about 20 pC to -35 pC, shapers with the gain of 118 mV/pC and the peaking time of 0.7 μs, sample and hold circuits and a multiplexer. The TA32CG2 contains fast shapers with peaking time of 75 ns and discriminators, which make the trigger signals. Figure.5.2 shows a schematic diagram of the data acquisition system for the performance test of CP80168. The multiplexed 64 channels data are digitized by a flash ADC on the CP80168 and sent to the VME sequence module via FPGAs. It takes 164 μs to read 64 channels.

5.1.2 Attenuator board

When using a combination of a GSO(Ce) crystal and the H8500, the dynamic range of VA32_HDR11 is insufficient, and hence the H8500 has to be operated with a low gain of about 10^5. Our previous paper [9] reported that if the H8500 is operated with such a low gain, the incident-energy dynamic range is insufficient and the energy resolution is worse, compared to the operation of the H8500 with the adequate gain. Actually, using the GSO(Ce) and the H8500 with a low gain,

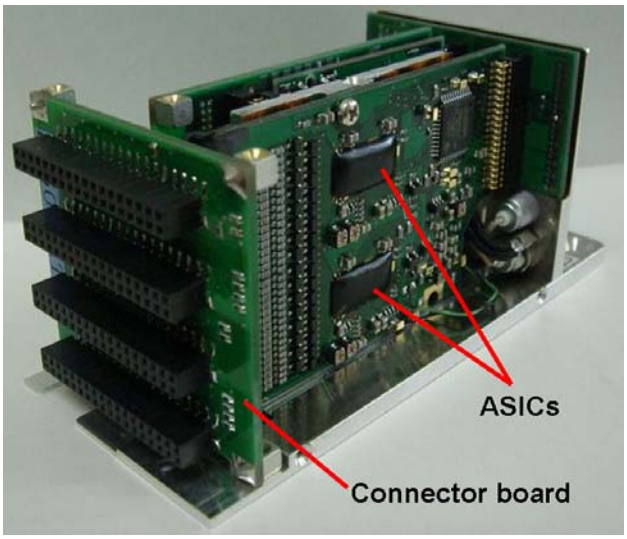

Figure 5.1: Picture of CP80168. CP80168 consists of the board containing two VA32_HDR11 chips and two TA32CG2 chips, and the connector board which connects ASIC chips to the H8500. The connector board is replaceable.

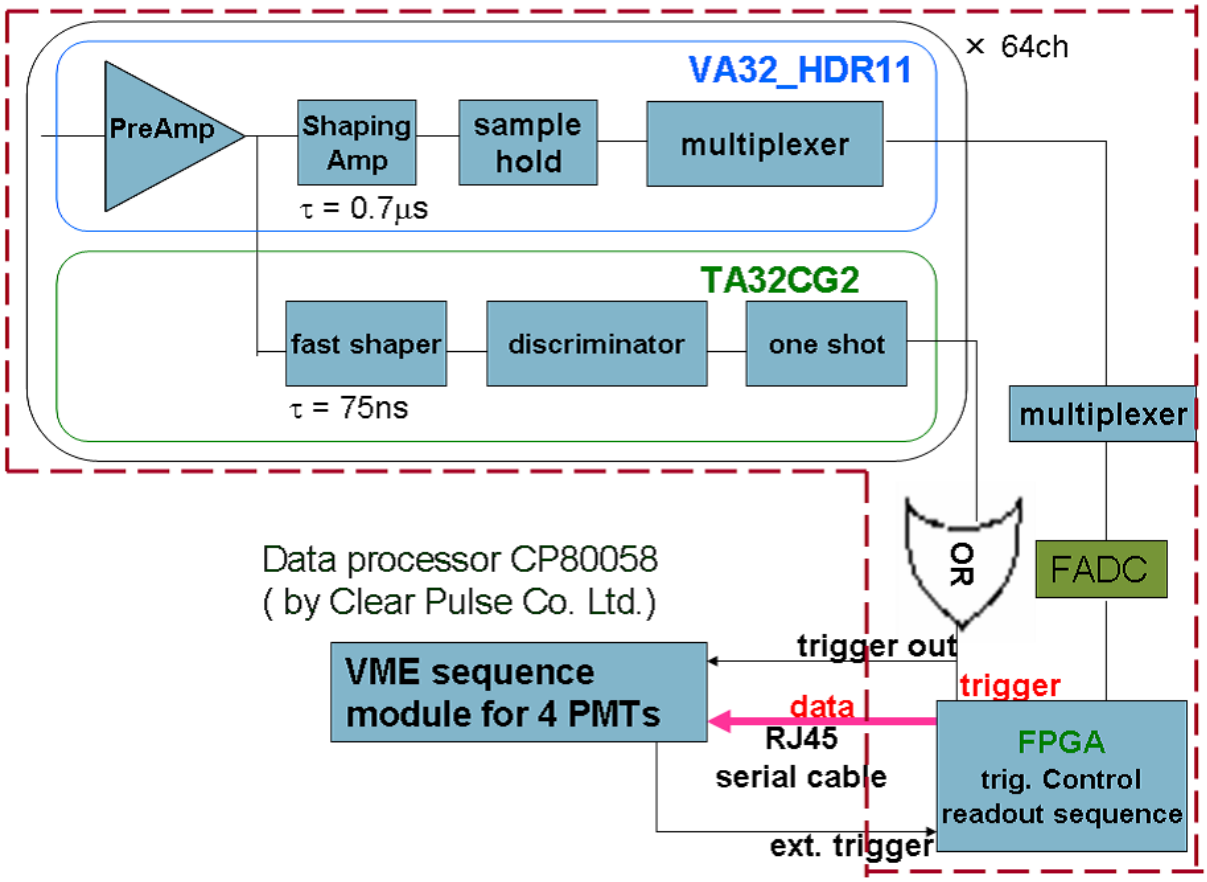

Figure 5.2: Schematic view of data acquisition system. Red block box shows the CP80168.

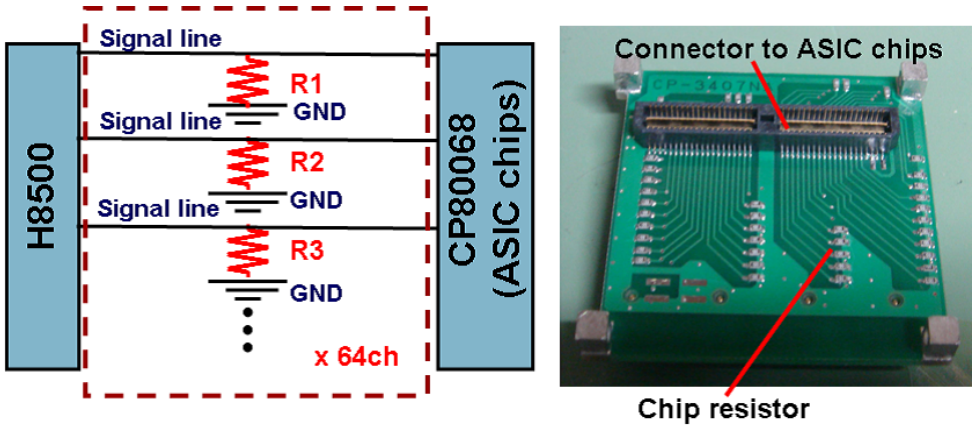

Figure 5.3: Schematic view of the attenuator board(left, dashed line) and picture of the attenuator board(right). The connector board (Figure 5.1) can be replaced with the attenuator board.

we measured a range of from ∼120 to 800 keV and an energy resolution of 12.5%(FWHM) at 662 keV. In order to to resolve these problems, we developed an attenuator board. The concept of the attenuator board is to obtain a scintillation camera with a good energy resolution, and thus signals with a gain of about 10^6 in the H8500 are obtained. Because of the narrow dynamic range of the VA32_HDR11, the obtained signals from the H8500 are attenuated within the input range before the VA32_HDR11. In addition, considering the anode gain variation of the H8500, those signals are made uniform before the VA32_HDR11. The attenuator board is shown in Figure 5.3, which has 64 singular resistors adjusted to the anode gain, and uniforms variation of the anode gains of the H8500. Because the board has the same size as the connector board of the CP80168 (Figure 5.3), we only replace the connector board by the attenuator board, and thus the total size of the CP80168 and the scintillation camera does not change.

5.1.3 Measurements and results

We irradiated the GSO(Ce) PSA with 662 keV gamma rays from a 1 MBq ^{137}Cs source at a distance of 30 cm. For the energy calibration, ^{54}Mn (835 keV), ^{57}Co (122 keV), ^{22}Na (511 keV), and ^{133}Ba (31, 81, 356 keV) were also used. The H8500 was operated with a gain of about 10^6 under a HV of ∼900 V.

We investigated the relation between the resistance and the attenuation factor. Considering the relation, we chose a discrete and not a variable resistance of a commercial resistor for the attenuator board in order to make the board compact. The minimum to maximum gain ratio of the 662 keV peak values of 64 channels is expected to be 1:1.9±0.3 (RMS), while the anode uniformity of the H8500 is 1:3.1. We measured the 662 keV peak values of 64 channels to be as shown in Figure 5.4. The measured ratio with the attenuator board is 1:1.6±0.1, which is in agreement with our expectation.

The obtained flood irradiation image of ^{137}Cs are shown in Figure 5.5. The position of the hit point of the GSO(Ce) PSA is reconstructed to calculate the center of gravity of 64 channels

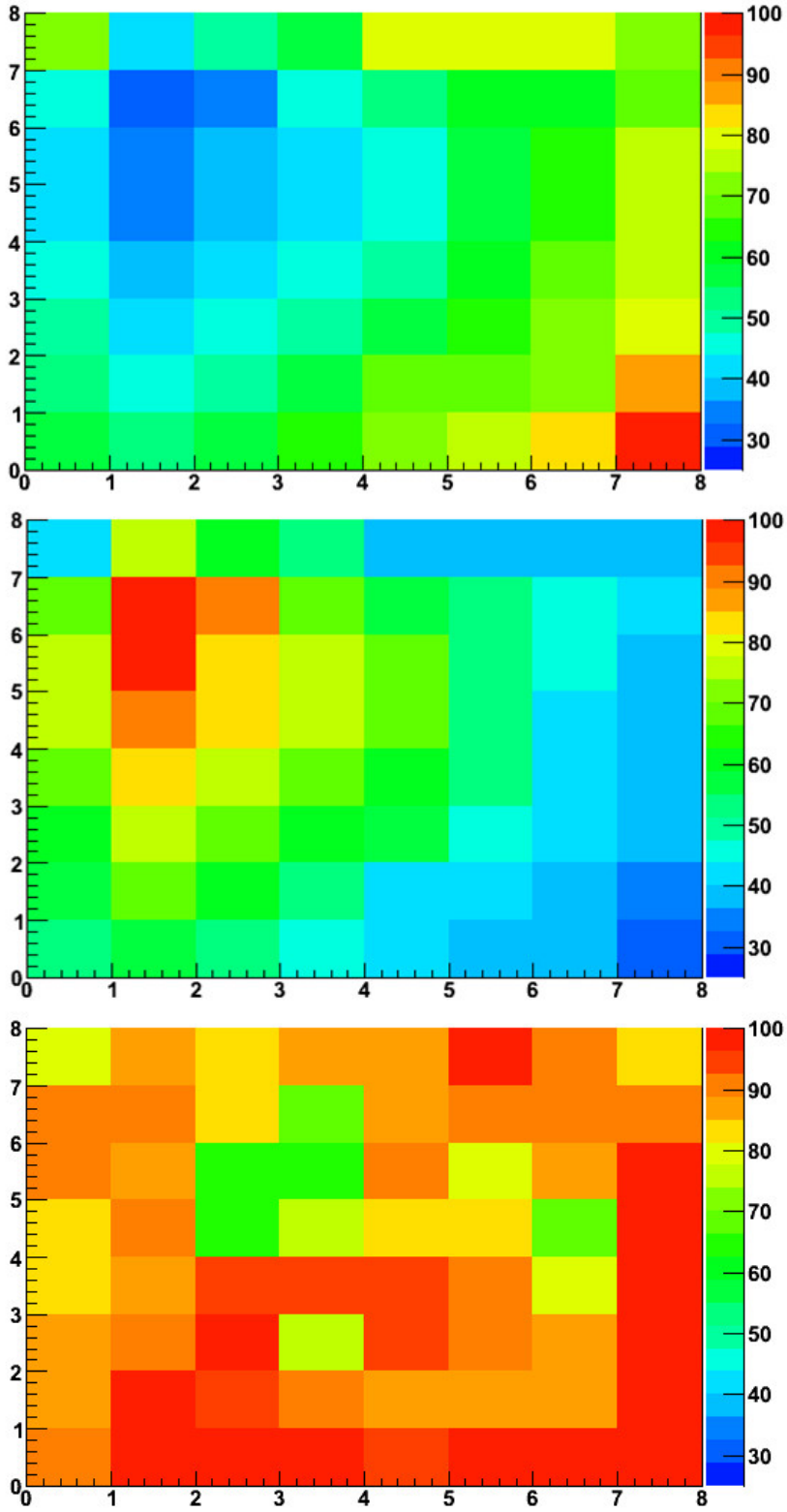

Figure 5.4: Anode gain uniformity map of the H8500 that we used (top), resistance value (in units of Ω) map of the attenuator board that we developed corresponding to the top one (middle), and the measured 662 keV peak map (bottom), where the maximum peak is normalized to 100.

ADC value using the following equations:

$$x = \frac{\sum_{i=1}^{64} P_i \cdot (i \ mod \ 8)}{\sum_{i=1}^{64} P_i}, \tag{5.1}$$

$$y = \frac{\sum_{i=1}^{64} P_i \cdot (i \ div \ 8)}{\sum_{i=1}^{64} P_i}, \tag{5.2}$$

where P_i is the ADC output of ith anode of CP80168 system. The peak-to-valley ratio of the x-projection of the flood irradiation image, as shown in Figure 5.5, is good: each of the 64 pixel is clearly resolved, and the position resolution is less than a pixel pitch of 6 mm. The energy spectrum of each pixel was measured as shown in Figure 5.5. The mean energy resolution is 10.6% at 662 keV (FWHM). Figure 5.6 shows the measured energy resolution with other sources. These are fit to

$$\frac{\Delta E}{E}(FWHM) = 10.6 \pm 0.6\Big(\frac{E}{662[keV]}\Big)^{0.49\pm0.03}, \tag{5.3}$$

where fit parameters are given with RMS errors in the range from 31 to 835 keV. The measurable energy dynamic range of the system is about 30 - 900 keV at all 64 pixels.

These results show that the system of the scintillation camera with the attenuator board performs adequately with both a good energy resolution and a wide dynamic range, which is satisfied low power consumption.

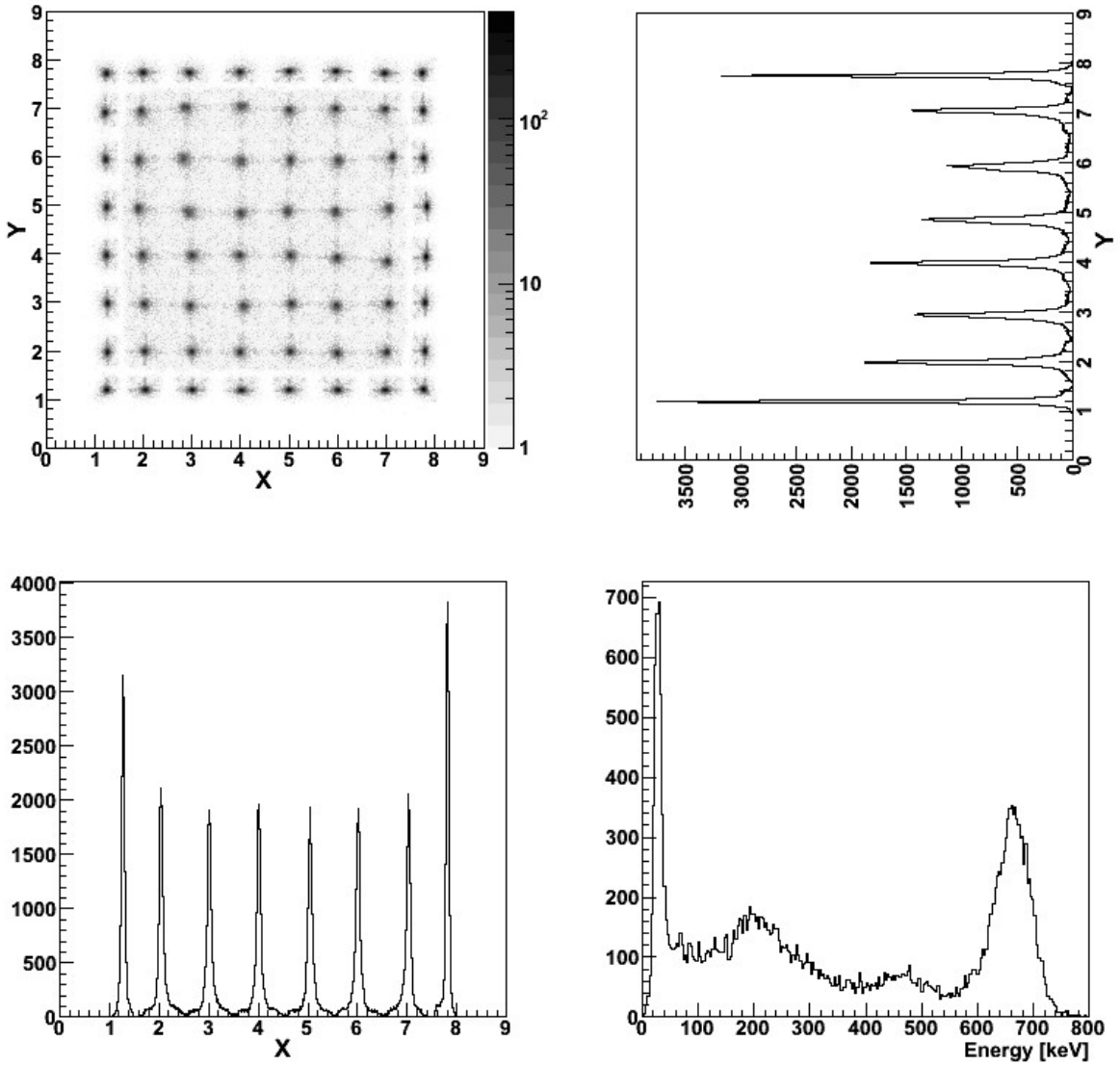

Figure 5.5: Flood field image of ^{137}Cs irradiation (upper left), x-projection of the image at the 2nd row (lower left), y-projection of the image at the 4th row (upper right), and typical energy spectrum (lower right).

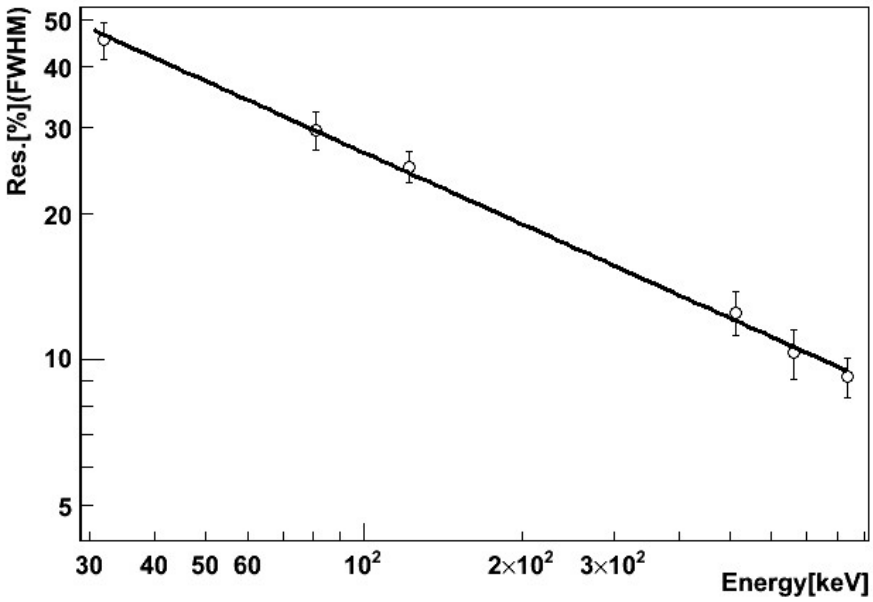

Figure 5.6: Measured energy resolution using the attenuator board. The best-fit line is described in the text.

Part III

First light of the gamma-ray telescope with pair creation mode

Chapter 6

Prototype telescope with pair creation mode

We started to develop a gamma-ray telescope operating with pair creation mode and achieved its first light using the gamma-ray beam. This and the following two chapters describe performances of the telescope.

6.1 Detector concept

6.1.1 Detector design

In principle, the pair creation events can be measured using the same telescope as the one with Compton mode as described in Chapter 3. However, since the electron and positron converted in the μ-TPC are greatly scattered by the aluminum plates of the gas vessel, the detection of those with the scintillation camera becomes difficult. Therefore, we made the new gas vessel using Carbon Fiber Reinforced Plastics (CFRP) instead of aluminum. CFRP has the lower density and larger radiation length than aluminum. Figure 6.1 shows the energy dependences of scattering angles of an electron in CFRP and aluminum, respectively, which are calculated by Geant4. The disadvantage of CFRP is only a difficulty of the processing. Then, the gas vessel was made by the combination of a G10 frame and the CFRP window.

Even if CFRP and G10 are used for the vessel window, energy loss of an electron and a positron at the window is not small to the energy of the incident gamma ray in the energy range from a few to several tens of MeV. Figure 6.2 shows the deposit energy at window when the energy of the incident gamma ray is 10 MeV, which is calculated by Geant4. As shown in this figure, the ratio of the energy loss to the energy of the incident gamma ray is more than 10 % at 10 MeV. Then, the uncertainty of the energy detected by the scintillation camera is large. Therefore, we used the scintillation camera for the trigger counter as the first step in this thesis.

6.1.2 μ-TPC for the prototype telescope with pair creation mode

We developed the μ-TPC for the prototype telescope with pair creation mode which includes the above improvement, as shown in Figure 6.3. This μ-TPC consists of 10×10 cm^2 μ-PIC (SN071220-2) (Figure 6.4), 10×10 cm^2 GEM (Figure 6.5), and the G10 drift cage with the length of 14.5 cm. The μ-PIC is put on an Al flange with the thickness of 16.7 mm. The GEM is placed at the distance of 4 mm above the μ-PIC. The gas vessel is filled with a gas and is sealed by O-ring.

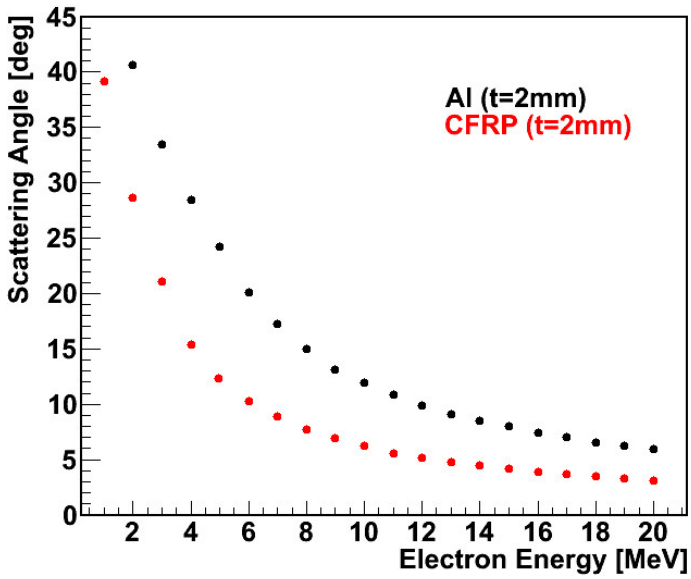

Figure 6.1: The energy dependencies of the scattering angles of electron in Al (Black) and CFRP (Red).

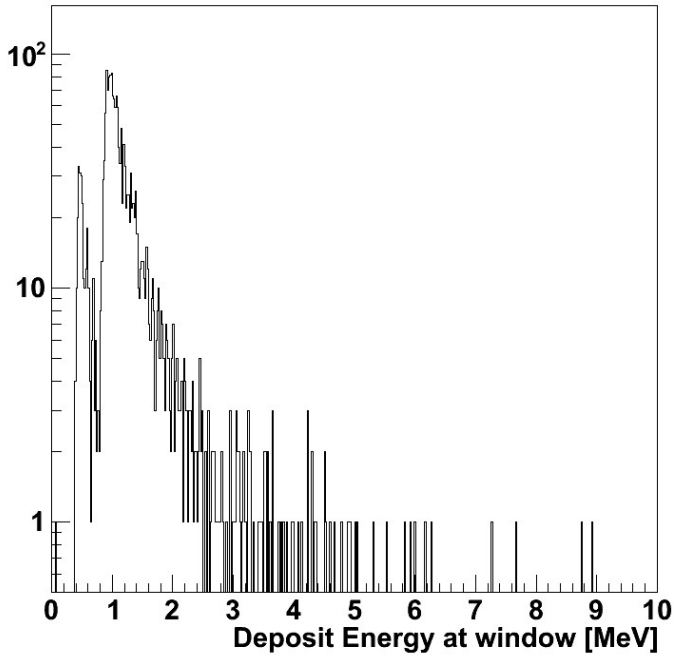

Figure 6.2: The energy loss in CFRP window for the incident gamma-ray energy of 10 MeV.

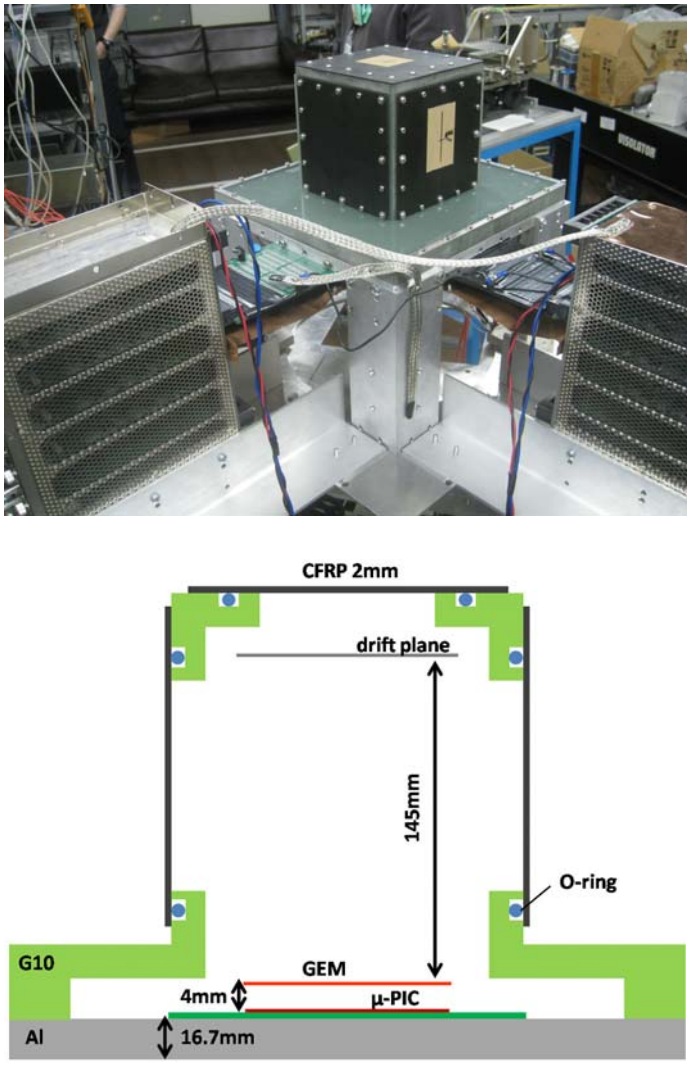

Figure 6.3: A photograph of μ-TPC for the gamma-ray telescope with pair creation mode (top) and a schematic view of that (bottom).

6.1.3 Scintillation camera for the prototype telescope with pair creation mode

We used the same scintillation camera as the one of $10\times10\times10$ cm^3 prototype telescope with Compton mode [54] basically for the gamma-ray beam experiment. Figure 6.6 shows the constructed scintillation camera for the prototype telescope with pair creation mode. In order to prevent incident gamma-ray beam passing the μ-TPC from entering the scintillation camera directly, the center unit of PSA was excluded.

6.2 New DAQ system for tracking

The key of the pair creation telescope is an accurate tracking of the electron-positron pair using the μ-TPC. Although multiple scattering of the electron (positron) in the gas is fewer than that in the silicon, the scattering angle of the electron in the gas is not zero. Especially, the influence of scattering is large to the low energy electron with the energy of about 10 MeV. The number

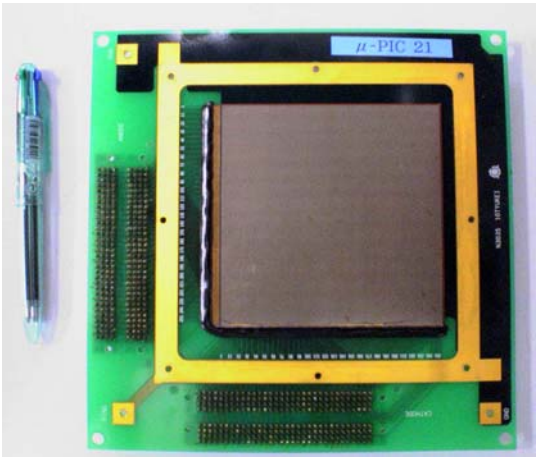

Figure 6.4: 10×10 cm^2 μ-PIC.

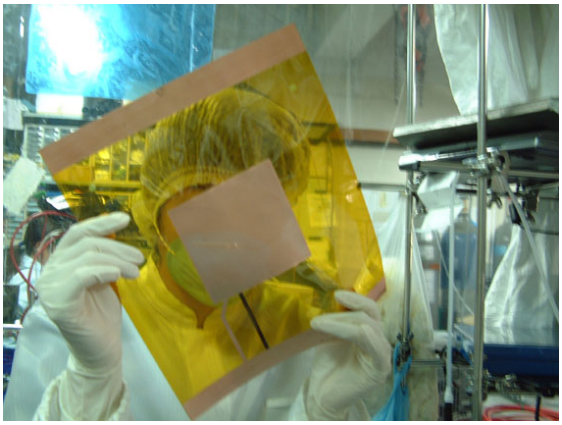

Figure 6.5: 10×10 cm^2 GEM.

Figure 6.6: Scintillation camera for the prototype telescope with pair creation mode.

of hit point of the track in the μ-TPC is very important. Therefore, we improved the DAQ for tracking which can detect the more points than the previous one used in SMILE-1 experiment.

6.2.1 TPC mode-II

In the case of the position encoding system described in Chapter 4, hit points from the anodes and the cathodes are recorded when they coincide in a 10 nsec clock interval, and delayed signals are discarded in order to improve the signal-to-noise ratio. However, the obtained number of hits is less than that in real, which causes deterioration in position resolution actually. Figure 6.7 shows the example of the coincidence signal by existing position encoding system. As shown in this figure, there are a lot of hits which has no coincidence. It is due to the time walk, the time jitter of the pulse signal, and different propagation delay at the individual ASD channels [64].

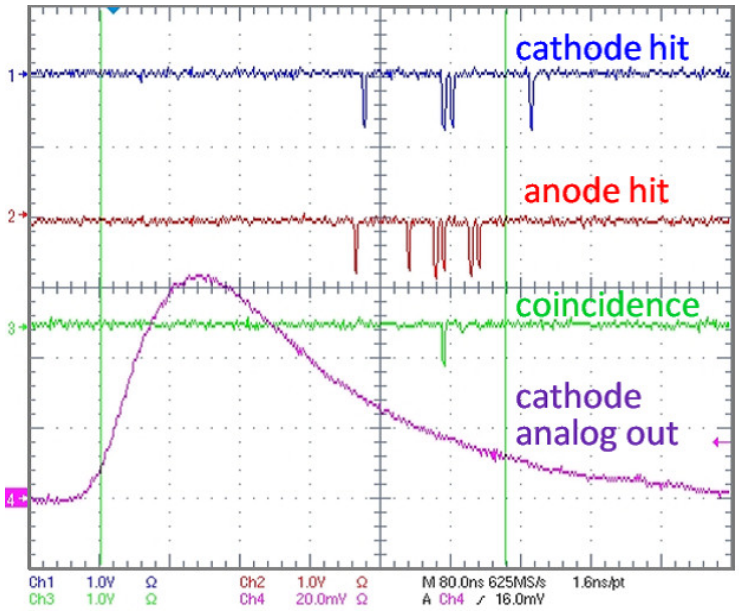

Figure 6.7: The coincidence signal of anode and cathode hits by existing position encoding system. The lines are cathode hits (blue), anode hits (red), coincidence of anode and cathode hits (green), and analog signal of cathode (purple).

Currently, since the μ-TPC has enough high gain and signal-to-noise ratio, the coincidence of the anode and the cathode hits of the μ-TPC is not indispensable for the position encoding system. Therefore, we developed the new position encoding mode, in which all hit data are recorded using the same hardware. We call the mode TPC mode-II. Figure 6.8 shows the block diagrams of the new and old modes. The TPC mode-II is basically the same as the existing mode. When the trigger signal is fed to the position encoding module, the 100 MHz clock counter starts. During 8 μsec, FPGA 7 (See Figure 4.13) judges whether there are signals from FPGA 1-6 to each clock. If the signals from FPGA 1-3 exists, the maximum and minimum positions of anode hit channels and that time are calculated in FPGA 7 and recorded. It is also similar for FPGA 4-6. In other words, the position information of the anode and the cathode is individually recorded, respectively.

6.2.2 Performance of TPC mode-II

The performance of the TPC mode-II was investigated using cosmic muons. Two plastic scintillators were located above and below the TPC. A coincidence of these scintillators was used for the muon trigger. Figure 6.9 shows the accumulated 5 tracks of the cosmic muons obtained with the TPC mode-II. X, Y, and Z refer to the strip numbers of the anode, that of the cathode, and the clock, respectively. In order to compare with the old encoding mode, the top figures in Figure 6.9 show the hit points from the anodes and cathodes only when they coincide in one clock, which is equivalent to the old encoding system. The bottom figures in Figure 6.9 show the all hit points, where the right one is obtained by coincidence of hit points of anode and cathode in two clocks. Here, since the time walk and time jitter is within two clocks in most cases, we selected this clock interval. Figure 6.10 shows the distributions of the number of hit points per muon track. The left and right figures are obtained by the old encoding mode and the TPC mode-II. As shown in this figure, the number of hit points by the new mode was increased about twice as much as that by the old one. These results show that the quality of the muon tracking

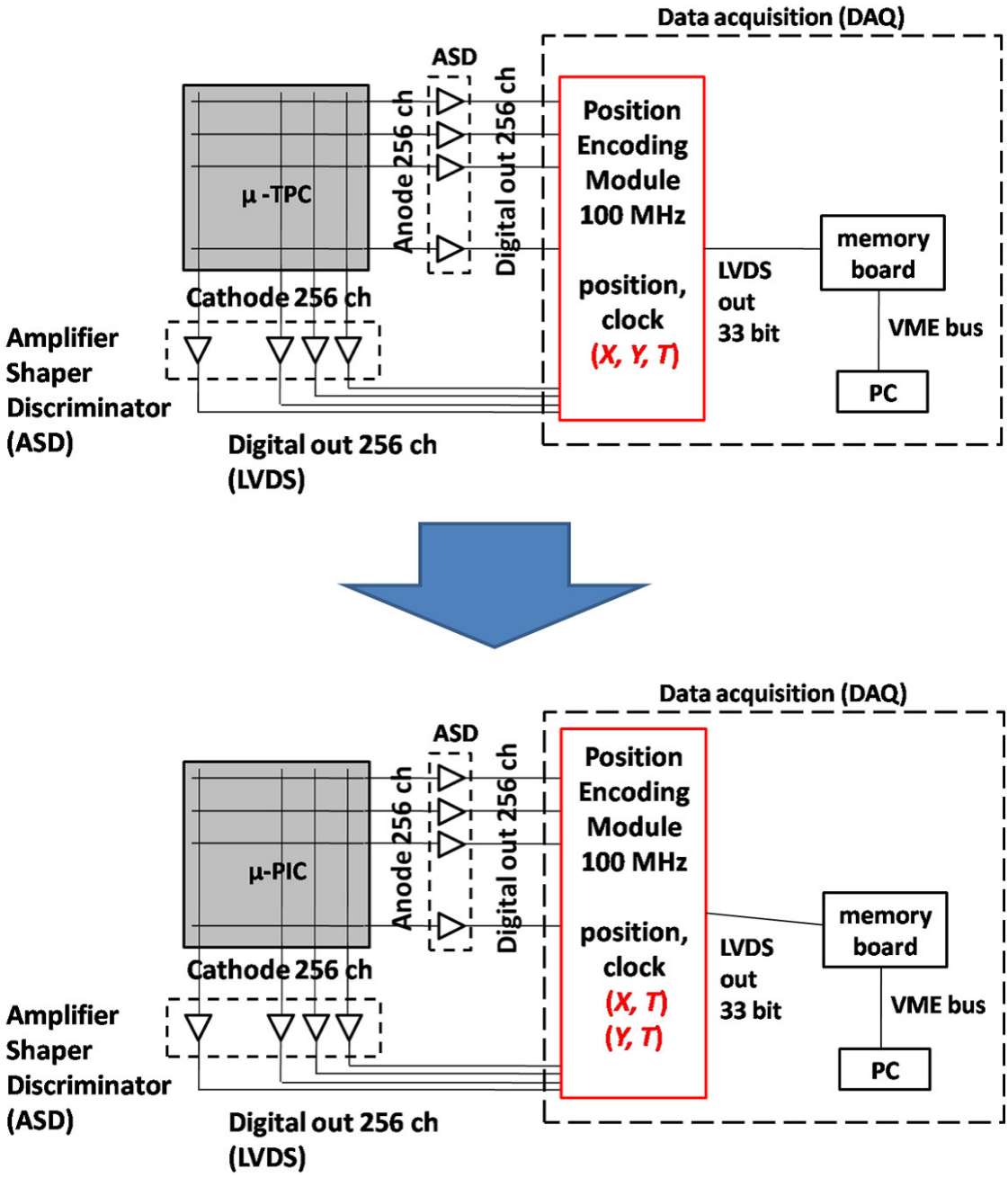

Figure 6.8: The old encoding mode (top) and the new one (bottom). X, Y, and T mean the hit point of anode, that of cathode, and the elapsed time, respectively.

was drastically improved by the TPC mode-II.

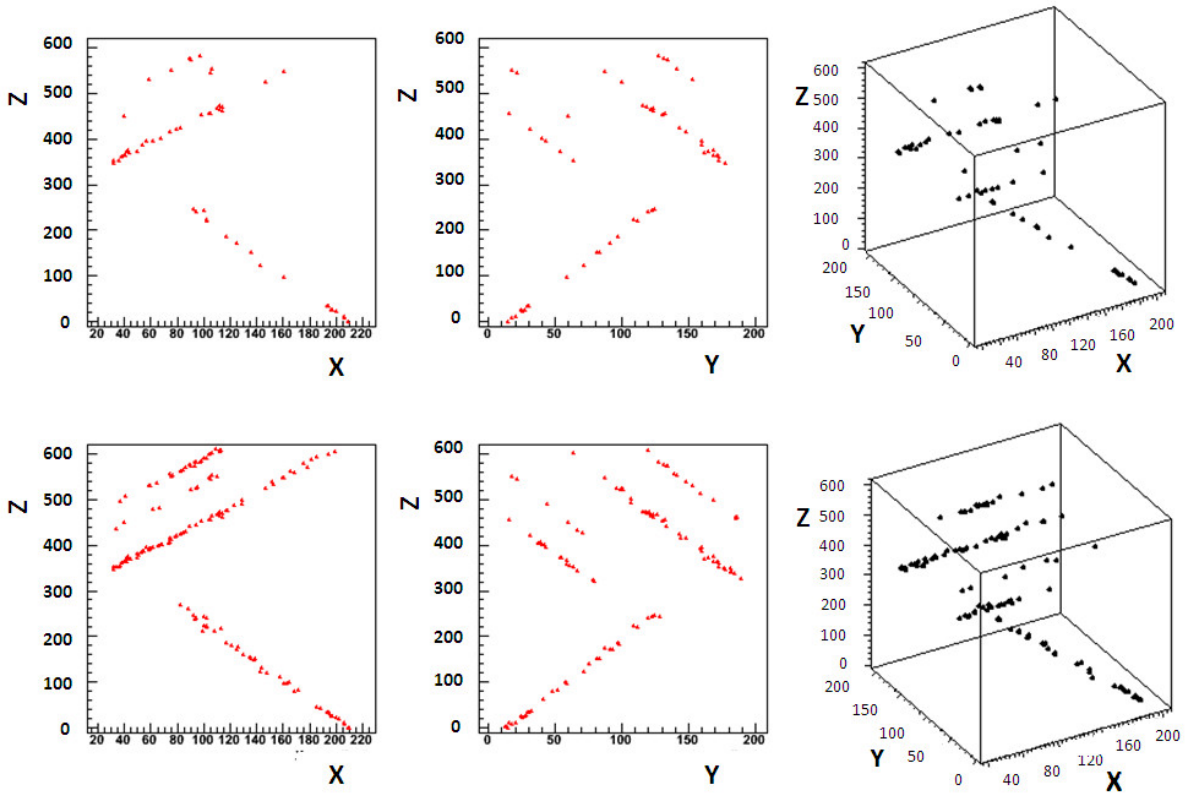

Figure 6.9: The tracks of cosmic muons. These are obtained by the old encoding mode (top) and the new TPC mode-II (bottom). X, Y, and Z are the strip numbers of the anode, that of the cathode, and the clock, respectively. In the bottom-right one, hit points from the anodes and cathodes when they coincide in two clocks interval are paired and plotted.

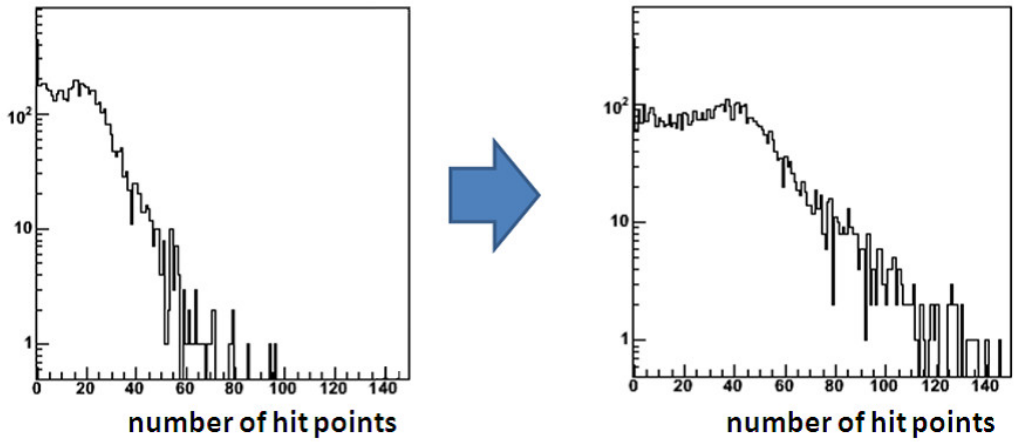

Figure 6.10: The numbers of hit points per cosmic muon with the old encoding mode (left) and the new TPC mode-II (right)

6.3 Performance of the μ-TPC

6.3.1 Gain uniformity

Gas vessel was filled with the gas mixture of Ar and C_2H_6 (90:10) at 1 atm. A drift voltage of -5.53 kV was supplied to the drift plane, which made a drift electric field of 0.32 kV/cm. The anode of the μ-PIC and the differential voltage of the top and bottom electrodes of GEM were 430 V and 300 V, respectively. The obtained gain uniformity is shown in Figure 6.11. The average of gas gain is about 3.6×10^4, and the RMS of the variation of the gain uniformity is 10.3 %.

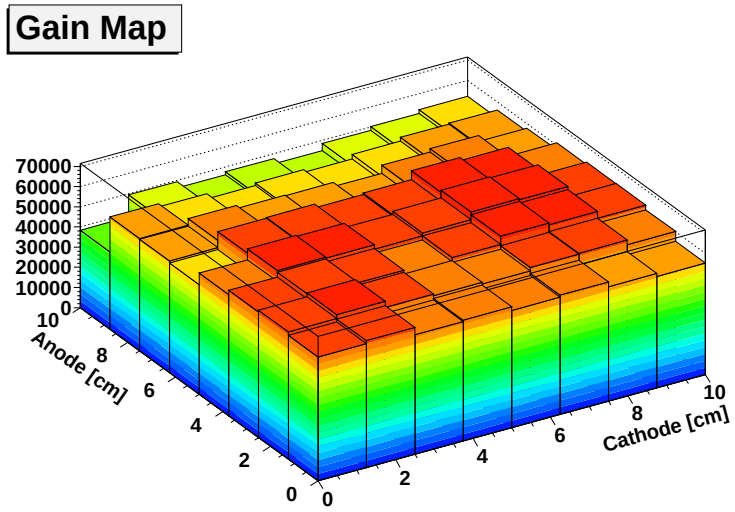

Figure 6.11: The gain uniformity of the μ-PIC of the pair mode telescope.

6.3.2 Energy resolution

Figure 6.12 is an obtained energy spectrum of the μ-TPC for ^{133}Ba source. Thus, the energy resolution of the μ-TPC were measured for the energy range between 8 and 31 keV using ^{109}Cd and ^{133}Ba sources. Figure 6.13 shows the energy resolution as a function of the energy of X-rays. The obtained energy resolution was 28 % (FWHM) at 31 keV. In Figure 6.13, the dashed line is obtained by fitting function described as follows,

$$\frac{\Delta E}{E}[\%] = 2.95 \times \left(\frac{E}{[\mathrm{keV}]}\right)^{-0.22}. \tag{6.1}$$

6.3.3 Drift velocity and position resolution

We measured the drift velocity of $10\times10\times15$ cm^3 μ-TPC using the cosmic muon. Figure 6.14 shows the distributions of the drift time of the anode and the cathode, where the drift region corresponds to the clock of 15 - 365 counts. The length of the drift region is about 14.5 cm, therefore the electron drift velocity is about 4.1 cm/μsec. Because the electric field in the drift region is 380 V/cm, the theoretical drift velocity is 4.1 cm/μsec from the calculation (Figure 6.15). Therefore, the measured velocity is well consistent to the Figure 6.15.

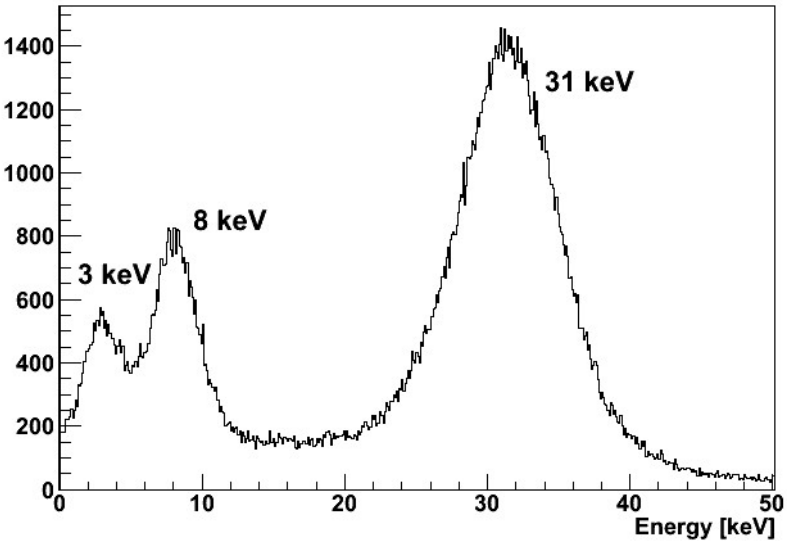

Figure 6.12: The typical energy spectrum of the X-rays from ^{133}Ba measured by the μ-TPC of the pair mode telescope.

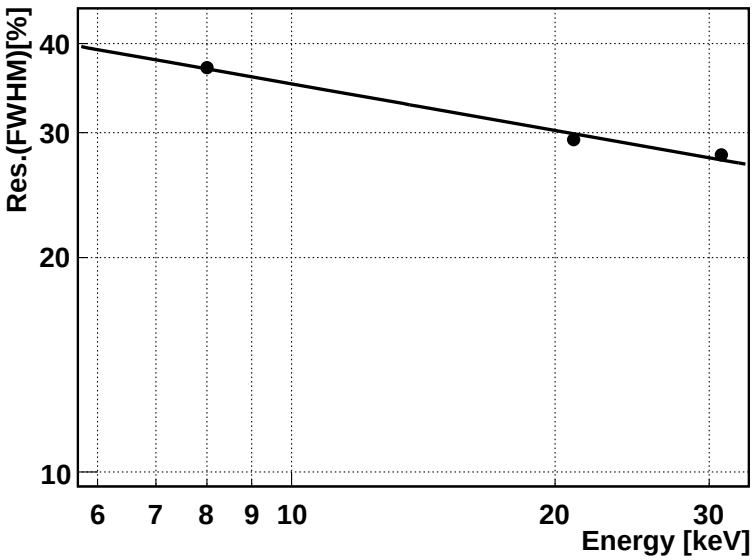

Figure 6.13: The energy resolution of the μ-TPC of the pair mode telescope.

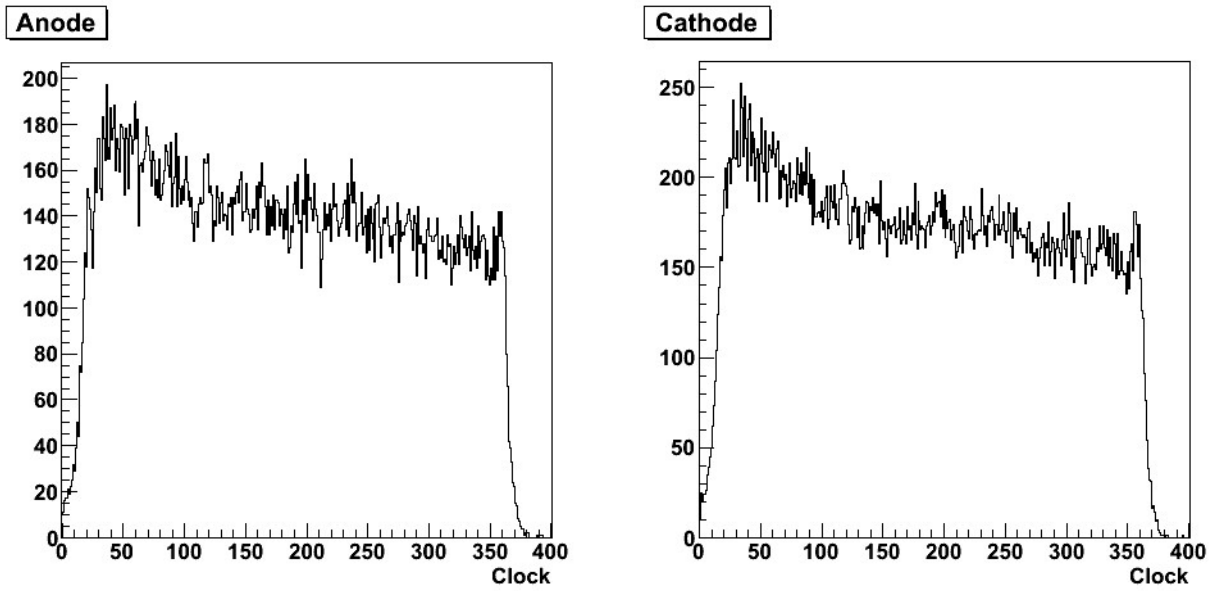

Figure 6.14: The histograms of the clock counter to the anode (left) and the cathode (right).

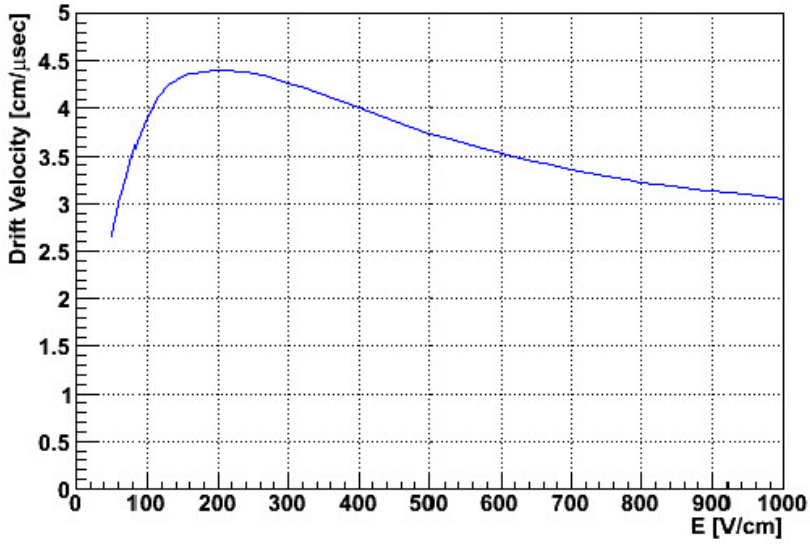

Figure 6.15: The drift velocity as a function of the electric field for the gas mixture of Ar and C_2H_6 (90:10) at 1 atm.

Typical muon tracks were reconstructed using the measured drift velocity. Using this result, we investigated the position resolution of the μ-TPC. Because the TPC mode-II was used, hit points of anodes and cathodes are obtained individually. We fitted the muon tracks with straight lines in anode planes, and the residual was calculated for each hit point. Figure 6.16 shows the histograms of the residual at the drift length of 8 - 9 cm. Each residual distribution was fitted by Gaussian, and we obtained the variance of Gaussian, σ^2. This is given in the same way as Equation (4.3) as follows,

$$\sigma^2(z) = \sigma_{det}^2 + (D\sqrt{z})^2, \tag{6.2}$$

where z, D, and σ_{det} are the drift length, the diffusion constant, and the detector intrinsic one-dimensional error term, respectively. Figure 6.17 shows σ as a function of drift length and fitted lines with Equation (6.2). As results of the fitting, $\sigma_{det} = 0.48\ mm$ and $D = 0.45mm/\sqrt{(}cm)$ were obtained.

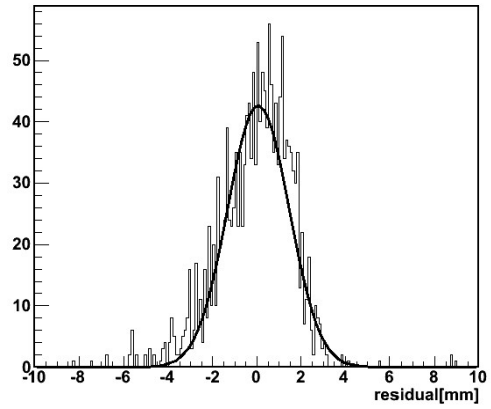

Figure 6.16: The histograms of residual between the obtained points and the fitted straight line at the drift length of 8 - 9 cm.

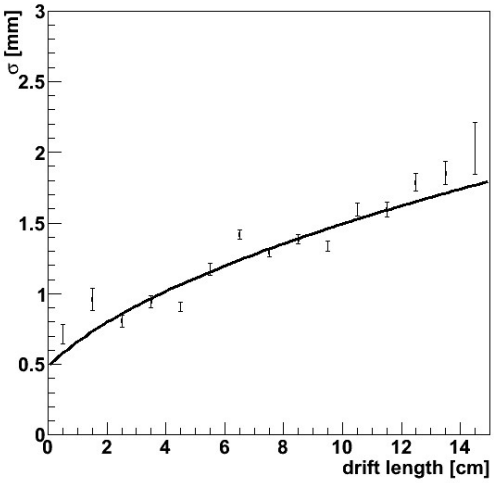

Figure 6.17: The one-dimensional position resolutions as a function of drift length.

6.4 Prototype telescope with pair creation mode

Using the 10×10×15 cm^3 μ-TPC and the 8 PSA units, we constructed the prototype gamma-ray telescope with pair creation mode as shown in Figure 6.18. The specifications of the scintillation camera and the μ-TPC in the prototype gamma-ray pair telescope are summarized in Table 6.1 and Table 6.2, respectively.

Table 6.1: The specification of the scintillation camera in prototype pair telescope.

Scintillator	GSO:Ce
PMT	Hamamatsu Photonics H8500
Pixel Size	$6 \times 6 \times 13$ mm^3
Camera Size	200 mm^2 (8 PMTs)
Energy Range	500 - 5000 keV
Energy Resolution	FWHM[%] $= 10.6 \times (E_\gamma/662 \text{ keV})^{-0.53}$

Table 6.2: The specification of the μ-TPC in prototype gamma-ray pair telescope

Gas	Ar 90 % + C_2H_6 10 %, gas sealed 1 atm
Volume	$10 \times 10 \times 15$ cm^3
Effective Volume	$10 \times 10 \times 14$ cm^3
Gas Gain	~ 36000
Drift Velocity	4.1 cm/μsec
Encoding Clock	100 MHz
Position Resolution	~ 480 μm
Energy Resolution	FWHM[%] $= 2.95 \times \left(\frac{E}{\text{keV}}\right)^{-0.22}$

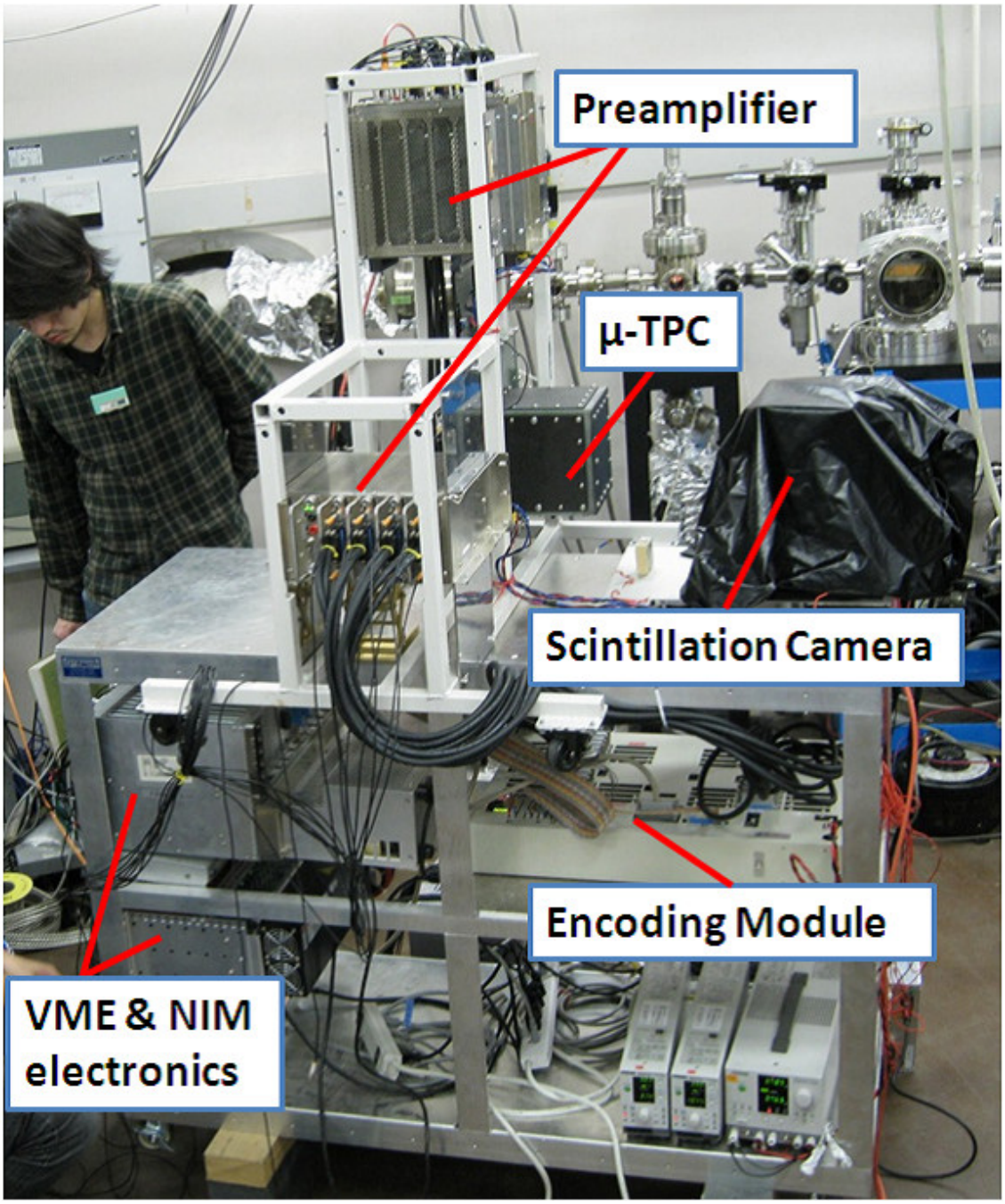

Figure 6.18: A photograph of the prototype of gamma-ray telescope with pair creation mode.

Chapter 7

Beam experiment

We performed a proof-of-principle experiment of our gamma-ray telescope with pair creation mode using a laser inverse Compton gamma-ray beam at National Institute of Advanced Industrial Science and Technology (AIST) Purposes of this experiment are to confirm our telescope can be used for the detection of pair creation events in the energy range of multi MeV and to investigate the fundamental performances.

7.1 Experimental setup

7.1.1 Laser-Compton scattering gamma ray

Although the measurement of the pair creation events needs at least more than about 5 MeV gamma rays, there are no commercial available radioactive sources emitting such high energy nuclear gamma rays. For example, the energy of gamma rays from ^{88}Y is at most 1.8 MeV. Therefore, the laser-Compton scattering (LCS) gamma-ray beam is an essential tool for this experiment.

The gamma-ray source of LCS was developed in the 1960's [65, 66], and it has been widely used for various scientific studies since 1990's [67–69]. The LCS gamma rays in the energy range from a few to several tens of MeV are produced with a high-energy electron storage ring and high-power laser system [70–72].

The energy of the LCS gamma ray, E_γ, is described as follows:

$$E_\gamma[MeV] = \frac{E_L(1-\beta cos\theta_1)}{1-\beta cos\theta_2 + \frac{E_L(1-\beta cos(\theta_2-\theta_1))}{E_e}}, \tag{7.1}$$

where $\beta = \sqrt{1-\gamma^2}$ and $\gamma = \frac{E_e[MeV]}{0.511}$. E_γ is a function of the collision and scattering angles θ_1 and θ_2. E_L and E_e are the energies of laser photon and electron, respectively. Because the gamma rays in the highest energy are scattered along the beam axis, they are easily monochromatized with a divergence-discrimination of low-energy photons by a collimator set on the beam axis [73].

7.1.2 AIST LCS gamma-ray facility

Currently, there are only three LCS gamma-ray beam lines in the world, which can be used as the cooperative research facility: Tsukuba Electron Ring for Acceleration and Storage (TERAS) at AIST, NewSUBARU at University of Hyogo, and High-Intensity Gamma-ray Source (HIGS) at Duke University. We carried out the beam experiment in AIST LCS gamma-ray facility. TERAS is the electron storage ring which stores 300 - 800 MeV electrons up to 300 mA. ND:YVO_4 laser system is usually operated in fundamental (1064 nm) and higher-harmonic modes up to third

order (532 nm for second and 266 nm for third harmonics in wavelength). Using this high-energy electron and this laser beam, the LCS beam facility serves 1 - 40 MeV quasi-monochromatic and energy-tunable gamma-ray beams of 10^6 photons $cm^{-2}s^{-1}$ at maximum [73, 74].

7.1.3 Setup of the prototype telescope

Figures 7.1, 7.2, and 7.3 are the photograph, the schematic view, and the top view of the experimental setup, respectively. We set up the gamma-ray telescope on the beam axis. The distance between the gamma-ray telescope and the originating point of the beam was 13 m. In order to monochromatize and focus the gamma-ray beam, two lead collimators with the thickness of 20 cm and 15 cm and the hole size of ϕ1.8 mm were put between the telescope and the originating point of the beam. The resulting beam diameter and the divergence were obtained to be 1.8 mm and 80 μ rad, respectively, at the position of the telescope. For the measurement of the relative intensity and the spectrum of the gamma-ray beam, NaI(Tl) scintillator with the size of ϕ20 cm $\times$ 30 cm was put on the downstream side of the telescope. The distance between the telescope and the NaI scintillator was 96.5 cm.

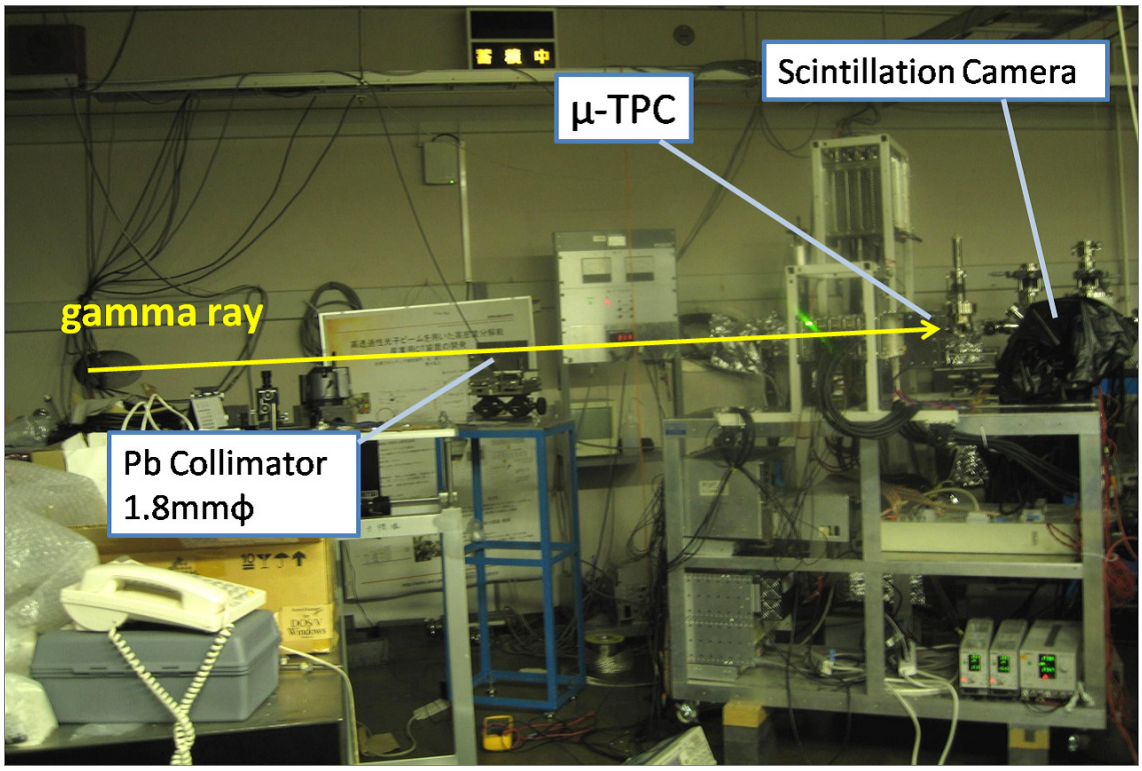

Figure 7.1: The photograph of the experimental setup.

7.2 Status of beam experiment

The experiment was carried out using the gamma-ray beams with the maximum energy of 10 MeV (Experiment 1) and 20 MeV (Experiment 2) on October 13th and 14th, 2009.

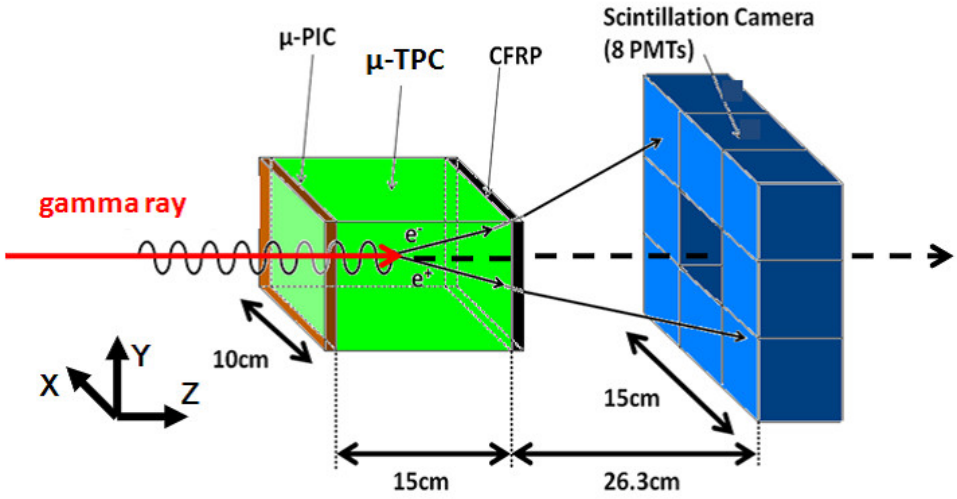

Figure 7.2: The schematic view of the experimental setup.

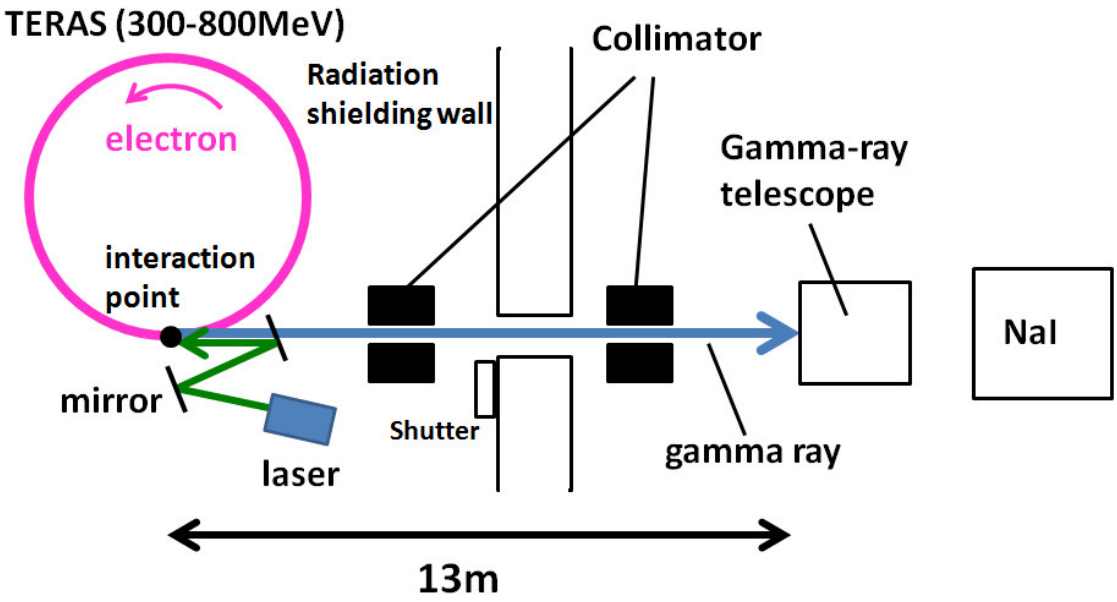

Figure 7.3: Top view of the experimental setup.

7.2.1 Experiment 1

At first, the TERAS accumulated 762 MeV electrons with 220 mA. Here ND:YVO_4 laser with the wavelength of 1064 nm and the power of 1 W was used. This combination makes 10 MeV gamma rays at maximum energy. The storage current was monitored with a DC current transformer. The decay curve of the stored current is shown in Figure 7.4. In order to measure the relative intensity of only RCS gamma rays, we set the energy window above 4 MeV for the NaI counter. Figure 7.5 shows the measured rate of the NaI counter. During the Experiment 1, the beam rate decreased from 3.6 kHz to 3 kHz. The DAQ trigger rate and the DAQ live time ratio to the real measured time were also obtained as shown in Figure 7.6. The mean trigger rate and the mean ratio of the live time in the Experiment 1 were 74 Hz and 50 %, respectively. The gamma-ray flux was examined in the past on a similar condition [73] and given by 77.3 $gammaW^{-1}mA^{-1}s^{-1}$. Thus, in this experiment, the total photon number was estimated to be about 8.0×10^7 in measurement time (187 minute).

Figure 7.7 shows the obtained spectrum measured by NaI, where we can see several peaks due to the background emission, for example 2.6 MeV from ^{208}Tl and 1.5 MeV from ^{40}K. In this figure, we obtained the mean energy of the incident gamma rays, which the value is 8.7 MeV.

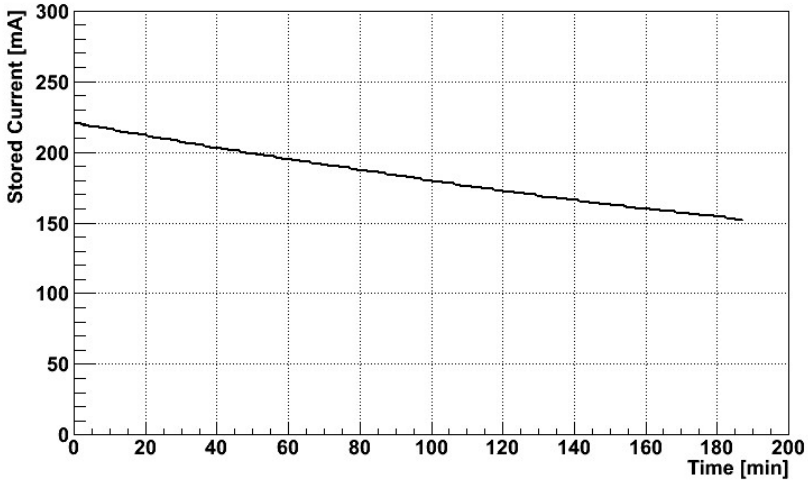

Figure 7.4: The decay curve of stored current. (Experiment 1)

7.2.2 Experiment 2

Next, the TERAS accumulated electrons with the same energy as those in Experiment 1 by 250 mA. The wavelength of the laser was changed to 532 nm by the two-photon linear crystal, and we obtained 20 MeV LCS gamma rays at the maximum energy. The decay curve of the stored current is shown in Figure 7.8. Figure 7.9 shows the NaI hit rate. During the Experiment 2, the beam rate decrease from 1.1 kHz to 0.9 kHz. The DAQ trigger rate and the DAQ live time ratio to the real measured time were also obtained as shown in Figure 7.10. The mean trigger rate and the mean ratio of the live time in the Experiment 1 were 64 Hz and 47 %, respectively. The total photon number was estimated to be about 2.9×10^7 in measurement time (176 minute).

The energy spectrum of the 20 MeV LCS gamma rays also measured as shown in Figure 7.11. In this figure, the mean energy of the incident gamma rays is 18.0 MeV.

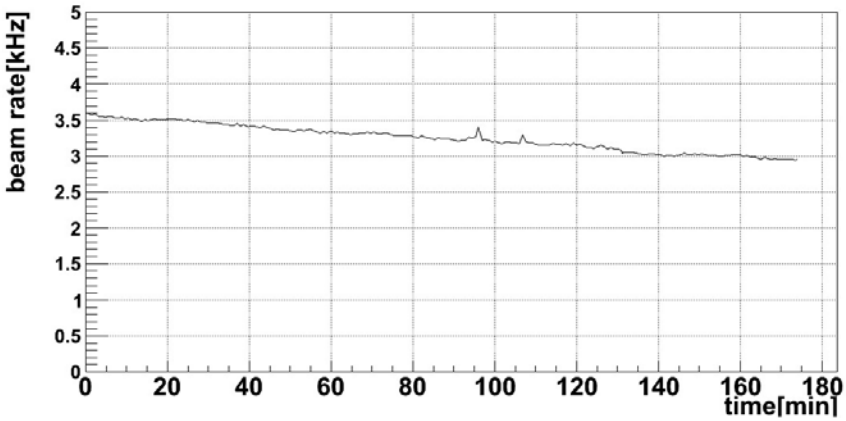

Figure 7.5: NaI hit rate. (Experiment 1)

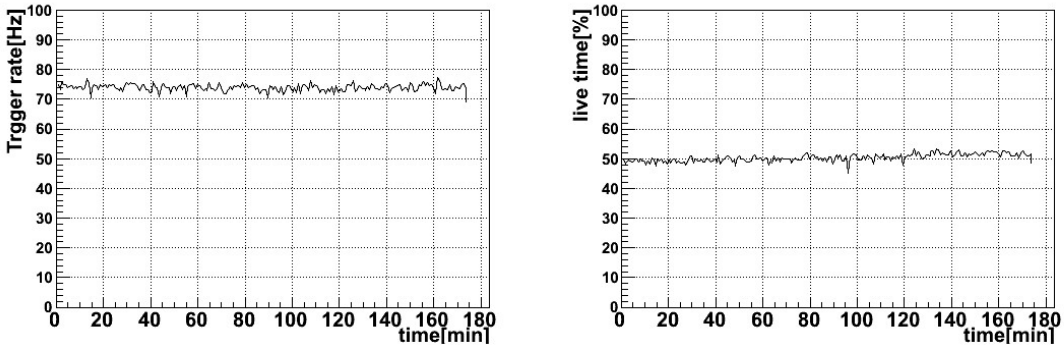

Figure 7.6: The DAQ trigger rate (left) and the ratio of the DAQ live time to the real measured time (right). (Experiment 1)

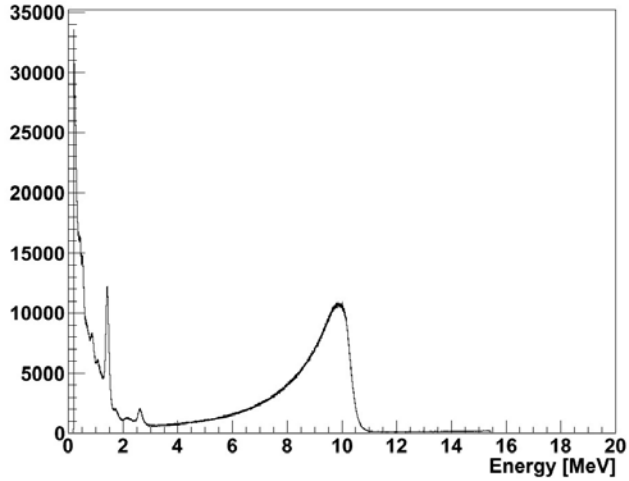

Figure 7.7: The energy spectrum of the 10 MeV LCS gamma rays measured by NaI. The mean energy of LCS gamma rays is 8.7 MeV.

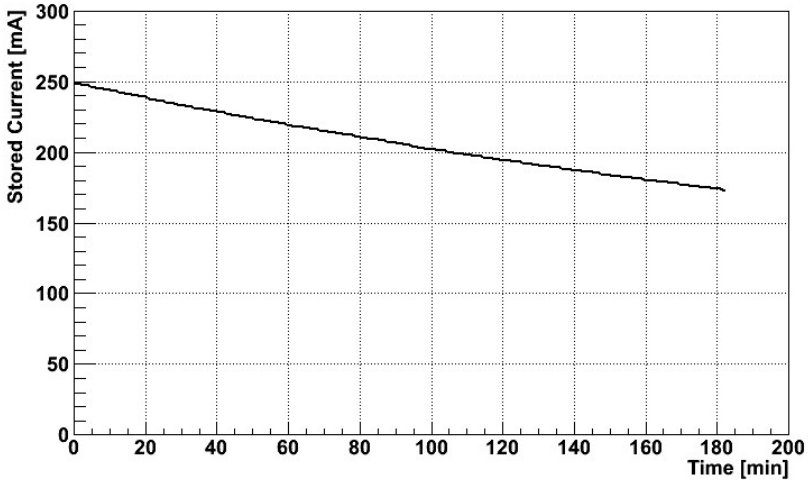

Figure 7.8: The decay curve of stored current. (Experiment 2)

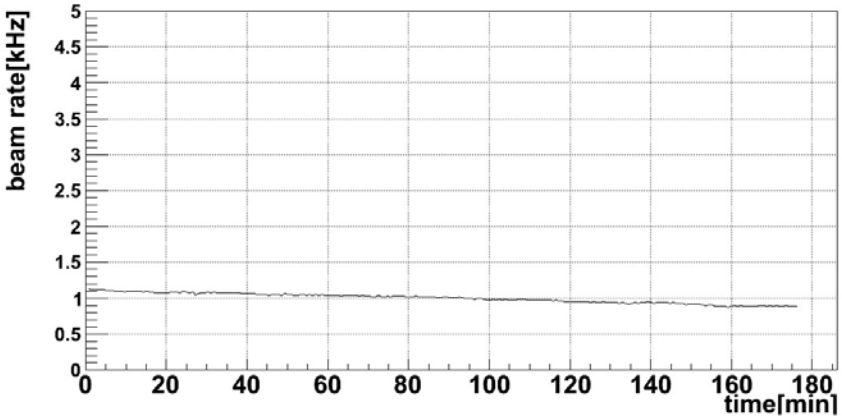

Figure 7.9: NaI hit rate. (Experiment 2)

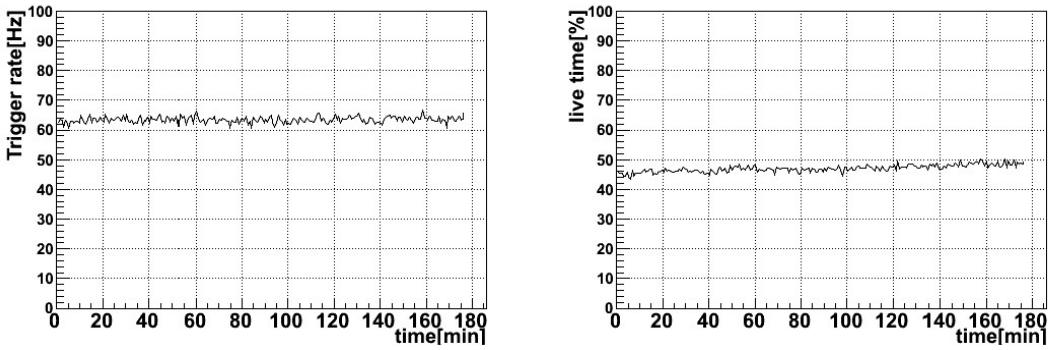

Figure 7.10: The DAQ trigger rate (left) and the ratio of the DAQ live time to the real measured time (right). (Experiment 2)

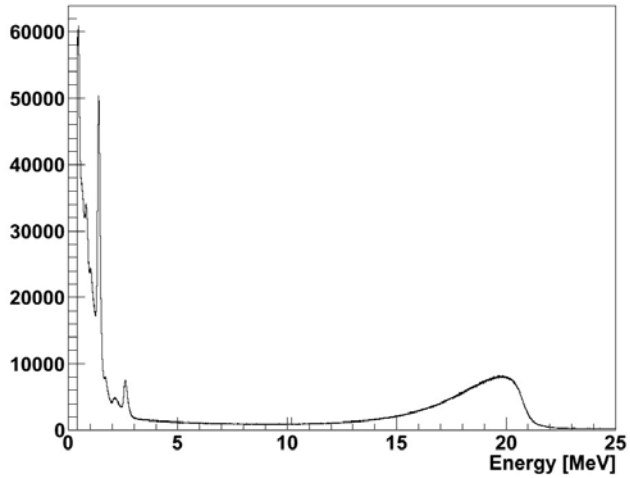

Figure 7.11: The energy spectrum of the 20 MeV LCS gamma rays measured by NaI. The mean energy of the incident gamma rays is 18.0 MeV.

7.2.3 Run summary

The run properties are summarized in Table 7.1.

Table 7.1: Run summary of the beam experiment using the prototype pair telescope.

run	maximum energy	mean energy	live time	photon number
Experiment 1	10 MeV	8.7 MeV	5580 sec.	8.0×10^7
Experiment 2	20 MeV	18.0 MeV	4980 sec.	2.9×10^7

Chapter 8

Event reconstruction

Although tracks of electron-positron pair creation and those of charged particles look to generate the different hit patterns in the gamma-ray telescope, it is not so easy to find true electron-positron events due to a large number of hit points in the μ-TPC. Then, we have developed two methods including both the track finding and the event reconstruction for the pair creation event. At first, we carried out the track finding and the event reconstruction using a simple clustering method, and confirmed the validity of it applying to the experimental data. However, this method is not enough to reconstruct all events because its efficiency depends on the direction of the incident gamma ray, and hence hit points near the vertex point cannot be used. Therefore, we developed a new tool using Hough transform. Here we assume that the incident energy of gamma ray is a known parameter in the present work.

In this chapter, we describe the details of the track finding and the reconstruction methods, and then confirm the validity of that method using simulation data.

8.1 Clustering method

In the pair-creation event, an electron and positron pair makes the hit pattern like a "V" character shape in the μ-TPC. In the clustering method, the data region in the μ-TPC is divided to two regions along the gamma-ray beam as shown in Figure 8.1, and then two clusters are usually found in the region of down-stream side. Each cluster is fitted by the straight line. If only one cluster is found, the event is regarded as a small opening angle event, and the hit points of the cluster is fitted by the one straight line. Here, we have to note that since we know the direction of the incident gamma rays from the beam line, above division of the region easily can be defined. However, for the actual experiment, we have to develop some method to find it.

In following subsections, the outline of the clustering method, and the details of each step of the outline are explained.

8.1.1 Outline of the clustering method

Because the incident gamma rays come along the Z-axis in this experiment, we can deal with the data as two 2-dimensional data projected on X-Z and Y-Z planes, respectively. In those two planes, vectors are defined in the clusters and reconstructed as below.

Figure 8.2 shows the flow chart of the clustering method. Firstly, for the obtained event, we select the true hit points roughly as described in subsection 8.1.2. Then, we carry out the cluster-finding for the selected event in both X-Z and Y-Z planes. The event is distinguished between large and small opening angle events as described in subsection 8.1.3. Next, using the obtained clusters, the vector which electron-positron pair makes and the vertex point is determined for the large and small opening angles separately (subsection 8.1.4 and 8.1.5). Using

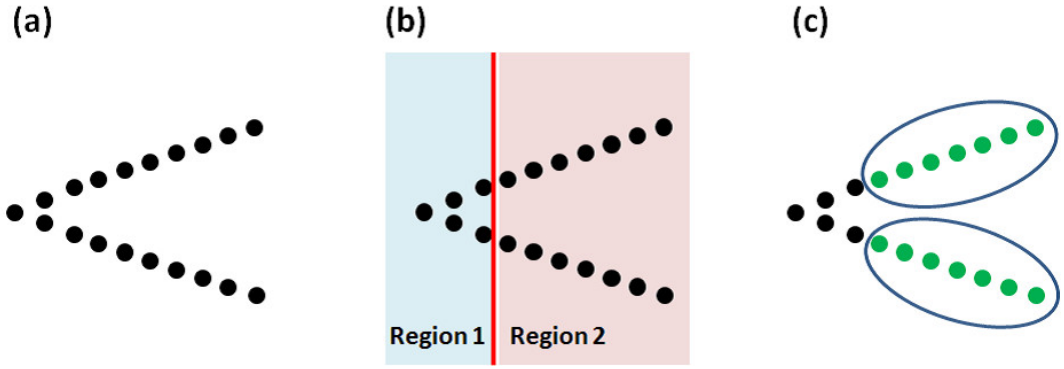

Figure 8.1: The concept of track finding in the clustering method. Hit points of an electron and positron pair (a) are divided by two regions (b), and then two clusters are found (c).

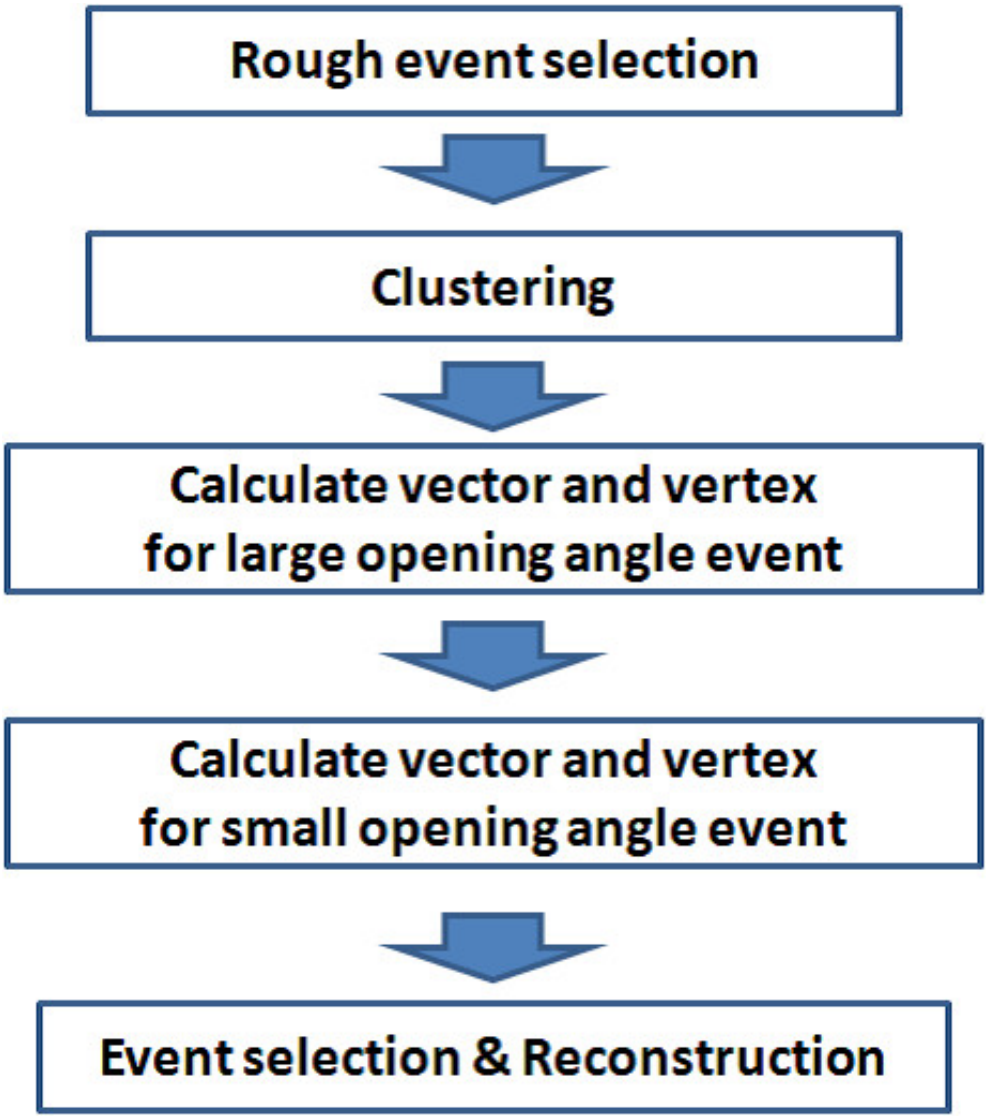

Figure 8.2: The flow chart of clustering method.

the obtained vertex point, the true event is selected. Finally, the direction of the incident gamma ray is calculated using the vector and the vertex (subsection 8.1.6).

8.1.2 Rough event selection

In the experiment, we obtain the data set (x_i, z_i) and (y_j, z_j) $(i = 1, 2, \cdots, n, j = 1, 2, \cdots, m$, n and m are the number of hit points) in X-Z plane and Y-Z plane, respectively.

At first, we roughly check whether the event is interacted in the gas. In order to reject the events generated in the vessel material or out of the vessel, the fiducial volume in the TPC is defined. True pair creation event at least has to have no hit points out of the fiducial volume on the beam-upstream side. The fiducial volume in X-Z plane is defined as follows:

$$-4.6[cm] < x < 4.6[cm], \tag{8.1}$$

$$2.4[cm] < z < 14.4[cm]. \tag{8.2}$$

Same fiducial area is defined for Y-Z plane:

$$-4.6[cm] < y < 4.6[cm], \tag{8.3}$$

$$2.4[cm] < z < 14.4[cm]. \tag{8.4}$$

If the hit points on the beam-upstream side are out of the fiducial volume, the event is rejected as shown in Figure 8.3.

8.1.3 Clustering

Next, we group the hit points to one or two clusters. In order to classify the events, the hit points are grouped in two regions, beam-upstream and beam-downstream sides. The region of beam-downstream side is defined as the clustering region as shown in Figure 8.4, and satisfies the condition as follows:

$$\frac{z_{cog} + z_0}{2} < z < z_{max}, \tag{8.5}$$

where z_0 and z_{max} are the edge of the fiducial volume on the beam-upstream and beam-downstream side, respectively. z_{cog} is the center of gravity of the z-element of all hit points, which is given by

$$z_{cog} = \frac{\sum_{i=1}^{n} z_i}{n}. \tag{8.6}$$

The hit points in the clustering region are clustered.

Figure 8.5 shows the steps of the clustering. As the first step of clustering, X-Z (Y-Z) plane is divided into $S \times T$ areas, and each part of the areas is tagged as (X_p, Z_q) $(p = 1, 2, \cdots, S, q = 1, 2, \cdots, T)$. S and T are determined by the resolution of the detector. In this experiment, $S = 128$ and $T = 10$ are used. Then, if there are the hit points in (X_p, Z_q), the flag is attached to the area:

$$f(X_p, Z_q) = 1. \tag{8.7}$$

After attaching the flag, whole area is scanned and the neighbor region which has the flag are grouped:

$$\begin{aligned} & f(X_p, Z_q) - f(X_{p\pm1}, Z_{q\pm1}) = 0, \\ \cup\ & f(X_p, Z_q) - f(X_{p\pm1}, Z_{q\mp1}) = 0, \\ \cup\ & f(X_p, Z_q) - f(X_{p\pm1}, Z_q) = 0, \\ \cup\ & f(X_p, Z_q) - f(X_p, Z_{q\pm1}) = 0, \\ \Longrightarrow\ & C_a \ni ((X_p, Z_q), (X_\alpha, Z_\beta))(\alpha = p, p \pm 1, \beta = q, q \pm 1)), \end{aligned} \tag{8.8}$$

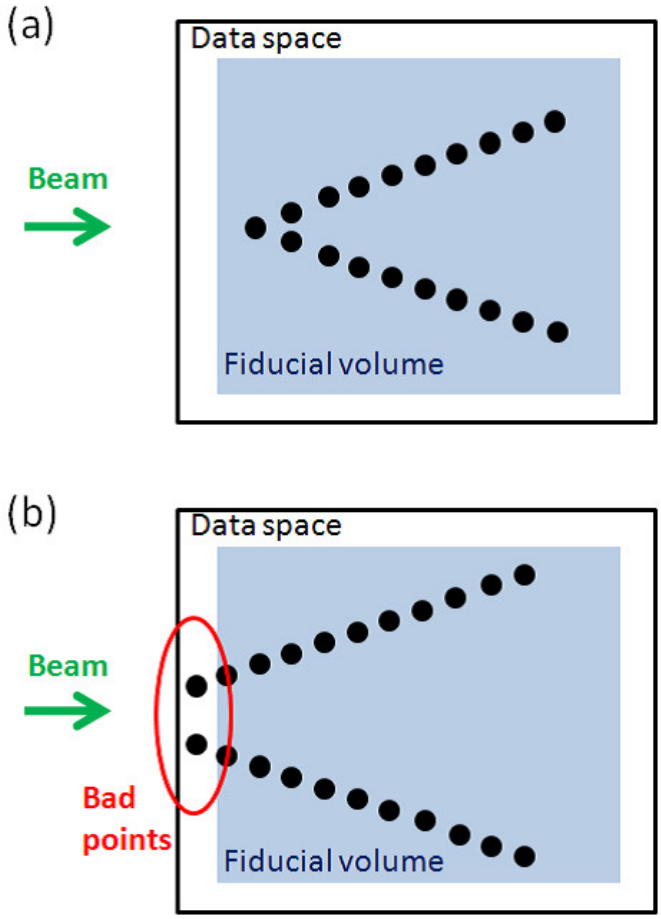

Figure 8.3: Rough event selection. (a) All hit points of true pair creation event are in fiducial volume. (b) If there are hit points out of the fiducial volume, the event is rejected.

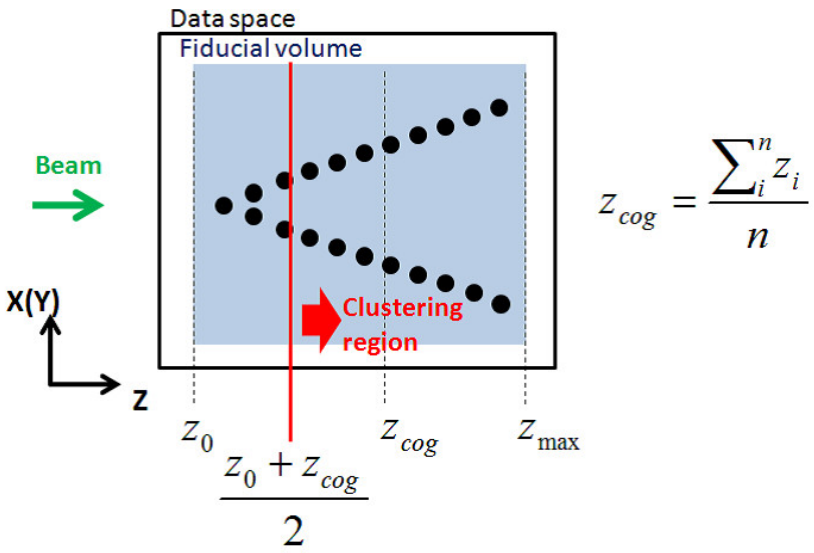

Figure 8.4: The definition of the clustering region corresponding to the region of beam-downstream side.

where C_a and a are the cluster and its number, respectively. Finally, the clusters are permuted in order by the numbers of hit points in the cluster. Eventually, the maximum cluster is tagged as C_1, the second cluster is tagged as C_2, and so on.

If there are two or more clusters after clustering, the event is regarded as the large opening angle one. On the other hand, if only one cluster is found, the event is regarded as the small opening angle one. In following next 2 subsections, we treat the event with two or more clusters and one cluster separately.

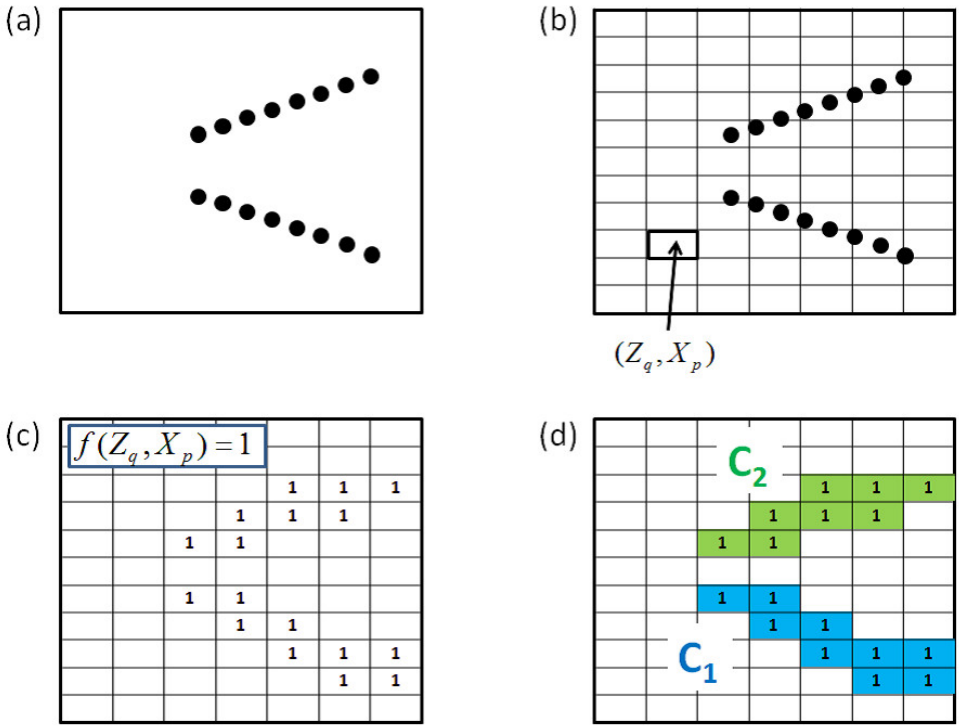

Figure 8.5: The example of clustering. (a) The hit points in the clustering region are obtained. (b) X-Z (Y-Z) plane is divided by S × T regions and each area is tagged as (Z_q, X_p) $(p = 1, 2, \cdots, S, q = 1, 2, \cdots, T)$. (c) If there exist hit points in (Z_q, X_p), $f(Z_q, X_p) = 1$ is applied. (d) Neighboring regions are clustered. C_1 and C_2 are the maximum and secondary maximum clusters, respectively.

8.1.4 Calculation of vector and vertex point of electron-positron pair for two or more clusters event

At first, we determine the vertex point of electron-positron pair, and then the vector of the incident gamma ray in X-Z and Y-Z planes for the two or more clusters event are defined.

The hit points in C_1 and C_2 in X-Z plane are fitted with straight lines respectively as follows,

$$x = sz + t \ (in\ C_1), \tag{8.9}$$

$$x = uz + w \ (in\ C_2), \tag{8.10}$$

where s, t, u, and w are free parameters. The cross point, (x_{verXZ}, z_{verXZ}), of two fitting lines is calculated by (8.9) and (8.10). This cross point is considered as the vertex point, if the event is the true pair creation event. For Y-Z plane, the fitting lines and the cross point, (y_{verYZ}, z_{verYZ}), are also calculated.

The unit vectors of the incident gamma ray in X-Z and Y-Z planes are calculated. The incident gamma-ray vector projected to the X-Z plane, $\vec{e}_{XZ}$, is calculated by two fitting lines in Equation (8.9 and 8.10). The vector $\vec{e}_{YZ}$ is also calculated in Y-Z plane. Using Equation (3.18), we obtain the vector:

$$\vec{e}_{XZ} = \vec{e}_{pXZ} + \vec{e}_{eXZ}, \tag{8.11}$$
$$\vec{e}_{YZ} = \vec{e}_{pYZ} + \vec{e}_{eYZ}, \tag{8.12}$$

where $\vec{e}_{pXZ}$, $\vec{e}_{eXZ}$, $\vec{e}_{pYZ}$, and $\vec{e}_{eYZ}$ are the unit vectors of the positron and electron in X-Z and Y-Z planes respectively. Note that whether the origin of each track is the electron or positron cannot be distinguished.

8.1.5 Calculation of vector and vertex point of electron-positron pair for one cluster event

Next, we calculate the vertex point of the electron-positron pair and the vector of the incident gamma ray in X-Z and Y-Z planes for the one cluster event.

The hit points in C_1 in X-Z plane are fitted with one straight lines using Equation (8.9), If the event with the one cluster is a true pair-creation one, the pattern of hit points is like a straight line (but slightly near the "V" shape). In order to reject the event which is not obviously the true one, we apply two selection to the fitted event. One is the χ^2 cut for rejection of the event which is not rectilinear. If reduced $\chi^2 > 15$, the event is rejected. The other is the "V" shape selection for rejection of the event which is not near the "V" shape. We require that the electron and positron tracks are consistent with a "V-like" shape. To find "V-like" event, we use the selection parameter, R, defined by:

$$R = \frac{\sigma_d}{\sigma_u}, \tag{8.13}$$

where, σ_d and σ_u are the root mean squares of the residual distributions from the single-line fit for hit points on the downstream side and upstream side of the center of gravity for the electron-positron track, respectively. If R $>$ 1, the event is considered to be "V"-like. The event which R $\leq$1 is rejected.

For the survived event, the point of the upstream side edge is considered to the vertex point, (x_{verXZ}, z_{verXZ}). For Y-Z plane, the cluster is fitted and the vertex point, (y_{verYZ}, z_{verYZ}), is calculated as well as X-Z plane.

The projected vectors of the incident gamma ray, $\vec{e}_{XZ}$ and $\vec{e}_{YZ}$ in X-Z and Y-Z planes, respectively, are given by the fitting lines and the vertex points as mentioned in 8.1.4.

8.1.6 Event selection

In order to select out the true pair creation event interacted in the μ-TPC, we apply two event selections to the event passed the above selections, fiducial and vertex cut.

The vertex point of the pair creation event must be in the fiducial volume of the μ-TPC, and its vertex point in X-Z plane is satisfied following conditions,

$$-4.6[cm] < x_{verXZ} < 4.6[cm], \tag{8.14}$$
$$2.4[cm] < z_{verXZ} < 14.4[cm]. \tag{8.15}$$

These conditions are also similar for the vertex point in Y-Z plane:

$$-4.6[cm] < y_{verYZ} < 4.6[cm], \tag{8.16}$$
$$2.4[cm] < z_{verYZ} < 14.4[cm]. \tag{8.17}$$

When the vertex point does not satisfy these conditions, the event is rejected.

Ideally, z-coordinate of the vertex point on X-Z and Y-Z planes should be equal to $z_{verXZ} - z_{verYZ} = 0$. However, due to the position resolution of the μ-TPC and the accuracies of the clustering and fitting, the events which satisfy the following conditions are selected as the pair creation events.

$$z_{verXZ} - z_{verYZ} < \sigma_{ver}, \tag{8.18}$$

where σ_{ver} is the standard deviation of the distribution of $z_{verXZ} - z_{verYZ}$.

The event which passes through above steps is considered as a pair creation event. The unit vector of the incident gamma ray, $\vec{e}_{Inc}$ is given by $\vec{e}_{XZ}$ and $\vec{e}_{YZ}$:

$$\vec{e}_{Inc} = \frac{\vec{e}_{XZ} + \frac{(\vec{e}_{XZ})_Z}{(\vec{e}_{YZ})_Z}\vec{e}_{YZ}}{\left|\vec{e}_{XZ} + \frac{(\vec{e}_{XZ})_Z}{(\vec{e}_{YZ})_Z}\vec{e}_{YZ}\right|}. \tag{8.19}$$

Here, $(\vec{e}_{XZ})_Z$ and $(\vec{e}_{YZ})_Z$ are the z-element of $\vec{e}_{XZ}$ and $\vec{e}_{YZ}$, respectively.

8.2 Hough transform method

Hough transform method is more versatile for the reconstruction of incident gamma rays than clustering method, which is independent of the incident gamma ray direction. Hough transform [75, 76] is one of the feature extraction technique used in digital image processing. The purpose of this technique is to identify the characteristic shape like a line, a circle, and so on in the image. There are few examples using the technique for the astrophysics. More details of the technique will be explained in next subsection. In the Hough transform method, two lines which compose "V" character shape are identified in the data plane. If the event has a small opening angle, only one line is found using the same method. Each line is used for the event reconstruction after the event selection.

8.2.1 Hough transform

At first, we describe the principle of Hough transform using the simple example for detecting one straight line.

For any one point in the image, there is infinite number of straight lines which pass through this point in the any direction. It is the basic principle of the Hough transform. The purpose of the Hough transform is to find the best line in all lines, which pass through the "characteristic point" in the image This line suits the one which we find intuitionally in the image. In order to confirm which lines pass through the "characteristic point", parameterization of the lines is used. In the normal Hough transform, the line in the data space (X-Y plane) is expressed using two parameters, r and θ, as follows:

$$r = x\cos\theta + y\sin\theta, \tag{8.20}$$

where (x, y) is the data point passed through by the line in the X-Y plane. It is noted that r and θ correspond to the distance between the line and the origin and the angle of the vector from the origin to this closest point, respectively, as shown in Figure 8.6.

The set of (r, θ) is able to associate with each line in the data space, which is unique if $\theta \in [0, \pi]$ and $r \in \mathbb{R}$ or if $\theta \in [0, 2\pi]$ and $r \geq 0$. The r-θ plane is referred to as Hough space for the set of straight lines. As described above, an infinite number of lines can pass through one point in X-Y plane.

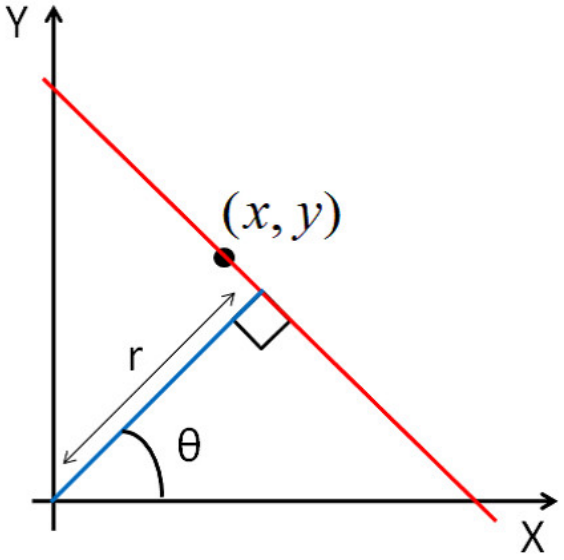

Figure 8.6: The example of the parameterized line with r and θ in X-Y plane.

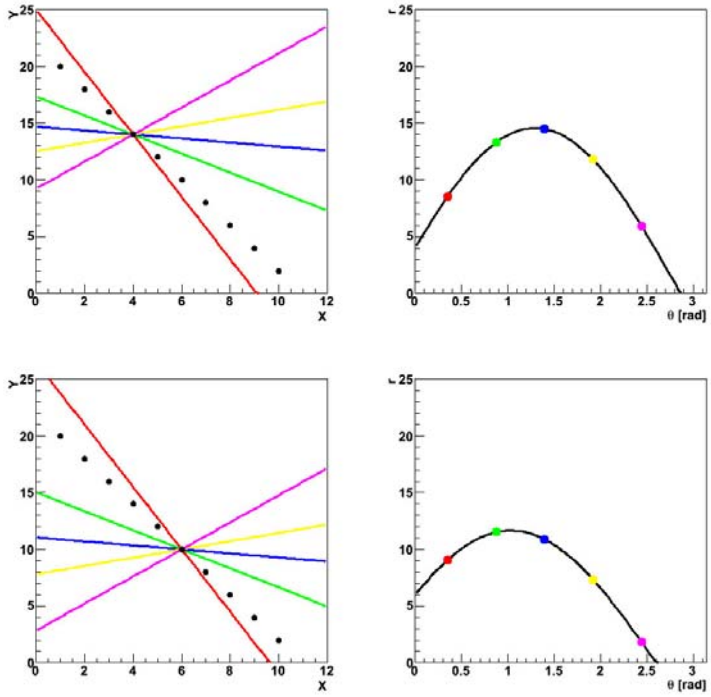

Figure 8.7: Two examples of the $r(\theta)$ in the r-θ plane (right) corresponding to all lines passing through the one point in X-Y plane (left). Each line in the X-Y plane (left) corresponds to each point on the sine curve as the same color in r-θ plane (right).

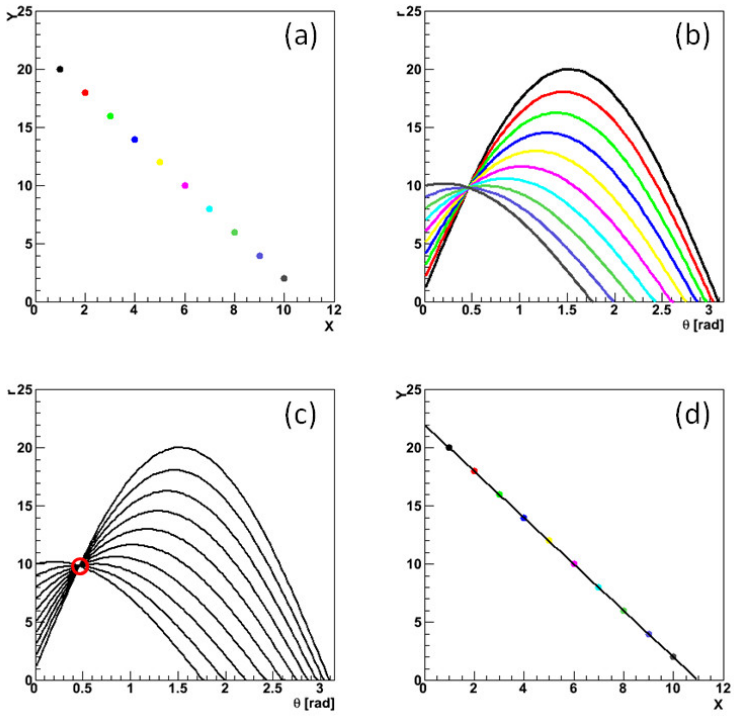

Figure 8.8: The example of the Hough transform.

If there are the data set of (x_i, y_i) $(i = 1, 2, \cdots, n,$ n is the number of the point) in the data space, all the lines going through each point obey the following equation:

$$r(\theta) = x_i \cos\theta + y_i \sin\theta. \tag{8.21}$$

This $r(\theta)$ corresponds to a sine curve in the r-θ plane, which is unique to each point in X-Y plane as shown in Figure 8.7. If the curves corresponding to data points are superimposed, the point where all sine curves cross in Hough space corresponds to the line in X-Y plane which passes through the all points in the data space as shown in Figure 8.8. After all, the set of the points on the line in the data space produce the set of the sine curves which cross at the parameter for that line. In (a) of Figure 8.8, we consider that there are 10 points in the data space (X-Y plane). For each point, the sine curve, $r(\theta)$, corresponding to the lines passing through the point is given by Equation (8.21). Each sine curve in the Hough space corresponding to each point in the data space is plotted using the same color as shown in (b). In the Hough space, the peak corresponding to the intersection point of sine curves is found, and then the set of (r, θ) is given as shown in (c). From this (r, θ), we obtain the line as follows:

$$y = -\frac{1}{\tan\theta}x + \frac{r}{\sin\theta} \ (\theta \neq 0), \tag{8.22}$$

$$x = r \ (\theta = 0). \tag{8.23}$$

This line passes through all points in the data space as shown in (d).

It is not always true that there is the complete straight line in the data for using the Hough transform. Therefore, usually the Hough space is quantized to some bins and the voting procedure for each bin is used. Each point in the data space votes all bins passed through by sine curve. After voting of all data points, the maximum bin corresponds to the most likely line which passes through all points. Thus, by finding the peak (maximum bin) in the quantized

Hough space, we get the approximate line which passes through all points. The simplest way of finding peaks is by applying some form of threshold. However, different technique may yield better result in different circumstances, for example in our experiment. The example for the event as described above is shown in Figure 8.9. In (a) of Figure 8.9, we consider that there are 11 points in the data space (X-Y plane) which do not make the line pattern and include a noise point. For each point, the sine curve, $r(\theta)$, is given as well as Figure 8.8. Each sine curve in the Hough space corresponding to each point in the data space is plotted using the same color as shown in (b). Hough space is quantized and each bin in it is voted by the sine curves as shown in (c). The peak (maximum bin) is found in (c), and then the set of (r, θ) is given. From the (r, θ), we obtain the line in the data space using Equation (8.22) as shown in (d). This line is the most likely line which passes through all points except for noise. This example shows that the Hough transform is quite effective for the data including noise points.

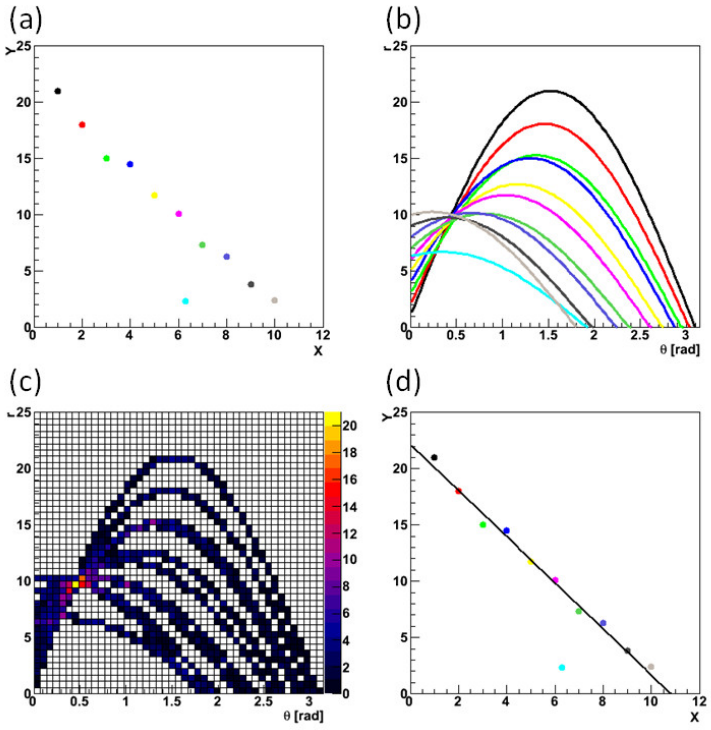

Figure 8.9: The example of the Hough transform.

8.2.2 Outline of the Hough transform method

As well as subsection 8.1.1, only the vectors of the electron and the positron are used for the event reconstruction. Coordinate system of the data space is also the same as that in 8.1.1.

Figure 8.10 shows the flow chart of the Hough transform method. Firstly, for the obtained event, we apply the Hough transform and distinguish the event between large and small opening angle events by means of the result of the Hough transform. The details of this step will be described in subsection 8.2.3. Next, as well as the clustering method, the vector which electron-positron pair makes and the vertex point are calculated for the large and small opening angle separately (subsection 8.2.4 and 8.2.5). Using the obtained vertex point, the true event is selected. Finally, the direction of the incident gamma ray is calculated using the vector and the vertex (subsection 8.2.6).

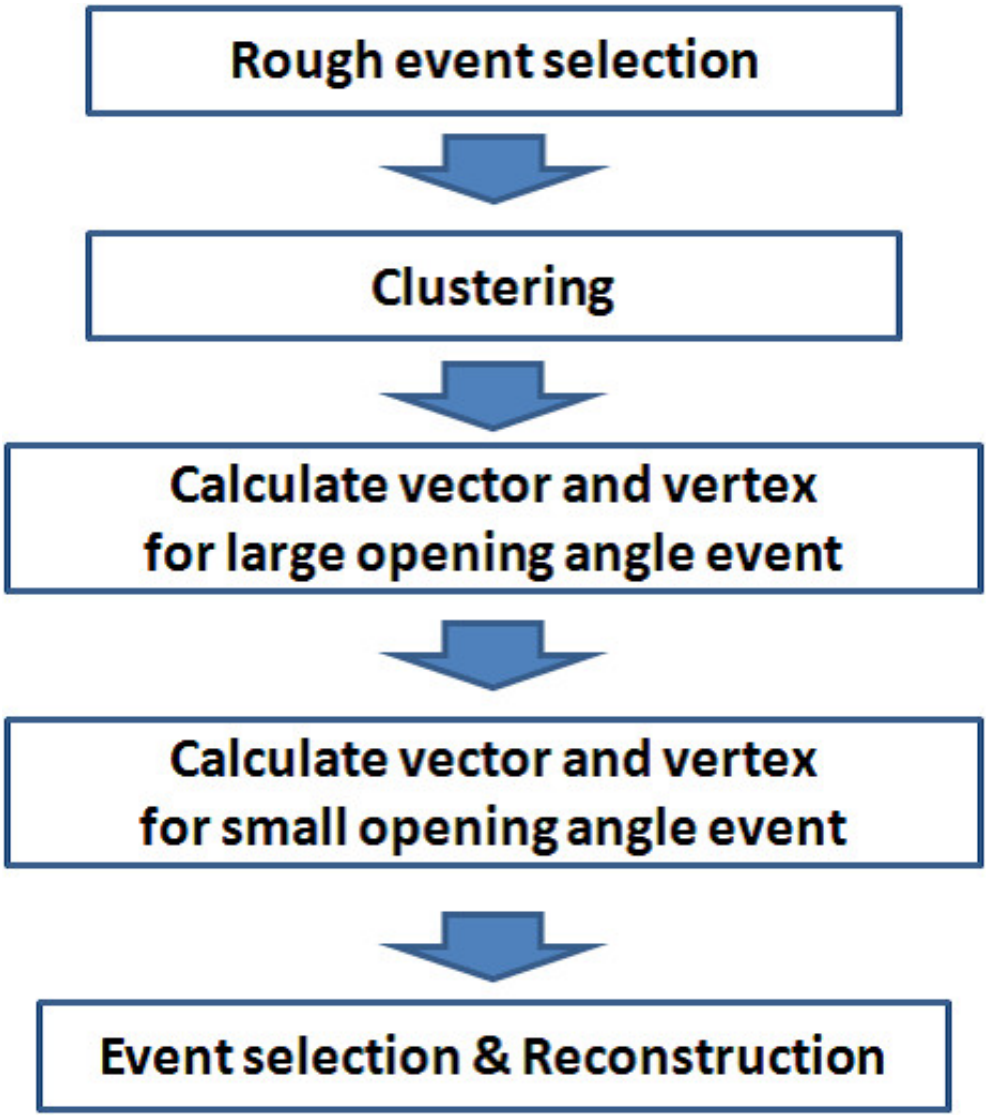

Figure 8.10: The flow chart of Hough transform method.

8.2.3 Hough transform for obtained data

In the experiment, we obtain the data set (x_i, z_i) and (y_j, z_j) $(i = 1, 2, \cdots, n, j = 1, 2, \cdots, m$, n and m are the number of hit points) in X-Z and Y-Z planes, respectively. Then, we apply the Hough transform to each point, (x_i, z_i), and obtain sine curves in the Hough space. When applying the Hough transform, the quantization of the Hough space is needed because the data has few events which make complete "V" or line-like shapes. Thus, we divide the Hough space into 90×90 regions. For Y-X plane, the Hough transform is also applied.

If there exist the line shapes in the data space, the peaks should appear in the Hough space. For the true pair creation event, there appears one or two peaks in the Hough space, because such event makes "V" or line shape corresponding to the large or small opening angle one in the data space. Figure 8.11 shows the examples of the simulated events with a large and small opening angles, where such peaks are obviously found in the Hough space. In order to find two peaks in the Hough space, we find the maximum bin firstly. And then, we find the secondary maximum bin. When finding the secondary one, we consider two conditions: (1) the secondary one have to be 2 or more bins separated from the maximum one, and (2) the secondary one have to be local maximum point. We regard the event which has two peaks in the Hough space as a large opening angle event. If the secondary maximum peak is not found, the event is regarded as the small opening angle event. In following next 2 subsections, we treat the events with a large and small opening angles separately.

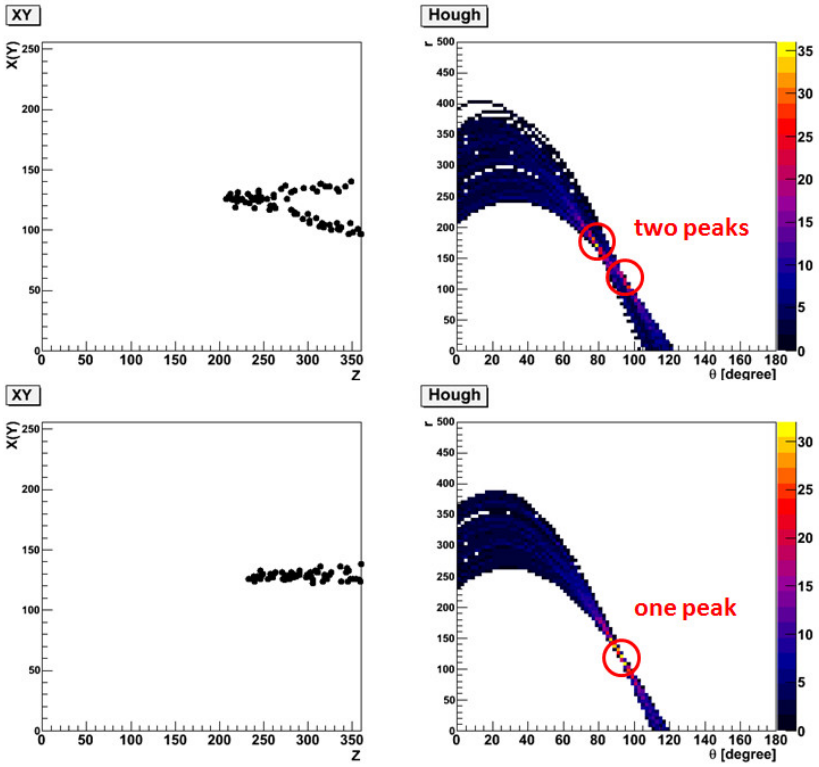

Figure 8.11: The examples of the events with large (top) and small (bottom) opening angle from simulation. Left figures are the events in data space. Right figures are the events in Hough space.

8.2.4 Calculation of vector and vertex point for large opening angle event

At first, we describe the event with a large opening angle. Using the two peaks derived from previous subsection and Equation (8.22), the approximate lines passing through the data points are calculated in X-Z (Y-Z) plane. It is not always true that the approximate lines are the best fit ones for the hit points. Then, we again cluster the hit points using the approximate lines, and each cluster is fitted by the straight line. Residuals between each approximate line and each hit point are calculated, and we obtain two residual distributions for the event in X-Z plane. In order to distinguish the hit points whether the hit points are near the approximate line or not, each distribution is fitted by Gaussian, and then the standard deviation, σ_{res}, is used for the clustering. We cluster the hit points which satisfy the following condition:

$$|residual| < \sigma_{res}. \tag{8.24}$$

Then, we obtain two clusters, C_1 and C_2, corresponding to electron and positron tracks in X-Z plane. Figure 8.12 shows the example of the clustering using the residual distributions as described above.

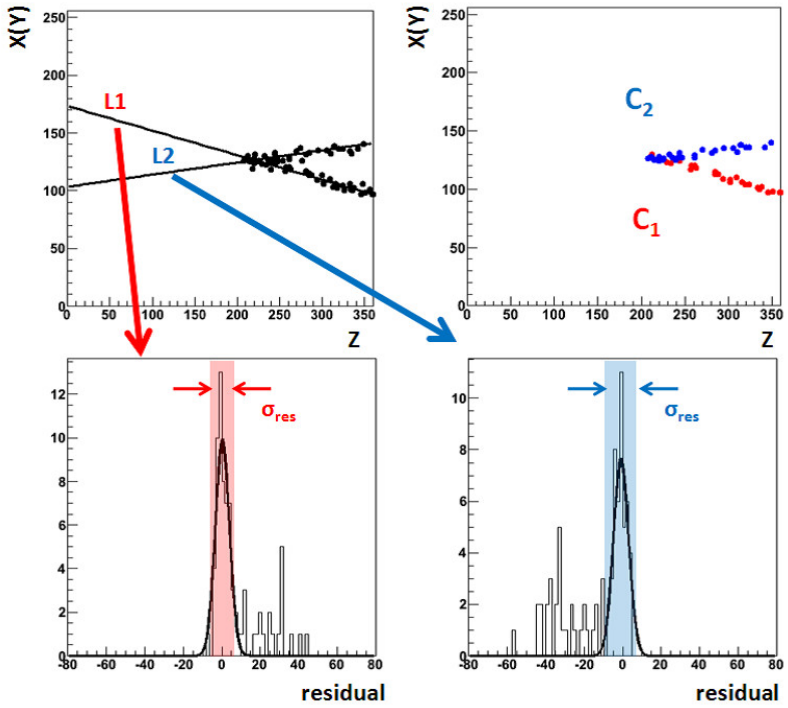

Figure 8.12: The simulated examples of the clustering using the residual distributions. Simulated hit points and the approximate lines, L1 and L2, given by Hough transform are plotted (upper left). Residual distributions of L1 (lower left) and L2 (lower right) are calculated by upper right one. For each distribution, the hit points with the condition of $|residual| < \sigma_{res}$ are clustered (upper right).

For each cluster, hit points in it are fitted by a straight line as well as Equations (8.9) and (8.10). Then we obtain two fit lines. Using these two lines, we calculate the vertex point, (x_{verXZ}, z_{verXZ}), in X-Z plane. For Y-Z plane, the fitting lines and the cross point, (y_{verYZ}, z_{verYZ}), are also calculated.

The unit vectors of the incident gamma ray projected to X-Z plane ($\vec{e}_{XZ}$) and to Y-Z plane ($\vec{e}_{YZ}$) are calculated using these fitting lines as well as subsection 8.1.4.

8.2.5 Calculation of vector and vertex point for small opening angle event

Next, events with a small opening angle is mentioned. Using the peak derived from subsection 8.2.3 and Equation (8.22), the approximate line passing through the data points are calculated in X-Z (Y-Z) plane as shown Figure 8.13. It is not always that the approximate line is the best fit one for the hit points as well as subsection 8.2.4. Thus, we cluster the hit points using the approximate line and then the cluster is fitted by the straight line. The residual distribution is calculated and the hit points satisfying the following condition are clustered:

$$|residual| < \sigma_{std}. \tag{8.25}$$

where σ_{std} is the standard deviation of the distribution. The hit points in the cluster are fitted by the straight line. In order to reject the event which is not obviously the true one, we apply "V" shape selection (Equation (8.13))to the fitted event.

For the remaining event, the point of the upstream side edge is considered to the vertex point, (x_{verXZ}, z_{verXZ}), in X-Z plane. For Y-Z plane, the cluster is fitted and the vertex point, (y_{verYZ}, z_{verYZ}), is calculated as well as X-Z plane. The projected vectors of the incident gamma ray, $\vec{e}_{XZ}$ and $\vec{e}_{YZ}$ in X-Z and Y-Z planes, respectively, are given by the fitting lines and the vertex points as well as subsection 8.2.4.

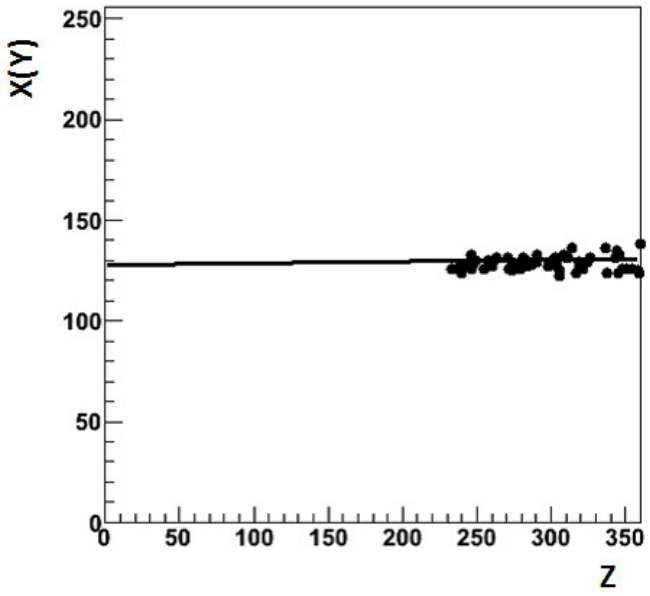

Figure 8.13: The examples of the hit points from simulation and the approximate line from the Hough transform.

8.2.6 Event selection and reconstruction

In order to select out the true pair creation event interacted in the μ-TPC, we apply two event selection to the event, fiducial and vertex cut, as well as subsection 8.1.6. Finally, the event which passes through above steps is considered as pair creation event. The unit vector of the incident gamma ray, $\vec{e}_{Inc}$ is given by $\vec{e}_{XZ}$ and $\vec{e}_{YZ}$ as well as subsection 8.1.6.

8.3 Validity confirmation

We confirmed the validity of the clustering method and the Hough transform method using Geant4 simulation. The physics models used in the simulation were the same as those in the ideal simulation in Section 3.4. Furthermore, the diffusion in the μ-TPC was also considered to that. Figure 8.14 shows the gamma-ray telescope in the simulation, which is the same geometry as that in the experiment. The beam parameters of the incident gamma ray (diameter and dispersion) were also the same as that in the experiment, which are investigated in past research [77].

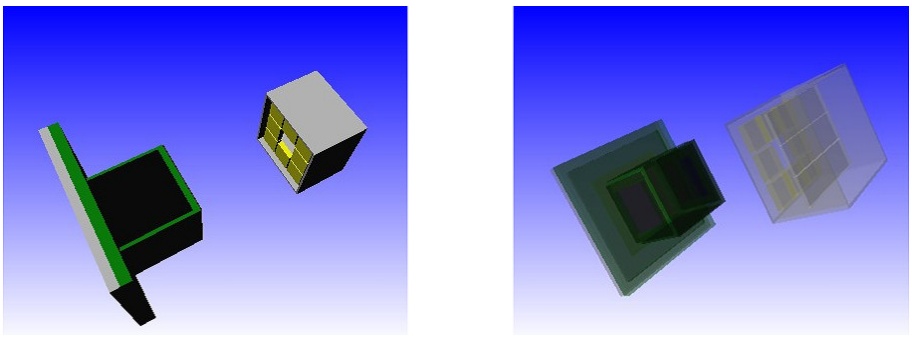

Figure 8.14: The gamma-ray telescope in the simulation, which is the same geometry as that in the experiment.

Using the gamma ray with the monochromatic energy of 10 and 20 MeV, the validity of the reconstruction with both the clustering and the Hough transform methods was confirmed, and two methods were compared. Figure 8.15 shows the reconstructed images and the distributions of the squared angular deviation (θ^2) between the reconstructed and generated direction of 10 and 20 MeV gamma rays using the clustering method. In these results, the method is available for the reconstruction of the pair creation event. The angular resolutions (68% containment) of 10 and 20 MeV gamma rays were expected to 9.3 and 7.8 degrees, respectively. The detection efficiencies of 10 and 20 MeV gamma rays were also estimated to 1.6×10^{-5} and 2.0×10^{-5}, respectively. Figure 8.16 shows the reconstructed images and θ^2 distributions of 10 and 20 MeV gamma rays using the Hough transform method. In these results, we can say that the Hough transform method is also available for the reconstruction of the pair creation event. The angular resolutions of 10 and 20 MeV gamma rays are expected to 8.1 and 6.4 degrees, respectively. The detection efficiencies of 10 and 20 MeV gamma rays were also estimated to 2.3×10^{-5} and 2.7×10^{-5}, respectively.

From these results, the angular resolution and the detection efficiency at 20 MeV gamma rays using the Hough transform method were better than those using the clustering method by factors of 1.2 and 1.4, respectively. Thus, we can say that the Hough transform method is effective for the reconstruction of pair creation events compared with the clustering method.

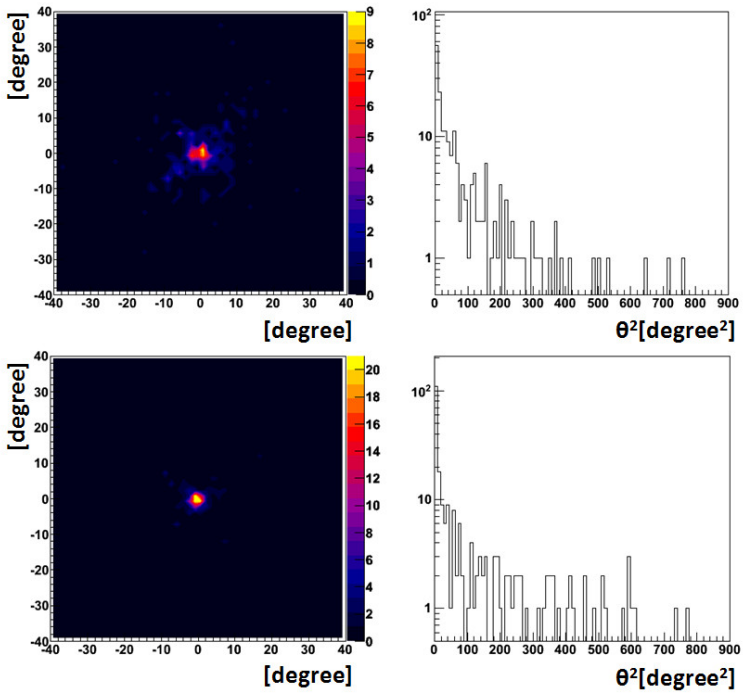

Figure 8.15: The reconstructed image (left) and the distribution of the squared angular deviation between the obtained and real origin (right) of 10 (top) and 20 (bottom) MeV gamma rays using the clustering method.

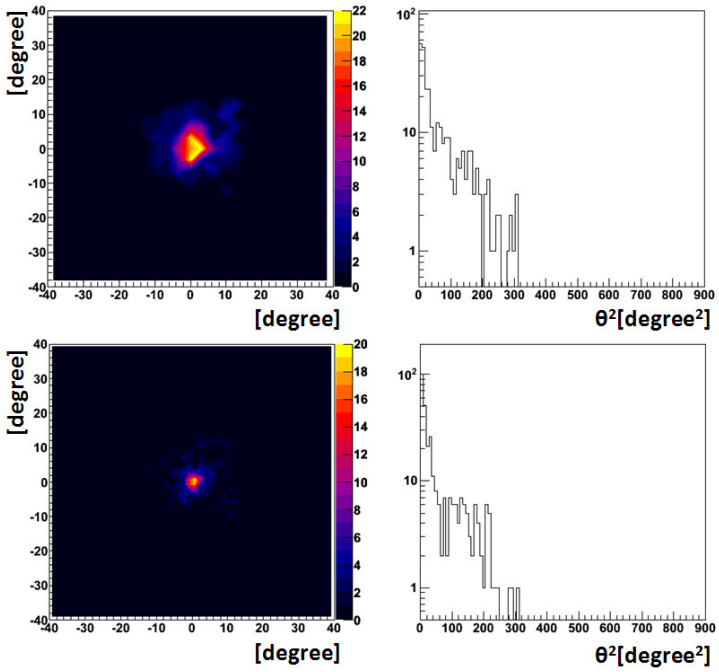

Figure 8.16: The reconstructed image (left) and the distribution of the squared angular deviation between the obtained and real origin (right) of 10 (top) and 20 (bottom) MeV gamma rays using the Hough transform method.

Chapter 9

Results

9.1 Results using clustering method

Top figures of Figures 9.1 and 9.2 show the typical pair creation events with large and small opening angles, respectively, which are obtained by the beam experiment. At first, we tried the clustering method and the results of track finding are shown in bottom figures of Figures 9.1 and 9.2. We can see that the clustering method is useful for the reconstruction.

Using the method, we obtained the 2-dimensional images of gamma rays at 8.7 and 18.0 MeV as shown in Figure 9.3. Figure 9.4 shows the θ^2 distributions for 8.7 and 18.0 MeV gamma rays, where θ is the angular deviation between the measured and real direction of the incident gamma rays. The angular resolutions, given as the half-angle cone containing 68 % of all reconstructed events, were 9.4±0.3 and 7.7±0.5 degrees for the 8.7 and 18.0 MeV gamma-ray beams, respectively. The energy dependences of the angular resolution are shown in Figure 9.5. For comparison, the angular resolutions of EGRET and MEGA [78] are also shown. Both the ideal angular resolutions with the use of the energy information of electron-positron pair and no-use of that (Equation (3.17) and (3.18)), given by subsection 3.4 are also shown in Figure 9.5, where multiple scattering in the gas and momentum transfer of the photon to nuclear was taken into account. The obtained angular resolutions are better by a factor of 1.5 over those of of the silicon strip detector of MEGA. However, the resolutions are worse than that of the ideal one (with no-use of the energy) by a factor of 2. This reason is discussed in next section.

The detection efficiency was defined by the ratio of the photon number of the reconstructed gamma rays to that of the incident ones, and it was estimated. Using the gamma-ray flux given by Table 7.1 and the results, we calculated the detection efficiencies for 8.7 and 18.0 MeV gamma rays. The estimated detection efficiency for 8.7 and 18.0 MeV gamma rays were $1.40\pm0.04\times10^{-5}$ and $1.40\pm0.08\times10^{-5}$, respectively. Figure 9.6 shows the estimated detection efficiency as a function of the energy of the incident gamma rays. Compared with the probability of pair creation in the μ-TPC, the obtained efficiency was smaller by an order of magnitude.

As described in Chapter 8, the clustering method is not complete one. Then, next we applied the Hough transform method to the obtained data and discuss the result in detail including the above results.

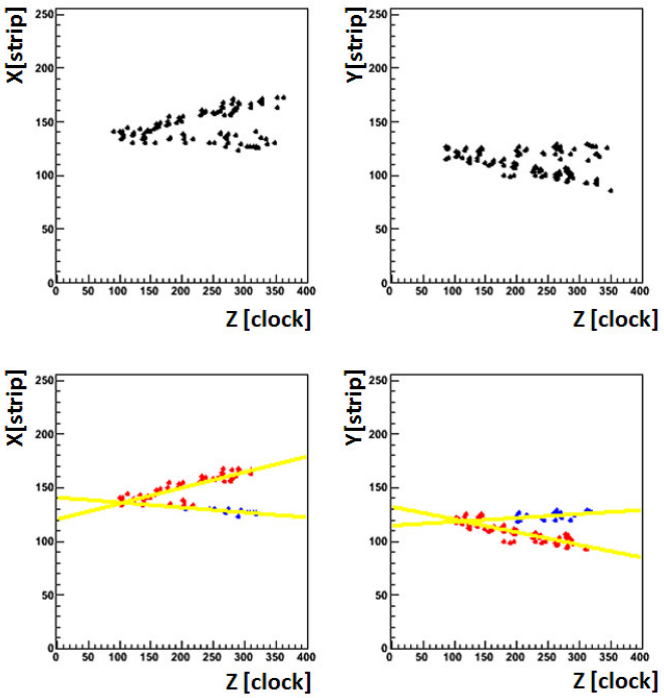

Figure 9.1: The event view of the pair creation event with large opening angle using the clustering method in the beam experiment.

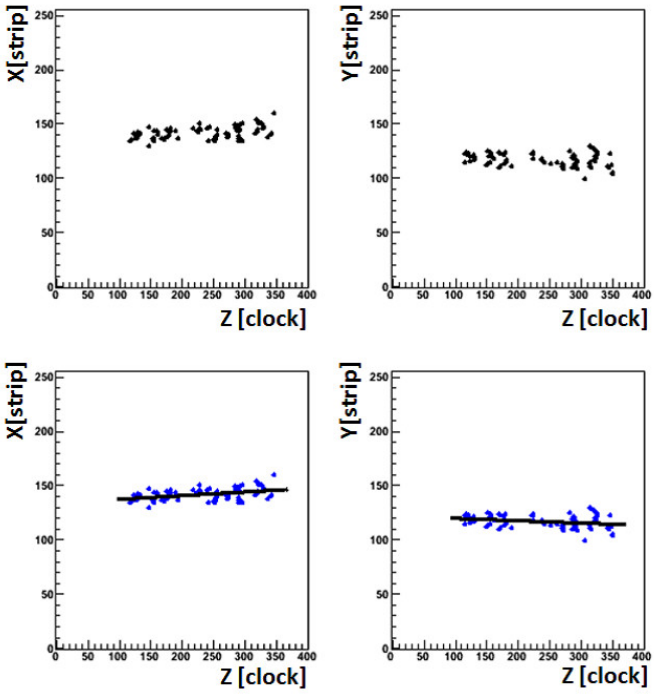

Figure 9.2: The event view of the pair creation event with large opening angle using the clustering method in the beam experiment.

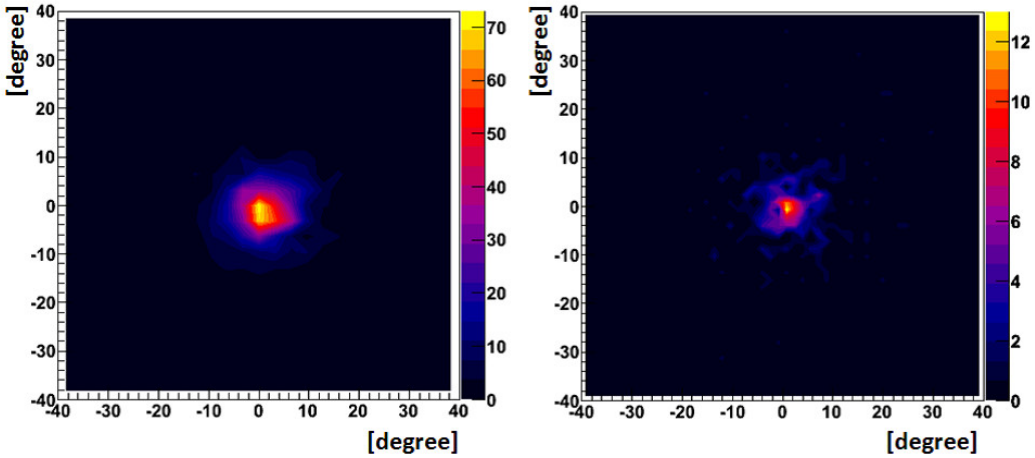

Figure 9.3: The obtained images at 8.7 (left) and 18.0 (right) MeV using the clustering method in the beam experiment.

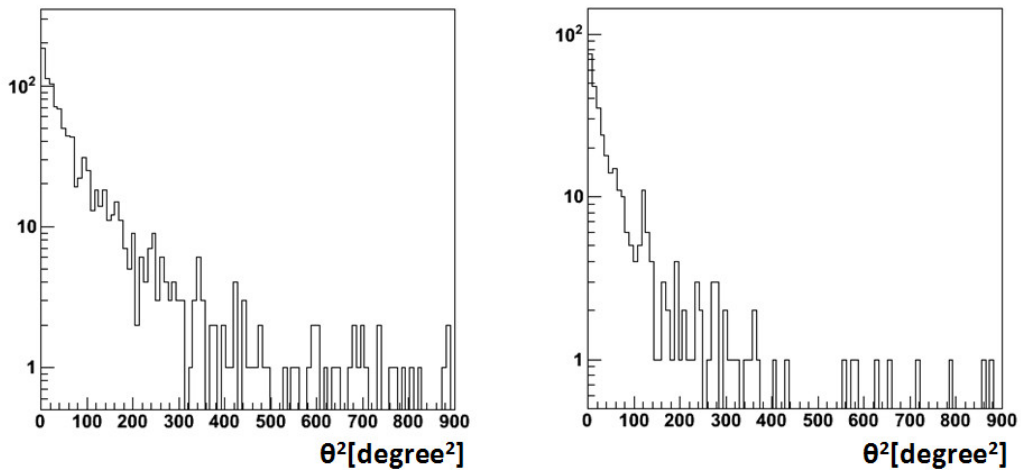

Figure 9.4: The θ squared distributions at 8.7 (left) and 18.0 (right) MeV using the clustering method in the beam experiment.

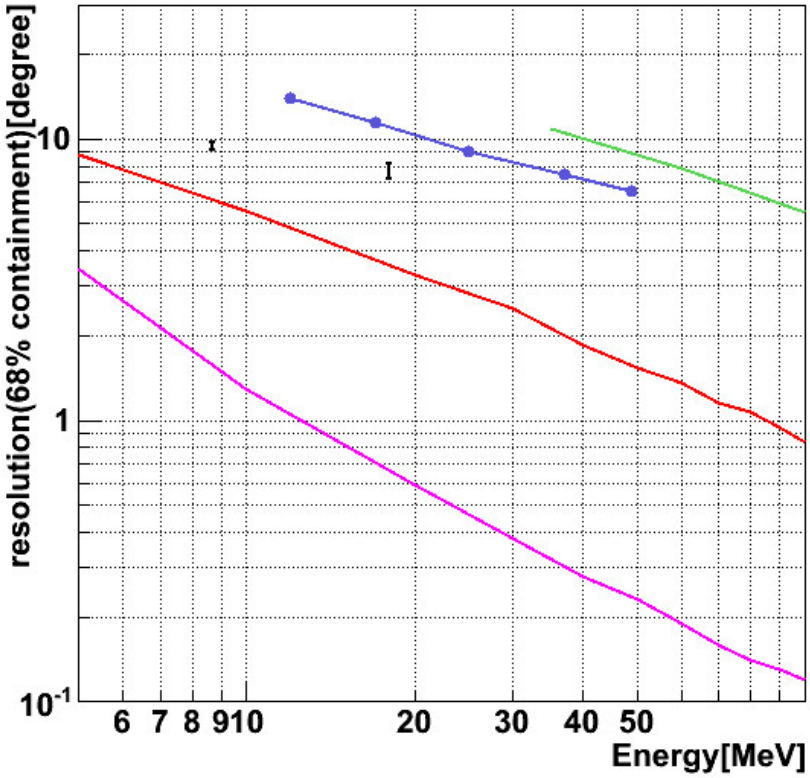

Figure 9.5: The angular resolutions of the gamma-ray telescope with pair creation mode (68% containment) The filled circles are the measured resolutions. For comparison, the resolutions of EGRET (green) and MEGA (blue) and the calculated ideal ones (pink and red)are also shown.

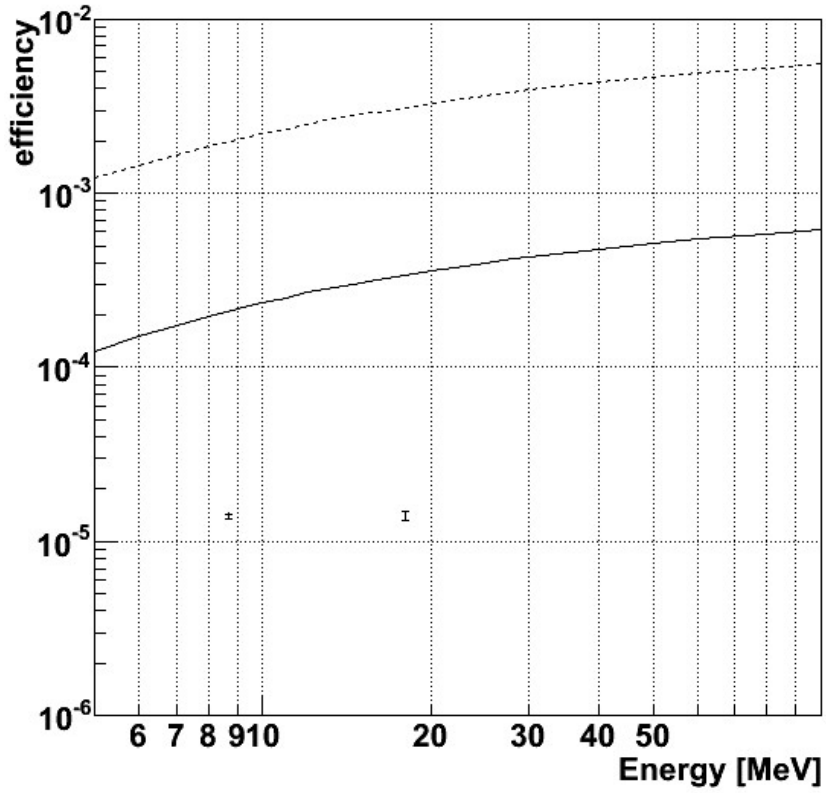

Figure 9.6: The estimated detection efficiency of the gamma-ray telescope with pair-creation mode using the clustering method. The solid line and dashed line are the probability of pair creation in the μ-TPC with Ar and C_2H_6 gas mixture (90:10) and Xe, respectively.

9.2 Results using Hough transform method

Figure 9.7 - 9.9 show the typical pair creation events obtained by the beam experiment, where the Hough transform method is applied. Here, upper and lower figures show the events in X-Z and Y-Z planes, respectively. (a) shows the obtained hit points and approximate lines derived from the Hough transform. (b) shows the events in the Hough space. (c) and (d) show the residual distributions between the approximate line and obtained hit points. It is noted that (d) is blank if there is only one peak in (b). (e) show the fitting lines. In this figures, we can see that the Hough transform method is also useful for the reconstruction.

Using the Hough transform method, we obtained the images of gamma rays at 8.7 and 18.0 MeV as shown in Figure 9.10. Figure 9.11 shows the θ^2 distributions for 8.7 and 18.0 MeV gamma rays. The angular resolutions, given as the half-angle cone containing 68 % of all reconstructed events as well as Section 9.1, were 8.4±0.3 and 7.0±0.4 degrees for the 8.7 and 18.0 MeV gamma-ray beams, respectively. The energy dependences of the angular resolution are shown in Figure 9.12. For comparison, the angular resolutions of EGRET and MEGA are also shown. Both the ideal angular resolutions with the use of the energy information of electron-positron pair and no-use of that given by subsection 3.4 and the resolutions given by clustering method are also shown in Figure 9.12. In addition, the resolutions simulated for this setup plotted in this figure. In this result, we can see that the angular resolutions are improved by a factor of 1.1 over those given by clustering method. Furthermore, the obtained angular resolutions are consistent with the simulated ones. The obtained angular resolutions are better by a factor of 1.7 or more than those of other detectors in other missions. On the other hand, the gaps of the resolutions between the ideal (without energy information) and obtained ones at 8.7 and 18.0 MeV are a factor of 1.5 and 2, respectively. Simulation shows that this gap is due to the loss of the small opening angle events by the hollow of the scintillator. The energy dependency of the gap is due to the tendency that the event with small angle increase when the energy increase. In the sky, the μ-TPC can be surrounded by the scintillation camera completely without the exclusion of the center unit. Thus, the angular resolutions are expected to be close to the ideal (without energy information). Furthermore, when we set the pixel readout system and set the scintillation camera inside the vessel, the energy information would be obtained and the energy loss by the vessel wall is reduced. Thus, the ideal (with energy information) angular resolution would be realized in future.

The detection efficiency was also estimated as shown in Figure 9.13. Using the gamma-ray flux given by Table 7.1 and the results, we calculated the detection efficiency for 8.7 and 18.0 MeV gamma rays as well as Section 9.1. For comparison, the probabilities of pair creation in the Ar based gas mixture and Xe at 1 atm in the μ-TPC are plotted. The estimated detection efficiency for 8.7 and 18.0 MeV gamma rays were $1.68\pm0.05\times10^{-5}$ and $1.77\pm0.08\pm0.35\times10^{-5}$, respectively, where the uncertainty due to the efficiency of two-photon linear crystal for the gamma-ray beam was considered to the error of the efficiency for 18.0 MeV. In this result, we can see that the detection efficiency at 18.0 MeV is improved by a factor of 1.3 over those given by clustering method. The results are roughly consistent with those from simulation with the systematic error of 10%. It is considered that the uncertainty of the position of the incident point of the laser makes the uncertainty of the gamma-ray flux and this makes the systematic error of 10%. In the high energy region, the detection efficiency decrease due to the detector design described above. Compared with the probability of pair creation in the μ-TPC, the obtained efficiency was smaller by an order of magnitude. This is because the area covered by the scintillation camera was not large enough, and also the influence of multiple scattering in the vessel was large. When we develop a larger scintillation camera and set it inside the vessel, the detection efficiency is expected to be close to the pair creation probability. Furthermore, we expect that the detection efficiency will be improved using a larger μ-TPC and selecting a gas

with high Z such as Xe, while the angular resolution using Xe is worse by a factor of 2 than that using Ar based gas mixture, as described in Figure 3.20.

As described in Chapter 4, we plan to use CF_4 gas for the μ-TPC in the Compton mode. Thus, we consider the potential of use of CF_4 gas for the pair creation mode. If we make the gamma-ray telescope with a volume of 1 m^3 filled with CF_4 gas at 2 atm and set the scintillation camera inside the vessel, the telescope should achieve an effective area of about 100 cm^2 as shown in Figure 9.14. For Comparison, the effective areas of current telescope and other detector of other missions are also plotted in this figure. The angular resolution in such condition achieve less than 1 degree at 50 MeV as shown in Fig 3.20. This effective area is similar to those of EGRET and Fermi at energies below 100 MeV, while its angular resolution would be better by a factor of 10. Thus CF_4 gas is available for the pair creation mode. Furthermore, we can say that our telescope is very useful for the observation of the several tens of MeV gamma rays.

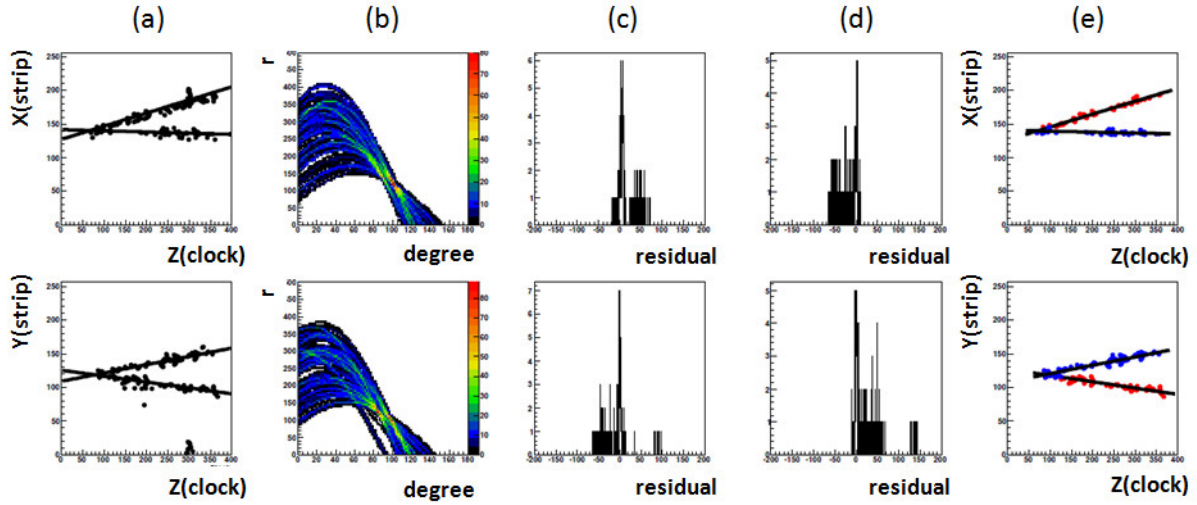

Figure 9.7: The event view of the pair creation event with large opening angle using the Hough transform method in the beam experiment.

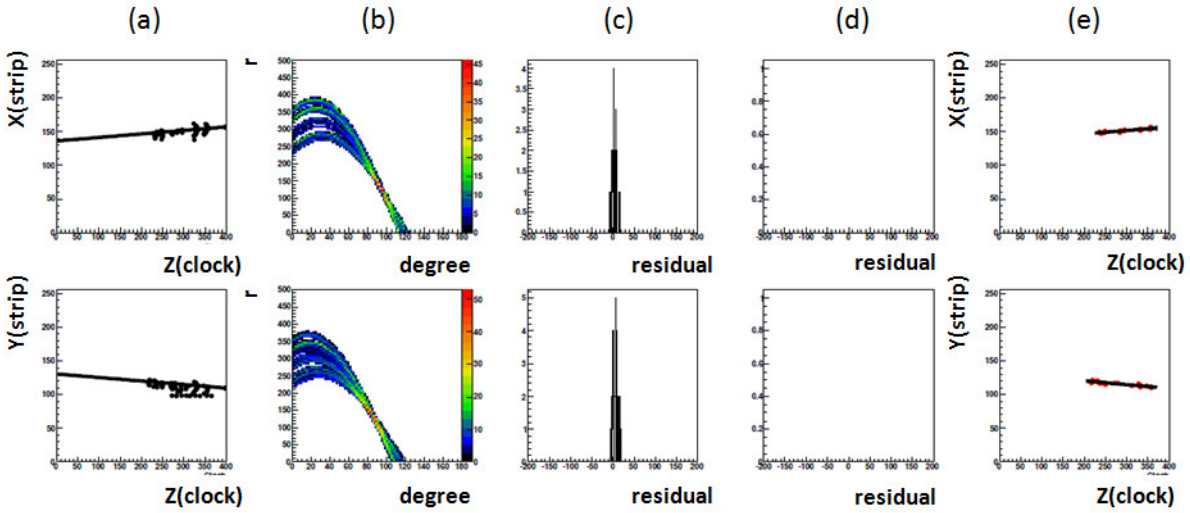

Figure 9.8: The event view of the pair creation event with large opening angle using the Hough transform method in the beam experiment.

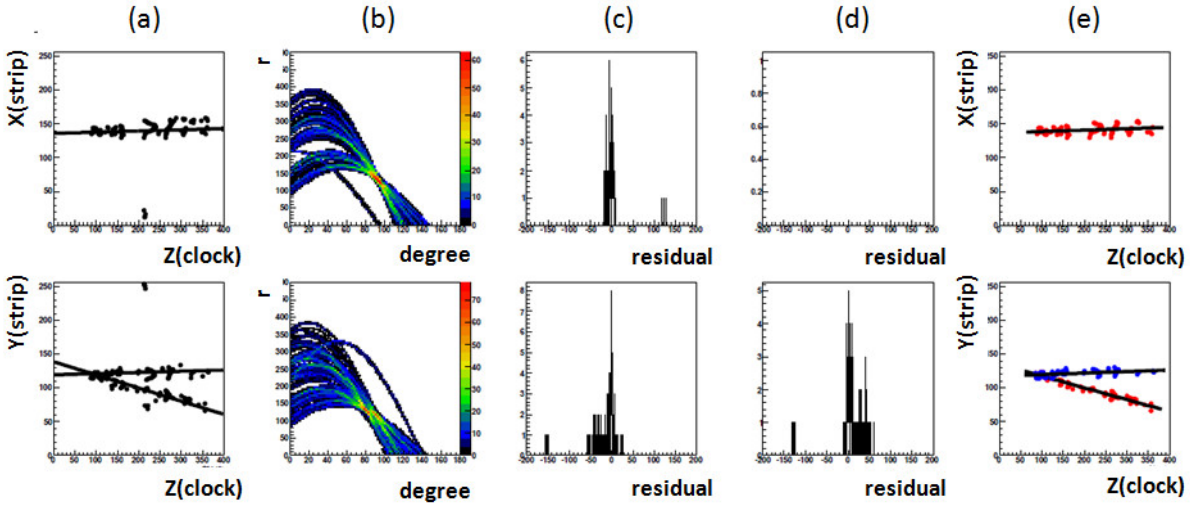

Figure 9.9: The event view of the pair creation event with large opening angle using the Hough transform method in the beam experiment.

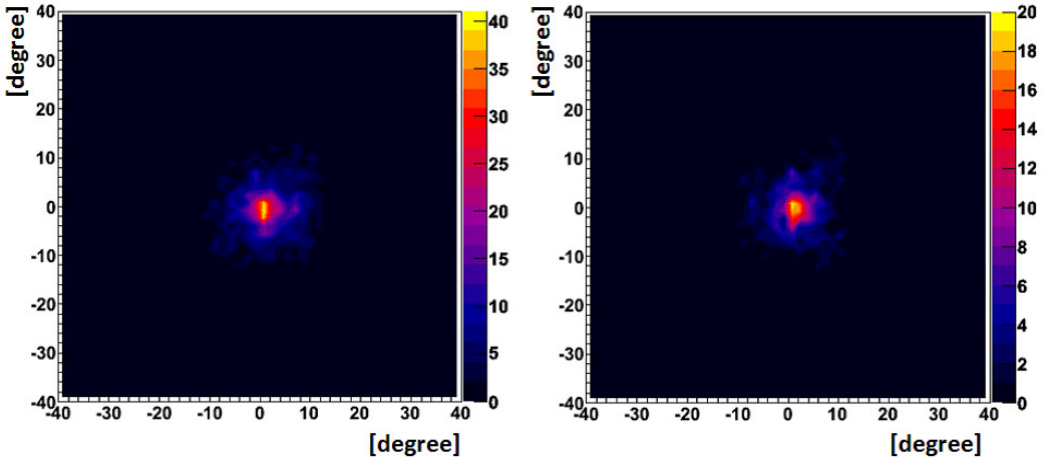

Figure 9.10: The obtained images at 8.7 (left) and 18.0 (right) MeV using the Hough transform method in the beam experiment.

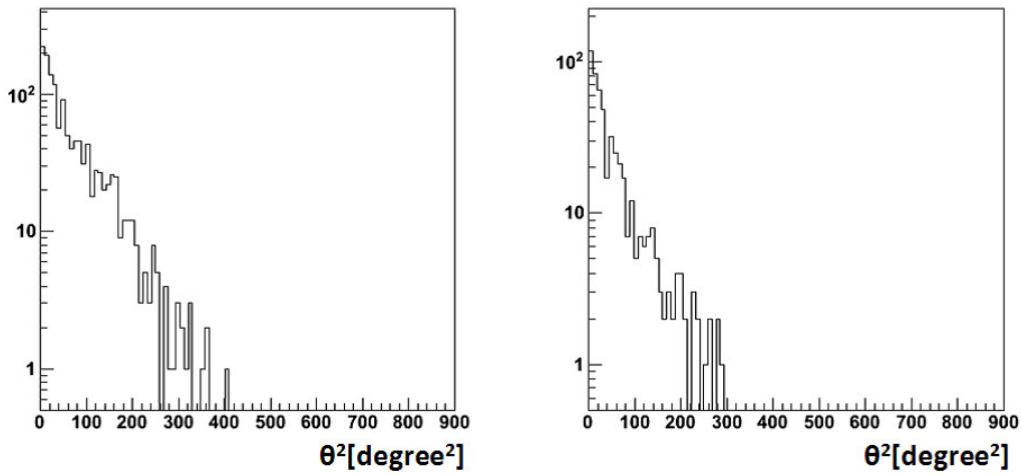

Figure 9.11: The θ^2 distributions at 8.7 (left) and 18.0 (right) MeV using the Hough transform method in the beam experiment.

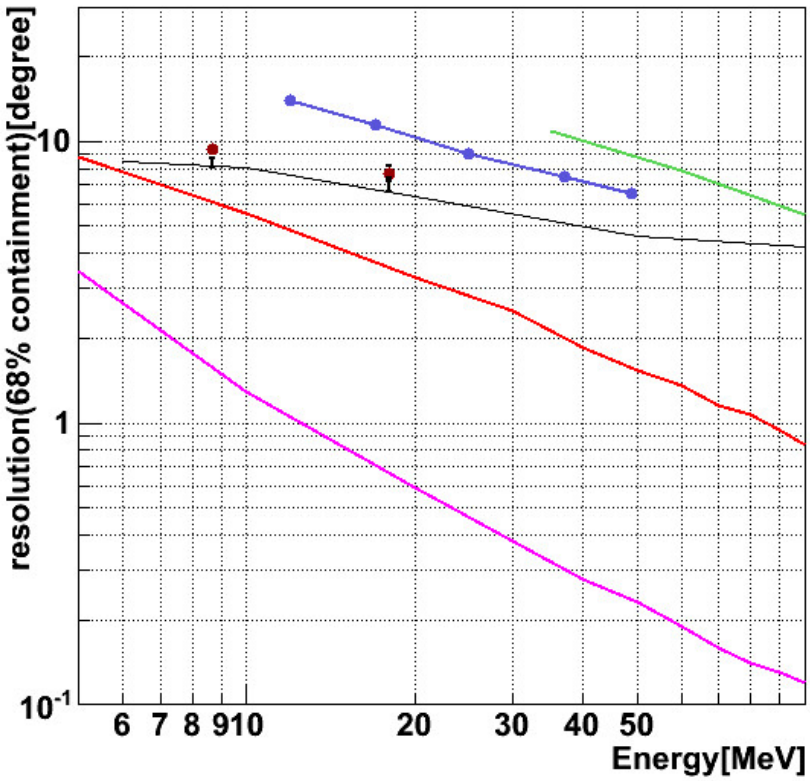

Figure 9.12: The angular resolutions of the gamma-ray telescope with pair creation mode (68% containment) using the Hough transform method. The resolutions using the clustering method are also plotted (filled brown circles). Black line show the ones from simulation. For comparison, the resolutions of EGRET (green) and MEGA (blue) and the calculated ideal ones (pink and red)are also shown.

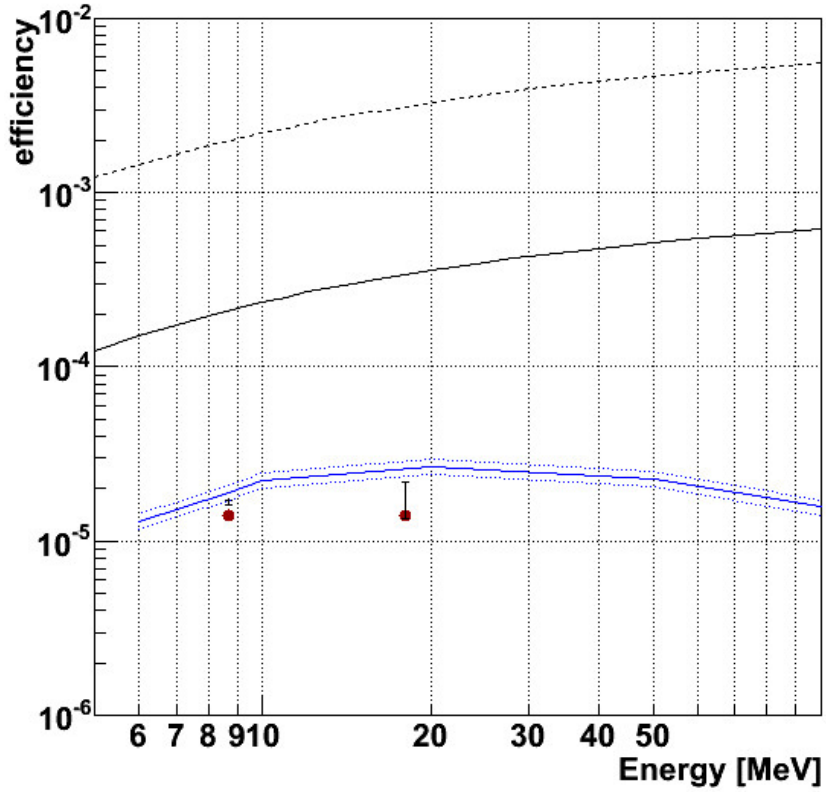

Figure 9.13: The estimated detection efficiency of the gamma-ray telescope with pair-creation mode using the Hough transform method. The efficiencies using the clustering method are also plotted. Blue solid and dashed lines show the ones from simulation and ones with the systematic error of 10 %, respectively. The black solid line and dashed line are the probability of pair creation in the μ-TPC with Ar and C_2H_6 gas mixture (90:10) and Xe, respectively.

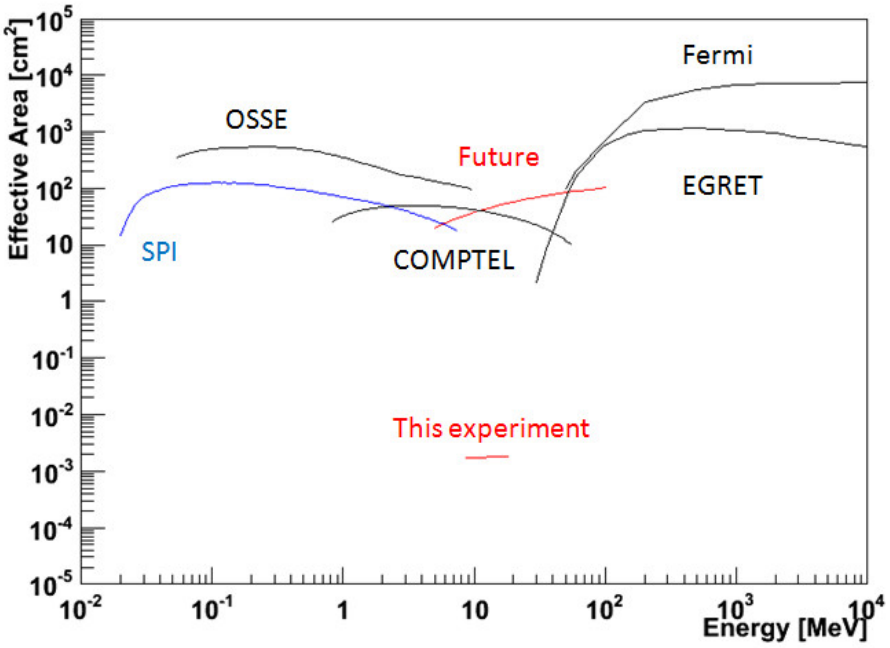

Figure 9.14: The expected effective area. For comparison, the effective area in other mission are also plotted [30, 79–81].

Part IV

Summary

Chapter 10

Discussion

We developed the large size gamma-ray telescope with Compton mode and investigated its fundamental performance. And the proof-of-principle experiment of the gamma-ray telescope with pair creation mode was also performed. There are still some items of improvement of the gamma-ray telescope for the all sky survey.

In this chapter, we describe the summary of current status of our gamma-ray telescope and the improvements. Then, the expected performance after improvements are estimated.

10.1 Current status

Figure 10.1 shows the angular resolution of our gamma-ray telescope with both Compton and pair creation modes, which are obtained by this work. For comparison, the angular resolutions of other missions are also plotted in this figure.

Using the results of this work, we also estimated the continuum detection sensitivity of the gamma-ray telescope with both Compton and pair creation modes. In the low energy region ($<\sim$ 10 MeV), diffuse cosmic and atmospheric gamma rays, and those induced by charged particles and neutrons, which were obtained by the first balloon experiment [54], would form the background when we observe a celestial source. On the other hand, in the high energy region ($>\sim$ 10 MeV), only diffuse cosmic gamma rays would form the background. The minimal detectable flux F_{min} for a point source at the significance of 3σ is described as

$$F_{min} = 3\sqrt{\frac{f\Delta E\Delta\Omega}{A_{eff}T_{obs}}}, \tag{10.1}$$

where f is the energy spectrum of background radiation in units of photons s^{-1} cm^{-2} sr^{-1} MeV^{-1}, and A_{eff}, T_{obs}, ΔE, and $\Delta\Omega$ are the effective area, effective observation time, energy resolution, and angular resolution, respectively [1]. Figure 10.2 shows the calculated sensitivity of the gamma-ray telescope, assuming $\Delta E = E$ and $T_{obs} = 10^6$s.

From these results, we found that more improvements of the angular resolution and the effective area of the gamma-ray telescope were needed.

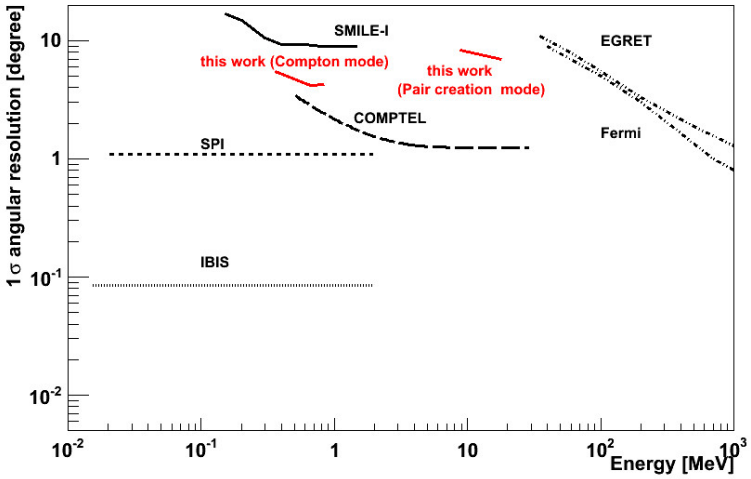

Figure 10.1: The angular resolution of our prototype gamma-ray telescope with both Compton and pair creation modes. For comparison, the angular resolutions of other missions are also plotted [30, 79, 80, 84, 85].

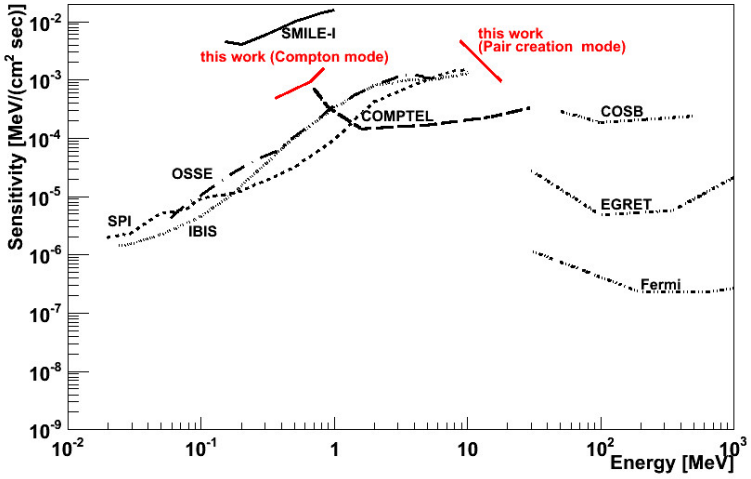

Figure 10.2: The sensitivity of our prototype gamma-ray telescope with both Compton and pair creation modes for continuum component. For comparison, the sensitivity of other missions are also plotted [30, 79, 80, 84, 85].

10.2 Future work

For the Compton mode, the angular resolution stems from the ARM. As described in Equation (3.4), the ARM depends mostly on the energy resolution of the scintillation camera. Thus, improving the energy resolution of the scintillation camera would give the telescope better angular resolution. A good ARM of 4 degrees (FWHM) at 662 keV was realized using a recently developed scintillator, $LaBr_3$(Ce) [82, 83]. From these results, the expected ARM would be 1.7 degrees (FWHM) at 2 MeV. For the pair creation mode, the angular resolution is expected to be less than 1 degrees when we use the energy information of electron-positron pair for the reconstruction and set the scintillation camera inside the vessel without the exclusion of the PSA unit, as described in previous chapter. With these improvements for the angular resolution, the expected angular resolutions are expected as shown in Figure 10.3. Expected angular resolution satisfies our requirements, "less than about 1 degrees in sub to 100 MeV gamma-ray region".

In order to improve the effective area, we have some ideas. First, we will develop larger telescope simply. If we construct the μ-TPC with the size of 1 m^3, the effective area improves by a factor of about 10^3 compared to the μ-TPC with the size of $10\times10\times15$ cm^3. Second, we will adopt CF_4 gas for the μ-TPC as described in Section 4.1. Compared with Xe gas (used for SMILE-1), the electron diffusion during electron drift and the multiple scattering effect of the Compton recoil electron and converted electron-positron pair are better. Thus, more accurate tracing of the electron/positron track is expected. Furthermore, for the Compton mode, the position resolution of the Compton points and the accuracy of the Compton recoil direction would be improved by updating the tracking algorithm.

If we realize the gamma-ray telescope with a volume of 1 m^3 filled with CF_4 gas at a higher pressure of 2 atm and the scintillation camera composed of $LaBr_3$ PSAs which surrounds the μ-TPC inside the vessel, the sensitivity will become ten times better than that of COMPTEL in the sub to 100 MeV region as shown in Figure 10.4.

From these estimations, we can say that it is possible to have the all sky survey with the ten times better sensitivity than COMPTEL with the angular resolution of about 1 degree in the energy range from sub to 100 MeV using the gamma-ray telescope based on the μ-TPC and the scintillation camera in the future.

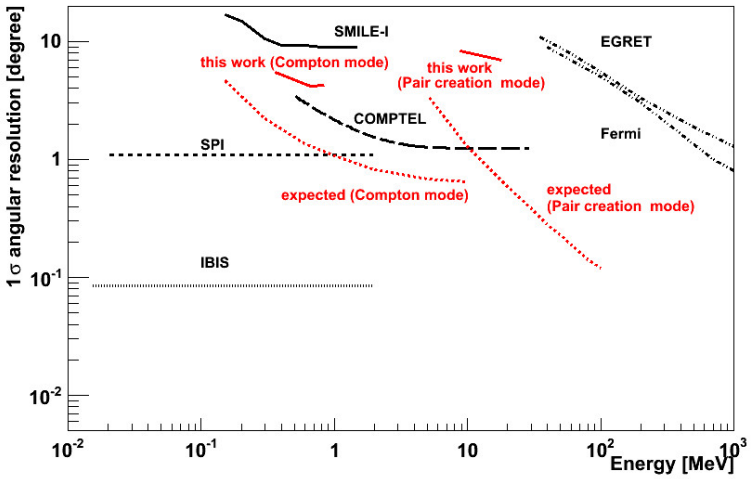

Figure 10.3: The expected angular resolution of our gamma-ray telescope with both Compton and pair creation modes.

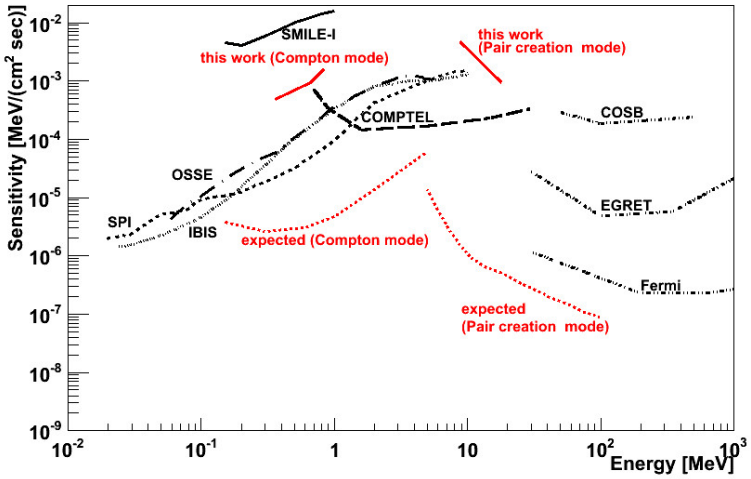

Figure 10.4: The expected sensitivity of our gamma-ray telescope with both Compton and pair creation modes.

Chapter 11

Conclusion

In the MeV and multi-MeV gamma-ray astronomy, some observations with telescopes using a Compton scattering or pair-creation, for example, COMPTEL and EGRET onboard CGRO, have been successful. However, the detection sensitivity and angular resolution of those in the energy range from sub to several tens of MeV are worse than those of detectors in the X-ray, GeV, and TeV gamma-ray regions. In the low-energy region where Compton scattering becomes dominant, the sensitivity is low since the telescope suffers from large background. In the high-energy region where pair creation becomes dominant, the angular resolution is bad because of influence of multiple scattering. Thus, a new observation technique for MeV gamma-ray telescope is required. Therefore, we have developed a tracking Compton and pair-creation gamma-ray telescope using a gaseous time projection chamber (μ-TPC) based on a micro-pixel chamber (μ-PIC) and a GSO(Ce) scintillation camera for the aim to conduct all sky survey with a sensitivity 10 times better than that of COMPTEL and an angular resolution of 1 degree. Several prototypes with a detection volume of $10\times10\times10$ cm^3 were developed and their performances with Compton mode in the low energy range were already studied. As the preliminary step toward the all sky survey, we proceed the balloon experiments, and first experiment for the purpose of the observation of the cosmic diffuse and atmospheric background gamma rays with Compton mode was done in 2006.

For the next experiment for the purpose of the observation of bright celestial objects, the enlargement of the telescope is needed in order to improve the effective area. Thus, for the first step to the next experiment, we developed and constructed the prototype of the large telescope which was based on a $30\times30\times30$ cm^3 μ-TPC using the sealed Ar and C_2H_6 (90:10) gas mixture at 1 atm and a 30×30 cm^2 scintillation camera. We succeeded in the gamma-ray imaging and investigated the fundamental performances of the telescope. For the 662 keV gamma rays, the energy resolution and the angular resolutions ARM/SPD were 16%, 10°, and 110° at FWHM, respectively. The effective area was 6.6×10^{-3}. Also the FOV of the telescope with Compton mode of 1 str. was obtained. In order to detect photons of a bright source like Crab or Cyg X-1, we need more improvement of the detection efficiency of the telescope. For the improvement, we consider the use of CF_4 gas for the μ-TPC at 2 atm. After adding this improvement, our telescope would be able to obtain a few hundred photons from Crab during a level flight for 6 hours, because the efficiency will be 10 times larger than that of the telescope of the first experiment.

Furthermore, for the next experiment, saving power consumption of all the system of the telescope in the sky is also quite important. In the first experiment, the readout system of the scintillation camera (33 PMTs) consumed the most power. For the next experiment, we need finally 108 or more PMTs in order to improve the effective area. Thus, we developed a new readout system with a commercial ASIC and an attenuator board, and investigated the performance of the scintillation camera with the system. We obtained good energy and position

resolutions of 10.6% (FWHM) and less than 6 mm, respectively, and a wide energy dynamic range of the scintillation camera of 30 - 900 keV with low power consumption of 1.7 W/64ch (1 PSA).

In parallel, we started to develop the gamma-ray telescope with pair creation mode. For the first step of the pair creation mode, we performed the principle-proof experiment of the telescope. The telescope was composed of a $10\times10\times15$ cm^3 μ-TPC with CFRP gas vessel and a 200 cm^2 scintillation camera which was used for only trigger counter. Using this telescope, we had a first beam-experiment using a laser inverse Compton gamma-ray beam at National Institute of Advanced Industrial Science and Technology (AIST) and succeeded in tracking electron-positron pair. The mean energies of the gamma rays were 8.7 and 18.0 MeV, respectively, and incident photon numbers of 8.7 and 18.0 MeV gamma rays were estimated to 8.0×10^7 (live time = 5580 sec.) and 2.9×10^7 (live time = 4980 sec.), respectively. For the reconstruction of the pair creation events, we developed new methods using the clustering and Hough transform. Using this method, the obtained data was reconstructed and we succeeded in the gamma-ray imaging for the pair creation events. Then, we investigated the fundamental performances of the telescope with the pair creation mode. For the 18 MeV gamma rays, the angular resolution was 7.0° at 68% containment. This value was better by a factor of 2 or more than that of other detector of other mission. The detection efficiency was 1.77×10^{-5}. This value was roughly consistent with the simulated one, which was 10 times worse than that of the probability of the pair creation in the gas due to the loss of the small opening angle events by the hollow of the scintillation camera in the beam-experiment setup. This results says that if we set the scintillation camera surrounds the μ-TPC completely, the efficiency is expected to be close to the ideal one with no-use of the energy information of the electron-positron pair. Furthermore, if we set the scintillation camera inside the vessel and apply pixel readout system for the μ-TPC, both the angular resolution and the efficiency is expected to be very close to the ideal ones (with use of the energy information of the electron-positron pair.

On the basis of the results described above, we expected that the angular resolution and the sensitivity of our gamma-ray telescope with both Compton and pair creation modes assuming some improvements achieve our goal. If we make the gamma-ray telescope based on a μ-TPC with the volume of 1 m^3 filled with CF_4 gas at 2 atm and a scintillation camera composed of $LaBr_3$ PSAs which surrounds the μ-TPC inside the vessel, we expect that the angular resolution and the sensitivity achieve our goal in the energy range of sub to several tens of MeV.

Reference

[1] V. Schönfelder; "The Universe in Gamma Rays", *Springer* (2001).

[2] M.Oda and K. Matshuoka; *Progress in Elementary Particles and Cosmic-Ray Physics*, **10** (1971), 305.

[3] K. S. Cheng, G. E. Romero; "Cosmic Gamma-Ray Sources", textitKluwer Academic publishers (2004).

[4] P. V. Ballmoos; *Experimental Astronomy*, **6** (1995) 85.

[5] V. Schönfelder et al.; *Astron. Astrophys. Suppl. Ser.*, **143** (2000) 145.

[6] R. C. Hartman et al.; *ApJS*, **123** (1999) 79.

[7] S. E. Boggs et al.; *ApJ*, **544** (2000) 320.

[8] M. Pohl; astro-ph/9807267.

[9] R. A. Chevalier; *Nature*, **355** (1992) 691.

[10] A. Lyne and F. G. Smith; "Pulsar Astronomy", *Cambridge* (2005).

[11] D. J. Thompson et al.; *ApJ*, **516** (1999) 297.

[12] L. Kuiper et al.; *A& A*, **378** (2001) 918.

[13] F. A. Aharonian, A. M. Atoyan; astro-ph/9803091.

[14] M. L. McConnell et al.; *ApJ*, **572** (2002) 984.

[15] W. R. Purcell et al.; *ApJ*, **491** (1997) 725.

[16] G. Weidenspointner et al.; *A & A*, **450** (2006) 1013.

[17] R. Schödel et al.; *Nature*, **419** (2002) 694.

[18] C. M. Urry, P. Padovani; (http://heasarc.gsfc.nasa.gov/docs/objects/agn/agn_model.html)

[19] M. Chiaberge et al.; *MNRAS*, **324** (2001) 33.

[20] L. Maraschi, F. Tavecchio; astro-ph/0102295.

[21] G. H. Share, R. J. Murphy; *ASP Conference Series*, **206** (2000) 377.

[22] M. S. Briggs et al.; *ApJ*, **524** (1999) 82.

[23] W. S. Paciesas et al.; *ApJS*, **122** (1999) 465.

[24] XCOM; Photon Cross Section Database
(http://physics.nist.gov/PhysRefData/Xcom/Text/XCOM.html).

[25] G. F. Knoll; "Radiation Detection and Measurement 3rd edition", *WILEY* (2001).

[26] M. S. Longair; "High Energy Astrophysics", *Cambridge university press*, (1994).

[27] Jean in't Zand; "Coded Aperture Imaging in High-Energy Astronomy",
(http://lheawww.gsfc.nasa.gov/docs/cai/coded.html).

[28] P. v. Ballmoos et al.; *Exp. Astron.*, **20** (2005) 253.

[29] P. v. Ballmoos; *Proc. of Astronomy with Radioactivities IV and MeV Gamma-Ray Telescopes*,
(http://www.mpe.mpg.de/gamma/science/lines/workshops/seeon03/ballmoos_1.pdf).

[30] V. Schönfelder et al.; *ApJS*, **86** (1993) 657.

[31] J. M. Ryan; *Proc. of Astronomy with Radioactivities IV and MeV Gamma-Ray Telescopes*
(http://www.mpe.mpg.de/gamma/science/lines/workshops/seeon03/ryan_1.pdf).

[32] T. Kamae et al.; *NIM*, **A260** (1987) 254.

[33] W. Coburn et al.; *Proc. SPIE*, **5898** (2005).

[34] P. F. Bloser et al.; *New Astronomy Reviews*, **46** (2002) 611.

[35] A. Zoglauer, G. Kanbach; *Proceeding of SPIE*, **4851** (2003) 1302.

[36] G. R. Lynch, O. I. Dahl; *NIM*, **B 58** (1991) 6.

[37] R. D. Evans; "The Atomic Nucleus", *McGraw-Hill Inc.* (1955).

[38] G. E. Modesitt and H. W. Koch; *Phys. Rev.*, **77** (1950) 175.

[39] R. Jost, M. Luttinger, and M. Slotnick; *Phys. Rev.*, **80** (1950) 189.

[40] Y. S. Tsai; *Rev. Mod. Phys.*, **46** (1974) 815.

[41] Y. S. Tsai; *Rev. Mod. Phys.*, **49** (1977) 421.

[42] L. Urban; "Cern Program Library", (1993)

[43] S. Agostinelli et al; *NIM*, **A 506** (2003) 250.

[44] GEANT4
(http://geant4.cern.ch/)

[45] Livermore low-energy electromagnetic models
(https://twiki.cern.ch/twiki/bin/view/Geant4/LoweMigratedLivermore)

[46] D. Cullen, J. H. Hubbell, L. Kissel; UCRL-50400, Vol.6, Rev.5.

[47] S. T. Perkins, D. E. Cullen, S. M. Seltzer; UCRL-50400, Vol.31.

[48] S. T. Perkins et al; UCRL-50400, Vol.30.

[49] L. Urban; CERN-OPEN-2002-070.

[50] L. Urban; CERN-OPEN-2006-077.

[51] M. Takahashi et al; *NIM*, **A** in press.

[52] A. Ochi et al; *NIM*, **A 478** (2002) 196.

[53] T. Nagayoshi et al; *NIM*, **A 513** (2003) 277.

[54] A. Takada; Ph. D. Thesis, Kyoto Univ. (2007)

[55] O, Sasaki and M. Yoshida; *IEEE Trans. Nucl. Sci.*, **46** (1999) 1871

[56] F. Sauli; *NIM*, **A 386** (1997) 531

[57] Hamamatsu Technical Data Sheet H8500-H8500B (http://www.hamamatsu.com/)

[58] H. Nishimura et al; *NIM*, **A 573** (2007) 115.

[59] T. Matsumoto et al; *NIM*, **A 521** (2004) 367.

[60] R. Pani et al; *NIM*, **A 513** (2003) 36.

[61] R. Pani et al; *NIM*, **A 527** (2004) 54.

[62] M. Gimenez et al; *NIM*, **A 525** (2004) 298.

[63] D. Herbert et al; *NIM*, **A 518** (2004) 399.

[64] K. Hattori; Ph. D. Thesis, Kyoto Univ. (2009)

[65] R. H. Milburn; *Phys. Rev. Lett.*, **10** (1963) 75.

[66] O. F. Kulikov et al; *Phys. Lett.*, **13** (1964) 344.

[67] A. M. Sandorfi et al; *IEEE Trans. Nucl. Sci.*, **30** (1983) 3083

[68] T. Nakano et al; *Nucl. Phys.*, **A 629** (1998) 559.

[69] T. Yamazaki et al; *IEEE Trans. Nucl. Sci*, **32** (1985) 3406.

[70] T. Nakano et al; *Nucl. Phys.*, **A 684** (2001) 71.

[71] S. Miyamoto et al; *Radiat. Meas.*, **41** (2007) 179.

[72] S. Amano et al; *NIM*, **A 602** (2009) 337.

[73] H. Toyokawa et al; *NIM*, **A 608** (2009) 41.

[74] H. Toyokawa et al; *Proc. Part. Acc. Conf.* (2003).

[75] P. V. C. Hough; *U.S. Patent* No. 3,069654. (1962).

[76] R. O. Duda and P. E. Hart; *Comm. ACM.* **15** (1972) 11.

[77] H. Toyokawa et al; *IEEE Trans. Nucl. Sci*, **55** (2008) 3571.

[78] G. Kanbach et al; *NIM*, **A 541** (2005) 310.

[79] Fermi LAT performance
(http://www-glast.slac.stanford.edu/software/IS/glast lat performance.htm)

[80] D. J. Thompson et al; *ApJS*, **86** (1993) 629.

[81] D. Attie et al; *A & A*, **411** (2003) 71.

[82] S. Kurosawa et al; *IEEE Trans. Nucl. Sci.*, **56** (2010) 3779.

[83] S. Kurosawa et al; *NIM*, **A 623** (2010) 249.

[84] G. Vedrenne et al; *A & A*, **411** (2003) 63.

[85] A. Bazzano et al; *NIM*, **A 513** (2003) 118.

Acknowledgments

I would like to express my gratitude to Professor Toru Tanimori for his guidance and encouragements in this work. This thesis would not be completed without his support. Special thanks also to Dr. Hidetoshi Kubo whose opinions and information have helped me very much throughout the production of this study. Also I would like to thank μ-PIC collaborators: Dr. K. Miuchi, Dr. S. Kabuki, Dr. J. D. Parker, Dr. Y. Kishimoto, S. Kurosawa, S. Iwaki, C. Ida, M. Takahashi, N. Higashi, T. Sawano, K. Taniue, K. Nakamura (Kyoto Univ.), Dr. T. Nagayoshi (RIGAKU), Dr. H. Sekiya (ICRR), Dr. K. Tsuchiya (Police), Y. Tsuchiya, Dr. H. Nishimura, and Dr. K. Hattori (Okayama Univ.). I am grateful to all the member of the cosmic ray laboratory in Kyoto University for their continuous discussions and encouragements.

I sincerely thank Dr. H. Toyokawa (AIST) for a lot of advices and assistances in performing this beam experiment.

This work was supported by the Global COE Program "The Next Generation of Physics, Spun from Universality and Emergence", a Grant-in-Aid for the 21st Century COE "Center for Diversity and Universality in Physics", a Grand-in-Aid in Scientific Research of the Japan Ministry of Education, Culture, Science, Sports, Technology (MEXT), "SENTAN" by the Japan Science and Technology Agency (JST), and JSPS Research Fellowships for Young Scientists.

Finally, I express my appreciation to my wife Eri and my parents for their lasting assistance and encouragements.